



**HAL**  
open science

# Conductivity of contact interfaces : a multi-scale study

Paul Beguin

► **To cite this version:**

Paul Beguin. Conductivity of contact interfaces : a multi-scale study. Materials. Université Paris sciences et lettres, 2024. English. NNT : 2024UPSLM021 . tel-04804021

**HAL Id: tel-04804021**

**<https://pastel.hal.science/tel-04804021v1>**

Submitted on 26 Nov 2024

**HAL** is a multi-disciplinary open access archive for the deposit and dissemination of scientific research documents, whether they are published or not. The documents may come from teaching and research institutions in France or abroad, or from public or private research centers.

L'archive ouverte pluridisciplinaire **HAL**, est destinée au dépôt et à la diffusion de documents scientifiques de niveau recherche, publiés ou non, émanant des établissements d'enseignement et de recherche français ou étrangers, des laboratoires publics ou privés.



**THÈSE DE DOCTORAT**  
**DE L'UNIVERSITÉ PSL**

Préparée à MINES Paris

**Conductivity of Contact Interfaces:  
A Multi-Scale Study**

**Conductivité des interfaces de contact :  
Une étude multi-échelle**

Soutenance par

**Paul BEGUIN**

le 11 janvier 2024

École doctorale n°621

**Ingénierie des Systèmes,  
Matériaux, Mécanique,  
Energétique**

Spécialité

**Mécanique**

Composition du jury :

Lars PASTEWKA Professeur, Universität Freiburg	<i>Rapporteur</i>
Stéphanie CHAILLAT Directrice de recherche CNRS, ENSTA Paris	<i>Rapporteur</i>
Michele CIAVARELLA Professeur, Politecnico di Bari	<i>President</i>
Zhi-Qiang FENG Professeur, Université d'Evry	<i>Examineur</i>
Lucas FRÉROT Maître de conférence, Sorbonne Université	<i>Examineur</i>
Vladislav A. YASTREBOV Chargé de recherche CNRS, MINES Paris - PSL	<i>Directeur</i>
Samuel FOREST Directeur de recherche CNRS, MINES Paris - PSL	<i>Directeur</i>
Cristian OVALLE-RODAS Chargé de recherche, MINES Paris - PSL	<i>Examineur</i>



## ■ ■ Résumé

Le problème de la résistance à la conduction aux interfaces de contact représente un défi important en ingénierie. À ces interfaces, la section réduite pour la conduction – définie comme la disparité entre les zones de contact réelles et nominales – entraîne une augmentation de la résistance. Ce phénomène affecte à la fois la conductivité thermique et électrique, marqué par un écart de température ou de potentiel à l'interface. Par conséquent, c'est un phénomène multi-échelle, découlant de la rugosité des surfaces en contact et ayant son origine à l'échelle microscopique. L'objectif de cette étude est d'approfondir notre compréhension des origines de ce phénomène.

Pour aborder le problème de conduction à l'interface de contact, une méthode des éléments de frontière rapide (BEM) a été mise en œuvre. Cette méthode, bénéficiant d'une formulation précise en demi-espace, démontre sa précision et sa cohérence géométrique. Simultanément, le Fast-BEM contourne la complexité excessive  $O(N^2)$  associée au stockage et à la construction d'une matrice dense, qui a été un goulot d'étranglement pour la BEM classique. Cette amélioration des performances est obtenue grâce à l'utilisation de matrices hiérarchiques (H-matrices), qui bénéficient d'une approximation de bas rang, telle que l'approximation croisée adaptative plus (ACA+). Cette mise en œuvre réduit considérablement le stockage en mémoire, encore amélioré par l'utilisation de la décomposition en valeurs singulières (SVD), et est finalement exploitée pour résoudre le problème avec un solveur itératif GMRES. Par conséquent, ce nouvel outil a démontré sa capacité à aborder des problèmes de conductivité impliquant des géométries complexes.

L'étude de la conductivité commence par une tache conducteur unique sur un demi-espace. Initialement, la forme la plus simple d'une tache non simplement connecté, un anneau, est examinée. Elle est suivie par une investigation de formes "multi-pétales", telles que des fleurs, étoiles et engrenages, révélant comment le nombre de pétales impacte la conductivité. L'étude de taches isolées se conclut par un examen élaboré de géométries auto-affines. Pour les taches multi-pétales et auto-affines, des modèles phénoménologiques sont développés, basés sur des caractéristiques géométriques pertinentes, incluant l'exposant de Hurst et les trois premiers moments spectraux du contour auto-affine. Ces modèles permettent de prédire la conductivité pour un nombre infini de "pétales" et dans la limite auto-affine fractale. Le rôle de la dimension fractale est également souligné, accompagné d'une brève exploration des flocons de Koch.

L'étude s'étend à un scénario multi-taches plus réaliste, employant le modèle de résistance à la constriction de Greenwood étendu pour inclure des taches multi-pétales, validé par des simulations BEM. Enfin, l'étude examine la conductivité des zones de contact réelles avec des morphologies complexes produites par le contact élastique entre surfaces rugueuses. Cette étude finale utilise la méthode FFT-BEM pour résoudre le problème de contact et de conductivité rugueux, en s'appuyant sur une analogie de poinçon plat entre la rigidité normale et la résistance thermique

ou électrique. De plus, le problème des surfaces rugueuses oxydées est exploré, fusionnant FFT-BEM et Fast-BEM avec des îlots d'oxyde isolants construits à partir d'un champ aléatoire auto-affine. Un modèle phénoménologique préliminaire est également suggéré.

Cette thèse représente une synthèse de la mise en œuvre de H-matrices pour le Fast-BEM, combinée à une caractérisation géométrique détaillée et une analyse physique complète de la résistance à la constriction. Cette analyse s'étend des interfaces conductrices à une seule tache aux zones de contact oxydées de topologie complexe produites par le contact de surfaces rugueuses. Une attention particulière a été accordée à maintenir la précision des résultats numériques. De plus, la mise en œuvre du Fast-BEM développée est disponible en open-source pour une utilisation plus large.

## Abstract

The problem of conduction resistance at contact interfaces represents an important engineering challenge. At these interfaces, the reduced section for conduction – defined as the disparity between the actual and nominal contact areas – results in increased resistance. This phenomenon affects both thermal and electrical conductivity, marked by a temperature or potential gap at the interface. Hence, it is a multi-scale phenomenon, stemming from the roughness of contacting surfaces and originating at the microscopic level. The objective of this study is to deepen our understanding of this phenomenon's origins at the microscopic scale.

To address the conduction problem at the contact interface, a Fast-Boundary Element Method (BEM) has been implemented. This method, benefiting from an accurate half-space formulation, demonstrates its precision and geometric consistency. Simultaneously, the Fast-BEM circumvents the excessive  $O(N^2)$  complexity associated with storing and constructing a dense matrix, which has been a bottleneck for the classical BEM. This performance enhancement is achieved through the use of hierarchical matrices (H-matrices), which benefit from a low-rank approximation, such as Adaptive Cross Approximation+ (ACA+). This implementation significantly reduces memory storage, further enhanced by employing Singular Value Decomposition (SVD), and is ultimately exploited in solving the problem with a GMRES iterative solver. Consequently, this new tool has demonstrated its capability to tackle realistic conductivity problems involving complex geometries. The conductivity study starts with a single conductive spot on a half-space. Initially, the simplest form of a non-simply connected spot, an annulus, is examined. This is followed by an investigation of "multi-petal" shapes, such as flowers, stars, and gears, revealing how the number of petals impacts conductivity. The study of single spots concludes with an elaborate examination of self-affine geometries. For both multi-petal and self-affine spots, phenomenological models are developed, grounded in relevant geometrical characteristics, including the Hurst exponent and the first three spectral moments of the self-affine contour. These models enable predicting conductivity for an infinite number of "petals" and in the fractal self-affine limit. The role of fractal dimension is also underscored, accompanied by a brief exploration of Koch snowflakes.

The study extends to a more realistic multi-spot scenario, employing the Greenwood constriction resistance model extended to include multi-petal spots, validated through BEM simulations. Ultimately, the study examines the conductivity of true contact areas with complex morphologies produced by elastic contact be-

tween rough surfaces. This final study utilizes the FFT-BEM method to resolve rough contact and conductivity problem, drawing on a flat-punch analogy between normal stiffness and thermal or electrical resistance. Additionally, the issue of rough oxidized surfaces is explored, merging FFT-BEM and Fast-BEM with insulating oxide islands constructed from a self-affine random field. A preliminary phenomenological model is also suggested.

This thesis represents a synthesis of H-matrices implementation for Fast-BEM, combined with detailed geometrical characterization and a comprehensive physical analysis of constriction resistance. This analysis spans from single-spot conductive interfaces to oxidized contact areas of complex topology produced by the contact of rough surfaces. Particular attention has been devoted to maintaining the precision of the numerical results. Furthermore, the developed Fast-BEM implementation is available as an open-source for broader use.



---

## Acknowledgements

---

Je remercie les membres du jury, tout particulièrement Mme Stéphanie Chaillat, et M Lars Pastewka pour avoir rapporté cette thèse, M Michele Ciavarella pour avoir fait l'honneur d'être président du jury, et enfin M Zhi-Qiang Feng et M Lucas Frérot d'accepter ce rôle d'examineur.

Ce travail de thèse a été réalisé au sein de l'équipe simulation mécanique SIMS du centre des matériaux des Mines. Je remercie tous les membres de ce laboratoire qui m'ont accompagnés dans ce projet, bien qu'il ne fut que passager dans la vie du centre, et un peu original dans son contenu. Votre attention, votre bienveillance et votre engagement m'ont beaucoup aidé pendant ces trois ans, auxquels finalement cette thèse doit beaucoup, et qui me font déjà regretter Evry.

Parmi ces membres, je remercie particulièrement mes encadrants. Tout d'abord Vladislav Yastrebov, à l'initiative de ce projet, simplement sans qui rien n'aurait pu commencer. Tout ayant commencé avec l'étude des séismes glacières, ce fut donc naturel de continuer avec la résistance de contact. Deux sujets a priori différents, mais rassemblés par ta curiosité. Ta rigueur, ta bienveillance, ton empathie, et ta gentillesse m'ont toujours impressé, et m'auront permis de grandir en tant qu'ingénieur et que personne. Je suis extrêmement fier d'avoir pu m'associer à toi pendant ces quatre années. Je remercie également Samuel et Cristian, pour votre engagement et le reste de l'encadrement. Avoir travaillé avec vous fut une chance incroyable et une réelle source d'inspiration. Mais je regrette de n'en avoir pas plus profiter.

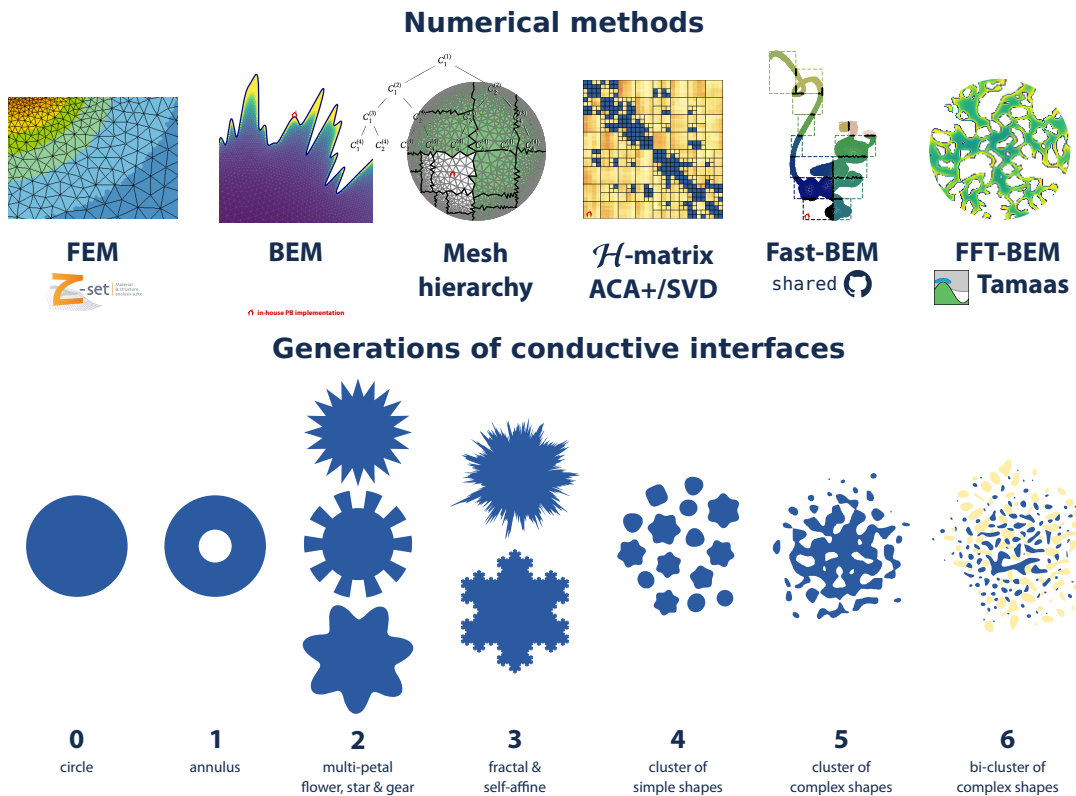
Je tiens également à remercier les autres doctorants du Centre des Matériaux. Je salue les trois générations d'apprentis chercheurs du B108, Aldo et Natan, Arjun, et enfin Elodie, Clément et Florian, pour cette dernière année. Je vous souhaite tous le meilleur, et je ne suis pas trop inquiet; mon portrait et celui du Pape François continueront de veiller sur vous je l'espère. Je salue également les autres doctorants, Edouard, Arthur, Flavien, Baptiste, Pierrick, Daniel et des autres promotions, Clément(x2), Régis, Rawad, Darhia, Nicolas.. Djamel et Vincent, je vous remercie pour m'avoir accompagné en tant que comité de suivi pendant ces trois ans. Enfin Basile et Laurent, je vous remercie pour votre aide indispensable en Python, Git, GMSH, toujours disponibles et redoutable d'efficacité.

Enfin, je remercie ma famille, à qui je dois tout. Nos vies suivent des trajectoires, inspirées par d'autres traces. Curieusement cette thèse en me ramenant à Evry, m'a aussi rapprochée de la campagne vénitienne. Pendant c'est trois années, j'ai parfois senti quelques difficultés à expliquer concrètement mon travail. Je dois mon salut à l'étude thermique du paté en croute, reconnectant ma thèse au monde réel. Culinairement, je suis aussi content de partager cette réussite avec celle de Fluffy; bravo à toi Hortense! Merci de m'avoir fait partager un temps la passion du brunch parisien, et de m'avoir tant soutenu. Moi non plus je sais pas ce que te rend aussi gentille; l'amour de Sylvie et Henri-Pierre et que tu remets dans tes pains de mie. Enfin je remercie mes amis, pour



tous les moments passés ensemble, les week-end à Diou, aux Poulies, les cocktails à la bétonnière, ou les barbecues fumés. Pour conclure, je crois que j'ai fait tout ce qui était en mon pouvoir, j'ai fait le maximum, à ce niveau là où on en est je crois qu'on peut dire à la grâce de Dieu: Thank you, Lord, for the gift of science!

## Graphical abstract



## Manuscript organization

**Chapter 1: Introduction & the State of the Art** This chapter sets the foundation for our exploration into the contact of surfaces and conductive resistance. Section 1.1 delves into the contact of smooth surfaces, drawing parallels with conductive resistance. It covers the mechanics of contact problems, the analogy to conductive resistance, and the intricacies of hardness and plastic deformation. Section 1.2 shifts the focus to the contact of rough surfaces, investigating the physics behind it, various models of roughness, analytical models for contact of rough surface, the concept of plasticity index, and numerical methods employed in this context. In section 1.3, we concentrate on conductive resistance, discussing the real conductance effect, material coatings, oxides and thermomechanical coupling.

**Chapter 2: Numerical Methods** Chapter 2 is dedicated to numerical methods focusing on conduction. It starts with an integral formulation for conduction, addressing the conductivity problem, the principle of reciprocity, the fundamental solution, and the solution for two-dimensional problems, among other topics. This is followed by an exploration of the classical Boundary Element Method (BEM): discretization, interpolation, numerical integration, and validation. The main focus is however put on an in-depth look at the Fast-BEM constructed through the concept of hierarchical matrices. It discusses approximation construction, error analysis, H-matrix theory, and practical applications of these approximations, all demonstrated in numerous examples.

**Chapter 3: Conductivity of a Complex Shaped Contact Spot** In Chapter 3, the discussion narrows down to the conductivity of single contact spots with complex shapes. It starts with the conductivity of not simply connected spots, presenting analytic and finite element results. The novel results are obtained by examining the conductivity of flower-shaped and self-affine spots, providing insights into the link between conductive

properties and geometrical characteristics. Phenomenological models for these geometries are constructed. A brief discussion of the Koch snowflake conductivity is also provided. The chapter is complemented by a discussion of a simple superposition model applied to two-mode spots.

**Chapter 4: Multi-Spot Conductivity and the Effect of Oxides** This chapter addresses the multi-spot conductivity and the influence of oxides. It starts with a simple multi-spot contact in which self-resistance is adjusted to go beyond circular spots of Greenwood's model. These results are compared with full BEM analysis and a very good match is found. Accuracy of the FFT-BEM method for conductivity problem using incremental stiffness and flat punch analogies are addressed. But the main focus of the chapter is the combination of the FFT-BEM with the Fast-BEM for the conductivity problem for the contact of a rough spherical indenter with a half-space for clean and oxidized surface. A simple model based on a random self-affine field is used to construct oxide distribution. In the set-up a multitude of realizations for different roughness and oxide parameters were studied to capture mean trends and dispersion of results.

**Chapter 5: Conclusion** This chapter provides a comprehensive conclusion of the entire document, summarizing the key findings, implications, and potential areas for future research.

**Appendices** The appendices offer detailed insights into specific methods and models discussed in the document. Appendix A presents a transient solution for the thermal diffusion problem between two bars. Appendix B provides a deeper look into numerical methods associated with the Fast-BEM, covering such aspects as singular and quasi-singular integration, reference elements, and others. Appendix C focuses on the geometrical characteristics of spots with complex shapes as well as the physical consistency of constructed phenomenological models.

<b>1</b>	<b>Introduction and the State of the Art</b>	<b>15</b>
1.1	Contact of smooth surfaces and a conductivity analogy . . . . .	16
1.1.1	Contact problems in mechanics . . . . .	18
1.1.2	Equivalence with conductive resistance . . . . .	23
1.1.3	Hardness & plastic deformation . . . . .	25
1.2	Contact of rough surfaces . . . . .	26
1.2.1	Physics of rough contact . . . . .	26
1.2.2	Models of roughness . . . . .	28
1.2.3	Analytical models of rough contact . . . . .	33
1.2.4	Plasticity index . . . . .	35
1.2.5	Numerical methods . . . . .	35
1.3	Conductive resistance . . . . .	36
1.3.1	Constriction resistance . . . . .	36
1.3.2	Real conductance effect . . . . .	40
1.3.3	Material coating . . . . .	42
1.3.4	Joule heating and coupling effect . . . . .	43
<b>2</b>	<b>Numerical Methods</b>	<b>45</b>
2.1	Integral formulation for conduction . . . . .	47
2.1.1	Problem of conductivity . . . . .	47
2.1.2	Identity of reciprocity . . . . .	48
2.1.3	Elementary solution . . . . .	49
2.1.4	Solution for two dimensional problem . . . . .	50
2.1.5	Limits for Boundary Integral Equation . . . . .	51
2.1.6	Boundary Integral Equation for $H$ . . . . .	53
2.1.7	Application to the conductivity of a contact spot . . . . .	53
2.2	Boundary Element Method . . . . .	58
2.2.1	Discretization and linear system definition . . . . .	58
2.2.2	Construction of the linear system . . . . .	62
2.2.3	Numerical integration . . . . .	64
2.2.4	Validation with circular contact spot . . . . .	74
2.3	Fast-BEM . . . . .	78
2.3.1	Approximation construction . . . . .	78
2.3.2	Error in function of the rank . . . . .	86
2.3.3	$\mathcal{H}$ -matrix . . . . .	87
2.3.4	Application of the approximations . . . . .	95
2.3.5	$\mathcal{H}$ -solver . . . . .	106

<b>3</b>	<b>Conductivity of Complex-Shaped Contact Spots</b>	<b>113</b>
3.1	Introduction . . . . .	115
3.2	Conductivity of not simply connected spot . . . . .	116
3.2.1	Analytic result . . . . .	116
3.2.2	Finite element results . . . . .	117
3.3	Conductivity of flower-shaped spots . . . . .	120
3.3.1	Geometrical reduction . . . . .	122
3.3.2	Conductivity results . . . . .	124
3.3.3	Other "multi-petal" spots . . . . .	126
3.4	Conductivity of self-affine spots . . . . .	130
3.4.1	Geometry of spots . . . . .	130
3.4.2	Geometrical characteristics . . . . .	132
3.5	Two-mode spots . . . . .	146
3.5.1	Results and modeling . . . . .	148
3.6	Koch snowflake . . . . .	149
3.7	Conclusion . . . . .	152
3.7.1	Flower-shaped spots and other simple forms . . . . .	152
3.7.2	Conductivity of self-affine spots . . . . .	152
3.7.3	Contact spots between rough surfaces . . . . .	153
3.7.4	Supplementary work, two-modes spots, and Koch snowflake . . . . .	153
3.7.5	Conclusion . . . . .	153
<b>4</b>	<b>Multi-Spot Conductivity and the Effect of Oxides</b>	<b>155</b>
4.1	Introduction . . . . .	157
4.2	Multi-spot contact . . . . .	157
4.2.1	Geometrical construction . . . . .	157
4.2.2	Greenwood's Model . . . . .	159
4.2.3	Comparison with BEM and conclusion . . . . .	160
4.3	FFT-BEM for conductivity problem . . . . .	162
4.3.1	Circular contact spot . . . . .	164
4.3.2	Comparison with BEM . . . . .	166
4.3.3	Flower-shaped contact spots . . . . .	167
4.4	Elastic contact of rough oxidized spheres . . . . .	168
4.4.1	Real contact area . . . . .	168
4.4.2	Conductivity of a clean rough contact . . . . .	173
4.4.3	Oxidation analysis and results . . . . .	178
4.4.4	Comparison with BEM results . . . . .	181
4.5	Conclusion . . . . .	186
4.5.1	Multi-spots area . . . . .	187
4.5.2	Results on real contact area with oxidation . . . . .	187
4.5.3	Conclusion . . . . .	187
<b>5</b>	<b>Conclusion</b>	<b>191</b>
<b>A</b>	<b>Transient solution for thermal diffusion problem between two bars</b>	<b>193</b>
<b>B</b>	<b>Additional results for Fast-BEM</b>	<b>197</b>
B.1	Integration of H-function on the boundary . . . . .	197
B.2	Element of reference and shape function . . . . .	198
B.3	Quasi-singular integration . . . . .	198
B.3.1	Cubic transformation . . . . .	198
B.4	Singular integration . . . . .	201
B.4.1	Parametrization . . . . .	201
B.4.2	Triangular singular integration . . . . .	202

---

B.5	Approximations . . . . .	202
B.5.1	ACA-full Algorithm . . . . .	202
B.5.2	ACA+ . . . . .	202
B.6	Cluster tree of a non-compact shape . . . . .	203
<b>C</b>	<b>Conductivity of spots with complex shape</b>	<b>211</b>
C.1	Geometrical characteristics of self-affine spots . . . . .	211
C.2	Physical consistency of the phenomenological model . . . . .	212
<b>D</b>	<b>HBEM repository</b>	<b>215</b>



---

## Introduction and the State of the Art

---


### Contents

<b>1.1</b>	<b>Contact of smooth surfaces and a conductivity analogy</b>	<b>16</b>
1.1.1	Contact problems in mechanics	18
1.1.2	Equivalence with conductive resistance	23
1.1.3	Hardness & plastic deformation	25
<b>1.2</b>	<b>Contact of rough surfaces</b>	<b>26</b>
1.2.1	Physics of rough contact	26
1.2.2	Models of roughness	28
1.2.3	Analytical models of rough contact	33
1.2.4	Plasticity index	35
1.2.5	Numerical methods	35
<b>1.3</b>	<b>Conductive resistance</b>	<b>36</b>
1.3.1	Constriction resistance	36
1.3.2	Real conductance effect	40
1.3.3	Material coating	42
1.3.4	Joule heating and coupling effect	43

### ■ ■ Résumé du Chapitre I

Cette partie vise à introduire le problème de la résistance de conduction créée par l'interface de contact, et dresser le cadre d'étude de cette thèse. A l'interface de contact, la réduction de la section conductrice, effet de la rugosité des pièces en contact, crée une diminution de la conductivité, et une augmentation de la résistance de conduction. L'étude de la résistance de conduction, autrement appelée *résistance de constriction*, apparaît comme un problème couplé à la mécanique de contact entre surfaces rugueuses. Cette introduction sera organisée en trois sous-parties. La première sous-partie présente le problème de mécanique de contact entre pièces lisses, dressant des parallèles avec le problème de conduction de contact. La seconde sous-partie introduira le problème de contact mécanique entre les surfaces rugueuses. Enfin cette partie sera conclue par la présentation du problème de conduction induite par des aires réelles de conduction.



 **Abstract for Chapter I** This chapter introduces the problem of conduction resistance of contact interfaces, setting the framework for this thesis. At the contact interface, the reduction of the conducting section due to contact of rough surfaces results in an increase in conduction resistance. The study of *constriction resistance* appears as a coupled problem between the conduction and the contact mechanics between rough surfaces. This introduction is organized into three sections. The first one presents the problem of contact mechanics between smooth surfaces, drawing parallels with the problem of conduction. The second one introduces the mechanical problem between rough surfaces in contact, roughness and associated analytical to handle contact are presented. The final section discusses the problem of conduction, oxidation and related phenomena.

## 1.1 Contact of smooth surfaces and a conductivity analogy

The mechanical contact problem is well-known as a non-linear problem in which the contact surface changes with the load. The analytical handling of contact problems is thus very limited. Numerical methods have proven highly effective in solving these problems and have undergone significant development especially within the finite element community [Kikuchi and Oden, 1988, Wriggers, 2006, Yastrebov, 2013, Konyukhov and Izi, 2015, Popp and Wriggers, 2018] successfully addressing various challenges from contact detection and surface smoothing to optimal convergence and accompanied modeling of various involved phenomena such as friction, lubrication, wear and thermo-mechanical coupling.

Fig. 1.2 outlines the mechanical problem of two bodies  $\Omega_1$  and  $\Omega_2$  brought in contact. The potential contact surface,  $\mathcal{A}$  should verify non-penetration/non-adhesion conditions: the gap  $g$  is non-negative  $g \geq 0$  and the surface tractions are compressive. To define the simple *normal gap*, one needs first to find for  $x \in \partial\Omega_1$  the closest point  $y \in \partial\Omega_2$  on the counterpart surface such that  $\forall y' \in \partial\Omega_2 : |x - y| \leq |x - y'|$ . So the gap represents the minimal signed distance for every point and is given by  $g = (x - y) \cdot \mathbf{n}(y)$ . This condition of non-negative gap is nothing but a *non-penetration* condition. To construct the full set of *Hertz-Signorini-Moreau* conditions (HSM), the non-penetration condition should be complemented by *non-adhesion* conditions  $\sigma_n = \mathbf{n} \cdot \boldsymbol{\sigma} \cdot \mathbf{n} \leq 0$  and also by a *complementary condition*,  $g \sigma_n = 0$ . These conditions are defined for all the points on the boundary.

$$g(X) \geq 0 \quad (1.1a)$$

$$\sigma_n(X) \leq 0 \quad (1.1b)$$

$$g \sigma_n(X) = 0 \quad (1.1c)$$

The mechanical equilibrium in absence of inertial and volumetric forces is governed by the second order partial differential equation

$$\operatorname{div} \boldsymbol{\sigma} = 0,$$

where  $\boldsymbol{\sigma}$  is Cauchy stress. In addition, the mechanical problem includes boundary condition: prescribed displacements (*Dirichlet* conditions),

$$u = 0, \text{ on } \Gamma_u$$

and prescribed tractions (*Neumann* condition),

$$\boldsymbol{\sigma} \cdot \mathbf{n} = \mathbf{t}, \text{ on } \Gamma_f$$

The second order stress tensor in the linear case follows Hooke's law

$$\boldsymbol{\sigma} = \mathbf{C} : (\boldsymbol{\varepsilon} - \boldsymbol{\varepsilon}_{th})$$

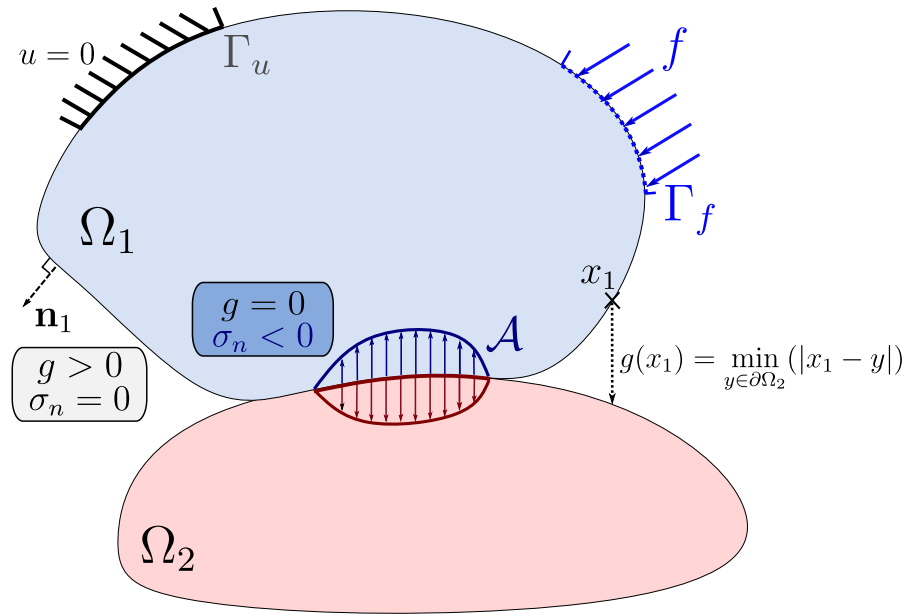


Figure 1.1: Diagram for two bodies in contact

where  $C$  is the fourth order elasticity tensor and  $\varepsilon$  is the tensor of infinitesimal deformations, and  $\varepsilon_{th}$  corresponds to thermal deformations.

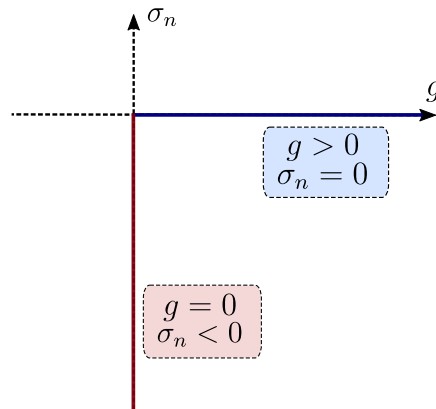


Figure 1.2: Relationship (multi-valued function) for the gap/contact traction defined by the Hertz-Signorini-Moreau (HSM) condition.

The mechanical contact problem can be further complicated by the inclusion of additional physical coupling, such as thermal responses. Following Wriggers [Wriggers, 2006], we can consider an illustrative example of thermo-mechanical coupled problem as shown in Fig. 1.3. Two distinct scenarios exist: (a) the gap is open or (b) closed. In the static regime of the thermal problem, the temperature of the bar is set at  $T_1$ . As a result of thermal expansion, the bar expands until it contacts the blue-colored wall, which is at temperature  $T_2$ . The bar is supposed homogeneous, with linear elastic properties, characterized by the Young's modulus  $E$ , the Poisson's ratio  $\nu$ , and the thermal expansion coefficient  $\alpha_T$ . Assuming  $T_1 > T_2$  and the temperature of the bar at the contacting wall is precisely  $T_2$ , the bar undergoes localized shrinkage. This leads to intermittent on-off contact, giving rise to thermal instability. The contact's thermal condition can be characterized in terms of flux exchange, which is governed by the conductance coefficient  $h_c$ . To mitigate the issue of thermal instability, this coefficient might be made dependent on the pressure  $p$  exerted at the contact point. In Appendix A, we derive analytical solu-

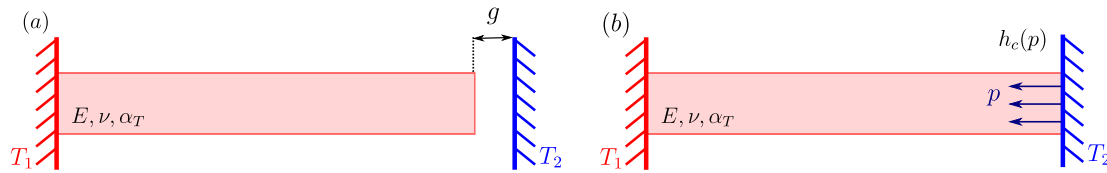


Figure 1.3: Thermal contact problem, with (a) an open gap, and (b) a closed gap, adapted from [Wriggers, 2006]

tions for transient thermo-mechanical contact between two bars including insulating or convective heat exchange conditions along the bars.

### 1.1.1 Contact problems in mechanics

#### Boussinesq problem

In some condition, the contact problem might be defined as a linear problem. For instance, consider the contact problem with a known contact area, for a half-space undergoing elastic deformation. Then the contact conditions in some cases could be seen as Dirichlet boundary condition. In a more general situation we aim to find such a pressure distribution which would result in a surface displacement enabling to accommodate the shape of the indenter. The link between surface pressure and displacements could be formulated for linear material through a superposition of a fundamental solution for a punctual normal force applied at the surface of a half-space  $z > 0$ . A harmonic function  $\Psi$  derives from a divergence-free problem, which adheres to *Laplace equation* as presented in [Green and Zerna, 1992, Barber, 2018]:

$$\Delta\Psi = 0 \quad (1.2)$$

Boussinesq [Boussinesq, 1885] initially addressed this problem in 1885, providing a harmonic function, in the frictionless problem, as illustrated in Fig. 1.4. This work, also known as the *Boussinesq problem* is acknowledged as a handy solution as presented by [Podio-Guidugli et al., 2014].

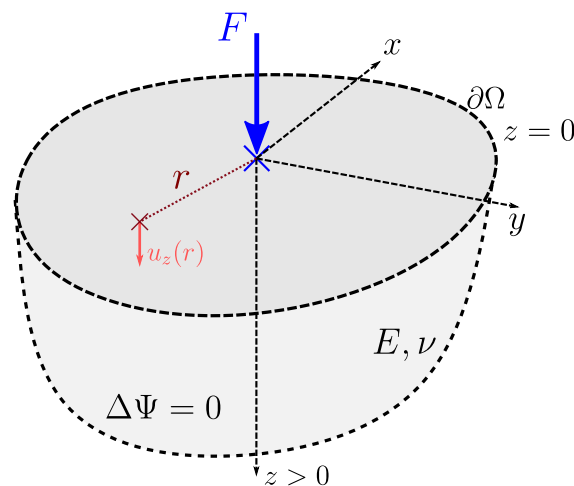


Figure 1.4: Action of a normal punctual load for a half-space geometry

This solution could be supplemented with a punctual tangent load known as *Cerruti problem*. It is related to the contact problem with frictional forces at the contact area. The related punctual  $\Psi_1$  is also harmonic solution, i.e. it verifies the Laplace equation.

For the Boussinesq problem, the harmonic solution enables to get the normal stress

component and the deflection at the free surface

$$\sigma_{zz}(x, y, 0) = -\frac{\partial^2 \Psi}{\partial z^2} \quad (1.3a)$$

$$u_z(x, y, 0) = -2\frac{1-\nu^2}{E} \frac{\partial \Psi}{\partial z} \quad (1.3b)$$

Accounting for the parametrization presented in Fig. 1.4, the harmonic solution is expressed as follows.

$$\Psi = -\frac{F}{2\pi} \ln(R+z), \quad R = \sqrt{r^2+z^2}, \quad r^2 = x^2+y^2 \quad (1.4)$$

This solution is axisymmetric, with  $r$  the radial distance between the load source position and the observation point. This solution is singular at the point of load application, which in fact inherits from the non-differentiability of a punctual load. Nevertheless, the solution is integrable, which allows the application of the superposition principle. It enables to define half-space's response to an arbitrary pressure distribution as shown in Fig. 1.5(a) for a pressure field  $p(x, y)$ . Strictly speaking this solution is valid only for a flat surface as presented in Fig. 1.5(b), but in practice, this solution is still quite accurate if surface slopes remain gentle. The resulting surface deflection  $u_z$  is defined as

$$u_z(x, y) = \frac{1-\nu^2}{\pi E} \int \int_{\mathcal{A}} \frac{p(\xi, \eta)}{r} d\xi d\eta \quad (1.5)$$

with  $r = \sqrt{(x-\xi)^2 + (y-\eta)^2}$ ,  $x, y$  are the coordinate of observation point,  $\nu$  is the Poisson ratio, and  $E$  represents the Young's modulus. The coefficient  $E^* = E/(1-\nu^2)$  stands for the effective Young's modulus. This relation aligns with convolution product of a kernel function  $\sim 1/r$  and the pressure field  $p(x, y)$ .

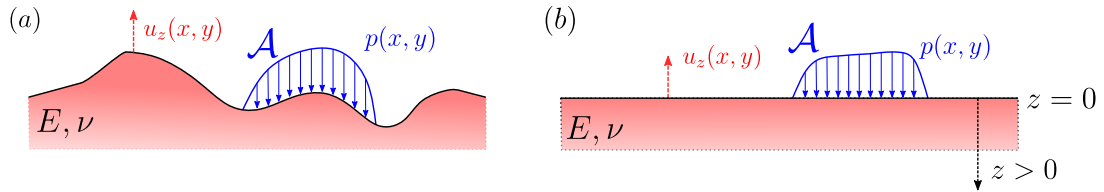


Figure 1.5: Problem of deformation due to a normal continuous pressure in the realistic configuration (a), and a flat interface (b), in a half-space

### Examples of deformation profile

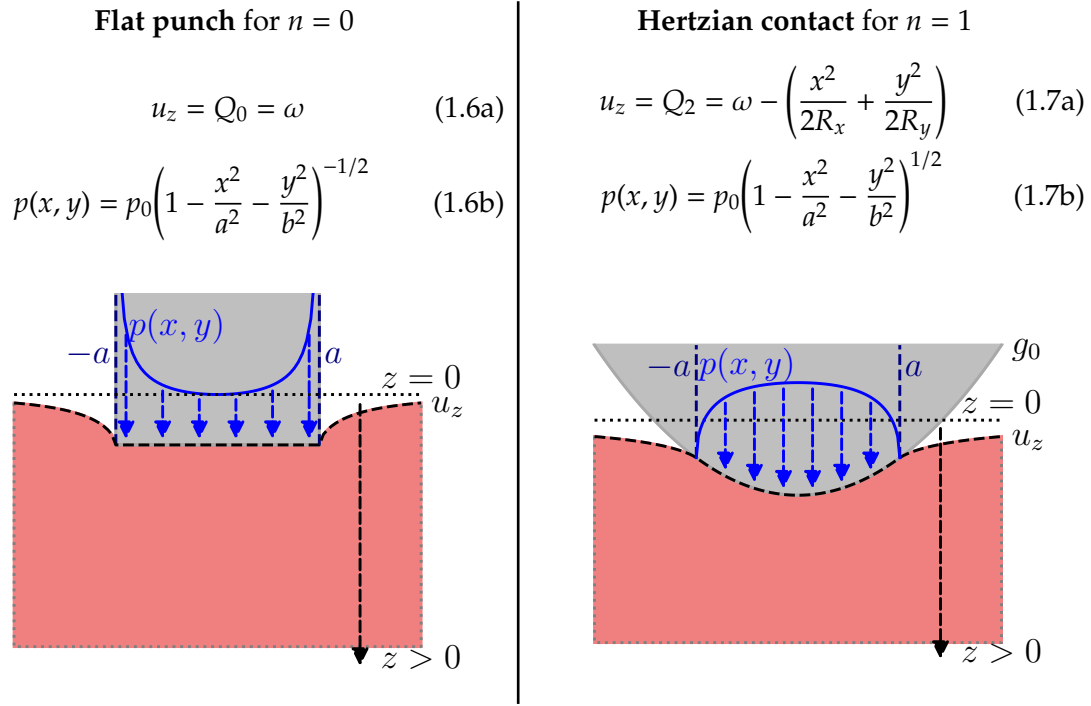
In the use case scenario of a circular contact area, the relation Eq. 1.5 might be applied. Galin [Galín, 1961] provided a relation for a polynomial pressure field and its deformation in the context of an elliptical contact spot. The following relation involves  $\mathcal{P}_n$  and  $\mathcal{Q}_{2n}$ , two polynomials of degrees  $n$  and  $2n$  respectively, both functions of spatial variables  $x$  and  $y$ .

$$u_z(x, y) = \mathcal{Q}_{2n}(x, y) \iff p(x, y) = \mathcal{P}_n(x, y) \left(1 - \frac{x^2}{a^2} - \frac{y^2}{b^2}\right)^{-1/2}$$

With  $n = 0$  and  $n = 1$ , this pertains to the pressure fields associated with a flat punch and a parabolic profile, respectively. The parabolic profile aligns with an elliptical shape for an indenter.

The constant  $p_0$  used above is the pressure value at the middle of the indenter. It yields the definition of the gap function,  $g$ , such as,

$$g(x, y) = u_z(x, y) - g_0(x, y) - \omega \geq 0$$



Where  $\omega$  represents the increment of displacement, and  $g_0$  is the initial undeformed profile of the indenter. The gap function is unknown in a general case, such for this case, ignoring the value of  $\omega$ . The two aforementioned examples represent fundamental problems in contact mechanics. The problem with a parabolic indenter is better known as the *Hertz problem* formulated in a very general case in [Hertz, 1881], it underpins many other results in contact mechanics.

**Flat punch.** For the flat indenter geometry, the pressure field is singular at the edge of the indenter. As argued by Johnson [Johnson, 1987] such a perfectly flat indenter should not exist in reality. In practice, there is always a radius which makes the edge of the flat punch curved, and thereby regularizes the stress field. Even though in any case, the elastic energy deformation remains finite, similar to the case of a crack tip undergoing elastic deformation. For the circular flat punch, with  $a = b$ , the total load is expressed as,

$$F = \int_0^{2\pi} \int_0^a p_0 \frac{r dr d\theta}{\sqrt{1 - r^2/a^2}} = 2\pi p_0 a^2$$

The pressure field relates to the surface deflection, entailed to Eq. (1.5). The increment of displacement, equal to the displacement at the flat indenter is expressed as follows,

$$\omega = \frac{1 - \nu^2}{E} p_0 \int_0^{2\pi} \int_0^a \frac{r dr d\theta}{\sqrt{1 - r^2/a^2}} = \frac{1 - \nu^2}{E} \pi p_0 a$$

It yields to the definition of an effective Young modulus  $E^* = E/(1 - \nu^2)$ . Substituting the term  $p_0$  by  $\omega E^*/\pi a$ , this leads to the expression of the load  $F$ .

$$F = 2E^* \omega a$$

Despite the pressure singularity, the total load is well-defined. It is noteworthy that the load proportional to the flat punch's radius  $a$ , the Young's modulus  $E^*$ , and the indent parameter  $\omega$ . The contact stiffness is then given by  $\partial F/\partial \omega = 2E^* a$ .

**Hertzian contact.** This issue relates to the elastic deformation resulting from the contact between two elliptical surfaces. The analysis is reduced to an elliptical profile facing a half-space with a flat free surface. The elliptical shape's parabolic profile pertains to first terms in series expansion of an arbitrary locally convex shape, along the two  $x$ ,  $y$ -axis. In contrast, the flat surface is characterized by a zero curvature. The elliptical profile can be defined by its semi-radii,  $a$  and  $b$ , or alternatively by the two curvatures,  $R_x$ , and  $R_y$ , respectively. As such, the elliptical profile is resumed by the height function  $g_0$  formulated as  $x^2/(2R_x) + y^2/(2R_y)$ , a function integral to Eq. (1.7a). In the context of spherical (parabolic) profiles, where  $R_x = R_y$ , the height function depends on the radial coordinate  $r$  only.

This topic has been thoroughly explored in literature, with comprehensive treatments available in key references such as [Barber, 2018, Johnson, 1987]. The expressions for elliptical contact are based on elliptic integral functions and are influenced by the eccentricity  $e = \sqrt{1 - (a/b)^2}$ . In the case of a circular contact, the methodology adapts to assess the pressure distribution, represented by  $p(r) = p_0 \sqrt{1 - (r^2/a^2)}$  for  $r \leq a$  within the contact zone. Integrating this pressure distribution yields the total load value.

$$F = \frac{2}{3}p_0A$$

with  $A$  the circular contact area,  $A = \pi a^2$ .

Similarly to the flat punch methodology, the evaluation of the deflection at the middle point of the indenter yields a relation between penetration  $\omega$  and the load  $F$ . The total load is commonly expressed in terms of the contact radius  $a$  which is proportional to  $\sqrt{\omega}$ .

$$F = \frac{4E^* a^3}{3R} \quad (1.8a)$$

$$a = \sqrt{R\omega} \quad (1.8b)$$

Therefore, the total load varies as a power law of  $\omega$  with an exponent of 3/2 as  $P \sim \omega^{3/2}$ . The stiffness could be readily found as

$$\frac{\partial F}{\partial \omega} = \frac{\partial F}{\partial a} \frac{\partial a}{\partial \omega} = 2E^* a,$$

which is exactly equivalent to the stiffness of the flat indenter of the same radius.

**Stress analysis.** One can readily access expressions for the potential function  $\Psi$  involving the integration of a continuous pressure field, derived from Eq. (1.3). Timoshenko & Goodier [Goodier and Timoshenko, 1970] and Johnson [Johnson, 1987] have provided insight into this development. Expressions for stress components can be readily employed through the application of integral functions. This gives access to the knowledge of stress fields, then enables to compute the von Mises stress, denoted as  $\sigma_{\text{Mises}}$  as

$$\sigma_{\text{Mises}} = \sqrt{\frac{1}{2} \left( (\sigma_{xx} - \sigma_{yy})^2 + (\sigma_{yy} - \sigma_{zz})^2 + (\sigma_{zz} - \sigma_{xx})^2 + 6\tau_{xy}^2 + 6\tau_{yz}^2 + 6\tau_{zx}^2 \right)} \quad (1.9)$$

The figures Fig. 1.6, and Fig. 1.7 represents the von Mises stress field in a half space which undergoes elastic deformation, for indenter of flat punch and parabolic profile, respectively. The von Mises stress derives from the norm of a deviatoric stress tensor. It pertains to the elastic deformation associated with shape distortion and with plasticity. For the flat punch, in Fig. 1.6, the von Mises stress is capped at a value of  $1.5p_0$ , as singular values arise at edges. Conversely, the von Mises stress is bounded in the case of the Hertzian contact. It reaches a maximum value along the middle axis at a depth of  $z \approx 0.5a$ . This is the position where plasticity first appears.

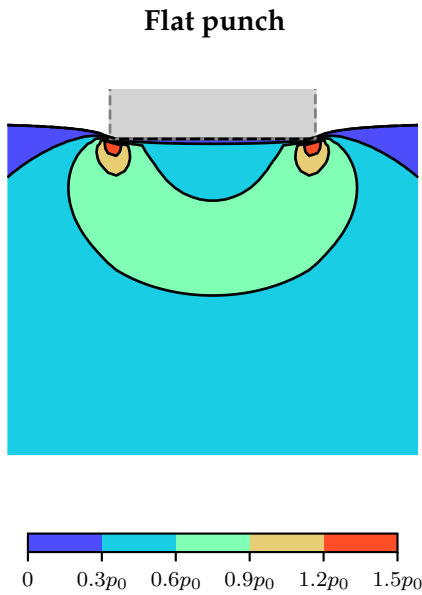


Figure 1.6: von Mises stress in an elastic half-plane with a flat punch indenter

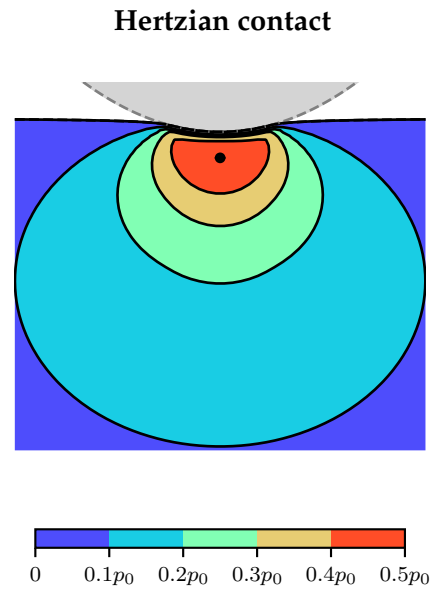


Figure 1.7: von Mises stress in an elastic half-plane with a parabolic shape indenter

**Rounded indenter.** The issue with the flat punch configuration is the occurrence of a singular value at its edge. However, as already mentioned this is not realistic, as mathematically sharp edges never occur in actual applications. Instead, the edge of the flat punch is more likely to be rounded. This situation can be modeled by considering the indenter as being perfectly flat up to  $r \leq a_i$ , and then rounded for  $r \in [a^i, a^o]$ . This particular aspect was investigated by Ciavarella [Ciavarella et al., 1998], with the resulting pressure field illustrated in Fig. 1.8. As illustrated Fig. 1.6, in the flat punch configuration, singular stress occurs on the edge of the indenter. Instead, the case of a rounded flat punch the peak stress occurs within the contact zone. The influence of the edge curvature was specially investigated by Ciavarella [Ciavarella et al., 1998]. The pressure field in the contact area is revised as illustrated in Fig. 1.8.

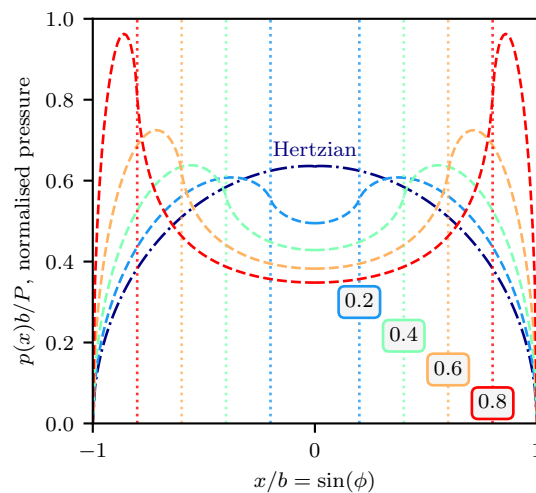


Figure 1.8: Normalized pressure field for a rounded indenter.

This problem aligns in meantime with the Hertzian problem when  $a^i/a^o \rightarrow 0$ , and with the flat punch problem when  $a^i/a^o \rightarrow 1$ . In addition, this problem illustrates how small changes in geometry might significantly affect the pressure field. This problem might

be also addressed by *stress intensity factor*. In this order, Sackfield [Sackfield et al., 2003] has proposed an expression for the maximal pressure field involving  $k_r$  a stress intensity factor.

$$p_{max} \approx \frac{1.8k_r}{\sqrt{a^i - a^o}} \quad (1.10)$$

This expression is correlated with experiences as presented [Hills et al., 2012]. It is observable that this pressure field leads to the formation of a partial slip area. Fretting wear and fretting fatigue issues can arise in assemblies and are often prompted by specific designs like dovetails in aircraft engine blades. Such fretting fatigue can eventually end in failure, highlighting the need for a deeper understanding of the contact mechanics in such situations. The domain of *fretting-fatigue*, delves into the mechanisms of failure and wear, dealing with multi-physical problem involving oxidation, the presence of a so called third body, and both adhesive and abrasive wear, as detailed in [Arnaud et al., 2021]. In practical scenarios, the durability of a material is experimented by sliding a pad over a specimen in repeating cycles. The pad-size is at the utmost importance, and notches are first initiated on the edge of this latter [Dini et al., 2006, Araújo and Nowell, 1999].

### 1.1.2 Equivalence with conductive resistance

In stationary regime, the thermal and electrical conduction are equivalent. For the half-space problem, the area of conduction is set equal to  $\mathcal{A}_c$  on its free-surface. Furthermore, the stress-strain problem follows Laplace equation. Let's denote the area of contact as  $\mathcal{A}$ . The correlation between mechanical and conduction problems has been highlighted by Barber [Barber, 2003]. This relation involves comparing the potential functions,  $\Psi$  and  $\Phi$ , associated with the stress-displacement problem and the conduction problem, respectively. This analogy presupposes the equality of the contact and conductive areas,  $\mathcal{A}_c = \mathcal{A}$ . The contact problem operates under the assumption of the elastic regime and infinitesimal strain. By analogy, the half-space exhibits constant isotropic conductivity characterized by a constant  $K$ , see color boxes below.

Elastic problem	Conduction problem
Partial differential equation in $\Omega$ :	Partial differential equation in $\Omega$ :
$\Delta\Psi = 0$	$\Delta\Phi = 0$
Boundary condition	$j = -K\nabla\Phi$ isotropic conduction
$u_z = -\frac{2}{E^*} \frac{\partial\Psi}{\partial z} = \omega, \text{ in } \mathcal{A}$	Boundary condition
$\sigma_{zz} = \frac{\partial^2\Psi}{\partial z^2} = 0, \text{ in } \bar{\mathcal{A}}$	$\Phi = \Phi_0, \text{ in } \mathcal{A}_c$
With	$j_n = -K \frac{\partial\Phi}{\partial z} = 0, \text{ in } \bar{\mathcal{A}}_c$
$\frac{\partial\Psi}{\partial z} \rightarrow 0, \text{ for } z \rightarrow \infty$	With
Total load	$\Phi \rightarrow 0, \text{ for } z \rightarrow \infty$
$F = \int_{\mathcal{A}} \frac{\partial^2\Psi}{\partial z^2}(x, y, 0)dxdy$	Total flux
	$Q = \int_{\mathcal{A}_c} \frac{\partial\Phi}{\partial z}(x, y, 0)dxdy$



At the initial stage, the bodies in contact undergo a displacement of  $\omega$ . Subsequently, an increment of displacement  $\delta\omega$  is applied, resulting in an increased load  $\delta F$ . The contact area is assumed to remain unchanged during the displacement increment, implying that  $\mathcal{A}(\omega + \delta\omega) \approx \mathcal{A}(\omega)$ . The elastic response is characterized by the superposition of two harmonic functions,  $\Psi$  and  $\Psi'$ , corresponding respectively to the two increments of displacement,  $\omega$  and  $\omega + \delta\omega$ . This leads to the establishment of a harmonic function,  $\Phi$ , which is relevant to a conduction problem, with appropriate boundary conditions as outlined in the upper box.

$$\frac{\partial^2 \Psi'}{\partial z^2}(x, y, z) = -\frac{E^*}{2\Phi_0 K} \delta\omega \frac{\partial \Phi}{\partial z}(x, y, z)$$

The integration of the last expression over the contact area  $\mathcal{A}$ , enables the establishment of a relation between the incremental load  $dF$ , and the conductive flux  $Q$ , on the left and right hand side, respectively. The ratio  $Q/\Phi_0$  represents the *constriction resistance*  $R_c$ , while  $dF/d\omega$  denotes the *stiffness*. Those two variables could be expressed one from another as

$$C \equiv \frac{1}{R_c} = \frac{2K}{E^*} \frac{dF}{d\omega}$$

The aforementioned constriction resistance derives from the reduction of section of conduction at the contact interface, which result in curving current flux lines through the conductive area. This topic of research was initiated by the pioneering works of Holm [Holm, 1967] and Greenwood [Greenwood, 1966]. Their objective was to examine the problem of conduction resistance caused by the contact interface, attributed to micro-scale roughness. This will be further elaborated in Section 1.3.

**Circular conductive area.** To illustrate the aforementioned equivalence, one could look at the problem of conductivity through a circular contact spot. This problem has a well-known solution, as detailed in the books by Carlaw [Carlaw et al., 1962], and Madhusudana [Madhusudana, 1996]. In reality, this problem takes over developments from the problem of indentation with a flat punch. Considering the displacement analogous to the potential, the boundary condition is defined setting a constant potential,  $\Phi_0$  over the conductive area. The problem is parameterized by a cylindrical coordinate system,  $\theta, r, z$ , but due to axisymmetric properties, the system is simplified to  $r, z$ . The conductive area is defined as  $r \leq a$ , with  $a$  being the radius of the contact area. The normal flux,  $j_n$ , is defined by Eq. (1.11a). This enables to find the total flux,  $Q_o$ , as presented in Eq. (1.11b). The flow through the contact point is equivalent to the pressure field, as indicated in Eq. (1.5), exhibiting a similar singularity at the edge for  $r \rightarrow a$ .

$$j_n(r) = \frac{2K\Phi_0}{\pi \sqrt{a^2 - r^2}}, \text{ for } r < a \quad (1.11a)$$

$$Q_o = \int_{\mathcal{A}_o} j_n(r) r dr d\theta = 4K\Phi_0 a \quad (1.11b)$$

Hence the constriction resistance  $R_o$ , follows from the ratio between the flux and the potential set,

$$R_o = \frac{\Phi_0}{Q_o} = \frac{1}{4Ka} \quad (1.12)$$

It is noteworthy that the constriction resistance is inversely proportional to the radius  $a$ , whereas the total flux  $Q_o$  is proportional to the contact radius.

**Hertzian contact.** The problem of the Hertzian contact could be also used to emphasize the aforementioned equivalence between the stiffness and the constriction resistance. The stiffness is given by

$$\frac{dF}{d\omega} = 2E^* \sqrt{R\omega} = 2E^* a$$

Hence the constriction resistance  $R_o$ , using Eq. (1.1.2) we get

$$\frac{2K}{E^*} \frac{dF}{d\omega} = 4Ka = \frac{1}{R_o}$$

It is noteworthy that the stiffness is not influenced by the height profile of the indenter. The constriction resistance depends solely on the contact spot's shape. For instance, for a given circular contact spot, both the stiffness and the constriction resistance can be equivalently studied by a parabolic or a flat punch indenter.

### 1.1.3 Hardness & plastic deformation

When the elastic regime is exceeded in ductile materials, it leads to plastic deformation within the bulk material. Once plasticity appears, the contact leaves an imprint on the contact surface. This imprint can be linked to the load by defining the *Hardness* property. Plasticity in contact is a frequent issue as it influences the life-cycle properties of materials. Hertz also endeavored to explore this problem, but it has needed to wait for the development of the theory of plasticity to get consistent development. For Hertzian contact, repairs to the Brinell hardness test, the plasticity first occurs at a depth of  $0.48a$ , when either the von-Mises or Tresca stress reach the yield stress  $S_Y$ . Johnson [Johnson, 1987] established a relationship between the hardness and the yield stress, according to either the von Mises criterion or Tresca, as will be detailed below. The force needed to reach the elastic limit is given by

$$P = \frac{21.2S_Y^3 R^2}{E^{*2}}$$

Beyond this force, when the load is removed, an imprint remains on the surface. However, it requires larger force to leave a visible indentation, as the plastic zone is initially embedded underneath the free-surface. Ultimately, when the load increases, the plastic zone breaks through the free surface. The *Hardness*,  $H$  is defined as the ratio between the load applied,  $P$  and the area of the observed permanent indentation  $A$ .

$$H = \frac{P}{A} \quad (1.13)$$

Tabor [Bowden and Tabor, 1967] have reckoned the hardness with  $S_Y$ , as  $H = 2.8S_Y$  for the Brinell test. But, this assumes that the load is constant over the contact area. Differently, Meyer [Meyer, 1908] determined that  $P \sim a^n$ , with  $a$  is the size of the observed permanent indentation, its radius in the case of Brinell test, and  $n$  is the *Meyer's* index. Considering  $H$  is constant throughout the loading implies that  $n = 2$ . Alternatively, the Meyer's index can be defined as  $n = 2 + \beta$ , where  $\beta$  is attributed to the work-hardening, like the power-law stress-strain approximation  $\sigma = (\epsilon_p - \epsilon)^\beta$  in the plastic regime.

The hardness test have gave incentives for its investigation in the light of numerical simulations. This was extensively studies for homogeneous and layered materials. Specifically, this led Komvopoulos [Ye and Komvopoulos, 2003, Kogut and Komvopoulos, 2004] to establish a relationship between hardness, bulk elastic modulus, and yield strength, again for the Brinell test with elastic-perfectly plastic materials.

$$\frac{H}{\sigma_Y} = 0.9 + 0.37 \log\left(\frac{E^*}{\sigma_Y}\right)$$

This latter law is lower than the constant value 2.8 proposed by Tabor. Subsequently, numerical computations expand this study to other shape of indenters, such as Berkovitch

and Vickers pyramidal shapes [Lichinchi et al., 1998], employing FEM for instance. The issue of plasticity in contact remains an important challenge for engineers, especially for conceiving systems like rail-wheel, as studied by [Bower and Johnson, 1989, Meymand et al., 2016]. The repeated passing of wheels could result in ratcheting. Such a mechanism contributes to wear, as explored in [Jiang and Sehitoglu, 1999], and this can eventually lead to failure, as presented in [Jiang and Sehitoglu, 1999].

## 1.2 Contact of rough surfaces

The exploration of contact between rough surfaces initially linked with the study of Coulomb's friction. But in general, roughness, a common phenomenon in nature, plays a significant role in a variety of physical problems, ranging from nanoindentation problems [Kim et al., 2007] to geological faults [Rice, 2017]. From an engineering standpoint, comprehending roughness is vital due to its impact on damage, wear, friction, lubrication and fatigue. The study of roughness gained traction with the improvement of surface measurement technologies. The process of characterizing roughness has undergone considerable advancements too with, for example, a seminal paper from Nayak [Nayak, 1971]. Within the field of contact mechanics, the interest for studying roughness, expanded to include investigations of the real contact areas, the concept that explained a lot of interfacial phenomena. It entailed the development of analytical and, at later stages numerical, methods to handling rough contact.

### 1.2.1 Physics of rough contact

#### Coulomb's law explanation

At the macro-scale, for polished parts, there is no clear evidence that roughness might play a significant role in the contact mechanics. In structural computations, boundary surfaces are typically assumed to be smooth, and the contact area is considered equal to its nominal definition. However, Bowden and Tabor [Bowden and Tabor, 1967] offered insights into Coulomb's law based on a different view. Specifically, they proposed that the coefficient of friction is derived from adhesive theory of contact and the *real contact area*. This real contact area constitutes a small fraction of the nominal one, where intimate contact and plastic deformations occur. The hardness  $H$  relies on the applied load  $P$  with the real contact area  $A$ , as detailed in Section 1.1.3. It means that the real contact area grows proportionally to the load whatever the nominal contact area is  $A = P/H$ . Combining with Coulomb's friction law, it results in the determination of the tangential force required for sliding,  $Q$ , as follows,

$$Q = \tau A = \frac{\tau}{H} P$$

with the definition of  $\tau$  as the maximal local shear stress due to adhesion. Ultimately this vision enables to retrieve the Coulomb's law  $Q = \mu P$  at the macroscopic scale.

These explanations are backed by experimental measurement. Some of this evidence emerges from electrical resistance measurements, as documented in [Holm, 1967, Bowden and Tabor, 1967], while other findings come from optical observations, such as those by Dyson & Hurst [Dyson and Hirst, 1954], particularly for polished metallic specimens. These optical observations provide insights into the growth of the real contact area. These areas are rippled with contact spots of few microns in size, and gathered within cluster of about 0.1 mm. This reveals that there are at least two scales of dimension at play, and as the load increases, the number of spots grows without much changing their size.

## Profilometry problem

For engineer, the roughness is influenced by both the material and the manufacturing process. For polished steel surfaces, the roughness may be on the order of a few microns, which emphasized the necessity for precision in measurements. Various profilometry techniques are available, with stylus (contact) measurement and optical and interferometric techniques. The contact measurement relies on a fine tip, crafted in a hard material, that moves across the specimen's surface or bends to touch the surface over a grid of points. Notably, it spans a much greater horizontal distance relative to the vertical distance, which is governed by the surface roughness. The operating mechanism of this method is illustrated in Fig. 1.9.

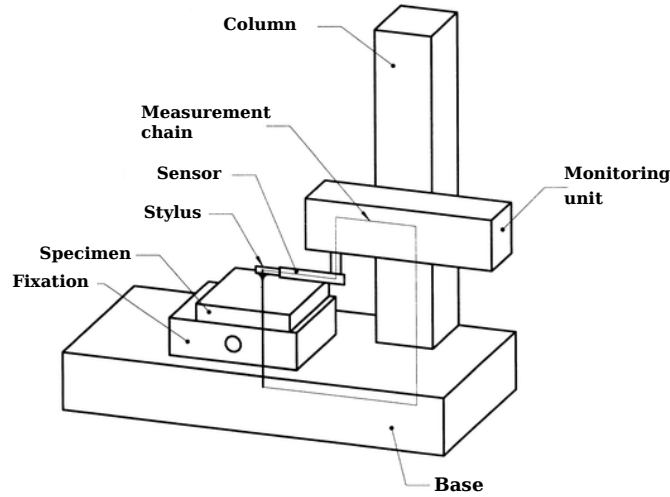


Figure 1.9: Diagram of operation for the stylus profilometry, adapted from standard ISO-3274-1196

Nevertheless, the *stylus-based* method is subject to certain uncertainties, as studied in [Lee and Cho, 2012]. These uncertainties arise from factors such as calibration, parameter settings, and even the stylus's radius, as detailed in [Park et al., 2006, Mendeleyev, 1997]. The verification of this method has motivated numerous studies in turns, such as [Leach et al., 2015]. In current practice, its application is guided by standards, as referenced in [Blunt and Jiang, 2003].

Profilometry also encompasses other techniques, like optical measurements and Atomic Force Microscopy (AFM). These methods rely on different operational principles, which result in them being associated with distinct measurement ranges and amplitudes, as depicted in Fig. 1.10.

**Bearing area curve.** The roughness profiles obtained give insight into the surface topography. It encompasses the location of peaks, their respective heights, and curvatures. The *bearing area curve*, denoted as  $B(h)$ , represents the cumulative distribution of the profile height, with  $h$  the depth variable. It is commonly assumed that the distribution of heights aligns with a *Gaussian distribution*, as presented by  $\Phi(h)$ . Insofar, the bearing area curve is represented by a Gaussian cumulative distribution.

$$\Phi(h) = \frac{1}{\sqrt{2\pi}\sigma} \exp\left(-\frac{(h - \bar{h})^2}{2\sigma^2}\right) \Rightarrow B(h) = \int_h^{\infty} \Phi(x)dx = 1 - \frac{1}{2} \operatorname{erf}\left(\frac{h - \bar{h}}{\sigma\sqrt{2}}\right)$$

In practice, few real surfaces follow such a Gaussian distribution. The distribution is notably affected by manufacturing process, as detailed in [Grzesik et al., 2007] and by the service conditions. The bearing area curve is especially valuable to assess of

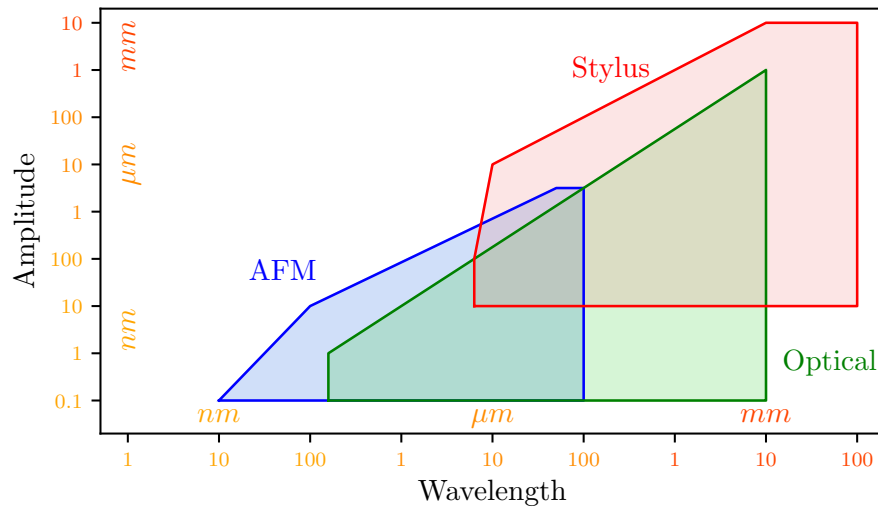


Figure 1.10: Domains of validity for techniques of profilometry, adapted from [Leach, 2014]

the isotropy of the surface or to measure the wear, as explored in [Kumar et al., 2000, Las Casas et al., 2008]. Microscopical wear or local plasticity both result in the development of plateaus near highest asperities.

## 1.2.2 Models of roughness

### Archard's model

In its pioneering work, Archard [Archard, 1957] proposed a model for rough surfaces. He streamlines rough height profile such as *protuberances on protuberances*, as illustrated in Fig. 1.11. This enables the establishment of a linear relationship between load and contact surface. Archard conceives a spherical indenter adorned with smaller spheres, and so on. This concept is an early representation of a model incorporating a fractal shape. Initially, the contact solution between a plane and a sphere is described by the Hertzian contact, leading to a relationship where  $A \sim P^{2/3}$ . At the second and third stages, the relationship evolves to  $A \sim P^{8/9}$  and  $A \sim P^{26/27}$ , respectively. Such a progression forecasts a relation of proportionality between the contact area and the applied load.

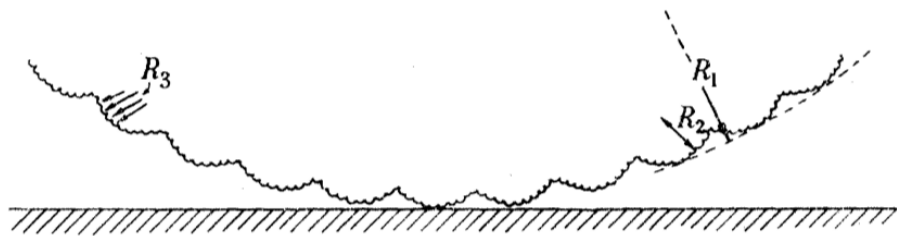


Figure 1.11: Illustration of protuberances on protuberances model, at the third level, designed by Archard and adapted from [Archard, 1953]

### Self-affine surface and fractal dimension

Similarly, other rough surfaces can be characterized by deterministic function, such as *Weierstrass function* Eq. (1.2.2). It looks like a Fourier series, but it also incorporates a

wavenumber,  $\gamma^n$ , raised to the exponent  $n$ .

$$z(x) = h_0 \sum_{n=1}^{\infty} \gamma^{(D-2)n} \cos(2\pi\gamma^n x/L_0)$$

Where  $D > 1$  represents the *fractal dimension*. This function yields the definition of a fractal height surface. Although the function is bounded, it is non-differentiable. This appeals the description through *Power Spectrum Density* (PSD) and related to the squared amplitude of each sinus component.

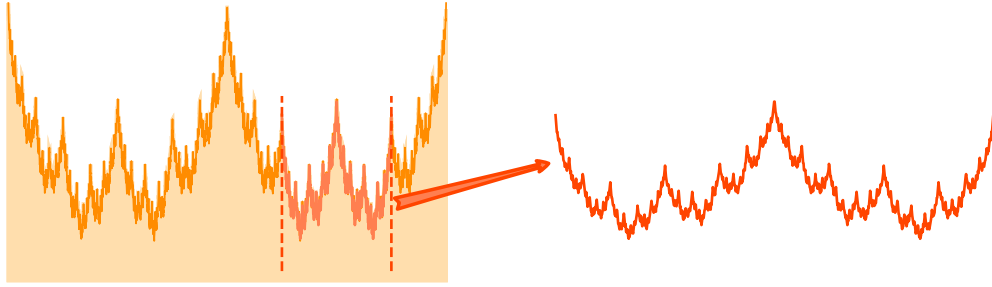


Figure 1.12: Height profile of Weierstrass function with  $\gamma = 2$ ,  $D = 1.5$ ; on the right - a zoom on a portion of the original function.

**Self-affine surface.** The Weierstrass function may offer an initial insight into fractal processes. In the 1970's, fractal shapes were extensively explored, notably by Mandelbrot [Mandelbrot, 1967, Mandelbrot, 1982, Mandelbrot, 1985]. Within this context, the *self-affine* property is introduced to connect height characteristics with those of wavelength. When the profile is magnified by a factor  $\lambda$  along the horizontal axis, it corresponds to a magnification of  $\lambda^H$  along the vertical axis, epitomizing the *self-affine* properties. This exhibits different scale of magnification.

$$z(x) \sim l \Rightarrow z(\lambda x) \sim \lambda^H l$$

With  $H$  being the *Hurst* parameter, defined in the range  $0 \leq H \leq 1$ . This results in a lesser vertical magnification compared to the horizontal when  $H < 1$ . The Hurst parameter is linked to the fractal dimension,  $D$  through the equation  $H = n + 1 - D$ , where  $n$  is the dimension of the object of interest ( $n = 1$  for curve,  $n = 2$  for surface).

### Power spectral density

At the microscopic scale, the analysis might be reduced to focus on a representative element of the surface. In this approach, the overall shape of the body is disregarded, assuming the surface is nominally flat and periodic. Roughness is characterized by its amplitude and wavelength. For describing the waviness of this periodic function, the *Fourier transform* is extensively used.

$$\mathcal{F}(z(k_x, k_y)) = 4\pi^2 \int_{\mathbb{R}} z(x, y) \exp(-2\pi i(k_x x + k_y y)) dx dy$$

This function is of complex value. The Fourier transform is defined in terms of  $(k_x, k_y)$ , denoting the wavenumber variable. It can be also defined in terms of pulsation, varying by a factor of  $2\pi$ . Furthermore, the *Power Spectral Density* (PSD),  $\Phi$ , serves as a measure of the magnitude in relation of the wavenumber  $(k_x, k_y)$ . The PSD study needs of a sufficiently large sample scale  $L$ .

$$\Phi(k_x, k_y) = \lim_{L \rightarrow \infty} \frac{1}{4L^2} \int_{-L}^L \int_{-L}^L z(x, y) \exp(-2\pi i(k_x x + k_y y)) dx dy$$

The *Auto-correlation* function, denoted as  $\mathcal{R}$ , also provides valuable insights into the surface roughness. This function proves its capability for identifying correlation between distant points. It could be also used to derive statistical features, including the *standard deviation*, which is represented by  $\sigma^2 = \mathcal{R}(0, 0)$ .

$$\mathcal{R}(x, y) = \lim_{L \rightarrow \infty} \frac{1}{4L^2} \int_{-L}^L \int_{-L}^L z(x_1, y_1) z(x + x_1, y + y_1) dx_1 dy_1$$

Another definition of the PSD function could be derived from the autocorrelation function  $\mathcal{R}$  as

$$\Phi(k_x, k_y) = \int_{\mathbb{R}} \mathcal{R}(x, y) \exp(-i2\pi(k_x x + k_y y)) dx dy$$

### Statistical analysis

In practice, rough surfaces involves random process, in contrast to the deterministic nature of the Weierstrass function. For deterministic surfaces, the key geometric features are often straightforward: for example, in a simple sinusoidal profile, the entire geometry is defined by its amplitude and wavenumber. However, for random rough surfaces would require feature definition in a more general sense. With its pioneering work on the ocean surfaces, Longuet-Higgins [Longuet-Higgins, 1957] introduced spectral moments. This work has been followed by Nayak [Nayak, 1971, Nayak, 1973], who delved into the characterization of rough surfaces as well. While their initial research centered on isotropic surfaces, their methods are adaptable to non-isotropic surfaces. A series of *spectral moments* that derives from the PSD function, are exposed as follows,

$$m_{p,q} = \int \int_{\mathbb{R}} \Phi(k_x, k_y) k_x^p k_y^q dk_x dk_y$$

For anisotropic rough surfaces, PSD function exhibits different behaviors along the  $x$  and  $y$  axes, as evidenced by integrations over  $k_x$  and  $k_y$ . In contrast, with isotropic rough surfaces, the PSD function demonstrates notable consistency across both  $k_x$  and  $k_y$ . Insofar the spectral moments could solely account for the renewed parameter wavenumber  $k^2 = k_x^2 + k_y^2$ , as follows,

$$m_n = \int_{\mathbb{R}} \Phi(k) k^n dk \quad (1.14)$$

Thanks to these moments, one could measure the standard deviation of roughness  $\sigma$ , the standard deviation of its gradient  $\langle |\nabla z|^2 \rangle$ , and the standard deviation of its laplacian  $\langle |\Delta z|^2 \rangle$ .

$$m_0 = \sigma^2 \quad (1.15a)$$

$$m_2 = \langle |\nabla z|^2 \rangle \quad (1.15b)$$

$$m_4 = \langle |\nabla^2 z|^2 \rangle \quad (1.15c)$$

In addition to these moment, *Nayak's parameter*  $\alpha$  naturally appearing in Nayak's description of the roughness, giving insights into the bandwidth of the spectrum, it represents a combination of spectral moments:

$$\alpha = \frac{m_0 m_4}{m_2^2} \quad (1.16)$$

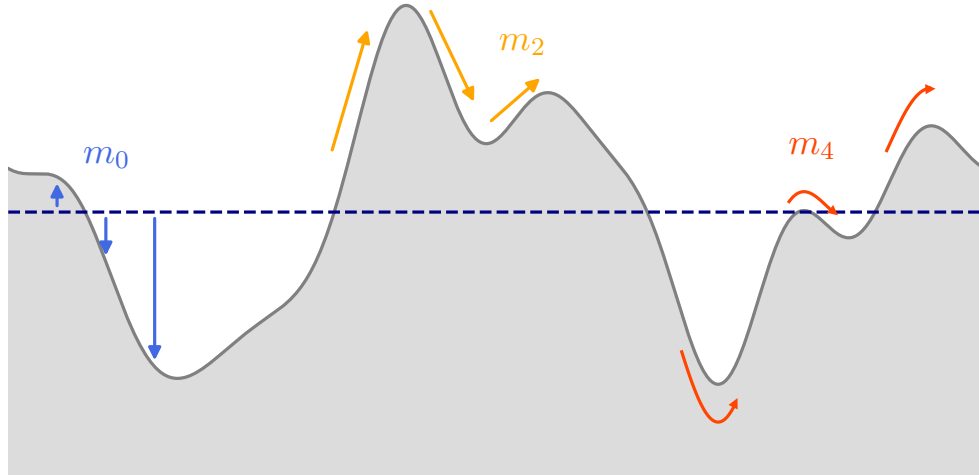


Figure 1.13: Illustration of features associated with spectral moments.

All these parameters underscore different characteristics, as illustrated in Fig 1.13. Nayak's parameter has a minimum value of  $3/2$ , linked to a height profile made of a single sine wave. However, in practical scenarios,  $\alpha$  typically takes much larger values, and can theoretically extend to infinity for an infinitely broad spectrum of a self-affine surface. The asperity density can be quantified through spectral moments. For advanced analysis, Nayak assumes Gaussian distribution for height profile. Consequently, the resulting set of variables,  $\xi_i$ , also follows a Gaussian distribution. Adhering to the central limit theorem, the likelihood of a specific occurrence can be determined through joint probability.

$$\xi_1 = z, \quad \xi_2 = \frac{\partial z}{\partial x}, \quad \xi_3 = \frac{\partial z}{\partial y}, \quad \xi_4 = \frac{\partial^2 z}{\partial x^2}, \quad \xi_5 = \frac{\partial^2 z}{\partial x \partial y}, \quad \xi_6 = \frac{\partial^2 z}{\partial y^2},$$

The summits of the surface are defined as follows

$$\xi_2 = 0, \quad \xi_3 = 0, \quad \xi_4 < 0, \quad \xi_6 < 0, \quad \xi_4 \xi_6 - \xi_5^2 \geq 0$$

Nayak demonstrated that the density of summits could be defined as

$$D_{sum} = \frac{1}{2\sqrt{3}} \left( \frac{m_4}{m_2} \right) \quad (1.17)$$

The height probability of summits is obviously asymmetric for small values of  $\alpha$ , but for  $\alpha \rightarrow \infty$  this distribution tends to the normal distribution of the roughness.

### Spectral content

The analysis of the PSD function reveals other characteristics, especially it decays following  $k^{-2(H+1)}$ , as presented in [Dodds and Robson, 1973, Majumdar and Tien, 1990]. The rate of this decay is closely linked to the fractal dimension, as was illustrated for Weierstrass function [Berry et al., 1980]. To impose a physical limit to the surface roughness, for example, at the atomic scale, one needs to incorporate an upper cutoff wavenumber,  $k_s$ , above which the mode amplitude is considered zero. Conversely, at lower wavenumbers (or on a larger scale), the spectrum also diminishes to zero, which entails the definition of a low cutoff wavenumber  $k_l$ . In some cases, as documented in [Kluppel and Heinrich, 2000, Persson et al., 2004], the spectrum exhibits a plateau,



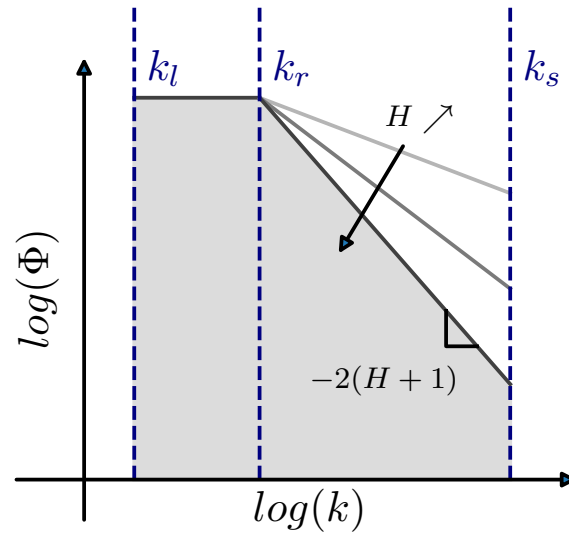


Figure 1.14: PSD definition in function of wavenumber parameters  $(k_l, k_r, k_s)$ , and of the Hurst parameter.

leading to the identification of a third wavenumber,  $k_r$ . Fig. 1.14 aims to illustrate the variation of the PSD helped by these parameters.

$$\Phi(k) = \begin{cases} C & \text{if } k_l < k < k_r \\ C\left(\frac{k}{k_r}\right)^{-2(H+1)} & \text{if } k_r \leq k \leq k_s \\ 0 & \text{otherwise} \end{cases} \quad (1.18)$$

The condition  $k_l \gg 1$  can be also used as a condition of representativity of the roughness [Yastrebov et al., 2012, Pastewka et al., 2013] or the proximity of its height distribution to a normal one. In many cases, the plateau could be neglected, considering  $k_l = k_r$ .

**Generation of random rough surfaces.** In a numerical setting, the combination of the PSD function with the Gaussian nature of the height distribution proves adequate for the generation of random rough surfaces. One of algorithms for this purpose was introduced in [Hu and Tonder, 1992], employing the Fourier transform. The process initiates with the creation of a white noise, which is based on a Gaussian distribution. Subsequently, the algorithm filters this noise using the PSD function in conjunction with the Fourier transform. This method is represented below

$$z(x, y) = \mathcal{F}^{-1}(\mathcal{F}(\text{noise}) \cdot \Phi(k)), \quad \text{noise} \hookrightarrow \mathcal{N}(0, \sigma), \quad (1.19)$$

where  $\mathcal{F}$  denotes the Fourier transform. The Gaussian nature of the random rough surface could be preserved as long as  $k_l$  is large enough. Examples of such surfaces are displayed in Fig. 1.15 generated by Tamaas library [Frérot et al., 2020] for different cut-off parameters.

### 1.2.3 Analytical models of rough contact

The Archard's first attempt, has been followed by other studies. In this framework, the study of rough contacts in the elastic regime has also benefited from subsequent analytical development. Rough surfaces are described through their statistical properties. In this particular section, three models are presented: the *Greenwood-Williamson* (GW) model, the *Bush-Gibson-Thomas* (BGT) model and the *Persson* model.

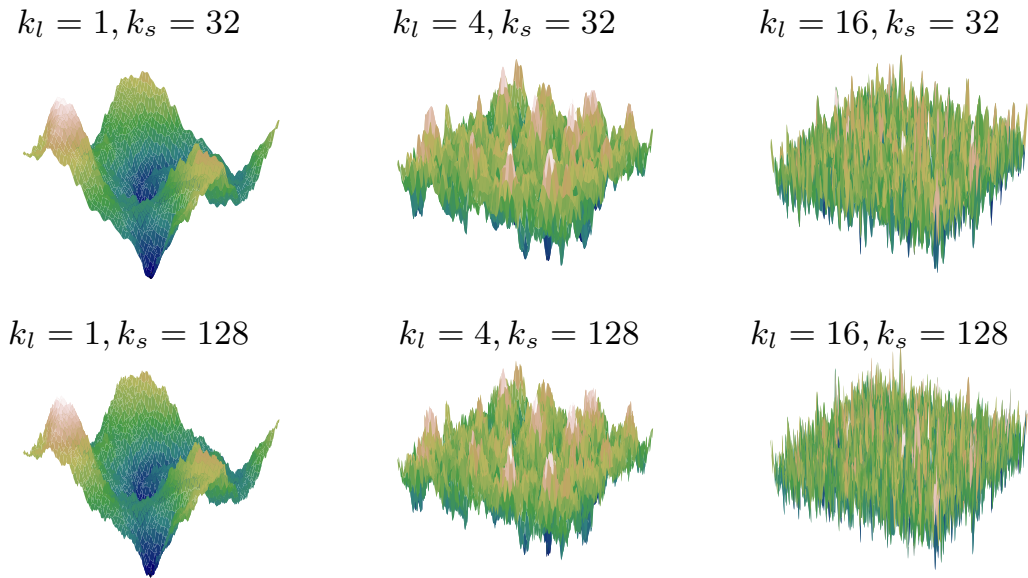


Figure 1.15: Generated random rough surfaces for different cutoffs  $k_l, k_s$  and for a constant  $H = 0.8$ .

### Greenwood-Williamson's model

Greenwood and Williamson [Greenwood and Williamson, 1966] developed a subsequent model studying the growth of real contact area for rough surfaces represented by asperities. This model, denoted as GW, presumes that all asperities have the same curvature  $\beta$  and only asperity tips are in contact and undergo elastic deformation following Hertz contact. A representation of this parametrization can be found in Fig. 1.16.

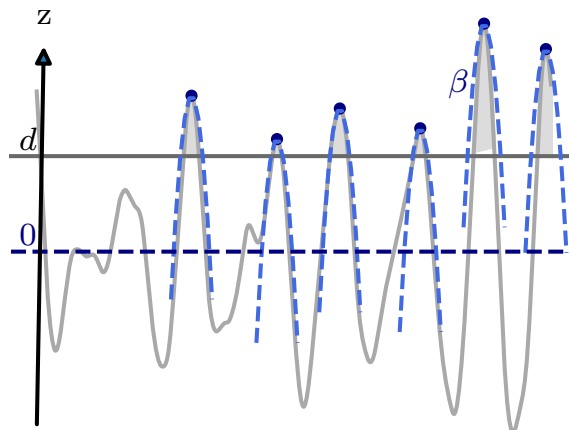


Figure 1.16: Asperities of a rough surface penetrate in the plane set at altitude  $d$ .

Using a normal distribution of asperity altitudes  $z$ , and recalling the Hertzian solution Eq. (1.8b), we can formulate the GW model. The penetration parameter is replaced by  $z - d$ , employed the integration of the summit distribution, resulting in the definition of a function  $F_n$ . This enables to define the real contact area  $A$ , and the applied load  $P$  along the altitude of the indenter  $d$ .

$$A = \pi\eta A_0\beta\sigma F_1(d) \quad (1.20a)$$

$$P = \frac{4}{3}\eta A_0\beta^{1/2}\sigma^{3/2}E^*F_{2/3}(d) \quad (1.20b)$$

$$F_n(d) = \int_d^{+\infty} (z-d)^n p_{sum}(z) dz, \quad (1.20c)$$

where  $\eta$  represents the density of summits,  $A_0$  is the nominal area,  $\sigma$  is the standard deviation of the asperity distribution, and  $E^*$  stands for the effective Young's modulus. The distribution of summits is summarized by the integral function  $F_n$ . For instance  $P(z > d) = F_0(d)$  is the probability of encountering a summit higher than the altitude  $d$ .

This model successfully establishes a proportional relationship between load and real contact area for relatively small loads. Actually, this model is constructed for small loads due to a few assumptions: (1) the curvatures are consistent for all asperities making contact (Hertzian contact is valid), (2) the deformation remains elastic, and (3) merging between expanding contact spots from adjacent asperities is neglected, but probably the most important assumption (4) is the lack of elastic interaction between asperities. Notwithstanding these limitations, GW model has paved the way for further studies in *multi-asperity models*.

### Bush-Gibson-Thomas' model

Bush-Gibson-Thomas [Bush et al., 1975], denoted as BGT, introduced an alternate model accounting for the asperities' properties derived from the statistical analysis of roughness. This aforementioned model is build upon the joint probability of summits, assuming a Gaussian distribution of heights. BGT model succeeds as well in the establishment of a proportional relation between real area of a contact,  $A$ , and  $p_0$  the nominal pressure, as follows,

$$\frac{A}{A_0} = \frac{\sqrt{\pi}}{\sqrt{m_2}} \frac{p_0}{E^*} \quad (1.21)$$

Where  $m_2$  represents the second spectral moment related to the variance the surface gradient. The model indicates that the real contact area is strongly dependent on the  $m_2$  characteristics of the roughness. It inherits the same limitations as the GW model, being applicable to only very small fractions of the real contact area. For further details one can see [Greenwood, 2006, Carbone and Bottiglione, 2008].

### Persson's model

The model proposed by Persson [Persson, 2001a, Persson, 2001b] (see also [Manners and Greenwood, 2006]) seeks to characterize the expansion of the real contact area up to a full-contact regime. Within this framework, Persson's model considers the contact pressure probability density  $P(p, V)$ . It operates with the pressure  $p$  and its variance  $V$ .

Noticably a sinusoidally varying pressure, represented as  $p(x) = p_m \cos(2\pi x/\lambda)$ , results in a profile deformation given by  $u(x) = p_m\lambda/E^*\pi \cos(2\pi x/\lambda)$ . The variance is determined using the same PSD function as that for profile height, employing the magnification parameter,  $\zeta$ , where  $\zeta = k_s/k_l > 1$ .

$$V(\zeta) = \langle |p|^2 \rangle = \frac{E^{*2}\pi}{4} \int_{k_l}^{k_l\zeta} k^2 \Phi(k) dk = \frac{E^{*2}m_2}{4}$$

Combining the expressions for  $P$  and  $V$ , it yields the establishment of a diffusion equation such as,

$$\frac{\partial^2 P}{\partial p^2} = 2 \frac{\partial P}{\partial V}$$

An explicit expression for the pressure distribution  $P(p, V)$  can be found if a specific Dirichlet boundary condition is imposed for this diffusion equation at zero pressure. Integrating it over the domain of pressure  $p \geq 0$  prescribed by the SHM condition, this enables to define the real contact area. This model gives a relation between the real contact area, and the applied load, as follows,

$$\frac{A}{A_0} = \operatorname{erf}\left(\frac{p_0}{E^* \sqrt{m_2}}\right) \quad (1.22)$$

With  $p_0$  is the mean pressure over  $A_0$  the nominal contact area.

This model, based on a cleverly formulated relationship, is applicable for a full contact regime. However its extension to partial contact is not fully justified [Manners and Greenwood, 2006]. Under a light load, when  $p_0 \rightarrow 0$ , this model predicts a linear relationship between the fraction of real contact area and the pressure. This model agrees with the BGT model, although it differs by a factor of  $\pi/2$  and predicts a lower contact area.

#### 1.2.4 Plasticity index

As the contact pressure increases, the number of contacting asperities rises as well. However, the pressure at these contacting asperities can remain relatively stable and might even decrease. Indeed, due to the growing number of asperities can distribute and possibly relieve the pressure for some contact spots. To assess of the amount of asperity undergoing plastic deformation, the plastic index has been introduced. Greenwood and Williamson [Greenwood and Williamson, 1966] defined one such index as the ratio of Young's modulus to hardness. It also incorporates the surface topography by including the standard deviation of the height surface profile  $\sigma$  and the mean curvature of summits  $\beta$ .

$$\Psi_G = \frac{E^*}{H} \sqrt{\frac{\sigma}{\beta}} \quad (1.23)$$

In [Cooper et al., 1969] another version of plastic index is defined. This rather considers the second spectral moment  $m_2$  to account for the roughness property, as follows,

$$\Psi_M = \frac{E^*}{H} \sqrt{m_2} \quad (1.24)$$

Johnson [Johnson, 1987] has proposed in turn another version of plastic index, composed, such as,

$$\Psi_J = \frac{E^*}{H} \sqrt{\sigma_s k_s} \quad (1.25)$$

Where  $\sigma_s$  is the standard deviation of summits, and  $k_s$  represents the root mean square curvature of summits (different from  $m_2$ ).

All these parameters take into consideration the ratio  $E^*/H$ , and they are all influenced by the roughness. It is clear that an increase in roughness leads to a higher plastic index. As  $\Psi$  grows, the plastic deformation among the contacting asperities also increases. A general rule of thumb is that for  $\Psi < 1$ , deformation predominantly stays within the elastic regime. However, with  $\Psi > 1$ , plastic deformation becomes the more likely occurrence. For a detailed assessment of plastic deformation, *Finite Element Method* (FEM) can be effectively utilized. Specifically, in [Gao et al., 2006], the researchers conducted an

analysis of the deformation of a height sine profile under an elastic-plastic constitutive law. This research contributed to the development of an equivalent plastic index, defined by the amplitude and wavelength of the height profile. Additional insights might be found in [Gao and Bower, 2006], which delves into deformation introducing height profile following Weierstrass function, as well as from investigations on random rough surfaces, as outlined in [Pei et al., 2005]. It demonstrates that asperities tend to experience more substantial plastic deformation as they decrease in size.

### 1.2.5 Numerical methods

There are various methodologies available for addressing problems related to rough surfaces. One of the most prevalent is the FEM, recognized for its robustness and versatility. It seems to be well-adapted at tackling both elastic [Hyun et al., 2004] and elastic-plastic scenarios [Pei et al., 2005, Gao et al., 2006, Yastrebov et al., 2011]. Another approach to address this problem might be using *Molecular Dynamic Method*, dealing with plastic deformation as proposed [Akarapu et al., 2011] as well as adhesion [Pastewka and Robbins, 2014]. Additionally, an alternative procedure was proposed by Polonsky and Keer [Polonsky and Keer, 1999]. Their approach benefits from the *Westergaard's solution* [Westergaard, 1939, Johnson, 1987], as presented below,

$$p(x) = \cos\left(2\pi\frac{nx}{L}\right) \leftrightarrow u(x) = \frac{2}{E^*n} \cos\left(2\pi\frac{nx}{L}\right) \quad (1.26)$$

The Westergaard solution is especially adapted to the study of random rough periodic surfaces decomposed in sine functions. This assumes elastic regime deformation, and allows the application of the theorem of superposition. Fig. 1.17 aims to illustrate the composure of pressure field and the resulting deformation.

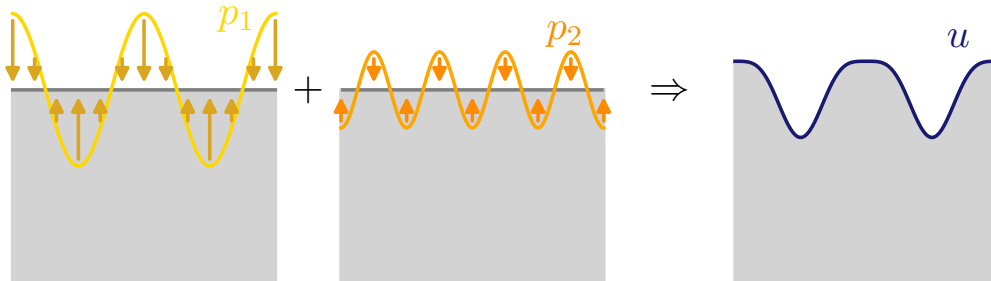


Figure 1.17: Elastic deformation induced by a bi-sinusoidal pressure field

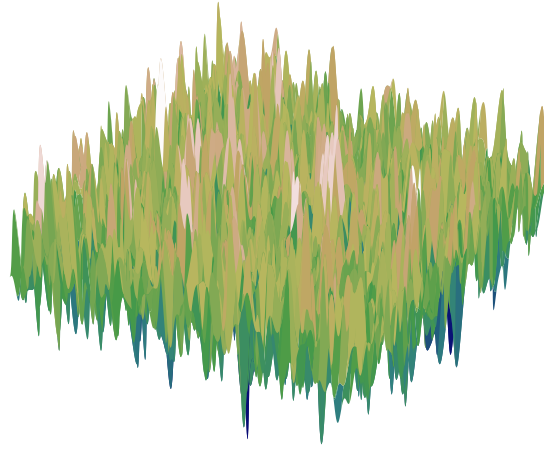
The procedure then includes a condition on gap, and the pressure. They both need to be positive in respect of the HSM condition. A monotonic loading is applied by increment, ensuring the HSM condition is respected. As the initial solution involves sine function, it appeals the use of *Fast Fourier Transform* (FFT). The deformation-pressure relation can be computed using the following relation, where  $\mathcal{F}$  stands for Fourier transform.

$$p(x) = \mathcal{F}^{-1}(\mathbf{k} \cdot \mathcal{F}(u(x))) \quad (1.27)$$

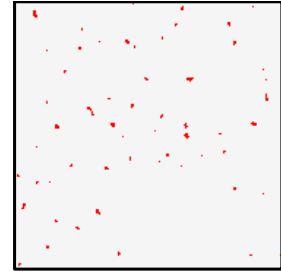
Where  $\mathbf{k} = \{2/(E^*n)\}$  for  $n \in [1, N]$ , and  $N = L/\Delta x$ .

We will refer to this method as *FFT-BEM*, named after FFT that speeds up the computation of the convolution. This was extensively used for rough surfaces problem in elastic deformation, as reported in the literature [Yastrebov et al., 2015b, Yastrebov et al., 2017b], see Fig. 1.18. This method now benefits from further developments. Tamaas library [Frérot et al., 2020] can be used to solve not only classical contact but also adhesive problem [Rey et al., 2017] and even elastic-plastic problems [Frérot et al., 2019]. This

$$k_l = 8, k_s = 32, H = 0.25$$



$$\omega = -0.01, A = 0.007$$



$$\omega = -0.02, A = 0.098$$

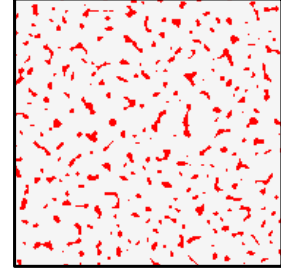


Figure 1.18: Rough surface and contact areas for different applied pressure computed using FFT-BEM [Frérot et al., 2020].

method can be also coupled with FEM, in the aims of multi-scale study, as proposed by [Carvalho et al., 2022]. FFT-BEM enables to solve the problem solely accounting for the surface height, without volume discretization. The rough surface is periodic and defined over a regular grid, prescribed by the use of FFT.

### 1.3 Conductive resistance

The investigation of the rough surfaces in contact now brings us to the study of conductivity at the aforementioned contact interface. It has been pointed out the height profile is not relevant for the lone problem of conductivity. Indeed considering snapshots of real conductive area, the study of constriction resistance is clear. Nevertheless, the contaminant oxide or fluid presence might alter the equivalence between contact stiffness and resistance demonstrated by Barber [Barber, 2003]. This section delves into the constriction resistance problem, studying the influence of conductive spot morphology. The problem of conductivity will be extended, addressing oxidation and coating concerns, and ending by the presentation of coupled problems.

#### 1.3.1 Constriction resistance

##### Influence of shape

As lately exposed, the constriction resistance roots from the shrinkage of the current lines. The morphology of the real conductive area, and of the separate spot are linked to the constriction resistance. The aforementioned real contact area exhibit various spot shapes, related to the roughness, the mechanical properties, and the loading regime. At lower loads, contact spots are typically well-separated and often take on elliptical shapes, for which solutions are well-established, as noted in [Holm, 1967]. In the case of these elliptical contact spots, the constriction resistance is quantified in relation to their

eccentricity and mean radius. It is observed that the constriction resistance decreases with this eccentricity when the area is kept constant. Aichi and Tahara [Aichi, 1994] performed experiments on the conductive resistance of a rectangle, maintaining a constant area. Their findings confirmed that the resistance decreases as the length-to-width ratio increases. In [Slade, 2017], values for constriction resistance for various contact spot shapes are listed, including square, circle, rectangle, and ring, all with equivalent areas.

**Boyer's model.** Investigating the influence of shape, Boyer [Boyer, 2001a] introduced a model in which the constriction resistance can be summarized by a shape factor, denoted as  $S$ , along with a length scale,  $l$ , as follows,

$$R = \frac{S\rho}{4l},$$

where  $\rho$  is resistivity. This provides an expression for the self-resistance. But the interaction between the contact spot is expressed as they were concentrated source points of potential, separated by a distance  $d$  between their centers:

$$R = \frac{\rho}{2\pi d}$$

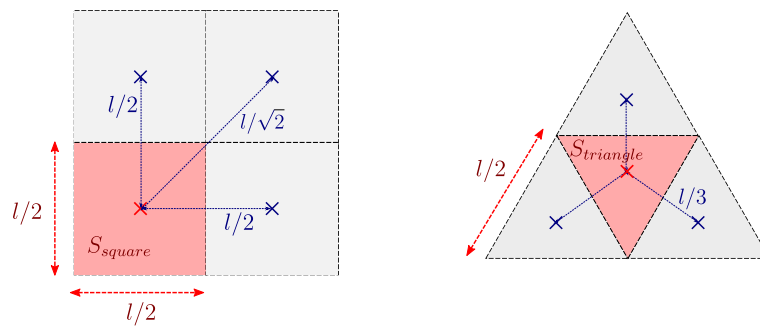


Figure 1.19: Square and triangle for Boyer's decomposition

Fig 1.19 illustrates applications of Boyer's model. In this model, the constriction resistance incorporates the shape factor  $S$ , and a hierarchical division is applied to introduce varying length-scales, initially  $l$  and then  $l/2$ . In cases involving square contact spots, an equal fraction of flux is present in each contact spot, accounting for a quarter of the total flux from the original contact. In contrast, with triangular contact spots, the distribution of flux among the sub-contact spots is uneven.

$$S_{square} = \frac{4 + \sqrt{2}}{2\pi} \approx 0.86$$

This result for the square spot is backed by the value computed with BEM by Nakamura [Nakamura, 1995], showing a deviation of less than 1%.

**Fabrikant's model.** Fabrikant [Fabrikant, 1986] provides an another model for the constriction resistance. This approach enables the calculation of shape factors for various contact spot geometries. The normal flux is assumed to exhibit the same singularity as observed in elliptical contact spots, which simplifies integration over the contact spot area. Its formula is detailed in Eq. (1.28), involving the contour radius,  $a(\theta)$ , where  $\theta$  represents the angular position, and  $j_0$  is the normal flux at the center of the contact spot. The distribution of the normal flux field is depicted in Fig. 1.20 for a square contact spot, as well as for a contact spot defined randomly.

$$j_n(r, \theta) = \frac{j_0}{\sqrt{1 - (r/a(\theta))^2}} \quad (1.28)$$

Insofar, one could compute the potential held on the spot,  $\Phi_0$ , by integration of the normal flux field over the contact area, and weighted by the Green function,  $\rho/2\pi r$ .

$$\Phi_0 = \rho \int_0^{2\pi} \int_0^{a(\theta)} \frac{j_n(r, \theta)r}{2\pi r} dr d\theta \quad (1.29)$$

Using these equation, shape factors for various shapes can be computed. Insofar for the squared contact spot, with size length equal of  $l$ , the radius is defined as  $a(\theta) = l/\cos(\theta)$ . This leads to the following shape factor,

$$S_{square} = \frac{2}{\ln(1 + \sqrt{2})} \approx 0.88$$

This result deviates by only 1.2% from the latter Nakamura's result.

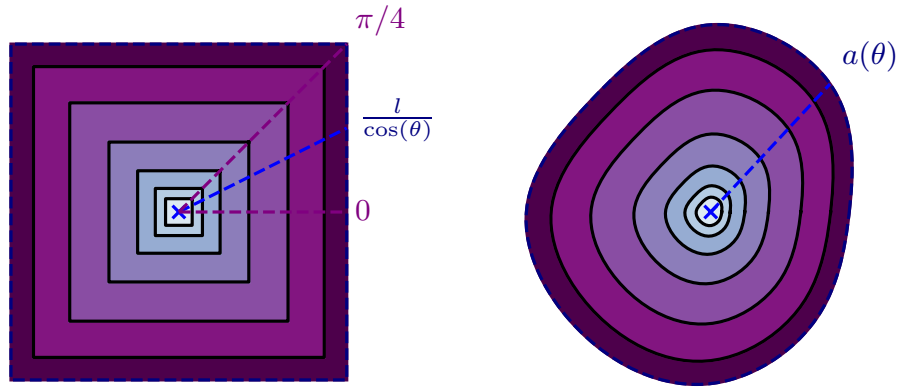


Figure 1.20: Diagram of normal flux within the contact spot under Frabikant's assumption

### Multi-spot resistance

Addressing the problem of constriction resistance in real contact areas, and drawing upon Dyson's observations [Dyson and Hirst, 1954], Greenwood [Greenwood, 1966] developed a model tailored for constriction resistance in a multi-spot surface. Greenwood's focus was on the real contact area, specifically examining the constriction resistance generated by a set of circular spots with radius  $a_i$  separated by distances  $d_{ij}$  between the spots indexed by  $i$  and  $j$ . An example of this model can be found Fig. 1.21, adapted from [Greenwood, 1966].

Greenwood expresses the constriction resistance in terms of heat production. This approach tends to overestimate the constriction resistance for this particular problem. The constriction resistance could be simplified assuming equal contact spots of radius  $\bar{a}$  as

$$R = \frac{\rho}{4n\bar{a}} + \frac{\rho}{2\pi n^2} \sum_{i \neq j} \frac{1}{d_{ij}} \quad (1.30)$$

This equation can be compared with the one proposed by Holm [Holm, 1967]. In this context, the interaction between spots goes streamlined by the definition of a length



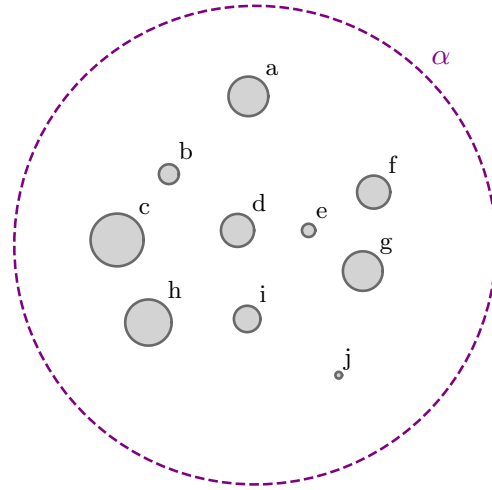


Figure 1.21: Example of real contact area for constriction resistance computation adapted from [Greenwood, 1966]

parameter,  $\alpha$ , which depicts the radius of the cluster encompassing the contact spots.

$$R = \frac{1}{4n\bar{a}} + \frac{1}{4\alpha} \quad (1.31)$$

The Holm's model is parallel with the Greenwood's resistance formula. The *Holm's radius*  $\alpha$  can be defined as follows,

$$\alpha = \frac{\pi n^2}{2} \left( \sum_{i \neq j} \frac{1}{s_{ij}} \right)^{-1}$$

Fig. 1.21 illustrates, that for the particular depicted case the Holm's radius could be larger than the true radius of the cluster. Holm's model does not consider the size or the distribution of the spots within a cluster. This observation aligns with the findings of Minowa and Nakamura [Nakamura and Minowa, 1986], who conducted FEM simulations on different distributions. Their results indicated that the outcomes are not significantly influenced by the arrangement of these points, unless they are concentrated around the periphery of the nominal contact zone.

Greenwood and Tripp's research [Greenwood and Tripp, 1967] suggests that contact spots are clustered for a parabolic body-shape profile around the middle point, but spread out of the contact radius given by the Hertzian contact. As the load increases, this clustering effect intensifies, making the contact spot distribution more consistent with the Hertzian pressure distribution.

### Validation with experiments

In Holm's model Eq. (1.31), the term  $1/4n\bar{a}$  decreases as the number of spots increases. For a high number of contact spots, the term involving the Holm's radius,  $\alpha$ , become predominant. The real area of contact might be defined as  $A = \pi\eta\alpha^2$ , where  $\eta$  represents the density of contact spots. In the plastic deformation regime, using Eq. (1.13), the constriction resistance relates to the load applied, as expressed below,

$$R = \frac{\rho}{4} \left( \frac{\pi\eta H}{F} \right)^{1/2} \quad (1.32)$$

The constriction resistance diminishes as the load applied increases, exhibiting an inverse square root relationship. This behavior has been corroborated by several experimental studies, which have observed this trend across various combinations of mechanical loads and materials. With the onset of plastic deformation, the contacting asperities become flattened, leading to a non-reversible change in constriction resistance. During unloading, the constriction resistance is lower compared to the loading phase, attributable to these flattened asperities. Besides plasticity, adhesion may also influence conductivity, with certain parts remaining conductive even under tensile loads.

In Cooper's pioneering work [Cooper et al., 1969], thermal resistance is examined, taking into account different asperity properties and load regimes. This study introduces the concept of thermal interfacial contact conductance,  $h_c$ , which is derived from a temperature drop,  $\Delta T$ , across the interface, as defined by  $R = 1/h_c A = Q/\Delta T$ . The authors consider the effect of roughness, building upon an asperity-based model. Their model establishes a relationship that includes a plasticity index, where  $\sigma$  represents the standard deviation of the asperity distribution, and  $|\tan(\theta)|$  indicates the average curvature slope. The parameter  $h_c$  is then articulated in terms of the mean pressure,  $p_m$ , and the hardness.

$$\frac{h_c}{k} \frac{\sigma}{|\tan \theta|} = 1.45 \left( \frac{p_m}{H} \right)^{0.985} \quad (1.33)$$

The exponent for the ration  $p_m/H$  results from the extrapolation of the results, but it appears to be at variance with Eq. (1.32).

### 1.3.2 Real conductance effect

#### Effect of the thermal convection with gas

The thermal conductance between rough surfaces also needs to consider the heat exchange due to convection. However, its influence is relatively minor, as highlighted by Lang [Lang, 1962]. This study leads to the identification of a characteristic length scale of the cavity, which pertains to the study of the height profile. In reality, gas is dispersed among the cavities formed between rough surfaces. The fluid within these cavities contributes to convection exchange, necessitating the definition of a convective heat transfer coefficient,  $h_g$ . The characteristic length scale of these cavities is thought to be the average thickness,  $\delta$ , combined with the thermal conductivity of the gas,  $k_g$ .

$$h_g = \frac{k_g}{\delta} \quad (1.34)$$

The thickness,  $\delta$ , is anticipated to be comparable in magnitude to the height of the surface roughness. This model is based on a static interpretation of the gas, differing from the dynamics characteristic of natural convection. In considering the heat convection exchange, the temperature difference between the gas and the surface temperature is taken into account. Following the heat exchange laws at the macro-scale, this would involve the mean surface temperature,  $T_s$  and the initial temperature of the gas,  $T_g$ . However, the actual temperature of the fluid within,  $T_f$ , might vary from these temperatures. It yields the definition of *accommodation coefficient*, denoted by  $\beta$ , which serves to adjust the temperature values:

$$\beta = \frac{T_f - T_g}{T_s - T_g} \quad (1.35)$$

The definition of the accommodation coefficient is experimentally studied discussing upon the influence of roughness [Semyonov et al., 1984, Song and Yovanovich, 1987, Bahrami et al., 2004]. It is found to be sensitive to the pressure gas, significantly increasing for high pressure. Otherwise the conductive resistance would be still dominant.

### Influence of oxidation

Oxidation is an ubiquitous problem in all applications involving metals. One of its effects is the reduction of the conductivity of the contacting surfaces. In practical scenarios, oxide crystals typically begin to nucleate at certain points and then expand, following the crystalline orientation of the metallic grains. This growth phenomenon is extensively detailed in the literature, as seen in [Thomas and Roberts, 1961, Doherty and Davis, 1963, Hart and Maurin, 1970]. Such occurrences are observable, as demonstrated in Fig. 1.22. Typically, oxide stains are likely defined by polygonal shapes. The crystal orientation and the shapes can be correlated through the use of interferometry techniques. As a result, the real conductive surface area is reduced in comparison with the real contact area. The constriction resistance increases while the contact stiffness remains practically unchanged between oxidized and clean surfaces.

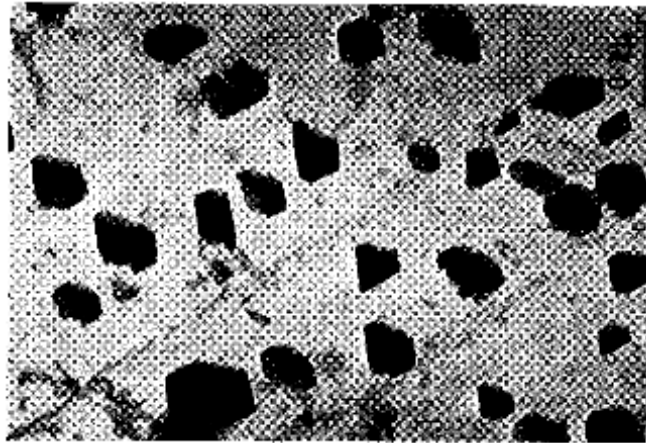


Figure 1.22: Result of direct observation for aluminum oxide on aluminum surface adapted from [Thomas and Roberts, 1961]

Oxidation is inherently linked to environmental conditions, with various classifications. First and foremost, humidity level plays a significant role in corrosion, which yields galvanic corrosion being at variance with dry corrosion. Temperature is another crucial factor that accelerates oxidation. Moreover, corrosion can be compounded by heating and thus being potentially linked to the Joule effect, a phenomenon explored by Urakawa [Urakawa et al., 2013]. The oxidation process results in the formation of a weakly conducting surface film.

Typically, such films exhibit the characteristics of brittle materials. Electrical contact is formed by metal flow through narrow cracks of oxide layers. The oxidized contactor can transmit flow following the fracture of the oxide layers, experiencing a load as noted by [Timsit, 1980] in the case of aluminum contactors. The constriction resistance is affected by the configurations of cracks and the modes of fracture, as additionally evidenced by [Osias and Tripp, 1966].

### 1.3.3 Material coating

In the purpose to reduce the corrosion, connectors are sometimes coated with noble materials like gold, silver, nickel, or tin. In addition, these coatings may have convenient effects on the mechanical properties at the interface, reducing both roughness and hardness. The current lines could be deviated by the coating conductive properties different from the bulk coated material, as illustrated in Fig. 1.23. In this figure, the two parameters of conductivity are defined as  $k_l$ ,  $k_s$  denote the conductivity for the layer material and the substrate, respectively. Ultimately when  $k_l \gg k_s$ , the conductive material may be reduced to the coating with thickness  $L$ . The current path is then constrained by the thin layer,

instead of letting the current spread toward the half-space. The curvature of the current travel introduces an additional resistance, known as *spreading resistance*, akin to the constriction seen at the contact spot. The development of micro-cables and printed circuits has spurred research into the latter subject. Zhang explored this topic in a series of studies [Zhang et al., 2011, Zhang et al., 2012], conducted by numerical simulations. These studies indicate that the resulting constriction resistance tends towards a limiting value of 0.28 as the coating thickness tends to zero.

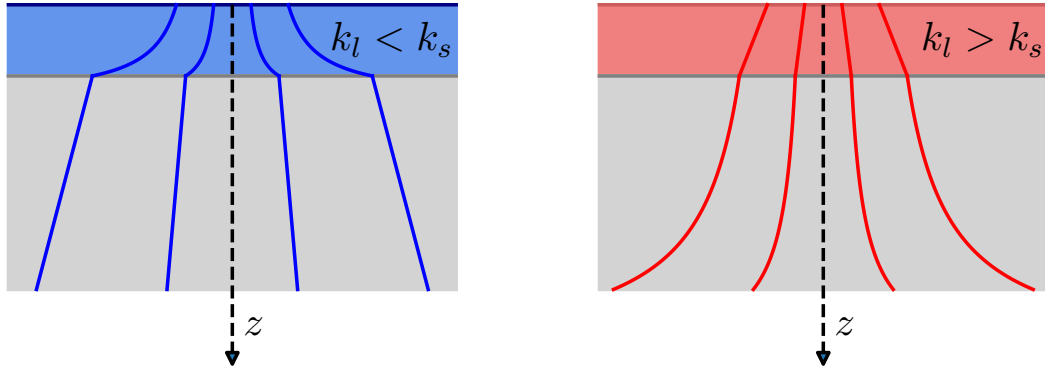


Figure 1.23: Illustration of current flow for layered material, for different conductivity couple

**Plating factor.** In a less extreme scenario, the resulting constriction resistance is influenced by  $k_l$ ,  $k_s$ , and  $L$ . Its evaluation still requires numerical computation. However, it is noteworthy when the thickness  $L$  is comparable to the radius of the contact spot, as shown on the right-hand side of Fig. 1.23, the current travels along straight vertical line. The constriction resistance within the substrate can be roughly estimated by Eq. (1.12), but the coating results in a conductive resistance of a cylinder with radius  $a$  and height  $L$ , as given below

$$R_t = \frac{1}{4k_s a} \left( 1 + \frac{4}{\pi} \frac{k_l L}{k_s a} \right) \quad (1.36)$$

Conversely, if the plating is thicker, it causes the current flow to curve, similarly to the one depicted on the left-hand side of Fig. 1.23 for  $k_l < k_s$ . Under these circumstances, the constriction resistance deviates from the previously mentioned expression and is more accurately represented by  $1/4k_l a$ , while disregarding the substrate. This relationship has been supported by the work of Nakamura and Minowa [Nakamura and Minowa, 1989], reinforced by computational results. In this context, comparing the constriction resistance with and without plating leads to the formulation of the *plating factor*, denoted as  $P_f$ :

$$P_f(L/a, k_l, k_s) = \left( \frac{1}{4k_{eff} a} \right) / \left( \frac{1}{4k_s a} \right) \quad (1.37)$$

where  $k_{eff}$  represents the effective conductivity of the plated material. Some results are reported in Fig. 1.24 for copper coupled with various coating material. The plating factor rises with the plating thickness, being always greater than 1, because the coating material is less conductive than the copper.

Despite the rise of the contact resistance, the overall behavior should benefit from the plating by the reduction of the contaminant film. Eventually, using softer materials yield to more plastic regime deformation, and result in a larger real contact area and thus small resistance. Evidence on the deformation mode and insights on contaminants can be found in [Pinnel and Bradford, 1980, Antler et al., 1975, Slade, 2017].

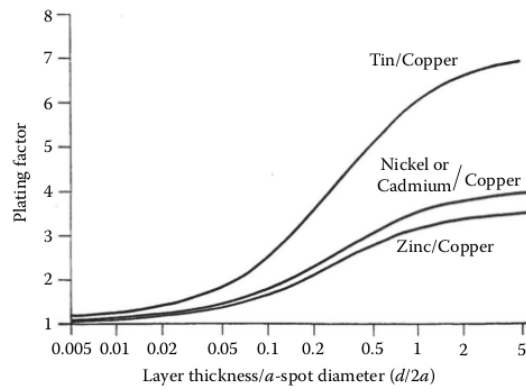


Figure 1.24: Influence of the plating factor for  $k_l < k_s$ , figure adapted from [Williamson and Greenwood, 1989].

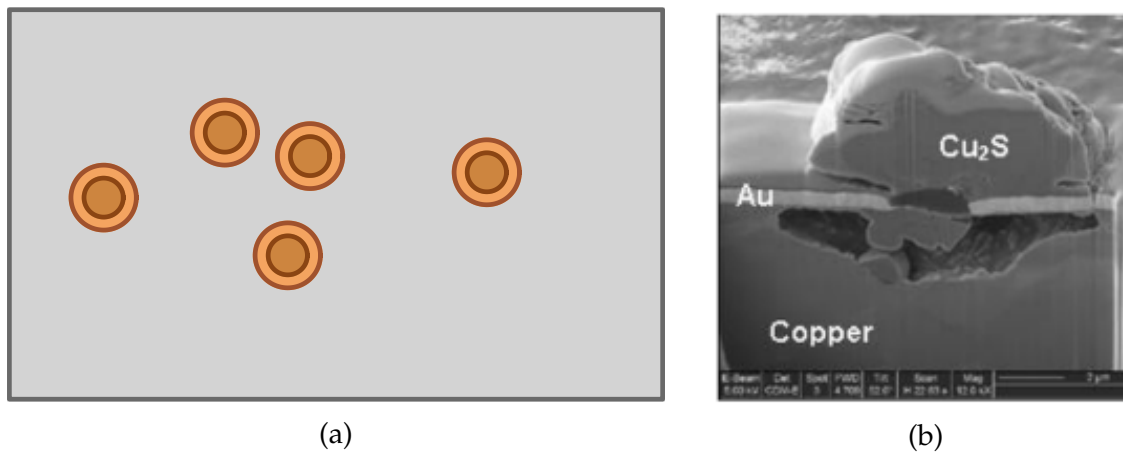


Figure 1.25: (a) Diagram of hole in plating surrounded by halo in pore corrosion, (b) observation of copper sulfide blossom, adapted from [Sun et al., 2007].

**Pore corrosion.** The efficiency of the plating depends on its thickness. Electronic connectors are commonly coated with gold, but the coating is eventually porous. This means the plating get holed, and corrosion could lies through those. This specific type of corrosion is known as *pore corrosion*.

Corrosion of the substrate results in the formation of cavities beneath the plating. This can lead to the emergence of oxide layers on top of the plating. Sun [Sun et al., 2007] explored this phenomenon for copper coated with gold. As a result, even with coating, the contact resistance may be adversely affected by oxidation and decline over time. In the meantime, the size of the oxide blossom increases with the size of the pore.

### 1.3.4 Joule heating and coupling effect

The electrical contact problem might exhibit coupling thermal effect. Initially, the electrical issue relates to the thermal problem via the Joule effect: the flow of current heats the material due to its conductive properties. Therefore a rise in temperature results in a reduction of thermal conductivity,  $k$ , and an increase in electrical resistivity,  $\rho$ , by a proportional law in temperature, as follow,

$$k = k_0(1 - \beta T) \quad (1.38a)$$

$$\rho = \rho_0(1 + \alpha T) \quad (1.38b)$$

Where  $\beta$  and  $\alpha$  denote thermal conductivity and electrical resistivity constants, respectively. This relationship can be connected to the *Weidemann-Franz* law, given by  $k\rho = TL$ ,

where  $L$  is the Lorenz constant, valued at  $L = 2.44 \cdot 10^{-8} V^2 \cdot T^{-2}$ , illustrating the direct relation between an increase in  $\rho$  and a decrease in  $k$ . This law has shown its experimental consistency [Timsit, 1983] but inherently restricted by the melting point of metals. Interestingly, it evaluates a potential drop of merely one-tenth of a volt at the melting point.

This highlight the shortcomings of the ohmic resistance model. When the mean free path, denoted as  $l_{fp}$  is greater than the typical radius of the contact spots or the gap between contacting surfaces, electrons are capable of traversing these distances. Such behavior contributes an additional nano-scale resistance, referred to as Sharvin resistance. This concept diverges from the classical Ohmic resistance model and aligns more closely with a ballistic model, as detailed by Wexler [Wexler, 1966].

$$R = \frac{\rho}{4a} \Gamma(l_{fp}/a) + \frac{C}{a^2} \quad (1.39)$$

With  $C \sim 10^{-8} \Omega \cdot m^{-2}$  is the Sharvin resistance coefficient, and  $\Gamma$  is a function decreasing from 1 to 0.694. The ratio  $l_{fp}/a$  is known as the Kunder's coefficient. The value of  $C$  must be defined for each couple of metals, as reported in [Slade, 2017]. The model of constriction resistance is in good agreement in the extent that the mean free path is of magnitude of  $nm$ , for mean contact spot of  $0.1 \mu m$ .



### Contents

---

<b>2.1 Integral formulation for conduction</b> . . . . .	<b>47</b>
2.1.1 Problem of conductivity . . . . .	47
2.1.2 Identity of reciprocity . . . . .	48
2.1.3 Elementary solution . . . . .	49
2.1.4 Solution for two dimensional problem . . . . .	50
2.1.5 Limits for Boundary Integral Equation . . . . .	51
2.1.6 Boundary Integral Equation for $H$ . . . . .	53
2.1.7 Application to the conductivity of a contact spot . . . . .	53
<b>2.2 Boundary Element Method</b> . . . . .	<b>58</b>
2.2.1 Discretization and linear system definition . . . . .	58
2.2.2 Construction of the linear system . . . . .	62
2.2.3 Numerical integration . . . . .	64
2.2.4 Validation with circular contact spot . . . . .	74
<b>2.3 Fast-BEM</b> . . . . .	<b>78</b>
2.3.1 Approximation construction . . . . .	78
2.3.2 Error in function of the rank . . . . .	86
2.3.3 $\mathcal{H}$ -matrix . . . . .	87
2.3.4 Application of the approximations . . . . .	95
2.3.5 $\mathcal{H}$ -solver . . . . .	106

---



**■ ■ Résumé du Chapitre II** Cette partie vise à introduire les méthodes numériques utilisées pour la modélisation de la conduction aux interfaces de contact. Afin de tirer partie des hypothèses du problème physique, et définir de façon fiable et consistante les surfaces de contact, nous avons choisi de développer un modèle par Élément de Frontière. Cette partie sera ainsi organisée en trois sous-parties, détaillant les outils numériques développés pour cette méthode. La première sous-partie est dédiée à l'établissement de l'équation intégrale, permettant la formulation des Éléments de Frontière. Celle-ci tire partie des propriétés physiques du problème, de l'existence d'une solution particulière, et se réduit à la modélisation de la surface de contact. Une seconde sous-partie introduit les outils numériques, conduisant à l'établissement d'un système linéaire à résoudre. La mise en place de la Méthode par Elements de Frontière fait appel aux outils classique de maillage et d'interpolation, communs à d'autre méthode, tout en engageant des méthodes spécifiques pour l'intégration numérique. Cette sous-partie est conclue par une première étude de la tache circulaire de contact, s'agissant d'un classique problème de résistance de constriction. Enfin la dernière sous-partie détaille le développement d'une version *rapide* des Élément de Frontière, visant à réduire la complexité initiale en stockage et mémoire de  $O(N^2)$ , à un ordre de  $O(N \log(N))$  Cette implementation fait intervenir la définition de *matrice hiérarchique* ( $\mathcal{H}$ -matrice), et l'utilication d'approximation faible-rang.

**🇬🇧 Abstract for Chapter II** This chapter aims to describe numerical methods used for solving conduction problem at contact interfaces. To take advantage of the assumptions of the physical problem, and to define the contact surfaces in a reliable and consistent manner, we have chosen to develop a model using the Boundary Element method. This chapter is thus organized into three sections, detailing the numerical tools developed for this method. The first section is dedicated to the establishment of the integral equation, which forms the basis for the Boundary Element Method (BEM). This section takes advantage of the physical properties of the problem, particularly the existence of an elementary solution, which reduces the modeling to the contact surface. A second section will introduce numerical tools, leading to the establishment of the linear system to be solved. The implementation of the Boundary Element Method involves the use of common tools such as meshing and interpolation function, and employs specific methods for numerical integration. A first study of a circular contact spot, as a primary problem of constriction resistance, will be carried out. Finally, the last section give insights into the development of the *fast* version of the Boundary Elements, aiming to reduce the initial storage and memory complexity from  $O(N^2)$  to  $O(N \log(N))$ . This implementation involves the definition of *hierarchical matrix* ( $\mathcal{H}$ -matrix), and the use of low-rank approximation such as ACA and SVD. All details of the Fast-BEM implementation are presented and illustrated on numerous examples.

## Introduction & motivations

The constriction resistance is typically characterized by the conduction between two half-spaces in contact. One way to solve this problem could be using Finite Element Method. However, this requires modeling the body sufficiently large and possibly extrapolating the results in the scope of half-space geometry. Eventually one could get rid of the extrapolation by using the Infinite Elements, as suggested by [Bettess, 1977], but it still requires a volumetric mesh, which does not ensure the geometric consistency near the edges of the contact area.

On the other hand, the Boundary Element Method seems more suitable for this issue. It has been previously employed for circular contact spots [Nakamura, 1993], proving its effectiveness in addressing this type of problem. This allows to reduce the problem's geometry to the real contact area. Only a planar mesh is needed, which streamlines the evaluation of the flux transmitted through the real contact area.

This section is dedicated to presenting the integral equation foundational to the BEM formulation, followed by the Fast-BEM. The implementation was widely inspired by the BEM handbook by Bonnet [Bonnet, 1999] (in french), following its development for the integral equation formulation, and then the application of numerical tools. Concerning the Fast-BEM implementation, the book on  $\mathcal{H}$ -matrix by Bebendorf [Bebendorf, 2008], provides subsequent insights in the construction and the use of these matrices. The following development has an objective to be both as comprehensible and complete as possible.

## 2.1 Integral formulation for conduction

### 2.1.1 Problem of conductivity

In this part, the problem of conduction in a half-space will be developed intending to formulate its corresponding integral equation. The problem of conduction is identical for the thermal or electric problems, both in static regime. The geometry is generally considered as a body  $\Omega$ , such as a three-dimensional solid, bounded by a surface  $\partial\Omega$ . This body is assumed to be constituted by an isotropic and homogeneous material. The conductivity property is fully characterized by a scalar constant  $K$ .

The problem in  $\Omega$  is resolved in terms of a scalar potential function, denoted by  $U$ . It enables to equivalently study the electric and the thermal problems. The flux derives from the potential, denoted by  $j$ , as follows

$$j = -K\nabla U, \text{ in } \Omega \quad (2.1)$$

Where the symbol  $\nabla$ . stands for the gradient. This equation is supplemented by the equilibrium equation in  $\Omega$ . This is given by the following equation (2.2), considering the problem of conduction in its static regime, with no heat source.

$$\text{div}(j) = 0, \text{ in } \Omega \quad (2.2)$$

Such as the problem of conduction is assumed in its static regime, and with no *heat source*.

Substituting the flux in Eq. (2.2), by its relation with the potential in Eq. (2.1), results in the establishment of the *Laplace's equation*. This involves solely the potential  $U$  in a linear relation, and the conductivity  $K$  disappears, assuming this does not vary in space, nor depends on temperature.

$$\Delta U = 0, \text{ in } \Omega \quad (2.3)$$

To complete the problem formulation, one needs to prescribe boundary conditions: *Dirichlet's* and *Neumann's* conditions, in terms of potential and normal flux, respectively. Those are respectively defined in the following equations Eq. (2.4), Eq. (2.5).

$$\text{Dirichlet :} \quad u(y) = u^D(y) \text{ for } y \in \partial\Omega_u \quad (2.4)$$

$$\text{Neumann :} \quad j_n(y) \equiv \mathbf{j}(y) \cdot \mathbf{n}(y) = j^N(y) \text{ for } y \in \partial\Omega_j \quad (2.5)$$

Where  $\mathbf{n}$  is the outward normal.

In a general sense, a problem is deemed to be well-posed when a single condition is set at every point on the boundary. It is possible to combine two types of condition, but they must be applied within separate regions, as highlighted by the following conditions:

$$\partial\Omega_u \cup \partial\Omega_j = \partial\Omega, \quad \partial\Omega_u \cap \partial\Omega_j = \{\emptyset\}$$

### 2.1.2 Identity of reciprocity

The integral formulation of this problem relies on the *theorem of reciprocity*, for a linear problem. This section aims to introduce this type of formulation, taking on the Boundary Element Method as presented in [Bonnet, 1999]. The theorem of reciprocity parallels to the *Maxwell-Betti theorem* straightforwardly formulated in the case of a linear elastic problem. This assumes the problem linear, involving an isotropic and homogeneous material. The aforementioned problem of conduction respects this framework. This theorem is formulated for the *Poisson's equation*, as presented below in terms of potential  $u^1$ , and a heat source  $b^1$ , in  $\Omega$ :

$$\Delta u^1 + b^1 = 0$$

The flux  $j^1$  stems from to the potential,  $u^1$ , employing a constitutive behavior relation like *Fourier's law* Eq. (2.1), with a constant conductivity  $K$ .

In parallel, the second potential, denoted by  $u^2$ , is established within a domain  $E$ . This potential adheres to the same *Poisson's equation*, and its corresponding flux  $j^2$  is likewise derived from  $u^2$  by a *Fourier's law*. The theorem of reciprocity emerges from a scalar product between the first equilibrium equation and the second potential  $u^2$  in the domain  $E$  as presented in Eq. (2.6a). Similarly, a scalar product is defined between the first potential  $u^1$  and the second equilibrium  $b^2$  in Eq. (2.6b). These relations involves the *Poisson's equation* for  $u^1$  and  $u^2$ , respectively. As a result, due to the zero value of *Poisson's equation*, the product terms are identically zero, as are their integrals over the domain  $\Omega$

$$\int_{\Omega} (\Delta u^1 + b^1) u^2 dV = 0 \quad (2.6a)$$

$$\int_{\Omega} (\Delta u^2 + b^2) u^1 dV = 0 \quad (2.6b)$$

The terms  $\Delta u^1 u^2$ , and  $\Delta u^2 u^1$ , can be alternatively reformulated using *divergence's property* and product-derivation formula.

$$\Delta u^1 u^2 = \text{div}(\nabla u^1 u^2) - \nabla u^1 \cdot \nabla u^2$$

$$\Delta u^2 u^1 = \text{div}(\nabla u^2 u^1) - \nabla u^2 \cdot \nabla u^1$$

Substituting the terms  $\nabla u^1 u^2$ , and  $\nabla u^2 u^1$ , in the last integrals Eq. (2.6a), (2.6b), leads us to new expressions for those integrals:

$$\int_{\Omega} \text{div}(\nabla u^1 \cdot u^2) dV - \int_{\Omega} \nabla u^1 \cdot \nabla u^2 dV + \int_{\Omega} b^1 u^2 dV = 0 \quad (2.7a)$$

$$\int_{\Omega} \text{div}(\nabla u^2 \cdot u^1) dV - \int_{\Omega} \nabla u^2 \cdot \nabla u^1 dV + \int_{\Omega} b^2 u^1 dV = 0 \quad (2.7b)$$

Combining Eq. (2.7a) with Eq. (2.7b), allows us to get rid of the integral which involves  $\nabla u^1 \cdot \nabla u^2$  term. Subsequently, the two terms that employ divergence are reformulated into integral over the surface  $\partial\Omega$ , by the application of the divergence theorem. This results in the establishment of the following equation, which is consistent with the application of the *theorem of reciprocity*.

$$\boxed{\int_{\partial\Omega} (\nabla u^1 u^2 - u^1 \nabla u^2) \cdot n dS = \int_{\Omega} (b^2 u^1 - b^1 u^2) dV} \quad (2.8)$$

The vector  $\mathbf{n}$  stands for the normal vector at the surface element  $dS$ . The terms  $\nabla u^1$  and  $\nabla u^2$  are both vectors, and both rely on the flux  $\mathbf{j}^1$ ,  $\mathbf{j}^2$ , respectively, by the same conductivity  $K$ . The terms  $\nabla u^1 \cdot \mathbf{n}$  and  $\nabla u^2 \cdot \mathbf{n}$  are related to the normal flux. The left-hand side of the equation resumes the boundary conditions, while the right-hand side stems from the heat term in  $\Omega$ . For the linear elastic problem, the Maxwell-Betti theorem is based on the linear elasticity. Integrating this product over a closed domain yields a relationship between the energies of elastic deformation. It establishes the principle that the work done by one load distribution on the displacement field caused by a second, unrelated load distribution, is equal to the work done by the second on the displacement field caused by the first.

### 2.1.3 Elementary solution

Once the theorem of reciprocity is formulated for the conduction problem, the potential field  $u^1$  is replaced with the potential  $U$ , reverting to the physical notation aforementioned in Section 2.1.1. The second potential field  $u^2$  is associated with an *elementary solution*. Helped by the linearity of the problem, an elementary solution may serve a general purpose, with any complex solution being assembled through the *principle of superposition*. This solution is defined on an infinite set  $E$ , which encompasses the body  $\Omega$ , and belong to  $\mathbb{R}^3$ , as formulated below :

$$\Omega \subset E \subset \mathbb{R}^3$$

These subsets allow to consider a point of observation  $\mathbf{x} \in E$ , potentially out  $\Omega$ , and a source point  $\mathbf{y} \in \Omega$ . This yields the definition of the elementary solution, denoted by the scalar function  $G$  in  $E$ , as given by the equation,

$$\boxed{\Delta G(\mathbf{x}, \mathbf{y}) + \delta(\mathbf{x} - \mathbf{y}) = 0} \quad (2.9)$$

Where the function  $G$  arises from a Poisson problem with a *punctual heat source*. The symbol  $\delta$  stands for the *Dirac's function*.

Using this formulation, the heat source is equal to zero everywhere except at the source point location, when  $\mathbf{x} = \mathbf{y}$ . This elementary solution presented in Eq. (2.9), is known as the *Green's function*. This function involves the distance  $r$  between the observation point  $\mathbf{x}$  and  $\mathbf{y}$ ,  $r = \|\mathbf{x} - \mathbf{y}\|_2$ . The symbol  $\|\cdot\|_2$  stands for the Euclidean norm. Its expression for the stationary conductive problem is given by:

$$\boxed{G(\mathbf{x}, \mathbf{y}) = \frac{1}{4\pi r}} \quad (2.10)$$

In Eq. (2.8), the normal derivative is also needed. This yields the definition of the scalar function  $H$ , which derives from the gradient field of  $G$ , as presented :

$$H(\mathbf{x}, \mathbf{y}) \equiv \nabla G(\mathbf{x}, \mathbf{y}) \mathbf{n}(\mathbf{x}) = G_{,j}(\mathbf{x}, \mathbf{y}) n_j(\mathbf{x}) \quad (2.11)$$

The scalar function  $H$  is expressed by the following expressions,

$$H(\mathbf{x}, \mathbf{y}) = -\frac{1}{4\pi r^2} r_{,n} \quad (2.12a)$$

$$r_{,n} = r_{,i} \cdot n_i = \frac{y_i - x_i}{r} n_i \quad (2.12b)$$

Where the scalar function  $r_{,n}$  stems from the scalar product between the normal vector  $\mathbf{n}$  along the boundary, and the derivative of  $r$ . The coordinates  $x_i$ ,  $y_i$ , and  $n_i$  stands for the components of the  $\mathbf{x}$ ,  $\mathbf{y}$  and  $\mathbf{n}$ , respectively.

The *Green* function is continuous, and continuously derivable on  $\mathbb{R}^*$  following its variable  $r$ . Nevertheless, it is singular at the source point  $\mathbf{x} = \mathbf{y}$ , when  $r = 0$ . This singularity inherits of the punctual definition of heat source by the Dirac's source. Integrating the elementary problem Eq. (2.9) in  $\Omega$ , and using the divergence theorem, pertains to the following development

$$\begin{aligned} \int_{\Omega} \Delta G(\mathbf{x}, \mathbf{y}) dV_Y + \int_{\Omega} \delta(\mathbf{x}, \mathbf{y}) dV_Y &= 0 \\ \iff \int_{\partial\Omega} \nabla G(\mathbf{x}, \mathbf{y}) \cdot \mathbf{n}(\mathbf{y}) dS_Y + k &= 0 \\ \boxed{\int_{\partial\Omega} H(\mathbf{x}, \mathbf{y}) dS_Y + k = 0} & \quad (2.13) \end{aligned}$$

The expression of  $k$  stems from the properties of the Dirac function. It depends on the position of  $\mathbf{x}$ . Practically, this factor,  $k$ , is assigned to the value 0 if  $\mathbf{x}$  lies outside the body  $\Omega$ , such as  $\mathbf{x} \in \bar{\Omega}$ . The set  $\Omega'$  stands for the body  $\Omega$  deprived of its boundary  $\partial\Omega$ , such as  $\Omega' = \Omega \setminus \partial\Omega$ . Insofar,  $k$  is set equal to 1 if the source point falls within the body  $\Omega'$ . The case scenario when  $\mathbf{x} \in \partial\Omega$  needs to be thoroughly developed, as thereafter proposed.

$$k = \begin{cases} 1, & \text{for } \mathbf{x} \in \Omega' \\ 0, & \text{for } \mathbf{x} \notin \Omega \end{cases} \quad (2.14)$$

#### 2.1.4 Solution for two dimensional problem

For the problem within a two-dimensional space, the Green function takes a different expression:

$$G(\mathbf{x}, \mathbf{y}) = \frac{1}{4\pi} \log(r), \quad H(\mathbf{x}, \mathbf{y}) = \frac{1}{4\pi r} r_{,n}$$

This function is still continuous, but also diverges when  $r \rightarrow 0$ . However this function is integrable along a closed line  $\partial\Omega$ , for a point of observation part of the boundary,  $\mathbf{x} \in \partial\Omega$ . The interaction of the  $\log$  function yields an expression similar to  $r \log(r) - r$ , which has a finite value when  $r \rightarrow 0$ . This result gives a first insight into the existence of the factor  $k$ , when  $\mathbf{x} \in \partial\Omega$ , but needs to be thoroughly expanded in the case of a three dimensional space.

#### Boundary Integral representation for the potential

Recalling Eq. (2.8), this latter equation by substituting all physical fields with specific field variables. First the set of variable indexed by 1,  $(u^1, |^1, b^1)$ , is replaced by the potential  $U$ , its flux  $j$ , and we assume the relating heat source  $b = 0$ . The second field  $(u^2, |^2, b^2)$  assigns to the Green function, using  $G$  for the potential, its derivative,  $H$ , for the flux, and considering  $\delta$  for the heat source. This formulation takes advantage of the properties of Dirac function.

$$\int_{\partial\Omega} \left( \frac{j_n(\mathbf{y})}{K} G(\mathbf{x}, \mathbf{y}) - U(\mathbf{y}) H(\mathbf{x}, \mathbf{y}) \right) dS_Y = \int_{\Omega} \left( \delta(\mathbf{y} - \mathbf{x}) U(\mathbf{y}) - \underset{=0}{b(\mathbf{x})} G(\mathbf{x}, \mathbf{y}) \right) dV_Y \quad (2.15)$$

Where  $q_n = -\nabla U \cdot \mathbf{n}$ , is replaced by  $j_n/K$  which represents the normal flux with an inward orientation to  $\Omega$ . The term incorporating  $\delta$  reduces to

$$\int_{\Omega} \delta(\mathbf{y} - \mathbf{x}) U(\mathbf{y}) dV_y = k U(\mathbf{x}) \quad (2.16)$$

This enables to extract the potential value at any point  $\mathbf{x}$ . The Green function summarizes the effect of the sources in  $\Omega$  at the observation point  $\mathbf{x}$ . Finally we get the following integral function involving only the integral over the boundary surface  $\partial\Omega$ .

$$\int_{\partial\Omega} \left( \frac{j_n(\mathbf{y})}{K} G(\mathbf{x}, \mathbf{y}) - U(\mathbf{y}) H(\mathbf{x}, \mathbf{y}) \right) dS_y = k U(\mathbf{x}) \quad (2.17)$$

### 2.1.5 Limits for Boundary Integral Equation

In Section 2.1, a first integral equation has been set for the problem of conduction we aim to study. However, this can not be readily applied for our case. Indeed, the divergence theorem and its application require a closed outer surface. In our case, the outer surface is not closed, as the considered body is a half-space. Furthermore,  $k$  is defined only for an observation point located inside or outside  $\Omega$ . Its value at the boundary needs to be thoroughly computed, as presented in this section.

#### Reformulation with potential continuity

Before starting the limit development, we need to define the integral equation in a more convenient way, allowing us to study the continuity condition at the boundary for the potential field. In fact the definition of the identification function  $k$  is non continuous, but it relates to an integral formulation in term of  $H$ .

Using Eq. (2.13) multiplied by the potential  $U(\mathbf{x})$ , we get the following expressions:

$$\begin{aligned} k(\mathbf{x})U(\mathbf{x}) &= - \left( \int_{\partial\Omega} H(\mathbf{x}, \mathbf{y}) dS_y \right) U(\mathbf{x}) \\ \iff k(\mathbf{x})U(\mathbf{x}) &= - \int_{\partial\Omega} H(\mathbf{x}, \mathbf{y}) U(\mathbf{x}) dS_y \end{aligned}$$

Integrating this expression in the latter integral formulation Eq. (2.17), we get a new integral equation not containing the function  $k$ .

$$\int_{\partial\Omega} \left( \frac{j_n(\mathbf{y})}{K} G(\mathbf{x}, \mathbf{y}) - (U(\mathbf{y}) - U(\mathbf{x})) H(\mathbf{x}, \mathbf{y}) \right) dS_y = 0 \quad (2.18)$$

#### Definition of an inclusion

As was said earlier, the integral equation is only valid for the observation point inside or outside the finite body  $\Omega$ . The last integral equation Eq. (2.18) makes the same assumptions. To safely extend this integral formulation at the boundary an inclusion  $V_\epsilon$  is added at the boundary, embedded in the body  $\Omega$ , as presented in Fig. 2.1, with  $V_\epsilon \subset \Omega$ . The observation point  $\mathbf{x}$  is considered to be part of the inclusion  $\mathbf{x} \in V_\epsilon$ ,

A new body can be defined as  $\Omega_\epsilon(\mathbf{x}) = \Omega \setminus V_\epsilon(\mathbf{x})$ , i.e. the body  $\Omega$  deprived of the inclusion. The inclusion is spherical, with a radius of order  $\epsilon$ . The limit situation where  $\epsilon \rightarrow 0$  accounts for  $\mathbf{x} \in \partial\Omega$ .

The boundary can be readily reformulated accounting on this inclusion as  $\partial\Omega_\epsilon = (\partial\Omega \setminus e_\epsilon) \cup S_\epsilon$ .

The integral equation(2.18) can be reformulated accounting for  $\partial\Omega_\epsilon$

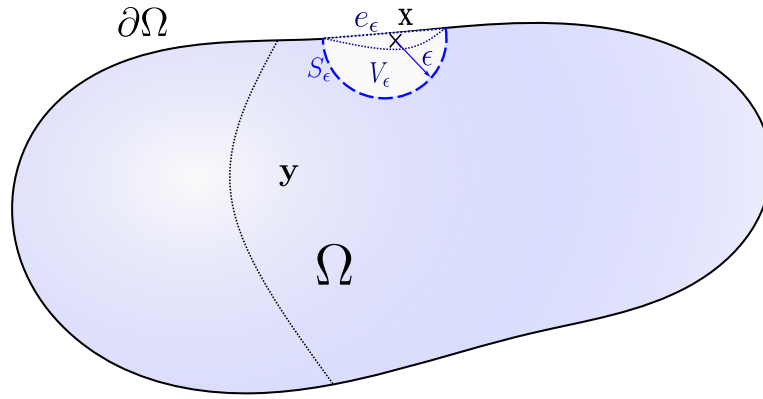


Figure 2.1: Definition of the inclusion on the boundary  $\partial\Omega$

$$\int_{\partial\Omega_\epsilon} \left( \frac{j_n(\mathbf{y})}{K} G(\mathbf{x}, \mathbf{y}) - (U(\mathbf{y}) - U(\mathbf{x})) H(\mathbf{x}, \mathbf{y}) \right) dS_y = 0 \quad (2.19)$$

### Condition of continuity

The last equation(2.19) seems to be more adapted to the problem of integration at the boundary dealing with a difference of potential. This formulation relies on the continuity of  $U$  and the definition of  $j_n$ . The potential can be reasonably assumed continuous in  $\Omega$ , like  $U \in C^2(\Omega)$  This property is physically consistent with the continuum equation of  $U$  in  $\Omega$  in term of laplacian, involving its second derivative. The potential  $U$  satisfies the  $\alpha$ -Hölder condition as expressed below.

#### Definition: $\alpha$ -Hölder continuity

Being  $f$  a real of scalar function on  $d$ -dimensional Euclidean space satisfies a  $\alpha$ -Hölder continuous, where there are two real constants  $C \geq 0$  and  $\alpha > 0$ , such that:

$$|f(\mathbf{y}) - f(\mathbf{x})| \leq C \|\mathbf{x} - \mathbf{y}\|^\alpha = Cr^\alpha \quad (2.20)$$

This condition is resumed for the potential function  $U$ , valid for  $\Omega$  as a 3-dimensional Euclidean space. A similar condition of continuity derives for the gradient of  $U$ , at observation point  $\mathbf{x}$ , where  $\mathbf{q} = -\nabla U$ ,

$$\exists \alpha > 0, \exists D \geq 0, \quad \|\mathbf{q}(\mathbf{x})\| \leq Dr^{\alpha-1} \quad (2.21)$$

The integrand term in equation(2.19) can be bounded, combining with the expression of  $G$  and  $H$ , Eq. (2.10) and Eq. (2.11), respectively. The terms involved are bounded by a function  $r^{\alpha-2}$ .

$$\exists \alpha > 0, \exists C' \geq 0, |(u(\mathbf{y}) - u(\mathbf{y})) H(\mathbf{x}, \mathbf{y})| \leq C' r^{\alpha-2} \quad (2.22a)$$

$$\exists \alpha > 0, \exists D' \geq 0, |\mathbf{q}(\mathbf{y}) G(\mathbf{x}, \mathbf{y})| \leq D' r^{\alpha-2} \quad (2.22b)$$

Those conditions enable us to bound at once the terms in the integral Eq. (2.19).

### Expression for the limits on the boundary

From the position of the point  $\mathbf{x}$ , for the integration of the inclusion boundary  $S_\epsilon$ , the radius  $\epsilon$  gives an order of the singularity of the Green function, and a measurement of distance to the point  $\mathbf{y}$ , like  $r \sim \epsilon$ . The integrating element is reformulated using radial

coordinates, like  $dS_y \sim \epsilon^2 d\omega$ , where  $\omega$  is a composure of angles between the axis  $(x, y)$  and an axis of reference.

Using the latter conditions of continuity (2.22a), (2.22b), combining with the equivalence measure of the surface element integration, the integrand is turned into a function of  $\epsilon$ , like  $\mathcal{O}(\epsilon^\alpha)$ . In fact the integrand can be bounded by a term of  $\epsilon^\alpha$ .

$$[q(\mathbf{y})G(x, \mathbf{y}) - (u(\mathbf{y}) - u(x))H(x, \mathbf{y})]dS_y = \mathcal{O}(\epsilon^\alpha) d\omega \quad (2.23)$$

For  $\alpha > 0$ , this demonstrates the existence of the integral, even for a source point  $x$  close to the boundary, or directly at the boundary. One can now study the limit when  $\epsilon \rightarrow 0$ . The integral on the boundary can be separated in two parts as  $\partial\Omega_\epsilon = (\partial\Omega \setminus e_\epsilon) \cup S_\epsilon$ . The integral exposed Eq. (2.19) can be linearly decomposed as follows:

$$\begin{aligned} \int_{\partial\Omega_\epsilon} \frac{j_n(\mathbf{y})}{K} G(x, \mathbf{y}) - (U(\mathbf{y}) - U(x)) H(\mathbf{y}, x) dS_y \\ = \int_{\partial\Omega \setminus e_\epsilon} \frac{j_n(\mathbf{y})}{K} G(x, \mathbf{y}) - (U(\mathbf{y}) - U(x)) H(\mathbf{y}, x) dS_y \\ + \int_{S_\epsilon} \frac{j_n(\mathbf{y})}{K} G(x, \mathbf{y}) - (U(\mathbf{y}) - U(x)) H(\mathbf{y}, x) dS_y \end{aligned} \quad (2.24)$$

Passing to the limit with  $\epsilon \rightarrow 0$ , we can first consider the integral on  $S_\epsilon$ , as ,

$$\lim_{\epsilon \rightarrow 0} \int_{S_\epsilon} \frac{j_n(\mathbf{y})}{K} G(x, \mathbf{y}) - (U(\mathbf{y}) - U(x)) H(\mathbf{y}, x) = \lim_{\epsilon \rightarrow 0} (\mathcal{O}(\epsilon^{\alpha+1})) = 0$$

Thus passing all the integral Eq. (2.24) to the limit, this yields the establishment of the integral equation on the boundary  $\partial\Omega$ .

$$\begin{aligned} \lim_{\epsilon \rightarrow 0} \int_{\partial\Omega_\epsilon} \frac{j_n(\mathbf{y})}{K} G(x, \mathbf{y}) - (U(\mathbf{y}) - U(x)) H(\mathbf{y}, x) dS_y \\ = \int_{\partial\Omega} \frac{j_n(\mathbf{y})}{K} G(x, \mathbf{y}) - (U(\mathbf{y}) - U(x)) H(\mathbf{y}, x) dS_y \end{aligned} \quad (2.25)$$

### 2.1.6 Boundary Integral Equation for $H$

Now the existence of the boundary integral representation set on the boundary, the problem can be simplified by computing the integral of  $H$  with a source on the boundary. Its computation is detailed in Appendix B.1. It results in a value of 1/2 on the boundary. The expression of the right hand side component under the integration can be developed using an observation point at the boundary, considering the last value.

$$\boxed{\int_{\partial\Omega} \frac{j_n(\mathbf{y})}{K} G(x, \mathbf{y}) dS_y = \frac{1}{2} U(x)} \text{ for } x \in \partial\Omega \quad (2.26)$$

This expression gives a rather simple form of integral equation which could be used for source point on the boundary. Ultimately it just involves the integration of the Green function with the normal flux. In our case, the normal or the potential could be solved according to the boundary condition set.

### 2.1.7 Application to the conductivity of a contact spot

#### Problem of conduction between two half-spaces in contact

Now that the integral equation is set, we propose to treat the problem of conduction between two half-spaces,  $\Omega_1$  and  $\Omega_2$  in contact. This problem was already considered in [Barber, 2003], as was presented in the introduction.



For the following, the same subscripts 1 and 2, will be kept for the denomination of all the variables in the respective half-spaces. The geometric configuration is displayed as in Fig. 2.2.

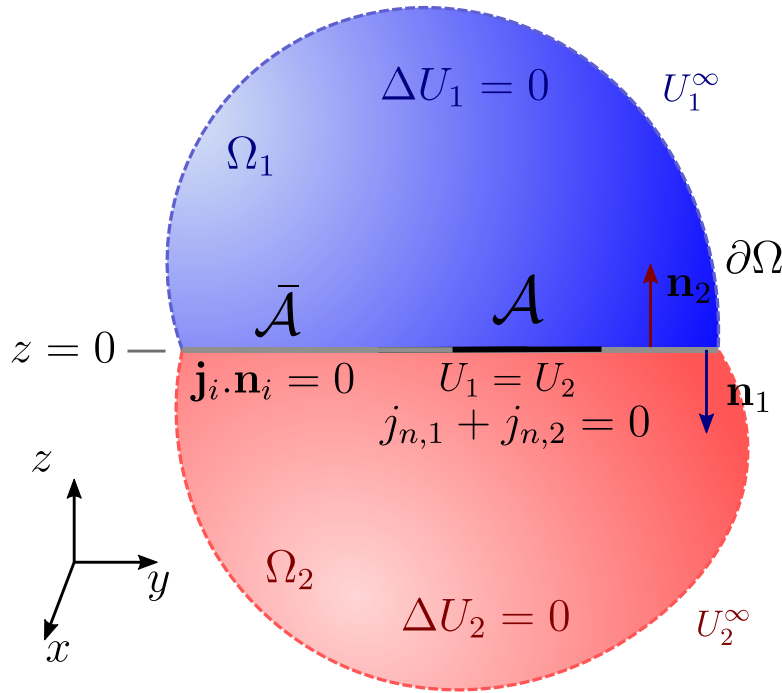


Figure 2.2: Diagram of the conduction problem for two half-spaces in contact

The free-surface, between half-spaces, stands for the plane parametrized by  $z = 0$ , while  $\Omega_1$  occupies the space  $z > 0$ , and conversely  $\Omega_2$  occupies  $z < 0$ .

### Boundary value problem

The potential field is studied in each half-space, denoted by  $U_1$  and  $U_2$ . For each half-space, we still consider the assumptions previously presented, namely the bodies are isotropic and homogeneous with linear conduction behavior. This yields the definition of the conductivities,  $K_1$  and  $K_2$ , for all  $\Omega_1$  and  $\Omega_2$ , respectively. In addition, the conduction is considered in its static regime. The two potentials follow Laplace equation :

$$\Delta U_i = 0 \text{ in } \Omega_i \quad (2.27)$$

### Boundary conditions

At the free surface, the boundary conditions is split in two parts. By  $\mathcal{A}$  we will denote the area of conduction, where the potentials are equal, Eq. (2.28a), and the sum of normal flux is equal to 0, Eq. (2.28b). Conversely, on  $\bar{\mathcal{A}} = \mathcal{A} \setminus \partial\Omega(z = 0)$ , the complement part of the free-surface, the normal flux are equal to zero, Eq. (2.29). This condition means the radiation and the convection are neglected out of the contact area, especially for the thermal problem. In the case of electrical potential, this assumes there is no tunnel-effect.

The exchange in term of thermal or electrical potential is set by a difference of potentials at infinity. A boundary condition in term of flux is impossible at infinity; it would lead to an infinite amount of energy. The distance from the center of the contact area  $\mathcal{A}$  is set to  $R = \sqrt{x^2 + y^2 + z^2}$ . The potentials at infinity are set to  $U_1^\infty$  and  $U_2^\infty$  for  $\Omega_1$  and  $\Omega_2$  respectively, as described in equations(2.30a),(2.30b).

**Definition: Boundary conditions**

Contact area, $x \in \mathcal{A}$	Outside contact, $x \in \bar{\mathcal{A}}$	At infinity, $R \rightarrow \infty$
$U_1(x) = U_2(x) = U_0$ (2.28a)	$j_{n,1} = j_{n,2} = 0$ (2.29)	$U_1(R) \rightarrow U_1^\infty$ (2.30a)
$j_{n,1}(x) + j_{n,2}(x) = 0$ (2.28b)		$U_2(R) \rightarrow U_2^\infty$ (2.30b)

In addition to those conditions, by symmetry, we could impose a uniform potential over the contact area  $\mathcal{A}$ . This stands as Dirichlet condition, where  $U_0$  represents the value of the potential at  $\mathcal{A}$ . In practice, this aligns with a low variance of the potential field over the contact area.

**Equivalent problem of conduction in a single half-space**

This problem of conductivity is linear, bringing a unique solution. The problem could be taken on by another, with a single half-space geometry. For this, let us consider a potential function  $\Phi$ , in a half-space  $\Omega$ , defined for  $z > 0$ . And this will be governed by the Laplace equation, illustrated Fig. 2.3.

$$\Delta\Phi = 0 \text{ in } \Omega \quad (2.31)$$

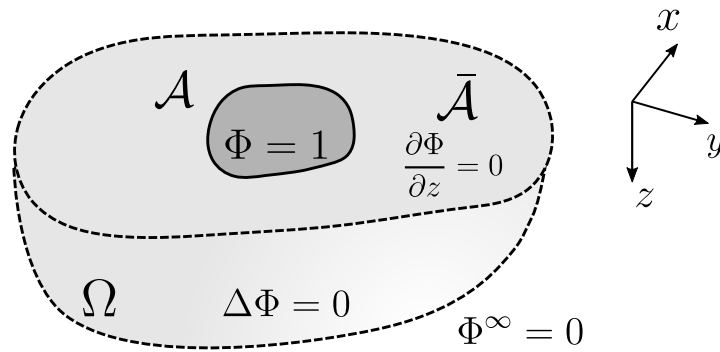


Figure 2.3: Diagram for the equivalent problem of conduction in single half-space

At the free-surface, similarly to the uniform potential condition Eq. (2.28a), the potential is set equal to 1 on  $\mathcal{A}$ . On the non-conductive contact area  $\bar{\mathcal{A}}$ , the normal flux is set equal to 0. Those boundary conditions are supplemented by the condition at the infinite, where the potential is set equal to 0. The difference of potential is namely imposed at the contact area  $\mathcal{A}$ .

**Definition: Boundary conditions for a single half-space problem**

Contact area, $x \in \mathcal{A}$	Outside contact, $x \in \bar{\mathcal{A}}$	At infinity, $R \rightarrow \infty$
$\Phi = 1$ (2.32)	$\frac{\partial\Phi}{\partial z} = 0$ (2.33)	$\Phi(R) \rightarrow 0$ (2.34)

From the function  $\Phi$ , it is possible to retrieve the two potentials  $U_1$  and  $U_2$ , by the linear combinations as:

$$U(x, y, z) = U_1^\infty + \frac{K_2(U_2^\infty - U_1^\infty)}{K_1 + K_2} \Phi(x, y, z), \text{ in } \Omega_1 \quad (2.35a)$$

$$U(x, y, z) = U_2^\infty + \frac{K_1(U_1^\infty - U_2^\infty)}{K_1 + K_2} \Phi(x, y, -z), \text{ in } \Omega_2 \quad (2.35b)$$

The normal flux at the free-surface derives from the function  $\Phi$ ,

$$q(x) = q(x, y, 0) = -\frac{\partial \Phi}{\partial z}(x, y, 0) \text{ for } x \in A \quad (2.36)$$

One could also retrieve the value of  $U_0$  at the contact area, from the potential  $\Phi$  defined as,

$$U_0 = \frac{K_1 U_1^\infty + K_2 U_2^\infty}{K_1 + K_2} \quad (2.37)$$

### Condition at infinity

This problem of potential in a half-space was already studied by Boussinesq [Boussinesq, 1885], in the late of XIX century. For a problem following Laplace equation, with a punctual normal load on its free-surface, he established a response in terms of a potential. He also settled for an elastic problem, that the displacement field decays as  $R^{-1}$  while for the stress component this decays as  $R^{-2}$ . The same observation holds the problem of conduction in terms of potential and flux. In this way, we can formulate a law of decay function of the distance  $R$ , when  $R$  is large enough compared to the dimension of the contact area.

$$\Phi = O(R^{-1}), \quad |\nabla \Phi| = O(R^{-2}) \quad (2.38)$$

### Application of the integral equation

This section aims to establish the integral equation according to the contact area definition. However, the integral equation formulated Eq. (2.26) appeals for a closed surface definition with  $\partial\Omega$ . This integral is not suitable for half-space geometry, this needs an additional law of decay for the potential field and the normal flux at infinity.

First, we need a closed surface definition, as presented Fig. 2.4. The geometry is now reduced to a semi-spherical body  $\Omega_R$ , with a closed boundary surface  $\partial\Omega_R$ . The radius of this sphere is set to  $R$ . But by passing to the limit for  $R \rightarrow \infty$ , we get back the initial half-space geometry  $\Omega$ .

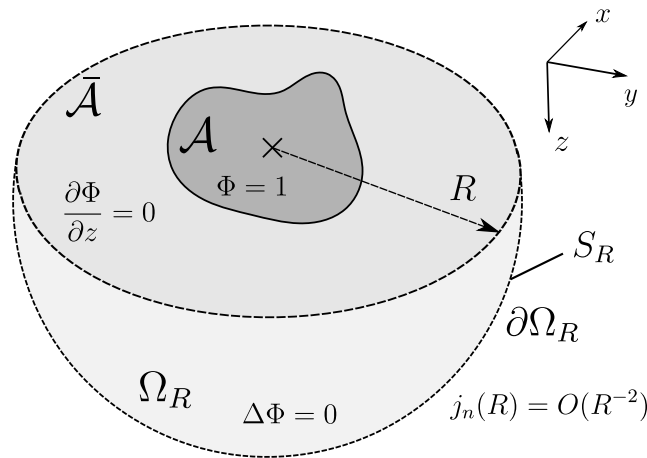


Figure 2.4: Definition of a closed media  $\Omega_R$  with a radius of  $R$

The boundary surface  $\partial\Omega_R$  would be decomposed as followed, helped by the definition of the areas at the free-interface  $\mathcal{A}$  and  $\bar{\mathcal{A}}$ ,

$$\partial\Omega_r = \mathcal{A} \cup \bar{\mathcal{A}} \cup \mathcal{S}_R, \quad \lim_{R \rightarrow \infty} (\partial\Omega_R) = \partial\Omega$$

The left-hand side of the integral equation (2.26) can be decomposed according to the latter surface definition :

$$\int_{\mathcal{A} + \bar{\mathcal{A}} + \mathcal{S}_R} j_n(\mathbf{y})G(\mathbf{y}, \mathbf{x})dS_y = \int_{\mathcal{A}} j_n(\mathbf{y})G(\mathbf{y}, \mathbf{x})dS_y + \int_{\bar{\mathcal{A}}} \underset{=0}{j_n(\mathbf{y})}G(\mathbf{y}, \mathbf{x})dS_y + \int_{\mathcal{S}_R} j_n(\mathbf{y})G(\mathbf{y}, \mathbf{x})dS_y$$

The integral on  $\bar{\mathcal{A}}$  can be simplified thanks to the condition of zero normal flux. The integral over  $\mathcal{S}_R$  can be expressed as function of  $R$ . For doing that, the element of integration is replaced by  $dS_y = R^2 d\omega$  using spherical parametrization. As the source point  $x$  is taken on the contact area  $\mathcal{A}$ , while the point of integration is defined on  $\mathcal{S}_R$ , the distance  $r$  in Green function is similar to  $R$ , when  $R$  assumed large enough. Ultimately the normal flux condition decay can be added to Eq. (2.38).

$$\begin{aligned} \int_{\partial\Omega_R} j_n(\mathbf{y})G(\mathbf{y}, \mathbf{x})dS_y &= \int_{\partial\Omega_R} \mathcal{O}(R^{-2})\mathcal{O}(R^{-1})R^2 d\omega \\ &= \int_{\partial\Omega_R} \mathcal{O}(R^{-1})d\omega \\ &= \mathcal{O}(R^{-1}) \end{aligned}$$

As  $R$  approaches infinity, the value of this integral tends to 0.

$$\lim_{R \rightarrow \infty} \int_{\partial\Omega_R} j_n(\mathbf{y})G(\mathbf{y}, \mathbf{x})dS_y = 0$$

Thanks to this limit, the integral over  $\partial\Omega$  can be defined as,

$$\int_{\partial\Omega} j_n(\mathbf{y})G(\mathbf{x}, \mathbf{y})dS_y = \int_{\mathcal{A}} j_n(\mathbf{y})G(\mathbf{x}, \mathbf{y})dS_y$$

Finally we get a new definition for the integral equation in a half-space, in particular for points on the contact area  $\mathcal{A}$ , as presented below.

$$\boxed{\int_{\mathcal{A}} j_n(\mathbf{y})G(\|\mathbf{x} - \mathbf{y}\|)dS_y = \frac{1}{2}\Phi(\mathbf{x})} \quad \text{for } \mathbf{x} \in \mathcal{A} \quad (2.39)$$

In the integral, we prefer the definition of  $G$  accounting for the distance  $r = \|\mathbf{x} - \mathbf{y}\|$ , which emphasizes the invariance by translation and rotation.

### Motivations for integral equation

The integral equation(2.39) takes advantage of the physical properties of the problem for conduction in the half-space. The problem is finally reduced to the true contact area  $\mathcal{A}$ . Nevertheless, this expression does not account for specific conditions at the contact area. But convective condition could be added, considering an integral component over  $\bar{\mathcal{A}}$ , being a function of  $U$  and  $H$ . Similarly, a source term, like in the Poisson equation, can be added. This would just induce an integration within the solid  $\Omega$ .

This problem is also equivalent to the problem of elasticity. In fact it could be resumed by an integral relation between pressure,  $p$ , and normal displacement  $u_z$ , on a contact area  $\mathcal{A}$ . It is noteworthy the problem of elasticity remains linear. The integral equation would rely on the *effective elastic modulus*,  $E^*$  as presented below.

$$\frac{2}{E^*} \int_{\mathcal{A}} p(\mathbf{y})G(\mathbf{x}, \mathbf{y})dS_y = u_z(\mathbf{x})$$

## 2.2 Boundary Element Method

The integral equation permits the resolution of the problem of conduction. Based on this equation, the Boundary Element Method (BEM) aims to solve this problem utilizing methodologies analogous to those found in the Finite Element Method (FEM). In essence, the integral equation necessitates the interpolation of the physical fields and the discretization of the boundary of the domain in question  $\mathcal{A}$ .

This section outlines the development and formulation for the BEM, tailored to the integral equation (2.39). This will involve numerical techniques, commonly used for the FEM, such as *shape functions* and *discretization*. A special care is brought to the definition of numerical integration. The BEM results in the definition of a linear system. Different models of interpolation and mesh element will be investigated, seeking for accuracy and physical consistency.

### 2.2.1 Discretization and linear system definition

#### Mesh definition

The first step of the discretization process involves partitioning the boundary into separate elements. The integral Eq. (2.39) is exclusively concerned with the geometry of the contact area. We start by discretizing  $\mathcal{A}$  into sub element of boundary, as follows:

#### Definition: Mesh discretization

For a surface  $\mathcal{A}$ , the discretization pertains to the definition of a set of separated elements  $\mathcal{A}_e$ , as :

$$\mathcal{A} = \bigcup_{e=1}^{N_e} \mathcal{A}_e \quad (2.40)$$

where  $\mathcal{A}_e$  represents the e-th element, part of the boundary, and  $N_e$  is the total number of these elements. The union of them reassembles the complete surface initially considered.

These elements inherit properties of the boundary, especially its dimension. The discretization of the boundary like  $\mathcal{A}$ , yields the separation of the equation(2.39) into a sum of integrals, as follows,

$$\sum_{e=1}^{N_e} \int_{\mathcal{A}_e} \frac{j_n(\mathbf{y})}{K} G(\|\mathbf{x} - \mathbf{y}\|) dS_y = \frac{1}{2} U(\mathbf{x}) \quad (2.41)$$

Where the integration point  $\mathbf{y}$  belongs to separated element  $\mathcal{A}_e$ .

#### Reference element

The BEM requires to compute the integral of the Green function over the mesh element. Each element has its own geometry. The reference element, denoted by  $\Delta_e$ , aims to streamline the computation for any boundary elements  $\mathcal{A}_e$ , hence the integration. First, it provides a common and simple shape of element of integration. The physical mesh geometry is defined through a discrete set of geometrical points  $\{\mathbf{y}_j\}$ . Secondly, it also reduces the physical space of the geometry. A curved boundary element becomes planar. Referring to this last point, two examples are presented in Fig. 2.5, and Fig. 2.6, for quadrangular and triangular elements, respectively. The physical space, depicted in blue, belongs to a three dimensional space,  $\mathbb{R}^3$ , while the element of reference is set within a two-dimensional space  $\mathbb{R}^2$ .

The reference space coordinates are denoted by  $\xi = (\xi_1, \xi_2)$ . In the context of our boundary element method, all the boundary elements  $\mathcal{A}_e$  are assumed to be planar,

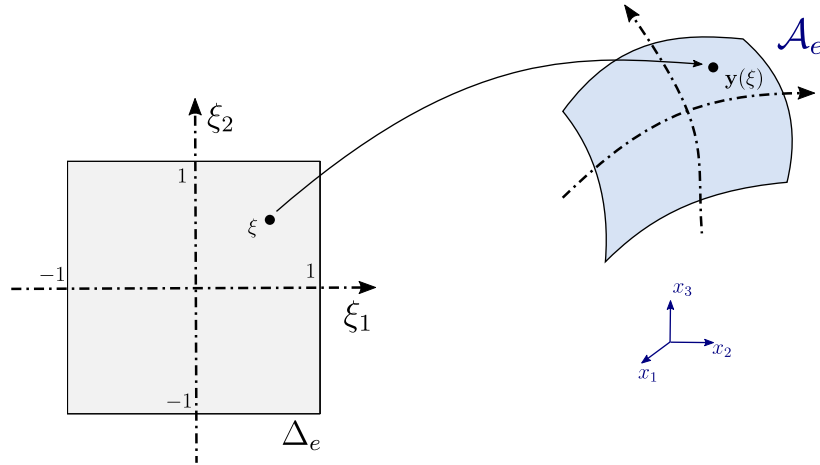


Figure 2.5: Regular square of the reference element (left) for a quadrangular boundary element in the physical space (right)

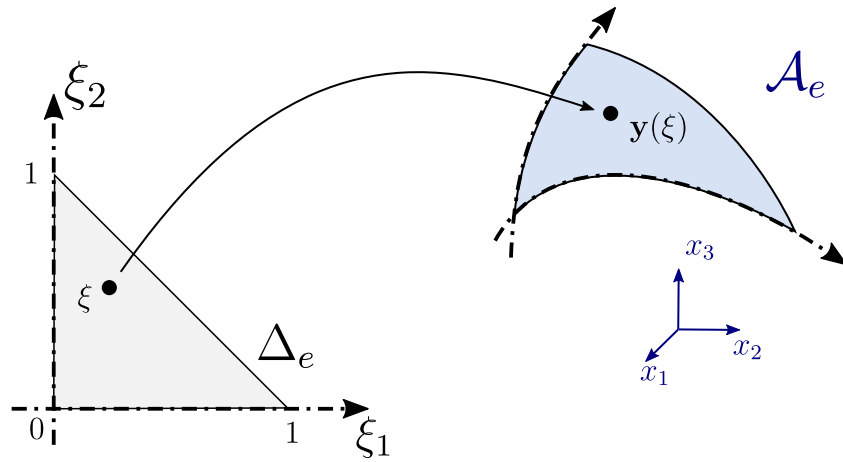


Figure 2.6: Isosceles triangle of the reference element (left) for a triangular boundary element in the physical space (right)

which simplifies the geometric considerations. Examples of commonly employed reference elements, including those for triangular and quadrangular shapes, are detailed in Appendix B.2.

### Shape functions

Once we get the geometry of the boundary element, and the reference element, we need the set of *shape functions*. Those are designed to create a bijection between a set of physical points  $\{y^i\}$  and a set of reference point  $\{\xi\}$  on  $\Delta_e$ . The parametrization is defined as shown below, in which the shape functions are denoted by  $N_i$ .

#### Definition: Shape functions change of variable

$N_i$  is the shape function related to the physical node  $y^i$ , and enables to define physical space coordinate  $y$  as considered in the following expression:

$$y(\xi) = \sum_{i=1}^{n(e)} N_i(\xi) y^i \quad (2.42)$$

With  $n(e)$  is the number of nodes on the element  $\mathcal{A}_e$ , and  $\xi$  is the coordinate in the reference element.

The set of physical points  $\{\mathbf{y}\}$  are defined in agreement with the degree of interpolation wanted for the geometry, and the shape of boundary element. An example is presented in Fig. 2.7, depicting a quadrangular element, bearing quadratic interpolation. Insofar, it brings the number of construction point  $n(e)$  to 9. In the formula(2.42), the physical points are labeled with an index  $i$ , related to the local numerotation of the boundary element  $\mathcal{A}_e$  as in Fig. 2.7.

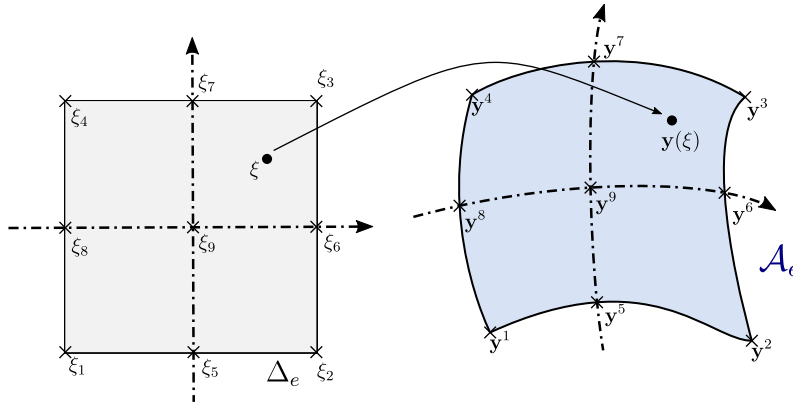


Figure 2.7: Representation of geometrical node for an example of quadratic quadrangular boundary element with 9 nodes

The shape functions used in boundary element methods are commonly represented by polynomials. Some examples of those are presented in Appendix B.2. The shape functions must ensure to get the physical coordinates at the corresponding reference nodes. This condition is summarized as,

$$N_i(\xi^j) = \delta_{ij} \quad (2.43)$$

where  $\delta$  stands for the Kronecker's symbol. Subsequently, these shape functions provide a partition of unity on the reference element as:

$$\sum_{i=1}^{n(e)} N_i(\xi) = 1, \text{ for } \xi \in \Delta_e \quad (2.44)$$

Considering a polynomial for the shape function, these are acknowledged for their simplicity, and their geometric consistency. The needed order of interpolation depends on the shape of the boundary element, or on the desired accuracy of interpolation. They allow to follow curved boundary element with quadratic interpolation, or even with Bezier curves in the case of isogeometric analysis (IGA) [Hughes et al., 2005].

### Change of variable and integral

The use of shape functions allows us to establish a relation between the physical coordinates  $\mathbf{y}$  and the reference coordinates  $\xi$ . In addition, the aforementioned parametrization allows to streamline the computation of the integral (2.41).

Using  $\xi$  as the variable of integration instead of  $\mathbf{y}$ , reduces the integration over reference element. The change of variable is borne by the defined of the *Jacobian* function,

which stands for the *determinant of the Jacobian matrix*. The Jacobian function and the Jacobian matrix are defined as follows,

$$J_{ij} = \frac{\partial y_i}{\partial \xi_j}, \quad J = \det(J) \quad (2.45)$$

With  $J$  represents the Jacobian function, and  $J$  is the Jacobian matrix.  $J$  is a matrix, and its components are defined as the derivatives of the physical coordinates  $\mathbf{y}$  along the reference coordinates  $\xi$ . The Jacobian function varies with  $\xi$ . However, for the linear shape functions, whose derivatives are constant, the components of  $J$  are also constant hence the Jacobin function. It is worth noticing that the geometric interpolation is injective, which makes the change of variables valid. In a general sense, the integral with a kernel function  $f$  over the surface  $\mathcal{A}_e$  can be reformulated using  $\xi$  over an element of reference, as follows,

$$\int_{\mathcal{A}_e} f(\mathbf{y}) dS_y = \int_{\Delta_e} g(\xi) J(\xi) dS_\xi \quad \text{with } g = f \circ \mathbf{y} \quad (2.46)$$

Recalling Eq. (2.41),  $f$  stands for the Green function multiplied to the normal flux  $j_n$  divided by the conductivity  $K$ . The field  $j_n$  is approximated by the field interpolation, which involves the definition of interpolation function in turns. The next section aims to detail this process.

### Discretization for the unknown

This part will give details of the representation of fields on the boundary following a similar approach as used in the FEM. The fields  $U$  and  $j_n$  integrated in Eq. (2.41) are approximated by  $\tilde{U}$  and  $\tilde{j}_n$ , as follows,

$$\tilde{U}(\xi) = \sum_{k=1}^{m(e)} M_k(\xi) U^k, \quad \text{for } \xi \in \Delta_e \quad (2.47a)$$

$$\tilde{j}_n(\xi) = \sum_{k=1}^{m(e)} M_k(\xi) j_n^k \quad \text{for } \xi \in \Delta_e \quad (2.47b)$$

Where  $M_k$  is the *interpolation* function, which could be different from those used for the geometry ( $N_i$ ). The fields are sampled out over a set of  $m(e)$  number of node fields, denoted by  $\{\mathbf{y}^k\}$ . Those nodes are defined on the boundary element  $\mathcal{A}_e$ , such as  $U^k = U(\mathbf{y}^k)$  and  $j_n^k = j_n(\mathbf{y}^k)$ .

Different kind of interpolation functions may be considered. In a general sense, the interpolation can be either *iso-parametric*, *sub-parametric* or *super-parametric*.

If the parametrization is *conformal*, the same coordinates would be used for both the geometric nodes and the collocations points. This yields the interpolation functions being continuous at the neighboring elements. Conformal interpolation appears to be more straightforward, recognized for its simplicity and accuracy [Beskos, 1987]. Conversely, for *non-conformal* parametrization, different nodes are used for the geometry and the fields.

In an *iso-parametric* interpolation, the same shape functions,  $N_i$ , are employed as interpolation functions,  $M_k$ . This ensures the interpolation being conformal. It would result in a sub-parametric interpolation if the order of interpolation is smaller than this of shape functions, or super parametric for a higher degree. Like for the shape function, different interpolation functions might be explored, seeking for better consistency, or accuracy. In the sake of generality, the physical and geometric interpolations are assumed to be different in the next section 2.2.2. But at the end, we will use conformal sub-parametric, and iso-parametric configurations.



## 2.2.2 Construction of the linear system

All the mathematical tools are now available for the physical resolution of the integral equation(2.41). The discretization will provide a discrete physical description for the fields  $U$  and  $j_n$ , supported by the mesh definition. The integral equation is verified over a set of  $N_c$  physical nodes, also known as *collocation points*, with coordinates  $x^c$  ( $1 \leq c \leq N_c$ ). The normal flux is substituted by its approximate expression  $\tilde{j}_n$ , combining with the interpolation Eq. (2.47b), and as well for the potential replaced by  $\tilde{U}$  using the interpolation Eq. (2.47a).

$$\frac{1}{2}\tilde{U}(x^c) = \sum_{e=1}^{N_e} \int_{\mathcal{A}_e} \tilde{j}_n(\mathbf{y})G(x^c, \mathbf{y})dS_y \quad (2.48)$$

The integration on the boundary elements can be calculated using the integration on the reference element. The change of variable is expressed using the formula Eq. (2.46), which involves the Jacobian function. It incorporates a sum under the integral operation on the boundary element, and involves  $M_k$  (functions of interpolation). All these steps combined lead to the following formulation on collocation point  $x^c$ .

$$\frac{1}{2}U(x^c) = \sum_{e=1}^{N_e} \left( \sum_{k=1}^{m(e)} \left( \int_{\Delta_e} M_k(\xi)G(x^c, \mathbf{y}(\xi))J(\xi)ds_\xi \right) j_n^k \right) \quad (2.49)$$

Since we use conformal discretization the same  $\xi$  variable can be used under the integral. The formulation requires at least one collocation point in every boundary element, which means that the number of collocation points  $N_c$  must be greater or equal to the number of boundary elements  $N_e$ . The Green's function is singular, when  $x^c$  lies in the boundary element  $\mathcal{A}_e$ , but regular elsewhere. This singularity requires special treatment, making the integrating process. In Eq. (2.49), the location of the collocation points has not been specified yet. Different integration process are defined, according to the position of the collocation point, such as *quasi-singular* integration or *singular* integration. They will be detailed in the following Section 2.2.3. Ensuring accurate and efficient handling of these singularities is crucial for the successful resolution of the integral equation, otherwise the overall accuracy is jeopardized. First, the general algorithm for the construction of the matrix of integration is developed in the next sections.

### General algorithm for matrix construction

The expression(2.49) can be transformed into a linear system. The integration of the Green's function can be summarized in a matrix  $G$ , and be separated from the normal flux term. Each row of the matrix is multiplied by the normal flux vector taken at the physical node of field, and denoted by  $\{j_n^c\}$ . The right-hand side is given by the potential  $U^c = U(x^c)$  at points of coordinates  $x^c$ . This results in the following system of equations:

$$\frac{1}{2}\{U^c\} = [G]\{j_n^c\} \quad (2.50)$$

The explicit formulation of  $G_{ij}$ , does not appear very straightforward, due to the interpolation and the shape function use. Those components are computed according to the algorithm 1.

This algorithm relies on the definition of the integral functions  $I_{sing}$  and  $I_{nsing}$ , as detailed below:

$$I_{sing}(x^c, e, k) = \int_{\Delta_e} M_k(\xi)G(x^c, \mathbf{y}(\xi))J_e(\xi)ds_\xi, \text{ with } x^c \in \mathcal{A}_e \quad (2.51a)$$

$$I_{nsing}(x^c, e, k) = \int_{\Delta_e} M_k(\xi)G(x^c, \mathbf{y}(\xi))J_e(\xi)ds_\xi, \text{ with } x^c \notin \mathcal{A}_e \quad (2.51b)$$

**Algorithm 1:** Implementation of the matrix  $G$ 


---

```

1 for  $i \leftarrow 1$  to  $N_c$  do
2    $\mathbf{x}^c \leftarrow X_c[i]$ ;
3   for  $e \leftarrow 1$  to  $N_e$  do
4     for  $k \leftarrow 1$  to  $n(e)$  do
5       if  $\mathbf{x}^c \in \mathcal{A}_e$  then
6          $\mathbf{G}_{ij} = \mathbf{G}_{ij} + I_{sing}(\mathbf{x}^c, e, k)$ 
7       else
8          $\mathbf{G}_{i,j} = \mathbf{G}_{i,j} + I_{nsing}(\mathbf{x}^c, e, k)$ 

```

---

These functions differ from the location of the physical node  $\mathbf{x}^c$  (also known as *collocation point*), to the boundary element  $\mathcal{A}_e$ . The index  $k$  relates to the shape function  $M_k$ .  $I_{sing}$  stands for the integration process when the collocation point lies in the boundary element, while  $I_{nsing}$  is defined for a collocation point outside of this element. Nevertheless, when the collocation point is outside of the boundary element, it can still require special treatment to enhance the accuracy of the integration. Special use case will be next developed, which could emphasize the key aspect of the need in accuracy.

Algorithm 1 involves three loops in total. The first one refers to the collocation point definition,  $i$  stands for the line index. The second one is made to explore the boundary element. And the last loop travels along  $k$ , the index on the interpolation function.

The matrix component  $\mathbf{G}_{ij}$  is incremented at line and row positions  $i$  and  $j$ , respectively, calling the integral functions  $I_{sing}$  or  $I_{nsing}$ . This process will define the matrix  $\mathbf{G}$  entirely. This matrix appears to be fully-populated, unlike the stiffness matrix in FEM for instance. The fully-populated nature of the matrix  $[\mathbf{G}]$  represents a significant drawback for the BEM. It arises that the complexity is about  $\mathcal{O}(N_c^2)$ , demonstrating in terms of time and memory requirements. Tackling this problem, various techniques collectively referred as *Fast-BEM* have been developed. These techniques aim to improve the efficiency and scalability of the BEM, and will be discussed in more detail in section 2.3.

**Simplification for a constant physical interpolation**

The last implementation suggests a definition of the matrix  $[\mathbf{G}]$ , in a general sense. However, an important simplification may arise from the constant interpolation. With  $M_k = 1$ , it entails a single collocation point for each boundary element, reasonably defined as barycenter point of the boundary elements. The collocation point and the boundary element could share the same indexation, revealing  $N_c = N_e$ , likewise the number of collocation point is equal to the number of boundary element. The normal flux on the boundary element  $\mathcal{A}_e$  is defined as  $j_n^e = j_n(\mathbf{x}^e)$ . This simplification yields a new integral formulation:

$$\frac{1}{2}U(\mathbf{x}^c) = \sum_{e=1}^{N_e} \left( \int_{\Delta_e} G(\mathbf{x}^c, \mathbf{y}(\xi)) J_e(\xi) ds_\xi \right) j_n^e \quad (2.52)$$

It retains, however, the definition of the integral functions, for singular and non-singular use case,

$$J_{sing}(\mathbf{x}^c, e) = \int_{\Delta_r} G(\mathbf{x}^c, \mathbf{y}(\xi)) J_e(\xi) ds_\xi, \text{ for } c = e \quad (2.53a)$$

$$J_{nsing}(\mathbf{x}^c, e) = \int_{\Delta_r} G(\mathbf{x}^c, \mathbf{y}(\xi)) J_e(\xi) ds_\xi, \text{ with } c \neq e \quad (2.53b)$$

Those functions simply take as input  $\mathbf{x}^c$  (the point coordinate), and  $e$  the index of the boundary element. Those functions return straightforwardly the components of  $G$ , without incrementation. It leads to a simplified algorithm 2, which just involves two loops. Only the diagonal term are computed as singular integral.

---

**Algorithm 2:** Implementation of the matrix  $G$  for constant interpolation
 

---

```

1 for  $i \leftarrow 1$  to  $N_e$  do
2    $\mathbf{x}^c \leftarrow X_c[i]$ ;
3   for  $j \leftarrow 1$  to  $N_e$  do
4     if  $i = j$  then
5        $G_{i,j} = J_{sing}(\mathbf{x}^c, j)$ 
6     else
7        $G_{i,j} = J_{nsing}(\mathbf{x}^c, j)$ 

```

---

### 2.2.3 Numerical integration

The construction of the matrix  $G$  pertains to compute integrals holding for its components. The integration process can be speed up by *Gaussian quadrature* technique, commonly used for FEM. The calculation of integral relies on a weighted sum that provides a reliable method in most cases. This method is acknowledged for its precision, in the case of a polynomial function, like for FEM. However, it presents some limitations for non-polynomial kernel function, which are common for BEM kernels. This section aims to present numerical methods for the integration used for BEM.

#### Gauss quadrature

##### Method: Gaussian quadrature

The *Gaussian quadrature method* enables to transform an integral into a weighted sum, as follows,

$$\int_{-1}^1 f(x)dx \approx \sum_{i=1}^N w_i f(x_i) \quad (2.54)$$

With  $N$  is the number of the weighted terms involved in this sum. The coordinates  $x_i$  represent the *Gauss point*, and  $w_i$  are their associated *weights*.

The integral on the left-hand side relies on the segment  $[-1, 1]$ . The coordinates of these points and the weights are tailored to make this formula exact for monomial integration as long as its degree is less than  $2N$ , that enables to compute exactly the integral of the polynomial  $x^k$  over the segment  $[-1, 1]$ , as follows,

$$\forall 0 \leq k \leq 2N - 1, \quad \int_{-1}^1 x^k dx = \sum_{i=1}^N w_i x_i^k \quad (2.55)$$

In the case of FEM, the kernel function is polynomial. The degree of this latter depends on these of the shape and interpolation functions. Thus, the number  $N$  of Gauss points is tuned according to the order of interpolation, the rank of the shape functions.

The Gauss points are defined within the integration segment, i.e.  $\forall(i, N), x_i \in [-1, 1]$ . The weights are all positive. The Gauss point distribution is symmetrical around the center of this integration segment, as the same for the weights, i.e.  $\forall(i, N), x_i = x_{i-N}, w_i = w_{i-N}$ . The approximation can be extended to the integration on any surface element, or for a

volume. The example of the following integral represents the integration of a kernel function  $f$  over an arbitrary element  $\Delta_e$ .

$$\int_{\Delta_e} f(\xi)J(\xi)dS_\xi = \int_{-1}^1 \int_{-1}^1 f(\xi_1, \xi_2)J(\xi_1, \xi_2)d\xi_1d\xi_2 \approx \sum_{i=1}^N \sum_{j=1}^N w_iw_j f(x_i, x_j)J(x_i, x_j) \quad (2.56)$$

Where  $\det(J(\xi_1, \xi_2))$  is the determinant of the Jacobian matrix which maps the reference element to the physical one.

The integration of other shapes, such as the triangular, is quite straightforward. The corresponding Gauss point coordinates and weights are well known, and are commonly used as those for quadrangular elements. Some values are reported in appendix B.2.

### Integration for Green function

In scenarios where the kernel function, such as the Green's function in the BEM, exhibits singular behavior, the traditional Gaussian quadrature may not provide an accurate approximation. A numerical discrepancy arises when the source point is close to the element of integration, rendering the polynomial approximation ineffective. For a clear understanding, consider a numerical example as depicted in Fig. 2.8, where we study the integration over a regular square built like a reference element.

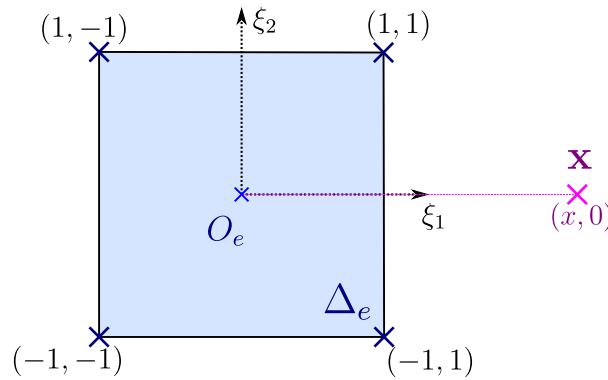


Figure 2.8: Geometrical representation of the practical use case for numerical integration assessment

The objective is to evaluate the integration error using Gaussian quadrature when a source point, denoted by  $x$ , is placed at varying distances along the  $x$ -axis from the center of the element. The source point's alignment along the abscissa simplifies the calculation of the interaction coefficient, as :

$$I(x) = \int_{\Delta_e} G(x, \xi)dS_\xi, \text{ for } x \in \mathbb{R}^+ \quad (2.57a)$$

$$G(x, \xi) = \frac{1}{4\pi \sqrt{(x - \xi_1)^2 + \xi_2^2}} \quad (2.57b)$$

When the source point, denoted by  $x$ , falls within the interval  $[0, 1]$ , this also falls within the reference element. This proximity to the element induces a singularity in the function  $G$ , when  $\xi = x$ . Nonetheless, the integral of interest remains well-defined, and must be computable. Some results are presented in Fig 2.9 where the integral function  $I$  is evaluated using a varying number of Gauss points, intending to improve its precision.

In Fig. 2.9, a dark region highlights the domain where the kernel function becomes *singular*, such for  $x \leq 1$ . This dark region is surrounded by a lighter gray area, which

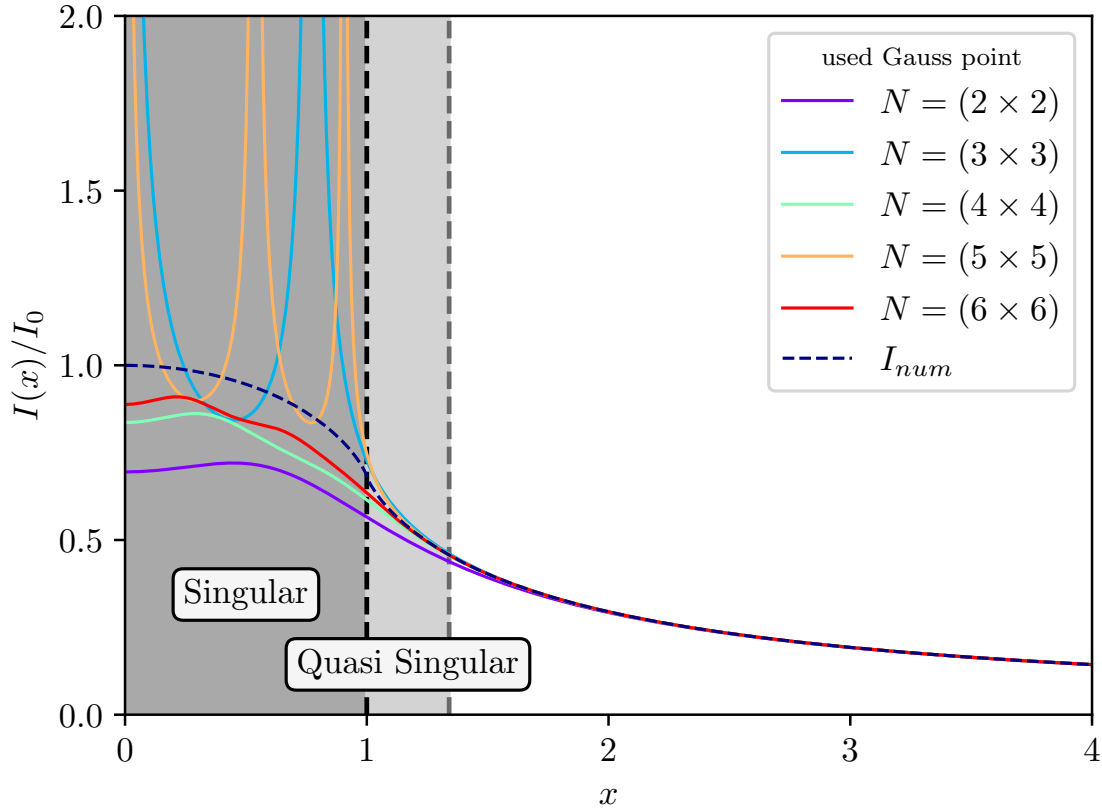


Figure 2.9: Integral computation comparison for different number of Gauss point along the distance

describes a *quasi-singular* domain. This area delineates the range in which the precision of the numerical integration method is most vulnerable due to the near-singular nature of the Green's function. The transition from the singular to the quasi-singular region is critical and necessitates careful numerical treatment to ensure the accuracy of the integration. For comparison, the exact solution is reported as  $I_{num}$ , in Fig. 2.9.

The curves in Fig. 2.9 vary with the number of used Gauss points. Specifically, when an odd number of Gauss points is aligned along an axis—considering cases where  $N = \{1, 3 \times 3, 5 \times 5\}$ , the curves reveal strong singularities, as some Gauss points are placed along this  $\xi_1$ -axis. Thus the source point can intersect those, inducing singular behavior as  $r = \sqrt{(x - \xi_1)^2 + \xi_2^2} \rightarrow 0$ . The results are normalized by the potential maximal value, denoted by  $I_0$ . It is obtained for  $x = 0$ , when the source point aligns with the middle of the reference element. Its analytical calculation is reported below.

$$I_0 = \int_{-1}^1 \int_{-1}^1 \frac{1}{4\pi \sqrt{\xi_1^2 + \xi_2^2}} d\xi_1 d\xi_2 = 8 \int_0^{\pi/4} \int_0^{1/\cos(\theta)} \frac{r}{4\pi r^2} dr d\theta \quad (2.58)$$

$$\Leftrightarrow I_0 = \frac{2}{\pi} \int_0^{\pi/4} \frac{d\theta}{\cos \theta} = \frac{4}{\pi} \tanh^{-1} \left( \tan \left( \frac{\pi}{8} \right) \right)$$

$$\Rightarrow I_0 \approx 0.56110$$

The precision required depends on the specific needs of the problem being solved. However, due to the ill-conditioning of the matrix  $G$ , a high level of accuracy is generally needed to obtain reliable results. Notably, errors exceeding 1% have the potential to significantly impact the ultimate solution.

### Definition of severity

Defining *index of severity*  $Is$ , provides an enlightening measurement of the relative position of the source point  $x$  with respect to the element of integration. The formula for  $Is$  was empirically determined reported in [Rezayat et al., 1986].

$$IS = (2.37 + 0.424 \cos(\theta)) \frac{D}{d} \quad (2.59)$$

With  $D$  represents the size of the element,  $d$  is the distance from the source point to the center of the element ( $d = \|O_e X\|$ ), and  $\theta$  is the angle defined between the normal vector  $n$  and the vector  $O_e X$ . All these parameters are illustrated in Fig. 2.10. This index can be used to define the number of Gauss points needed :

$$N = \lfloor IS \rfloor + 1, \quad IS \leq 5 \quad (2.60)$$

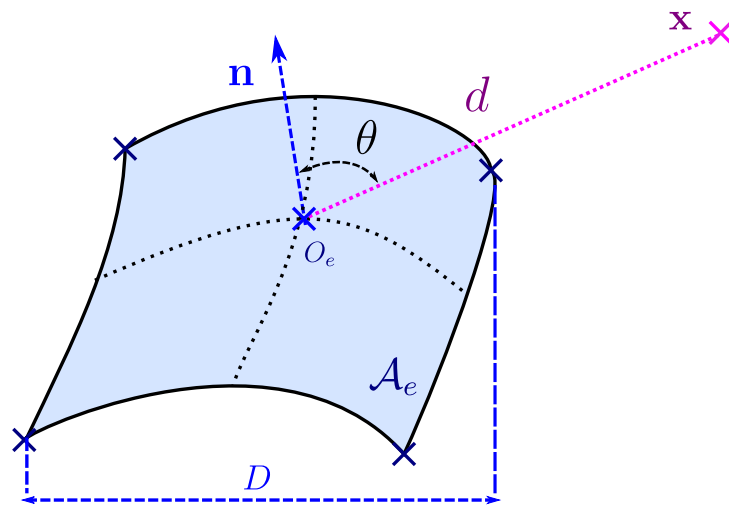


Figure 2.10: Representation of a curved element with parameters defined for the index of severity

Since the entire boundary surface  $\mathcal{A}$  is flat in our case, the angle  $\theta$  between any source point and any boundary element is equal to  $\pi/2$ . It simplifies the formulation of  $IS$ , just involving to the ratio of  $D$  and  $d$  as,

$$Is = 2.37 \frac{D}{d}$$

The order of integration  $N$  is determined based on the index of severity  $Is$ , which is calculated as its upper integer part, but bounded by 5. The resulting error is depicted in Fig. 2.11. The accurately calculated integral numerical function,  $I_{num}$  is considered as the solution of reference, enhanced by a loop of convergence. Different regions are annotated according to their  $Is$  values, highlighting the different rank  $N$  used. This facilitates the selection of a suitable order  $N$  for the Gaussian quadrature method, guaranteeing an acceptable accuracy threshold for the problem being addressed.

The figure Fig. 2.11, reveals that the error decreases as the rank  $N$  increases. The definition of the index of severity  $Is$  enables to adapt the rank  $N$  based on the absolute value of the integral and the relative distance  $d$  between the source point and the element of integration. However when the rank  $N$  increases, the computation time rises in turns. Overall, the combination of Gaussian quadrature with adaptive rank selection based on the index of gravity  $Is$  provides a balanced trade-off between precision and computational efficiency.

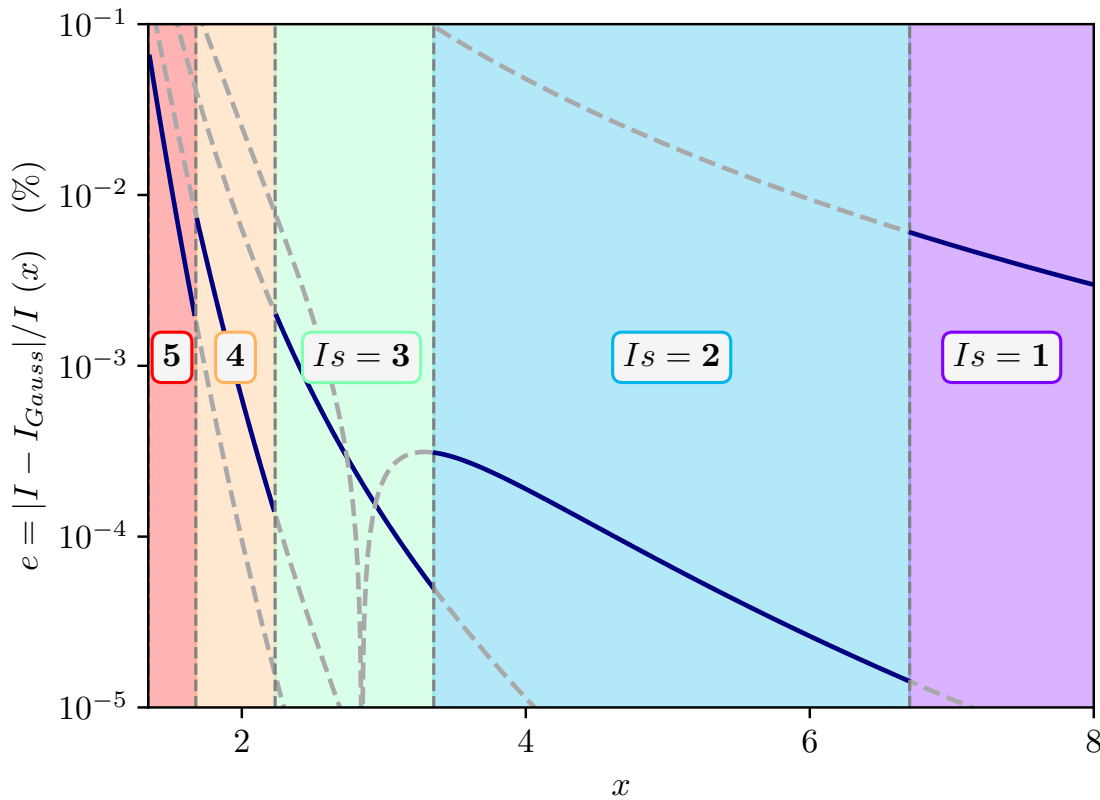


Figure 2.11: Integral computation comparison for different number of Gauss point along the distance

In the numerical example presented, the error remains relatively low, even at the boundary of the quasi-singular interval. This limit is defined when  $Is = 5$ , so  $x = 2.37 \cdot 2 \sqrt{2}/5 = 1.37$ . However, as the source point is deriving within the *quasi singular* domain, the error increases markedly. This emphasizes the necessity for further strategies to manage the quasi-singular zone. These strategies are outlined below, comparing these different methods to tackle quasi-singular integration.

### Quasi-singular integral

To adapt the Gaussian quadrature technique for application within the quasi-singular range, an initial approach might be to increase the number used of Gauss points. This adjustment would, without doubt, refine the accuracy of the solution even in the presence of the quasi-singularity caused by Green's function. A smarter strategy, however, would involve devising a transformation that aligns with the behavior of the integrand function field.

Within this section, we detail three such transformations aimed to regularize the near-singular nature of the integrand. The first involves a straightforward cubic polynomial transformation, whereas the subsequent two employ transformations based on radial coordinates.

**Cubic transformation** This transformation aims to gather points in agreement with the integrand function. Telles [Telles, 1987] provides a method of regularization by applying a cubic transformation, following the next definition.

$$\eta = \frac{1 - J_\eta}{1 + 3\bar{\xi}^2} \left( (\xi - \bar{\xi})^3 + \bar{\xi}(\bar{\xi}^2 + 3) \right) + J_\eta \xi \quad \in [-1, 1] \quad (2.61)$$

This method appeals to the definition of a new set of integration coordinates, substituting  $(\xi_1, \xi_2)$  by  $(\eta_1, \eta_2)$ . The initial coordinate  $\xi$  lies within the interval  $[-1, 1]$ , as well as the new coordinates  $\eta$ . The definitions of  $J_\eta$  and  $\bar{\xi}$  involved in equation Eq. (2.61) are detailed in Appendix B.3.1. Fig. 2.12, illustrates the chain of coordinate definition from the physical coordinates belonging to the boundary element geometry  $\mathcal{A}_e$ , to the reference element. The system of coordinate  $\eta$  remains unchanged concerning the reference element  $\Delta_e$ .

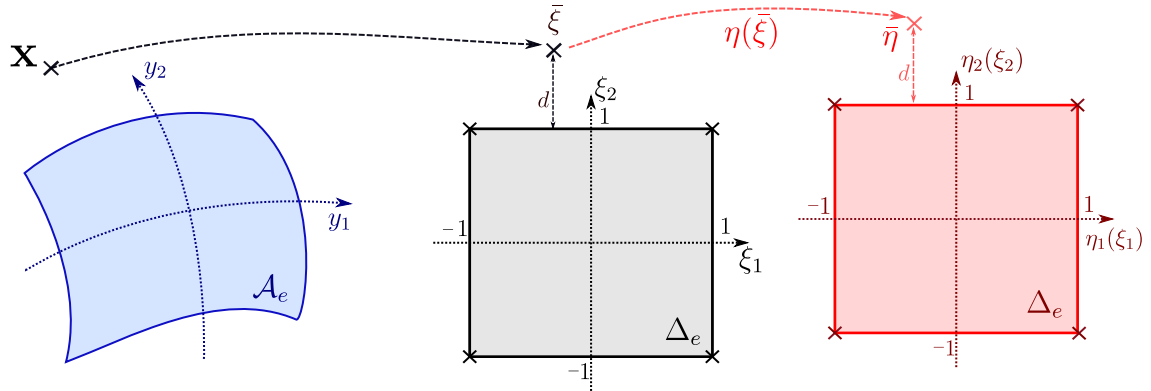


Figure 2.12: Chained coordinate, with a near source point definition

The source point  $x$  is assumed to be outside of the boundary element  $\mathcal{A}_e$ , but quite close to it, making the index of severity high. Its coordinates correspond to  $\bar{\xi}$  and to  $\bar{\eta}$  through successive changes of variables. The distance  $d$  is normalized as it is considered in the element of reference  $\Delta_e$ . The shape of the transformation is adapted from this distance, by  $J_\eta$ . The closer the source point is, the tighter the transformation would be around  $\bar{\xi}$ . Two examples are displayed in Fig. 2.13, using each  $(8 \times 8)$  points of integration.

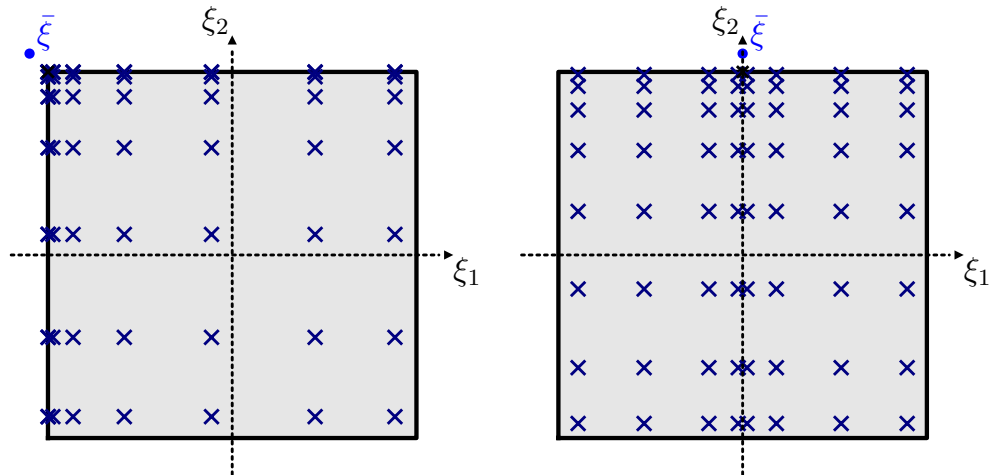


Figure 2.13: Examples of repartition of integration points, using a self-adapted cubic transformation

The distribution of the integration points are now changed from the original Gauss point arrangement. The integration will account for the additional change of variable  $(\xi_1, \xi_2) \leftarrow (\eta_1, \eta_2)$ , entailing modified weights  $\bar{\omega}$  for the Gaussian quadrature integration (see Appendix B.3.1).

**Cylindrical transformation** Considering the form of the kernel function, it appears that the radial transformation can also be used to evaluate it with the highest accuracy. Indeed,



a function varying as  $1/r$ , multiplied by a term equivalent to the distance  $r$ , becomes regular, or even constant. This term can be obtained through the radial transformation.

This transformation can be expressed by triangulating the reference element. It is valid for both triangular and quadrangular elements. An example is shown in Figure 2.14.

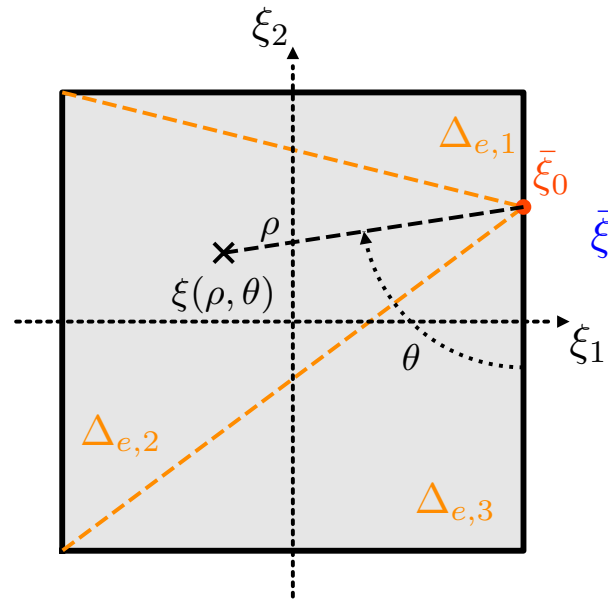


Figure 2.14: Example of triangular separation and cylindrical parametrization on a element of reference

The point  $\bar{\xi}'$  represents the orthogonal projection of  $\bar{\xi}$  onto the edge of the closest segment of the reference element. Having identified this projection, we proceed to partition the reference element into separate triangular segments. This subdivision enables the determination of  $\xi$ 's coordinates using the cylindrical system denoted by  $(\rho, \theta)$ . Within each triangular segment  $\Delta_{e,n}$ , the angular coordinate  $\theta$  varies within a range,  $(\theta_n^m, \theta_n^M)$ . Fig. 2.14 gives an example of the parametrization, displaying three triangular divisions. It is worth noticing, when  $\bar{\xi}'$  coincide with a vertex, the division is reduced to two triangles.

The radial coordinate limit  $\rho$  relates to the angular location  $\theta$ . The height of the triangle is denoted by  $h_n$  and its angular position is defined as  $\alpha_n$ . The integration transformation leveraging these parameters, and further details are presented Appendix B.3.1. Like for the cubic transformation, the radial transformation entails the modification of the weights. Two examples showing the distribution of integration points are demonstrated in Fig 2.15, taking the advantage of the radial transformation.

**Projection and Angular and Radial Transformation (PART)** Compared to the radial transformation the location of integration points around the mean radial position may be subsequently adjusted according to the position of the projection  $\bar{\xi}$ . This has motivated the PART method, which uses additional radial and angular transformations [Hayami and Matsumoto, 1994]. The initial radial coordinates, defined as  $(\rho, \theta)$ , are then transformed into  $(R, t)$ . These transformations accounts for the late radial transformation, with  $h$  the height of the triangular part, and  $\alpha$  its angular position.

The angular transformation is defined as

$$t = \frac{h}{2} \log \left\{ \frac{1 + \sin(\theta - \alpha)}{1 - \sin(\theta - \alpha)} \right\} \quad (2.62)$$

While the radial transformation could account for either  $L_1$  or  $L_2$  transformation, as

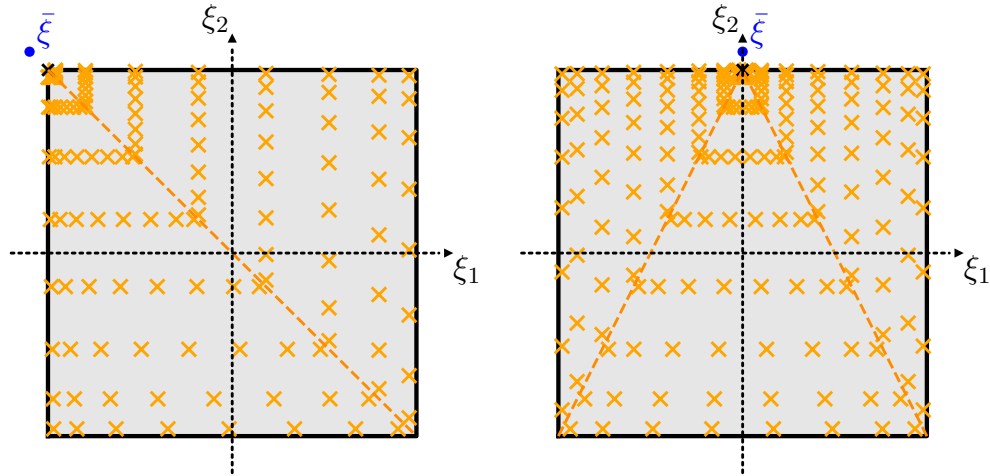


Figure 2.15: Examples of repartition of integrating point, using a cylindrical scattering. The left-hand side accounts for two separating triangular elements (the projection  $\bar{\xi}$  aligning with a vertex), and the right-hand side comprises three parts. Each triangular section is constructed using a grid of  $8 \times 8$  Gauss points, with a concentration around the location  $\xi$ , and its projection  $\bar{\xi}$ .

follows:

$$L_1 := R = \exp(\rho/\rho_{max}) \quad (2.63a)$$

$$L_2 := R = \exp((\rho/\rho_{max})^2) \quad (2.63b)$$

Where  $\rho_{max}$  is the contour radius. The derivative of the angular transformation is equal to  $dt = d\theta/\rho_{max}$ . The two variables  $(R, t)$  are then readjusted to align with the initial intervals  $[0, \rho_{max}]$  and  $[\theta^m, \theta^M]$ , respectively. Those transformations for angular and radial component are presented on the left and right hand side of Fig. 2.16, respectively. These transformations take into account  $\alpha = 0$ ,  $h = 2$ , and  $\theta \in [-\pi/4, \pi/4]$ , which refers to the middle triangle geometry on the right-hand side in Fig. 2.15. The radial transformation,  $R$  is scaled with  $\rho_{max}$ , following the prescribed bounds.

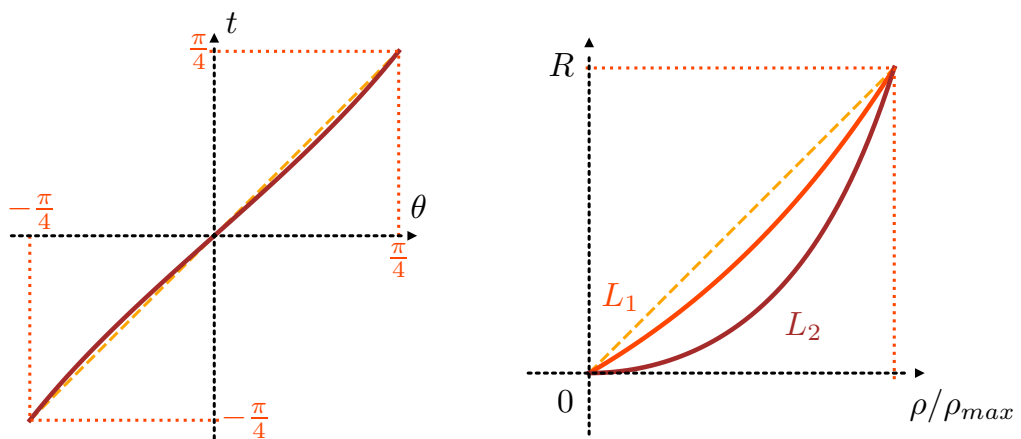


Figure 2.16: Representation of the angular (left), and the radial (right) transformation using in the PART method

The PART transformation is twofold motivated. First, the radial transformation concentrates integration points closer to the  $\rho = 0$  region. These radial transformations are designed to get a minimal derivative value at  $\rho = 0$ , as shown

in [Hayami and Matsumoto, 1994]. The authors rather recommend the use of  $L_1$  transformation than  $L_2$ . Second, the angular transformation redistributes integration points, distancing them from the edges of the triangular segments. However, this transformation is nearly linear in nature, which casts doubt on its potential for substantial improvement. Illustrations of these transformations are depicted in Figure 2.17, which allows for a direct comparison with the previously discussed radial segmentation (highlighted by orange points). The effect of the radial transformation is evident in the denser clustering of integration points around the point  $\bar{\xi}'$ .

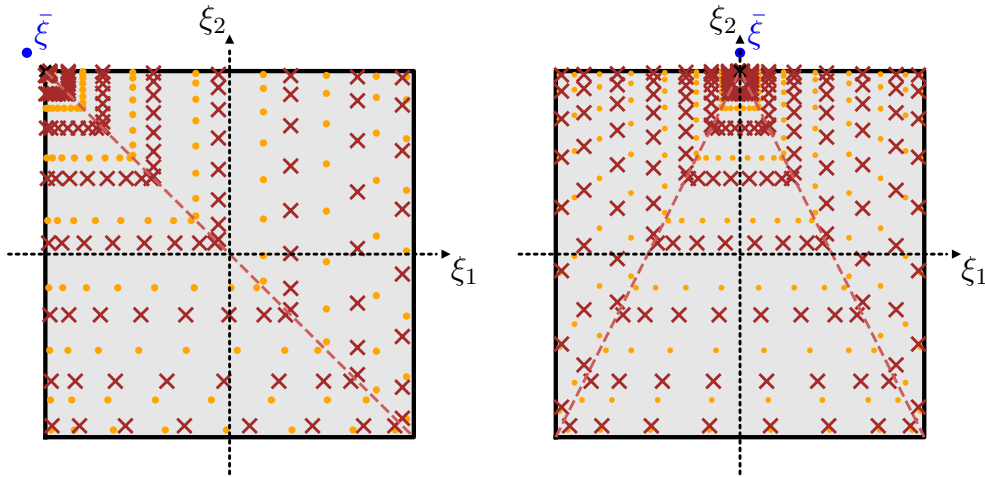


Figure 2.17: Examples of repartition of integrating point using Part method (red), and original cylindrical parametrization (orange)

**Performance** In summary the method's capability, we evaluate the error against a varying number of integration points. We consider the case presented by the geometry on the right-hand side of figures 2.13, 2.15, and 2.17. The results in terms of error are summarized in Fig. 2.18. The example accounts for a source point  $\bar{\xi}$  located at  $\eta' = (0, 1.1)$ , with the distance parameters  $d_1 = 0$ , and  $d_2 = 0.1$ , for the cubic transformation.

The decay of the error as a function of the number of integration points is observable, and the efficacy of the PART method over a simple cylindrical parametrization is evident. Despite this, the cubic transformation presents better performance, although its error decay is non-monotonic along the number of integration points. This observation might incline us to favor the cubic transformation over others, as it does not the need for additional steps for the geometric division into triangular sections. Regrettably, this transformation is not applicable for triangular boundary elements. For triangular boundary elements, we opt for the PART method. We also decide to use it for quadrangular boundary elements in the sake of consistency.

### Singular integral

The study of quasi-singular integral brings us now to the study of singular integrals. The methods presented in the previous section can be readily applied to a quadrangular reference element, with few adjustments.

Along this section we will consider the most uncertain example, as the observation point is located at the middle of the element of integration. However, in a general sense, the singular integration could stand for any point of observation inside the element of integration, like on the edges or vertex of the element of integration as presented Fig. 2.7.

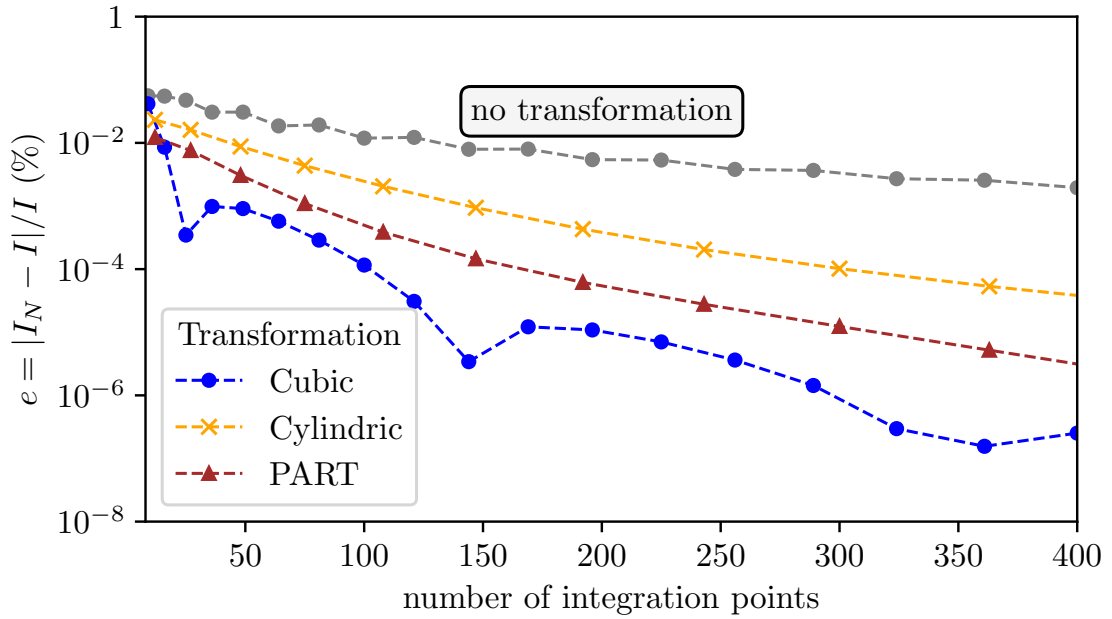


Figure 2.18: Examples of repartition of integrating point using PART method (red), and original cylindrical parametrisation (orange)

**Parametrizations** Now, the observation point  $\mathbf{x}$  is located within the reference element. For this investigation, we will focus exclusively on a source element positioned at the center of the reference element, denoted by  $\boldsymbol{\eta} = (0, 0)$ .

Beginning with the cubic transformation, its implementation is quite straightforward in this context. The cubic transformation is directly defined as  $\eta_i = \xi_i^3$  for  $i \in 1, 2$ , to the limits of the reference element, with  $\xi \in [-1, 1]$ . However, this works only for an even number of Gauss points, as the point must not coincide with  $\boldsymbol{\eta} = (0, 0)$ .

The radial and PART method both entail the division of the reference element into four triangular sections. All the geometric parameters needed are presented in Appendix B.4. With the observation point's location predetermined, the division into triangular areas is well established. Unlike the process for quasi-singular integration, here, the placement of integration points solely depends on the number of used Gauss points. The distribution of point of integration are shown in Fig 2.19 for the cubic, cylindrical, and PART methods.

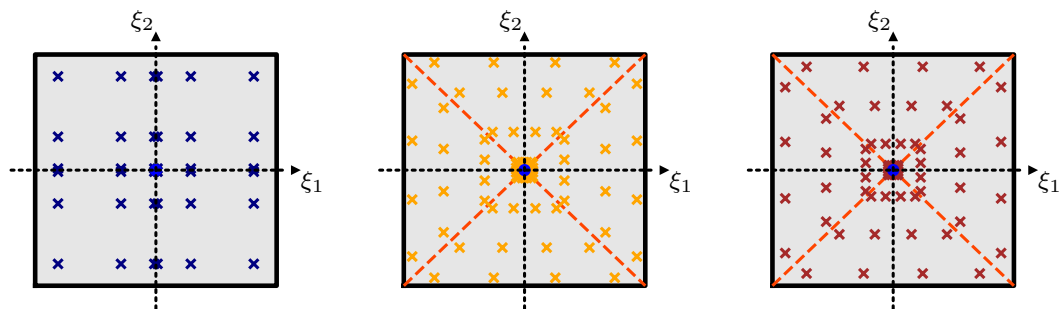


Figure 2.19: Distribution of the integrating point for the cubic (left) , cylindric (center), and PART (right) transformations in the case of the singular integral computation

**Performance** The exact value of integral of the Green function is known for that geometry, notably  $I_0 \approx 0.56110$  Eq. (2.58). The results of the integration can be readily compared with this value. The resulting error is presented in Fig. 2.20, for a varying number of

point of integration.

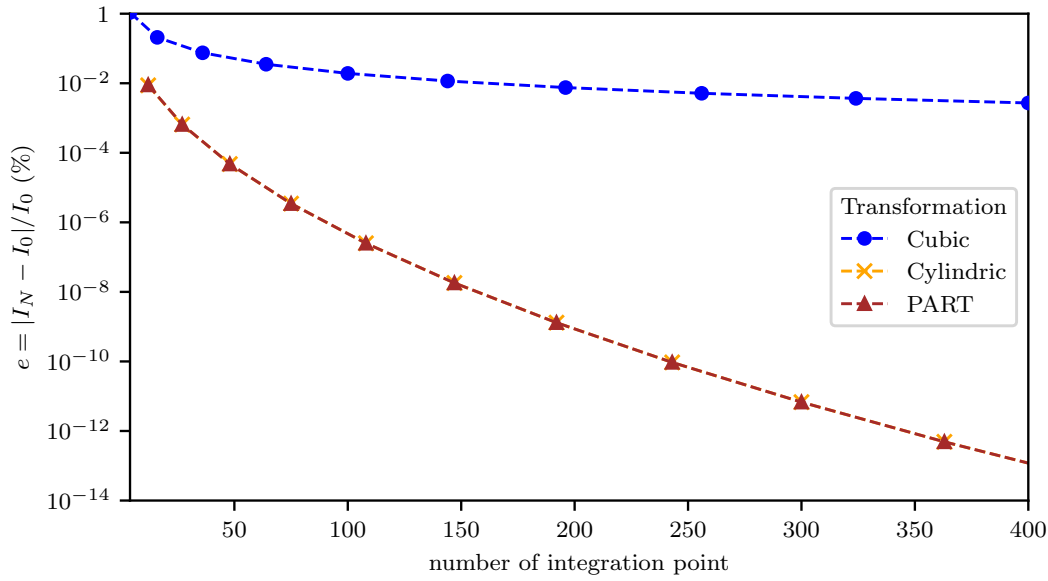


Figure 2.20: Precision comparison of different transformation for the singular integration

The error decreases as the number of integration points increases. Yet, unlike the quasi-singular integration outcomes, the cubic transformation now appears less precise, reaching a minimum error of 0.27% for 400 integration points. Both the cylindrical transformation and the PART method yield identical results. The supplementary steps taken by the PART method appears useless in this context. Nevertheless, these strategies seem particularly effective for singular integrals, resulting in even smaller errors compared to those observed in quasi-singular integration scenarios.

A similar analysis can be executed for triangular elements, positioning the point of at  $\eta = (1/3, 1/3)$  within the reference element. The precise value for this reference element is also well-documented.

These findings are detailed in Appendix B.4 and include assessments of the cylindrical and PART transformations. They both deliver consistent results, though the accuracy is approximately  $10^{-6}$  for 400 integration points. This indicates a slightly lower precision for triangular elements than for quadrangular ones.

## 2.2.4 Validation with circular contact spot

The integration procedure is ready to assemble the matrix  $G$ , after which the linear system as defined eq. 2.50 can be solved. Our method has been developed with a broad perspective, without any limitations neither on the shape of the mesh elements nor the interpolation functions used.

This section is dedicated to present some results and evaluating the overall method's performance. For this purpose, we have focused on the example of the circular contact spot subjected to a constant potential condition. As outlined in the initial part of this text, this particular problem has the advantage of a known analytical solution, which provides the normal flux field and the total flux transferred through the contact spot.

### Model and mesh

Testing different configurations, we compared the results obtained by different element shapes, notably triangular and quadrangular, with constant and linear interpolation, denoted by  $\mathcal{P}^0$ , and  $\mathcal{P}^1$ , respectively.

As we know, the flux is singular at the edge of the contact spot. Its simulation will require special attention controlling the mesh size on the edge. For mesh construction, we refine the mesh at the edge and coarsen in the center, aiming to minimize the quantity of unknowns. In practice, an element size  $h_{min}$  is set on the edge, and  $h_0$  conversely at the center of the spot, with  $h_0 > h_{min}$ , specifically we set  $h_0 = 2h_{min}$ .

The four numerical settings are presented Fig. 2.21. These figures showcase some outcomes of the normal flux overlaid by the designated mesh layout. The number of collocation points is equal to the number of elements when constant interpolation  $\mathcal{P}^0$  is used. For the linear interpolation  $\mathcal{P}^1$ , or *iso-parametric*, the mesh nodes coincide with the physical locations of the unknowns.

The fields so computed look different on the edge from the two different interpolation  $\mathcal{P}^0$ , and  $\mathcal{P}^1$ . In fact for the linear interpolation  $\mathcal{P}^1$ , the unknowns are located on the edge, where the singularity is lying. This will disturb the positiveness of the normal flux near the edge, where the negative flux value can happen. Conversely, in the case of constant interpolation  $\mathcal{P}^0$ , the normal flux remains positive at every point.

### Total flux

The total flux is readily calculable by combining the array of elemental areas  $\{|\mathcal{A}_e|\}$  with the corresponding nodal normal fluxes  $\{j_{n,c}\}$ . In the examples at hand, the total flux computation is governed as follows for  $\mathcal{P}^0$ , and  $\mathcal{P}^1$  interpolations.

$$\begin{array}{l} \mathcal{P}^0 \text{ interpolation} \\ Q = \sum_c^{N_c} |\mathcal{A}_c| j_{n,c} \end{array} \quad (2.64) \quad \left| \quad \begin{array}{l} \mathcal{P}^1 \text{ interpolation} \\ Q = \sum_e^{N_e} \left( |\mathcal{A}_e| \sum_{c \in \mathcal{A}_e} \frac{j_{n,c}}{m} \right) \end{array} \right. \quad (2.65)$$

With  $m$  the number of nodes per element. This leads to a factor of one quarter for quadrangular element, and of one third for triangular shape element, that arises from the integration of the shape function across the element.

The error value is then defined in term of the total flux compared to  $Q_o$  for the circular contact spot (see Section 1.1.2),

$$Er = \frac{|Q - Q_o|}{Q_o}$$

### Influence of the element size

Notably the physical representation of the normal flux depends on the mesh size  $h$ , and on the degree of interpolation,  $p$ . It is commonly assumed that FEM convergence is as  $h^p$  for stresses. However, as in the BEM, the order of interpolation is related to the flux, then the order  $p$  is 1 for  $\mathcal{P}^0$ , and 2 for  $\mathcal{P}^1$ . It shall be the same for BEM. To assess of the convergence behavior, we compute the solution of a circular contact, for various element size  $h$ . The outcomes are presented in Fig. 2.22.

The flux varies as an affine function of the element size, as :

$$Q = Q_\infty + bh$$

Where  $Q_\infty$  represents the limit of the flux when  $h \rightarrow 0$ ,  $b$  is the convergence slope rate related to  $h$ .  $b$  is negative for  $\mathcal{P}^1$  interpolation, and positive for  $\mathcal{P}^0$  interpolation. All the coefficients are summarized in Table 2.1, with the coefficient of correlation  $r^2$  included.

In every model, the error appraise the numerical accuracy, and the self-consistency of BEM. The convergence features differ between different models. The affine trend in the convergence of the total flux is also related to Richardson's method of result extrapolation [Richardson, 1911]. This technique relies on the extrapolation of the total

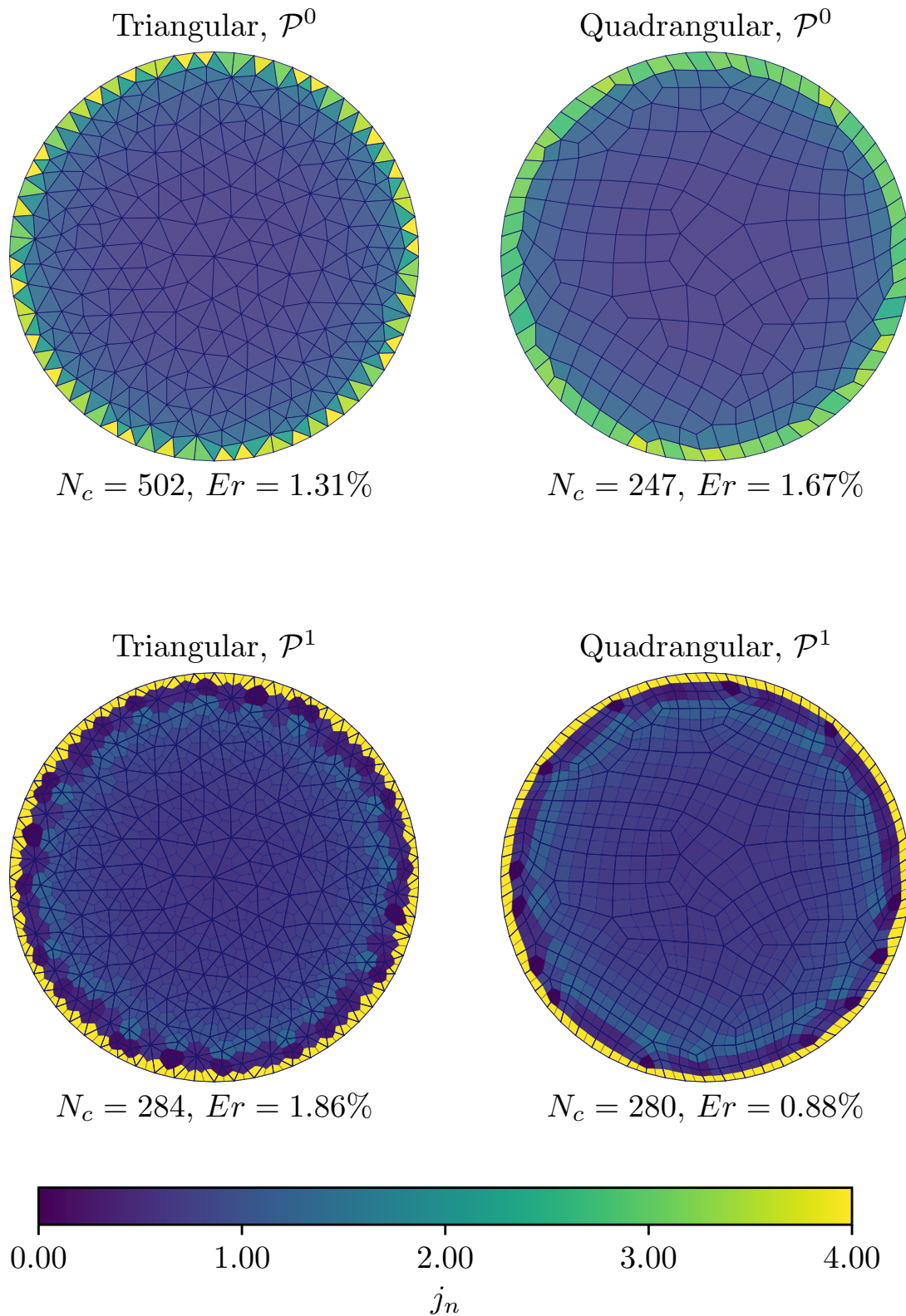


Figure 2.21: Result of normal flux with triangular and quadrangular elements, using constant or linear interpolation, with  $h_{min}/r_0 = 0.1$  and  $h_0/r_0 = 0.2$  as element size, at the edge and in the center, respectively

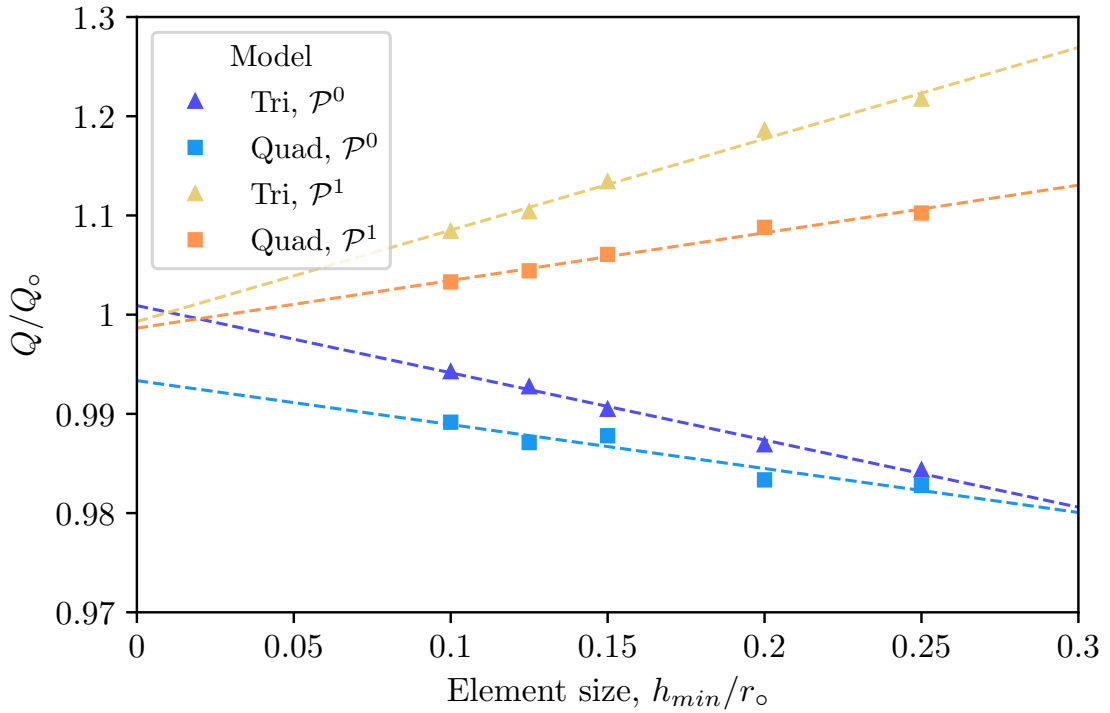


Figure 2.22: Result of the integrated flux as a function of the element size,  $h_{min}$ .

Model	Coefficients		Error	
	$\frac{Q_\infty}{Q_0}$	$\frac{b}{Q_0}$	$\frac{ Q_\infty - Q_0 }{Q_0}$	$r^2$
Triangular, $\mathcal{P}^0$	1.0007	-0.067	0.09%	0.996
Quadrangular, $\mathcal{P}^0$	0.996	-0.059	0.67%	0.914
Triangular, $\mathcal{P}^1$	0.999	0.0914	0.07%	0.994
Quadrangular, $\mathcal{P}^1$	0.999	0.0467	0.14%	0.988

Table 2.1: Results of the total flux linear regression

flux value, presupposing a linear convergence in relation to element size. To forecast the precise solution,  $Q_{extra}$ , one only requires two distinct, yet adequately fine element sizes,  $h_1$  and  $h_2$ .

$$\left. \begin{aligned} Q_1 &= Q_{extra} + bh_1 \\ Q_2 &= Q_{extra} + bh_2 \end{aligned} \right\} \implies Q_{extra} = \frac{Q_1 h_2 - Q_2 h_1}{h_2 - h_1} \quad (2.66)$$

Using this approach, and taking advantage of the integrated flux values. The extrapolated results are presented in Table 2.2, computed two element sizes with the smallest mesh size  $h_1/r_0 = 0.1$  and  $h_2/r_0 = 0.125$ , corresponding to those depicted in Fig. 2.22.

Model	$\mathcal{P}^0$		$\mathcal{P}^1$	
	Tri	Quad	Tri	Quad
$\frac{ Q_{extra} - Q_0 }{Q_0}$	0.031%	0.26%	0.058%	0.12%

Table 2.2: Results of Richardson's extrapolation for the total flux

The results in Table 2.2, appear more accurate than the ones proposed in Table 2.1, demonstrating the consistency of the method. Ultimately the triangular model with



constant interpolation provides the most precise result, in spite of its relative simplicity in comparison with the others.

## 2.3 Fast-BEM

The previous section prompted the development of classical BEM tailored for the conduction problem. It further introduced the validation of our integration techniques' precision. The resolution pertaining to the circular spot ultimately assess of the numerical performance of this model.

However, it has been pointed out that the matrix  $[G]$  is fully-populated. It arises subsequent challenges in terms of numerical precision, memory requirement, and computational complexity. As the number of elements increases - thereby enlarging the matrix dimensions - numerical complexity emerges as a substantial constraint, scaling with the order of  $O(N^2)$  for the evaluation of the matrix components.

To address these challenges, various methods have been developed, initiated by the *Fast Multipole Method* (FMM), which then enables the development of *low-rank approximations*. By combining these low-rank approximations with the concept of hierarchical matrices, the overall complexity of BEM can be significantly reduced to  $O(N \log(N))$ . This reduction in complexity allows much more efficient and still accurate simulations, dealing with a larger number of elements, thus enhancing the practicality and feasibility of BEM for tackling realistic problems.

### 2.3.1 Approximation construction

The *Fast-BEM*, as introduced, is develop to speed up the computation of the matrix  $[G]$ , introduced in Eq. (2.50), by dividing it into sub-blocks and approximating some of them. The current version of the Fast-BEM draws inspiration from the FFM, which is prescribed by *asymptotical smoothness* property of the kernel function [Börm et al., 2003].

#### Definition: Asymptotic smoothness

A function  $f : D_X \times D_Y \rightarrow \mathbb{R}$  is asymptotically smooth when exists such constants  $c_1, c_2 > 0$  and  $s \in \mathbb{N}$  so that for any index  $n \in \mathbb{N}^{*+}$

$$|\partial_y^n f(x, y)| \leq c_1 n! c_2^n |x - y|^{-n-s} \quad (2.67)$$

Where  $s$  represents the degree of singularity of the kernel function.

In the context of BEM, the function  $f$  stands for the Green function, underlying  $s = 1$  as degree of singularity. This condition yields the definition of panel clustering [Hackbusch and Nowak, 1989]. The matrix  $[G]$  is thus divided in sub-blocks, arranging the sub-block space around clusters of elements that satisfy the condition of admissibility [Grasedyck and Hackbusch, 2003]. All these notions will be introduced in detail in this section.

This section aims to present various approximation techniques that leverage the property of asymptotic smoothness. An example of *multipole expansion* is applied to a problem of potential computation. Subsequently it will serve to delineate various techniques of approximation within the context of Fast-BEM development. It will be then followed by an assessment of their performance.

#### Application to the computation of potential

In the pioneering work by Rokhlin [Greengard and Rokhlin, 1987, Rokhlin, 1985], a fast version of computation of potential field for particles relies on the computation of *multipole*

*expansion*. This case study considers a system where particles are subject to pairwise interactions, be they electrostatic or gravitational. For a system comprising  $N$  particles, the potential  $U$  acting on any given particle is the aggregate of potentials from all other particles. This potential is characterized by the scalar function  $\Phi$ .

$$U(\mathbf{x}_i) = \sum_{j \neq i}^N \Phi(\mathbf{x}_i, \mathbf{x}_j)$$

$$\Phi(\mathbf{x}_i, \mathbf{x}_j) = \frac{m_i m_j}{r_{i,j}} = \frac{m_i m_j}{\|\mathbf{x}_i - \mathbf{x}_j\|}$$

With  $\mathbf{x}_i$  is the position of the  $i$ -th particle, and  $m_i$  represents its mass. In that case, we assume gravitational interaction, with gravity constant  $\mathcal{G} = 1$ .

### Cluster definition

As an example, we might consider two different clusters, in which the particles are sparsely distributed. This example can be illustrated in Fig. 2.23. The weights are randomly defined, prescribed by a truncated normal distribution. The positions of those particles are as well randomly distributed within the cluster space. The particles are presented by color dots, colored accordingly to the potential of the particle.

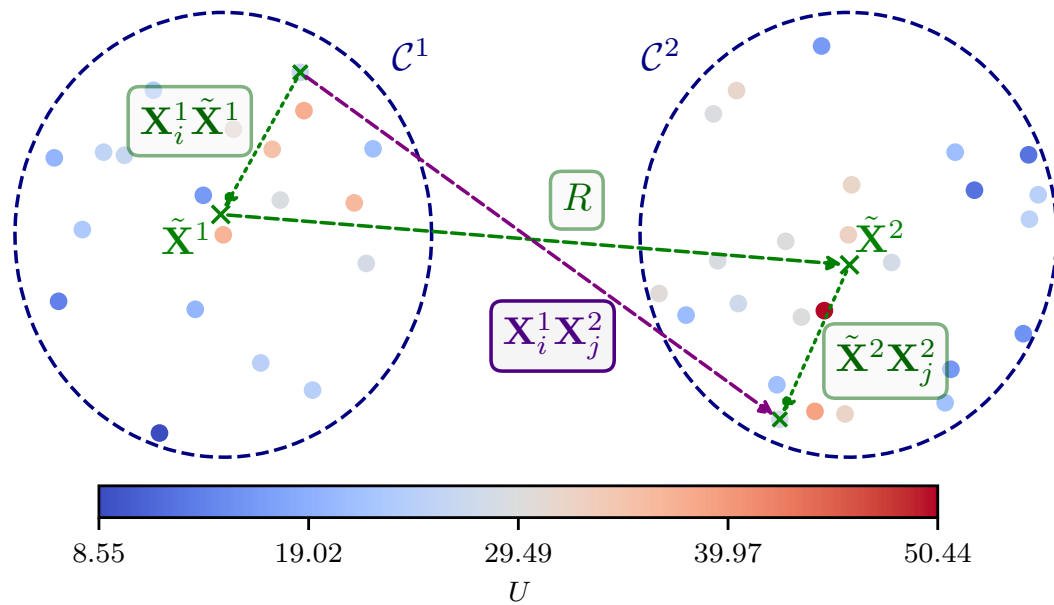


Figure 2.23: Potential for particles sparsely distributed within two clusters

**Sub-block matrix approximation** Two sets of particle position might be defined  $\{\mathbf{x} \in \mathcal{C}^1\} = \{\mathbf{x}^1\}$ , and  $\{\mathbf{x} \in \mathcal{C}^2\} = \{\mathbf{x}^2\}$ . The latter potential formula can be reformulated using a linear system, as follows.

$$\begin{pmatrix} [U(\mathbf{x}^1)] \\ [U(\mathbf{x}^2)] \end{pmatrix} = \begin{pmatrix} M^{11} & M^{12} \\ M^{21} & M^{22} \end{pmatrix} \cdot \begin{pmatrix} 1 \\ \vdots \\ 1 \end{pmatrix}, \quad M_{ij} = \Phi(\mathbf{x}_i, \mathbf{x}_j)$$

The matrix of potential interaction is parceled out in sub-blocks, following the two clusters set,  $\{\mathbf{x}^1\}$ ,  $\{\mathbf{x}^2\}$ . The multipole expansion aims to approximate the interaction between two

sets of particles well-separated. This appeals to focus on extra-diagonal sub-blocks,  $M^{12}$ , and  $M^{21}$ . As the potential function is symmetric, the sub-blocks are in turn symmetric, like  $M^{21} = (M^{12})^T$ . This example will solely concern the approximation of the sub-block  $M^{12}$ .

Considering the sub-block  $M^{12}$ , the set of observation point is represented by the subspace  $\{x^1\}$ , while  $\{x^2\}$  is analogous to the set of integration element. The length of those two sets are denoted by  $m$  and  $n$ , for  $\{x^1\}$ , and  $\{x^2\}$ , respectively. The multipole expansion relies on the vector decomposition of the distance vector, as presented in Fig. 2.23, like

$$x_i^1 x_j^2 = x_i^1 \tilde{x}^1 + \tilde{x}^1 \tilde{x}^2 + \tilde{x}^2 x_j^2$$

With the indexes  $i \in [1, n]$  and  $j \in [1, m]$ , as  $M_{ij}^{12} = (m_i m_j) / |x_i^1 x_j^2|$ . The points  $\tilde{x}^1$  and  $\tilde{x}^2$  represent the coordinate of the centroid point of the clusters  $C^1$  and  $C^2$ .

The multipole expansion relies on a *separation of variables*, which is developed as a *Taylor-type expression*. The number of derived functions involved gives the order of the multipole expansion. The separation of variables could be developed as the product function below,

$$M_{i,j}^{12} = \Phi(x_i^1, x_j^2) \approx f(x_i^1, \tilde{x}^1) g(|\tilde{x}^1 - \tilde{x}^2|) h(\tilde{x}^2, x_j^2)$$

Where  $R$  is distance by the centroids points, as  $R = |\tilde{x}^1 - \tilde{x}^2|$ , for which is derived the Taylor-type expansion. This might be summarized in a matrix system, illustrated in Fig. 2.24. This diagram accounts for a multipole expansion at the third degree. The sub-blocks in the matrices are of variable shapes, related to the dimension of the problem. For the latter example, the geometrical dimension is equal to two; the difference  $(x_i - \tilde{x}^1)$  is still of dimension two, and  $(x_i - \tilde{x}^1)^2$  might be composed of three components for instance. However the series of derivatives  $\nabla^n g(R)$  is still scalar, but might be multiplied to the right components in the other sub-blocks to return a vectorial component defined in the original geometrical coordinate system.

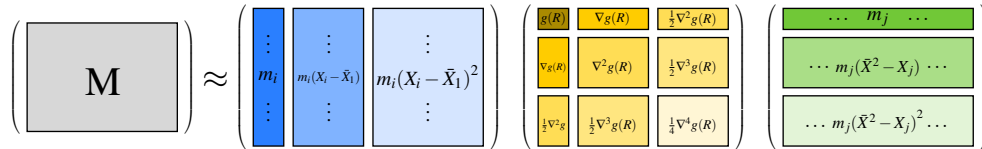


Figure 2.24: Diagram representing the FMM construction with a product of column and line vector matrices

Initially, the matrix  $M^{12}$  accounts for  $(m \times n)$  coefficients. At variance, the multipole expansion takes into account  $p$  multipoles. Given that  $p \ll \min(n, m)$ , the quantity of coefficients calculated and stored can be substantially decreased to  $(m.p + p.p + p.n) \approx (m + n).p$ . The asymptotic smoothness assumption relies on the error regulation entailed by the multipole expansion, thereby ensuring numerical stability. The error diminishes as the number of modes  $p$  increases.

The formulation of multipole expansions can entail complex analytical development; however, this subject benefits from an extensive literature, offering numerous practical examples in fields such as gravitational astronomy [Binney and Tremaine, 2011, Blanchet, 1998], wave propagation [Devaney and Wolf, 1974, Thorne, 1953], radiation problems [Bouwkamp and Casimir, 1954], and even quantum mechanics [Fiutak, 1963]. Detailed expressions for functions  $f$ ,  $g$ , and  $h$  are elaborated upon in the appendix.

The FMM was initially developed in the late 1980s [Rokhlin, 1985] [Greengard and Rokhlin, 1987] for calculating particle potential fields, and later extended to electromagnetic issues [Engheta et al., 1992], Laplacian problems [Greengard and Rokhlin, 1997], and issues governed by boundary integral

equations [Liu, 2009], benefiting from the advancements in multipole expansion. Ultimately, this method reduces computational costs from  $\mathcal{O}(N^2)$  to  $\mathcal{O}(N \log(N))$ .

**Perspectives for BEM, Fast-BEM** The BEM has reaped significant advantages from these advancements in the late 1990s. To enhance flexibility and decrease computation time, the FMM was replaced by low-rank approximations such as Adaptive Cross-Approximation (ACA), which will be discussed in detail later.

In analogy to particle interactions, the concept requires the definition of well-separated sets of elements, or clusters of elements. A blockwise structure can be developed using a *Hierarchical algorithm*. This approach has contributed to the development of hierarchical matrices, also known as *H-matrices* [Bebendorf, 2008].

### Adaptive-Cross-Approximation (ACA)

According to the asymptotic smoothness property, there exists a low-rank approximation for the sub-block matrix  $M^{12}$ . Consequently, the rank of  $\tilde{M}^{12}$  is  $p$ , which is less than the initial  $\min(m, n)$ , assuming that  $M^{12}$  is a full-rank matrix. The existence of such a low-rank approximation matrix is further supported by the following theorem, as demonstrated by [Goreinov et al., 1997].

#### Theorem: Existence of pseudoskeleton decomposition

Assume that  $(M, \tilde{M}) \in \mathbb{R}^{m \times n}$ , with  $R = M - \tilde{M}$ ,  $\text{rank}(R) \leq k$  and  $\|R\|_F \leq \epsilon$  for some  $\epsilon > 0$ , there exists a **pseudo-skeleton** decomposition, then there exists,

$$\|M - CGD\|_F \leq \epsilon \left(1 + 2\sqrt{p}(\sqrt{m} + \sqrt{n})\right) \quad (2.68)$$

Where  $C \in \mathbb{R}^{m \times k}$ ,  $G \in \mathbb{R}^{k \times k}$  and  $D \in \mathbb{R}^{k \times n}$ . Thus the sub-block approximation is defined by the matrix product  $\tilde{M} = CGD$ .

With  $\epsilon$  represents an *error coefficient* in order of the prescribed rank  $p$ , and  $\|\bullet\|_F$  stands for the Frobenius norm. This theorem announces that it exists a subspace between the set of point of observation  $\sigma$ , and the source point  $\tau$ . The length dimension of these set would be denoted by  $\dim(\sigma) = m$ , and  $\dim(\tau) = n$ . This theorem is reported as well in [Bebendorf, 2000], is used to demonstrate the existence of a low rank approximation for BEM, based on the asymptotic smoothness property. The details of its demonstration can be found in [Van Loan and Golub, 1996].

**Adaptive-Cross-Approximation** The Adaptive Cross-Approximation (ACA) is a class of methods for constructing low-rank approximations without depending on analytic multipole expansions, which differentiates it from the Fast Multipole Method (FMM). Unlike FMM, ACA techniques do not require a priori knowledge of the kernel function, allowing for greater flexibility. Several variations of the ACA method exists, each with its unique process, but all utilize the sets  $\sigma$  and  $\tau$ , as well as an error tolerance  $\epsilon$ . These methods incrementally search for pivotal elements, with coefficient values being approximated in real-time. The iterative process continues until the error in the approximation reaches the acceptable threshold determined by  $\epsilon$ .

- **ACA-full:** This approach requires the knowledge of the entire sub-block matrix for its operation, as presented by Bebendorf [Bebendorf, 2000]. It identifies the pivot, which is the maximal coefficient in the matrix, and then updates the working matrix by removing the corresponding row and column of the pivot. This step is iteratively repeated until the stopping criteria is fulfilled. One of the key benefits of ACA-full is its reliability. However, it is time-intensive since it necessitates the

assembly of the full matrix before decomposition. It is analogous to the Singular Value Decomposition (SVD) approach.

- **ACA-partial:** Contrary to ACA-full, ACA-partial [Bebendorf, 2003] does not require the full matrix to be known beforehand, thus expediting the approximation process by bypassing the full matrix assembly. The trade-off for this speed is a potential decrease in accuracy due to possibly suboptimal pivot selection. To address this, an enhanced version called **ACA+** [Grasedyck, 2005] has been developed, which employs a more robust pivot search mechanism to improve reliability.

These techniques are part of a broader, that also includes method such as *Nested-ACA*, as referenced in the literature [Bebendorf and Venn, 2012, Gujjula and Ambikasaran, 2022]. The *Nested-ACA* differs from the ACA variants by constructing the low-rank approximation components through a nested basis, and it is not heuristic in nature. Furthermore, there are proofs available that guarantee its convergence, although it remains an algebraic method at its core.

### ACA-full

Let us apply this method on the approximation of the sub-block matrix  $M$ . The approximation of this sub-block is supposed to be built on fly. The approximation at the  $k^{\text{th}}$  iteration is denoted by  $\tilde{M}^k$ , and  $R^k$  represents the residual matrix at this stage. These expressions are illustrated by the equations below.

$$\begin{matrix} & & j_{ref} & & \tau \\ & & \delta & & \\ i_{ref} & & & & \\ \sigma & & & & M \end{matrix}, \tilde{M}^1 = \begin{pmatrix} a_1 \\ \vdots \end{pmatrix} \times \begin{pmatrix} b_1 \\ \vdots \end{pmatrix} = \begin{matrix} a_1 \\ \vdots \end{matrix} \begin{matrix} b_1 \\ \vdots \end{matrix} = \begin{matrix} m_{i_{ref}, j_{ref}} \\ \vdots \end{matrix} \begin{matrix} \frac{m_{i_{ref}, j_{ref}}}{\delta} \\ \vdots \end{matrix}$$

Figure 2.25: Diagram illustrating the approximation built by ACA-full at the first step

The detailed procedure is elaborated in the Appendix B.5.1, initiating with a search for the optimal global pivot. Upon identifying this pivot, indicated as  $\delta$ , we document its precise location within the matrix by its row and column indices. The row and column associated with  $\delta$  are preserved as matrix vectors, denoted by  $A$  and  $B$  respectively. Subsequently, we compute the outer product of  $A$  and  $B$  and deduce this from the original matrix  $M$  to yield the residual matrix, denoted by  $R^1$  — this signifies the completion of the first iteration, with  $k = 1$  at this point. This process is illustrate in Fig. 2.25 for the first iteration,  $k = 1$ .

This iterative method continues on the residual matrix  $R^k$  at each subsequent  $k^{\text{th}}$  step, as illustrated for the second stage in Fig. 2.26. With every iteration, a new pivot is selected, and corresponding new vectors are added to the  $A$  and  $B$  matrices. This iterative process is maintained until the predetermined stopping criteria are fulfilled. Noticeably if the pivot found is equal to 0, the approximated matrix is perfectly equal to  $M$ , and the process is stopped as well. The stop condition is defined in terms of the norm of the residual matrix as

$$\|R^k\|_F = \|M - M^k\|_F \leq \epsilon \|M\|_F$$

$$\begin{aligned}
 M - \tilde{M}^1 &= \begin{pmatrix} \text{---} & \text{---} & \text{---} & \text{---} & \text{---} \\ \text{---} & \text{---} & \text{---} & \text{---} & \text{---} \\ \text{---} & \text{---} & \text{---} & \text{---} & \text{---} \\ \text{---} & \text{---} & \text{---} & \delta & \text{---} \\ \text{---} & \text{---} & \text{---} & \text{---} & \text{---} \end{pmatrix} = R^1 \\
 &\quad \begin{matrix} j_{ref}^2 \\ i_{ref}^2 \end{matrix} \\
 \tilde{M}^2 &= \begin{pmatrix} \text{---} & \text{---} \\ a_1 & a_2 \end{pmatrix} \times \begin{pmatrix} b_1 \\ b_2 \end{pmatrix} \\
 &\quad \begin{matrix} A^2 \\ B^2 \end{matrix}
 \end{aligned}$$

Figure 2.26: Diagram illustrating the approximation built by ACA-full for a matrix with a rank of 2

The algorithm might be evaluated in terms of its complexity. The Table 2.3 accounts for the computational cost of all steps. As the Frobenius norm accounts for the square root of the cumulative sum of all squared coefficients, thus the number of operation is linear to the number of coefficient,  $m \times n$ . The pivot search, the residual matrix computation and the residual error, are all again proportional to the number of coefficients, and repeated at each iteration, thus  $k$  times.

Step	Complexity
Initial norm, $\ M\ _F$	$O(m \times n)$
Pivot search, $\delta$	$O(m \times n)$
Residual matrix, $R^k$	$O(m \times n)$
Residual error, $\ R^k\ _F$	$O(m \times n)$

}  $\times k$  iteration

Table 2.3: Order of operation for the different step of ACA-full

The computational cost of the process is about  $O(k.m.n + m.n)$ . The complexity is contingent on the dimensions of the matrix  $M$ , and multiplied by the required number of iterations  $k$ , which might appear as a severe drawback. The final memory cost decreases to an order of  $O(k.(m + n))$ , compared to the initial  $O(n.m)$ .

### ACA+

In the last algorithm, all operations are completed on the whole matrix, increasing the complexity. The algorithm ACA+ aims to improve the complexity, shortcutting the work on the whole matrix, and its complete assembly. Differing from ACA-full, the sub-block matrix  $M$  is partially ignored. The pivot search could not span the entire matrix. A first line  $l_{ref}$  and a first column  $c_{ref}$  of the matrix are chosen and computed, as illustrated in Fig. 2.27. The pivot,  $\delta^*$ , is then identified as the maximal value located on these reference line and column, acknowledging that  $\delta^*$  might not be the absolute maximum of the whole matrix. Its position is recorded as  $(i^*, j^*)$ , and is next searched on this line and column, which is denoted by  $\delta^*$ , at the position  $i^*$  and  $j^*$ . Similarly to the ACA-full, each

iteration results in the addition of a new column and line vector to the matrices  $A$ , and  $B$ , respectively.

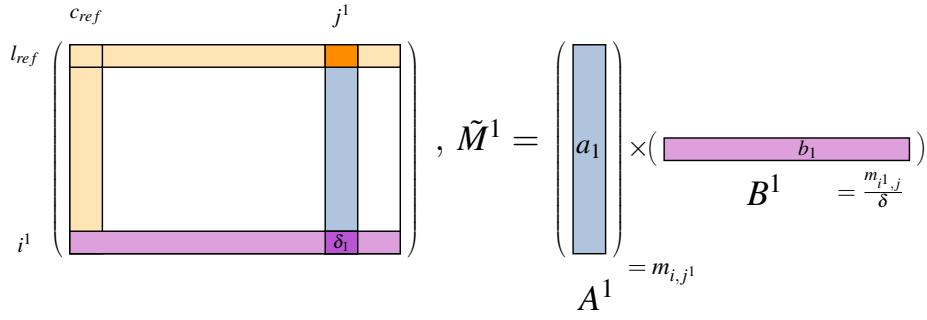


Figure 2.27: Diagram illustrating the approximation built by ACA-plus first the first stage

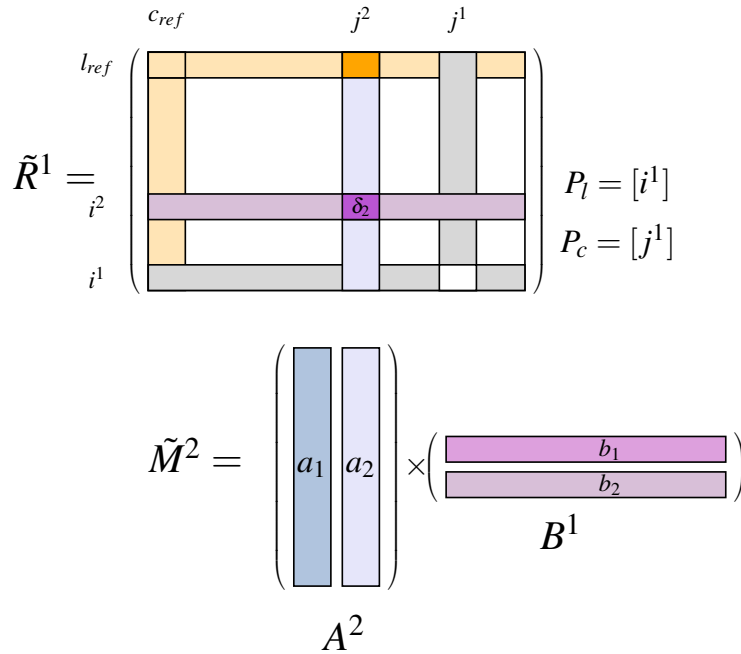


Figure 2.28: Diagram illustrating the approximation built by ACA-plus for a matrix with a rank of 2

The pivot search continues, resulting in an iterative process. A second step of the ACA-plus aims to be illustrated in Fig. 2.28. All indexes that were explored, are save in variables  $P_l$  and  $P_c$ , respectively for the row and column indexes. The indexes of reference are kept as long as the pivot do not coincide with  $i_{ref}$  or  $j_{ref}$ . When the pivot coincides with the index  $i^{ref}$  in row position or with  $j^{ref}$  in column position, the elements of reference are changed. Those elements of reference enables to explore the whole matrix; the algorithm increases its robustness against zero sub-part in the matrix, which may introduce some instabilities.

The residual of the matrix needs to be adapted due to its partial knowledge. The whole matrix  $M$  is replaced by the incremented matrix  $\tilde{M}^{k+1}$ .

$$\begin{aligned} \|M - \tilde{M}\|_F &\leq \epsilon \|M\|_F \\ \Rightarrow \|\tilde{R}^{k+1}\|_F &\leq \epsilon \|\tilde{M}^{k+1}\|_F \end{aligned} \tag{2.69}$$

with  $\widetilde{R}^k$  the a-priori residual matrix, that is expressed as the difference between the matrices  $\widetilde{M}^{k+1}$  and  $\widetilde{M}^k$ .

$$\widetilde{R}^{k+1} = \widetilde{M}^{k+1} - \widetilde{M}^k$$

The left-hand side in the expression Eq. (2.69), the coefficients of residual matrix is developed using line-column matrix product formula. This leads to the next simplified expression for  $\widetilde{R}^{k+1}$ , as

$$\widetilde{R}_{i,j}^{k+1} = \sum_{p=1}^{k+1} a_i^p b_j^p - \sum_{p=1}^k a_i^p b_j^p = a_i^{k+1} b_j^{k+1}$$

Notably it follows the norm of the residual matrix,

$$\begin{aligned} \|\widetilde{R}^{k+1}\|_F^2 &= \sum_{i=1}^m (a_i^{k+1})^2 \sum_{j=1}^n (b_j^{k+1})^2 \\ &\Rightarrow \boxed{\|\widetilde{R}^{k+1}\|_F^2 = \|a^{k+1}\|^2 \|b^{k+1}\|^2} \end{aligned} \quad (2.70)$$

This formulation for the residual matrix error allows us to separate the norm according to two single vector error. Thus its computation just involves  $m + n$  operations.

The term  $\|\widetilde{M}^{k+1}\|_F$  on the right-hand side in Eq. (2.69), requires a complete development of  $\widetilde{M}^{k+1}$  as presented below. It starts with the separation of the coefficients until  $k$ , from the last column and line vector at  $k + 1$  position. It reveals the term  $\|\widetilde{M}^k\|_F$  and the residual norm  $\|\widetilde{R}^{k+1}\|_F$ . Thus, this norm can be incremented by the  $k^{\text{th}}$  stage.

$$\begin{aligned} \|\widetilde{M}^{k+1}\|_F &= \sum_{i,j} \left( \sum_{p=1}^{k+1} a_i^p b_j^p \right)^2 \\ \Leftrightarrow \|\widetilde{M}^{k+1}\|_F &= \sum_{i,j} \left[ \left( \sum_{p=1}^k a_i^p b_j^p \right)^2 + (a_i^{k+1} b_j^{k+1})^2 + 2(a_i^{k+1} b_j^{k+1}) \sum_p^k a_i^p b_j^p \right] \\ \Leftrightarrow \|\widetilde{M}^{k+1}\|_F &= \|\widetilde{M}^k\|_F + \|\widetilde{R}^{k+1}\|_F + 2 \sum_{i,j} \sum_{p=1}^k a_i^p a_i^{k+1} b_j^p b_j^{k+1} \\ &\Rightarrow \boxed{\|\widetilde{M}^{k+1}\|_F = \|\widetilde{M}^k\|_F + \|\widetilde{R}^{k+1}\|_F + 2 \left( A^k \cdot (a^{k+1})^T \right) \cdot \left( B^p \cdot (b^{p+1})^T \right)} \end{aligned} \quad (2.71)$$

The last term on the right hand side can not be further simplified, but could be expressed as a matrix product between the matrices  $A^k$ ,  $B^k$ , and respectively the vectors  $a^{k+1}$  and  $b^{k+1}$ . The norm  $\|\widetilde{M}^{k+1}\|_F$  computation is incremented by the residual error, and supplemented by the last term of matrix product. This last part has the highest asymptotic complexity. At every iteration, it counts about  $k(m + n)$  operations. All the orders of number of operation are summarized in Table 2.4.

The complexity order is brought to  $\mathcal{O}(k^2(m + n) + k(m + n))$ . But the integration in pivot search is prevailing, that accounts for the computation of coefficients in the line  $l^*$ , and the column  $c^*$ . The time requirement grows as a law of  $\mathcal{O}(k(m + n))$ , as long as  $k \ll \min(m, n)$ .

### Example

In the context of the potential problem, we recall the problem of computation  $M^{12}$ , which relates to the computation of potential interaction between the cluster  $C^1$  and  $C^2$ . In this particular example, the source point set comprises  $\sigma = \{x^1\}$ , while the target point set



Step	Complexity
Value of reference, $c_{ref}, l_{ref}, i_{ref}, j_{ref}$	$O(m + n)$
Pivot search, $\delta^*, i^*, j^*$	$O(m + n)$
Residual error, $\ \tilde{R}^{k+1}\ _F$	$O(m + n)$
Matrix norm, $\ \tilde{M}^{k+1}\ _F$	$O(k(m + n))$

}  $\times k$  iteration

Table 2.4: Order of operation for the different step of ACA+

consists of  $\tau = \{x^2\}$ , each with respective lengths of  $n = 20$  and  $m = 25$ . The errors in the coefficients' results are presented Fig. 2.29 within the framework of FMM, ACA-full and ACA+. All these approximations utilize the same number of modes, which is limited to  $k = 6$  iterations.

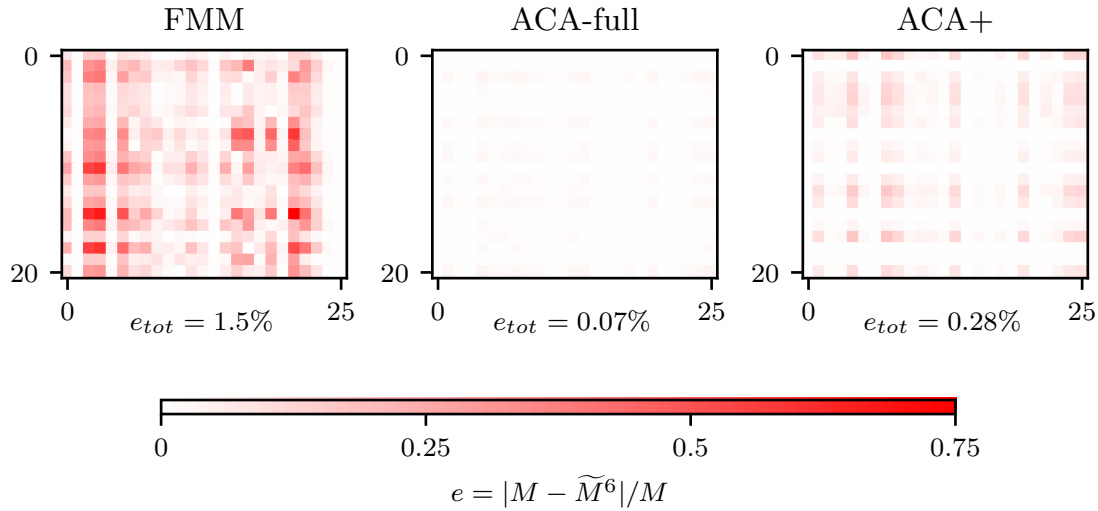


Figure 2.29: Error in matrix coefficient with approximation for FMM (left), ACA-full (center) and ACA+ (right)

In Fig. 2.29, the relative errors of the coefficients are depicted in reddish colors. The total error,  $e_{tot}$ , on the matrix encompasses the cumulative relative errors across all coefficients, a

In practical applications, an iterative low-rank approximation employs a termination condition based on error criteria, related to a coefficient of error  $\epsilon$ , conversely to FMM. This latter requires analytical developments for each subsequent mode. In this example, both ACA+ and ACA-full demonstrate their value, achieving total errors of 0.07% and 0.28%, respectively, which are lower than the error induced by FMM, approximately 1.5% in this case. Regarding the low-rank approximation, certain lines and columns exhibit error values of zero. These correspond to the pivot row and column indices fully computed or stored within the matrices  $A$  and  $B$ . This results in the exact values for those coefficients.

### 2.3.2 Error in function of the rank

The relationship between the rank number  $k$  and the error coefficient  $\epsilon$  can be expressed as follows:  $k \sim \log(\epsilon)$ . Fig. 2.30 represents the error associated with the approximated matrix for the sub-block  $M^{12}$  for an increasing number of modes  $k$ . Additionally, we present the results obtained from *Singular Value Decomposition* (SVD), taking only  $k$  first singular values. This latter is parallel to the ACA-full, and is known to offer a low-rank approximation that provides the best achievable approximation while minimizing

the rank number, as described in [Van Loan and Golub, 1996], however it is the most computationally expensive truncated at  $k$ .

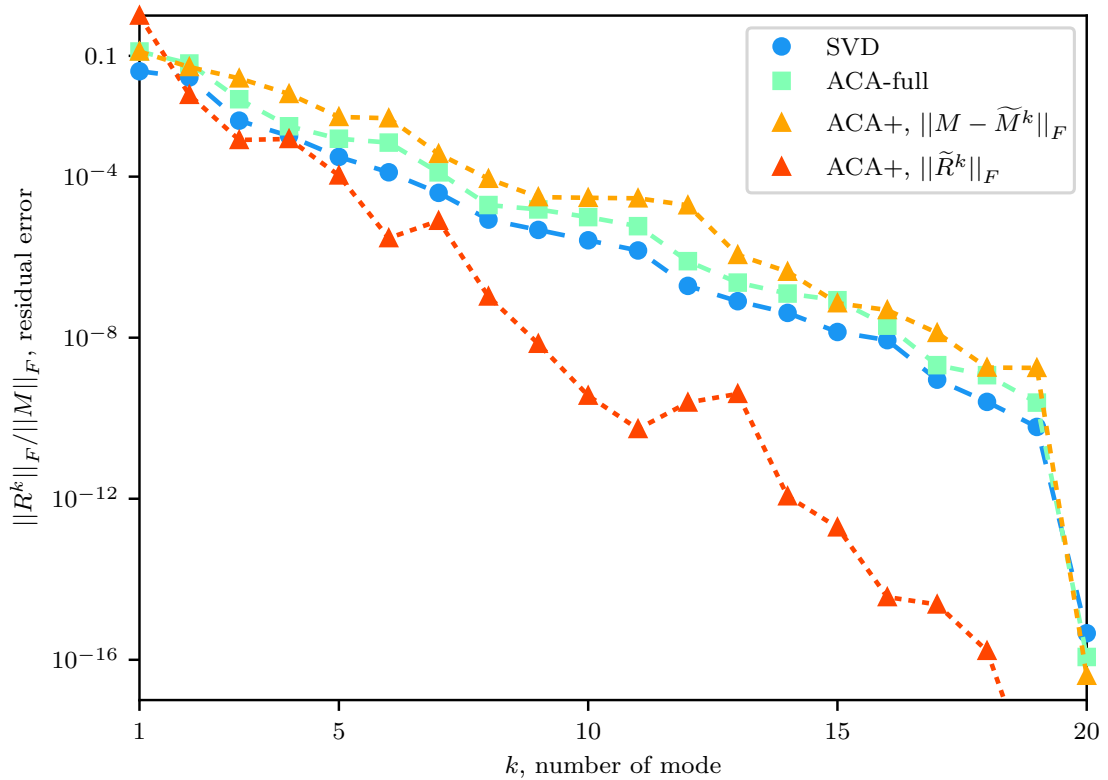


Figure 2.30: Residual error for in function of the number of mode the different low-rank approximation

Two types of errors are computed for the *ACA+* method. The orange line represents the actual error, which is calculated by comparing the entire matrix  $M$  with the approximated  $\tilde{M}^k$ . Meanwhile, the red line corresponds to the residual error, i.e.  $\|\tilde{M}^{k+1} - \tilde{M}^k\|_F$ , given by Eq. (2.70), which is actually employed in practice for the *ACA+* method. The red line is expectedly lower than the true error in orange line. This discrepancy could lead to misleading in error measurements. At the same time, the actual error values produced by the *ACA+* method are higher than the others, underestimating the number of modes really needed to reach the error command.

Nonetheless, the error for the *ACA+* method decreases as the number of modes increases, similar to the behavior of the others. Considering that the sub-block is non-deprecated, its rank would be equal to  $\min(m, n)$ . At this rank, a persistent error equivalent to the floating error remains, entailed by the matrix product operation. Comparing with the *SVD* method, which is akin to *ACA-full* and requires the knowledge of the entire matrix, despite having a higher error and uncertain convergence, we opt for the *ACA+* application. In practical applications, it allows us to speed up the integration process. For the memory optimization we may still employ the *SVD* method on the top of the matrix obtained by *ACA+*, as employed by [Grasedyck, 2005]. This approach will be discussed further in the section dedicated to optimization.

### 2.3.3 $\mathcal{H}$ -matrix

In the previous section, we delved into the development and the assessment of the low-rank approximation. This allows to shortcut the construction of the whole matrix and support the development of the Fast-BEM. The potential function  $\Phi$  is replaced by the Green's function integrated on the boundary element. The expansion of this

approximation to a continuous boundary element mesh hinges on our ability to define consistent clusters of elements. The integration process must be preceded by the cluster construction of mesh element. These steps are carried out hierarchically to preserve a certain level of geometrical coherence, ultimately leading to the definition of  $\mathcal{H}$ -matrices.

This section aims to introduce the specific structures of these matrices. Their construction starts with the definition of clusters and the hierarchical tree. We will then present the admissibility condition, initially rooted in the *asymptotic smoothness* property. Subsequently, we will explore clustering techniques in the context of their geometrical consistency and the resulting numerical performance implications.

### Admissible condition

First, the establishment of a blockwise structure is essential for defining the  $\mathcal{H}$ -matrix. The subspaces defining the row and column indices are closely tied to the clusters within the mesh. This necessitates a reinterpretation of the well-separating condition inherent in the asymptotic smoothness property. As illustrated in Fig. 2.23, considering two clusters,  $C^1$  and  $C^2$ , a criterion would rely on the size of the clusters, and the distances between those. It yields the definition of the so-called *condition of admissibility* [Bebendorf, 2008].

#### Definition: Condition of admissibility

Two clusters of element  $C^1$  and  $C^2$ , separated by a distance  $dist(C^1, C^2)$ , and of specific dimensions  $diam(C^1)$ ,  $diam(C^2)$  respectively, are considered admissible for reduction, when the following condition is fulfilled :

$$\max(diam(C^1), diam(C^2)) \leq \eta dist(C^1, C^2), \quad \eta \in \mathbb{R}^+ \quad (2.72)$$

Where  $\eta$  is the coefficient controlling the admissibility.

From a theoretical point of view, based on the asymptotic smoothness property, the value of  $\eta$  is bounded by the constant  $c_2$  found in Eq. (2.67). Thus for kernel function defines with Green function,  $\eta \leq 1$ , which appears very restrictive. In practice, higher values would return similar results, leading to better rate of compression as experimented by [Grasedyck, 2005].

An example of mesh is presented Fig. 2.31, for two definition of the distance  $dist(C^1, C^2)$ ,  $diam(C^1)$ , and the cluster size of  $diam(C^2)$ . The example is made up of a mesh of a rather elliptical surface,  $\Omega$ , and two arbitrary clusters,  $C^1$  and  $C^2$ .

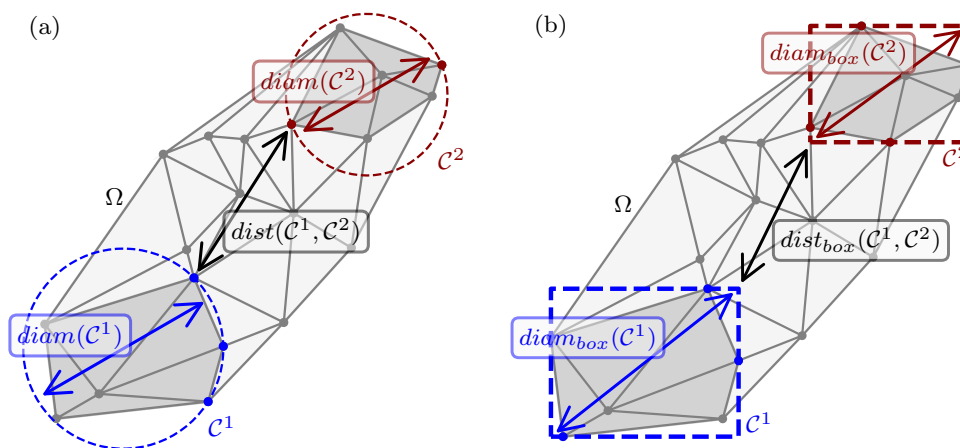


Figure 2.31: Example of admissibility condition with circles definition (a), and boxes (b)

Hence, Fig. 2.31 presents two potential definitions of the admissibility condition, distinguishing by both their separative distances and their cluster dimensions. In sub-figure (a) the  $diam(C^1, C^2)$  is computed as a circle circumscribed around the domain. However, this definition represents an intensive problem for computation. The travel along all the configurations results in a complexity order of  $N(N-1)(N-2)/6$  for  $N$  nodes. Moreover, it demands the verification of distances between every pair of mesh contour nodes, spanning from one cluster to another. In contrast, the box metrics shown in sub-figure (b) offers a streamlined interpretation of these parameters, making them more computationally affordable. The diameter is defined through a circumscribed box, which entails calculating the difference between maximum and minimum coordinates in each direction. Once these coordinates are determined, the separation distance can be directly inferred. These two parameters can be expressed as follows.

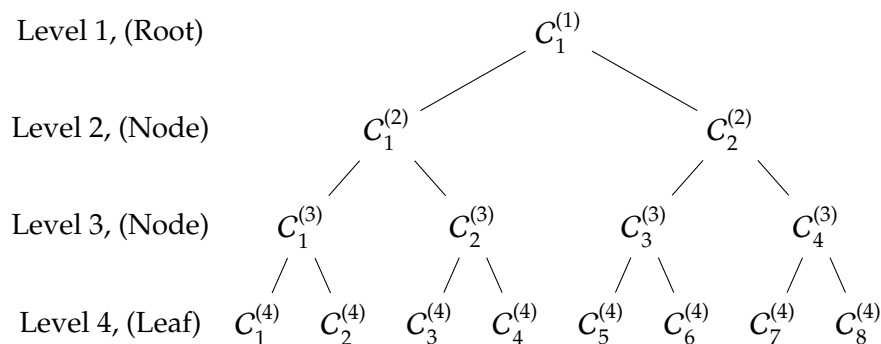
$$diam_{box}(C^l) = \sum_{i=1}^2 \left( \min(x_i^l) \max(x_i^l) \right)^2 \quad (2.73a)$$

$$dist_{box}(C^l, C^m)^2 = \sum_{i=1}^2 \left\{ \left( \max(0, \max(x_i^l) - \min(x_i^m)) \right)^2 + \left( \max(0, \max(x_i^m) - \min(x_i^l)) \right)^2 \right\} \quad (2.73b)$$

The *admissibility condition* can effectively incorporate these parameters since the condition based on the box definition is more stringent. This difference could be adjusted with the parameter  $\eta$  as well. The boxes' separation distance is smaller, while their diagonals are longer than the real cluster radii. Consequently, the two sides of the admissibility condition expression are brought closer together, rendering it more challenging to satisfy. Furthermore, establishing the minimum and maximum values within an array of length  $N$  follows a linear complexity of  $O(N)$ . This results in a less computationally expensive process while maintaining the integrity of the *admissibility condition*.

### Cluster definition

The definition of clusters is dedicated to the optimization of time integration and memory requirements. The ideal cluster is one that can accommodate the largest admissible clusters, and in meantime can conduct to the lowest rank in low-rank approximation. However, if these clusters do not meet the condition of admissibility, we may subdivide them, potentially reducing their size and dimension in an attempt to satisfy the admissibility condition. This is at the core of the definition of *hierarchical* procedure. This hierarchical approach enables the creation of a consistent structure for the admissibility condition and, consequently, for the approximation. This cluster definition inherits from the hierarchical structure, which is represented by an  $\mathcal{H}$ -tree. This tree serves as a summary of how clusters are interconnected and defines the inheritance relationships among them. An example of an  $\mathcal{H}$ -tree is presented below, in which clusters are denoted as  $C_i^{(l)}$ , with the index  $i$ , at the hierarchical level  $l$ .



In this instance, all clusters stem from a single root cluster, denoted as  $C_1^{(1)}$ . Progressing to the next level, the root divides into two branches, each resulting in one node. This identical process iterates until we reach the final level, where these nodes are also referred to as **leaves**. At all levels, there exist  $2^{l-1}$  nodes, with  $i \in \llbracket 1, 2^{l-1} \rrbracket$ . The maximum level in the  $\mathcal{H}$ -tree, denoted as  $l_m$ , is referred to the tree **depth**, entailing  $l \leq l_m$ .

We will assume an identical practice of splitting each node into two. Notably, the number of elements in the cluster defined at a same level may vary. If the stopping condition is defined in terms of a minimal number of elements at the bottom, this could result to an unbalanced tree, characterized by uneven depths along different paths. In fact the stopping condition could appear later, along a branch encompassing cluster with larger number of element. To avoid this problem, and enhance the navigability in the  $\mathcal{H}$ -tree, we decided to define the stopping condition rather in term of a maximal depth.

#### Method: Stopping condition

The stopping condition relies on a maximal depth  $l_m$ . When this depth is reached, the splitting process will stop. Notably, for all nodes  $C_i^{(l)}$ , with  $l + 1 \leq l_m$ , consistently gives rise to two clusters,  $C_{2i-1}^{(l+1)}$  and  $C_{2i}^{(l+1)}$ , at the subsequent level. The indexing remains standardized as long as the same depth is maintained across all paths within the  $\mathcal{H}$ -tree.

Ultimately, various methods can be employed to define clusters. Some are specifically tailored for hierarchical splitting, such as the *median* and *geometric* separation methods, while others can be applied globally, like the *K-means* method. Although similar, they may yield different leaf characteristics in terms of size and the number of elements.

**Direction of separation** The underlying idea of the cluster definition is related to the panel clustering [Hackbusch and Nowak, 1989]. Two splitting procedures are commonly presented, namely *median* and *geometric* [Grasedyck and Hackbusch, 2003]. They consist in splitting a set of mesh element in two sets, along a specific direction. They both rely on the definition of extremum coordinate along each direction in the cluster  $C_i^{(l)}$ , which subsequently informs the determination of the length  $d_i$  in a given direction  $i$ .

#### Method: Direction of separation

For a given cluster of elements  $C_i^{(l)}$ , different distance  $d$  along each dimensional direction, which is equal to the maximal difference between coordinates, as :

$$d_j = \max(x_j) - \min(x_j), \text{ with } x \in C_i^{(l)} \quad (2.74)$$

The direction chosen for the cluster separation, denoted as  $i_s$ , might inherently derive from this set of distance. The direction of separation is chosen as direction related to the maximal distance, :

$$i_s = \underset{i}{\operatorname{argmax}}(d_i) \quad (2.75)$$

This selection aims to achieve the most significant reduction in size.

The length definition is presented in Fig. 2.32, for an imaginary cluster  $C_i^{(l)}$ . This example is depicted in two-dimensional case, although readily extendable to three-dimensional case. With  $d_1 > d_2$ , the direction of separation is  $i_s = 1$ .

Nevertheless, it is noteworthy that the orientation of the geometry within an absolute coordinate framework influences the measurement of the distances, and the choice of axis for splitting in turn. The identical mesh geometry, but inclined at an angle of  $\pi/4$  is presented in Fig. 2.33. Consequently the direction of separation is changing, the splitting

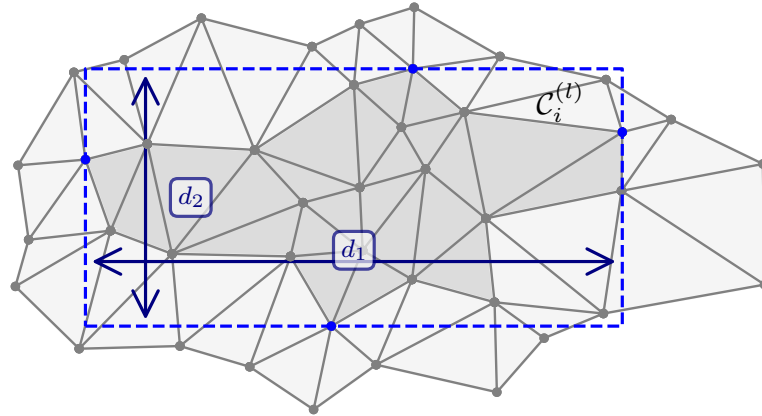


Figure 2.32: Example of distance lengths computation for a cluster of element

will not be the same. Potentially one might use instead a direction of separation aligning with the maximum node-to-node axis. However it leads to a higher complexity and thus to higher computational efforts.

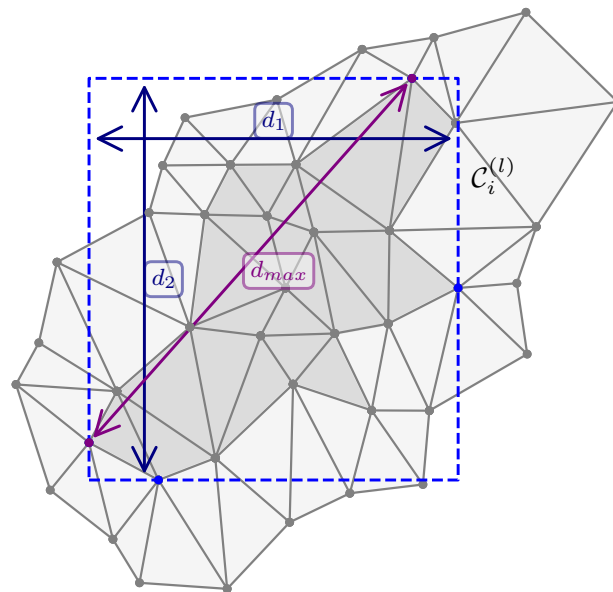


Figure 2.33: Definitions of box dimension and maximal distance of mesh with a modified orientation

**Median separation** After establishing the axis of separation, the elements can be partitioned along the  $i_s$  axis. The *median separation* relies on the definition of the median position based on the amount of mesh elements. This arises to the definition of cluster with identical number of element, or at most, a difference of one element if the original quantity of elements is an odd number. The categorization of the elements is based on the centroid location along the  $i_s$  axis, denoted by  $\bar{x}_{i_s}$ . The threshold for dividing the two clusters is determined by the median of these coordinates. This is articulated below and represented by  $x_{med}$ .

$$x_{med} = \text{median}(\bar{x}_{i_s}), \text{ with } x \in \Omega \quad (2.76)$$

This criterion prevails the consistency in terms of number of elements, among the different cluster at a certain level along the  $\mathcal{H}$ -tree. However, their geometric sizes might be different, exacerbated for mesh with local refinement.

---

**Algorithm 3:** Algorithm for median separation
 

---

```

1 Function MedianSplit (C):
2    $i_s \leftarrow \text{Is} (C)$ 
3    $C^1, C^2 \leftarrow \text{XMedian} (C, i_s)$ 
4   return  $C^1, C^2$ 

```

---

An example of the median separation is presented in Fig. 2.34. In these examples, the median separation helps to divide the initial cluster  $C_i^{(l)}$  into two clusters  $C_{2i-1}^{(l+1)}$  and  $C_{2i}^{(l+1)}$ . The contrast in these two mesh clustering highlights the possible impact of orientation and the resulting non-uniqueness of such a separation.

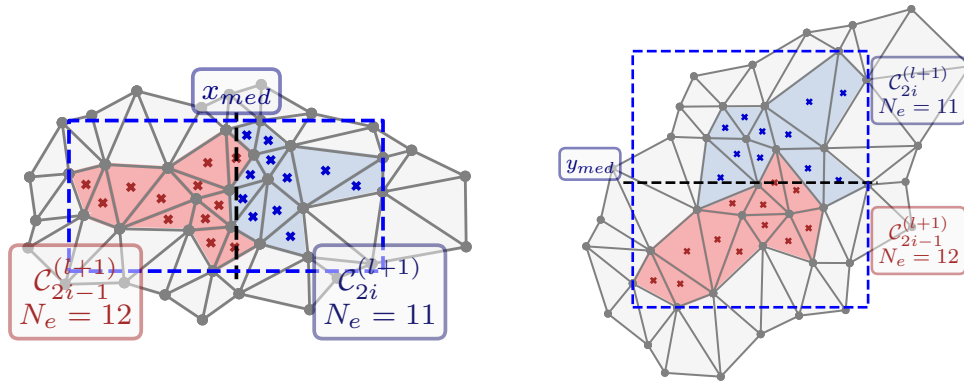


Figure 2.34: Examples of median separation for the same mesh differently oriented

**Geometric separation** Conversely, the *geometric separation* emerges as a criterion more rooted in geometry. It also establishes a boundary for dividing two clusters along the principal axis  $i_s$ . The geometric boundary, denoted by  $x_{geo}$ , is the midpoint of the encompassing box, which is defined as follows.

$$x_{geo} = \frac{1}{2} (\max(x_{i_s}) + \min(x_{i_s})), \text{ with } x \in \Omega \quad (2.77)$$

An application of this geometrical separation is presented in Fig. 2.35 taking back the same mesh geometry already studied for the median separation.

As announced, this criteria yields clusters that are not equal in number of element, but are more uniform in size. The two clusters created get 10 and 13 elements, respectively, each differing by 1 element from the clusters formed by the median separation. Once more, the definition of the clusters is contingent on the absolute position of the elements, thereby varying with the mesh's orientation.

**Possible enhancements** The two aforementioned criteria provide a straightforward and cost-effective method for cluster definition. Yet, it has been observed that these criteria are dependent on the coordinate system. Adopting the maximal distance as the separation direction, defined as  $d_{max}$  in Fig. 2.33, avoids any bias, and provides an absolute direction

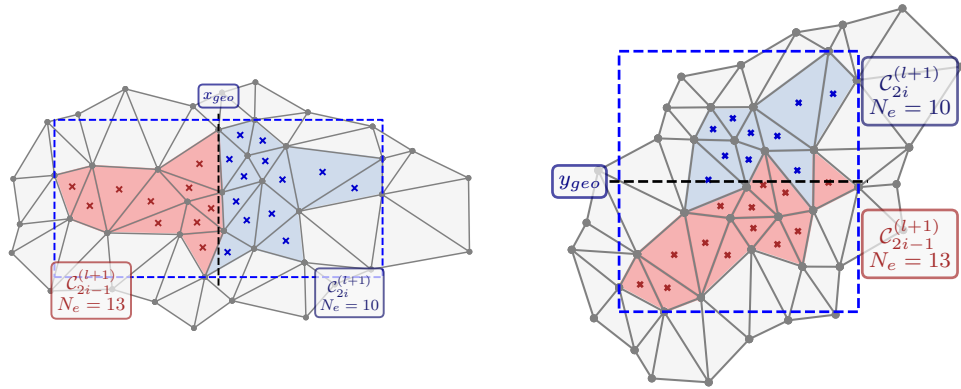


Figure 2.35: Examples of geometric separation for the same mesh differently oriented

for the cluster separation. Its application is presented in Fig. 2.36, using then the median separation criteria to target equal amount of mesh elements.

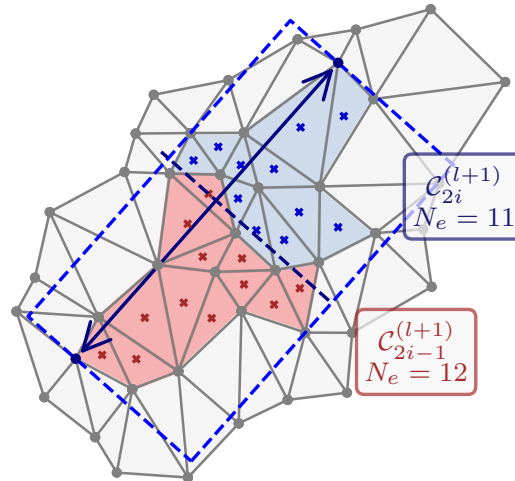


Figure 2.36: Example of median separation along the largest distance axis

Instead of specifying this maximal direction, the clusters might be defined employing *K-Means* algorithm as introduced by [MacQueen, 1967]. This method allows to make comparison with non-hierarchical cluster definitions. Clustering could be applied on the entire mesh boundary, instead of dividing it by increment and potentially accumulating bias. Subsequently, the  $\mathcal{H}$ -tree could be restructured by uniting the closest clusters in pairs, thereby elevating the hierarchy level. The clusters thus established are independent of orientation and preserve geometric consistency.

**Algorithm** The construction of the  $\mathcal{H}$ -tree, is encompassed with the construction of the list-object like  $C_H$ , as presented in Algorithm 4. This object  $C_H$  is implemented on fly by the function `Hcluster`, defined by recursive procedure. The inner variable  $l$  defines the current level in the  $\mathcal{H}$ -tree, of the input cluster  $C$ . When level reaches the depth  $l_m$ , the recursive procedure stops. Conversely, for  $l < l_m$ , the cluster  $C$  is separated in two, employing the function `Split`. The procedure continues to the next level, with  $C^1$ , and  $C^2$ , those are the two clusters returned. The separation is linked to the definition of the function `Split`.



**Algorithm 4:** Algorithm for  $\mathcal{H}$ -cluster

---

```

1  $C_{\mathcal{H}} = [[] \text{ for } i \text{ in range}(l_m)]$ 
2 Function Hcluster ( $C, C_{\mathcal{H}}, l$ ):
3    $C_{\mathcal{H}}[l].\text{append}(C)$ 
4   if  $l == l_m$  then
5     return  $C_{\mathcal{H}}$ 
6    $C^1, C^2 \leftarrow \text{Split}(C)$ 
7    $C_{\mathcal{H}} \leftarrow \text{Hcluster}(C^1, C_{\mathcal{H}}, l + 1)$ 
8    $C_{\mathcal{H}} \leftarrow \text{Hcluster}(C^2, C_{\mathcal{H}}, l + 1)$ 
9   return  $C_{\mathcal{H}}$ 

```

---

**Results on a mesh of a circular spot** Illustrations of  $\mathcal{H}$ -clustering are presented in Figs. 2.37, 2.38, 2.39, and 2.40, showcasing a circular mesh comprising  $N_e = 2984$  elements. This mesh is refined on its edge. The resulting clusters obtained from different tree depths  $l_m = \{4, 5, 6\}$ .

Utilizing the median method, the clusters at the maximal depth vary in size but maintain an equal number of elements. In contrast, the geometric approach tends to create a uniform grid across the mesh. It is evident that the central clusters comprise fewer elements compared to those at the periphery. The clusters in Fig. 2.39 appear broader at the center, resembling a pie being sliced into segments. The likelihood of fulfilling the admissibility condition for the cluster at the middle might be lower. Nevertheless, the clusters on the edge are more isolated and smaller in size, more likely to fulfill the condition of admissibility. Lastly, with the K-means clustering, the clusters appear tighter and more rounded. This clustering method seems to strike a balance between geometric and median divisions. Nevertheless, it does not seem to align well with the criteria for admissibility.

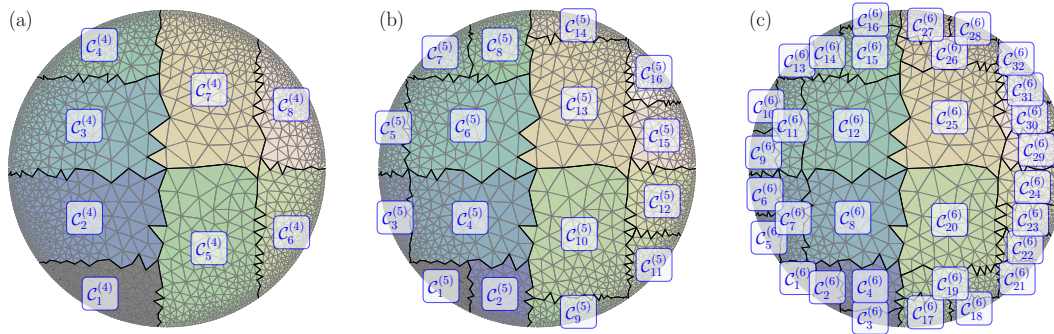


Figure 2.37: Clustering for a mesh of circular spot of  $N_e = 2984$  elements for median separation with (a)  $l_m = 4$ , (b)  $l_m = 5$ , (c)  $l_m = 6$

To assess the efficacy of the clustering methods, Fig. 2.41 reveals certain characteristics for two meshes with circular contact spots. One mesh is made of  $N_e = 804$  elements, marked by circles, and the other has  $N_e = 2894$  elements, denoted by crosses, the one which was used for cluster maps in Fig. 2.37, 2.38, 2.39, and 2.40. The Fig. 2.41(a) illustrates the largest different in the number of elements between two clusters, whereas Fig. 2.41(b) represents the greatest difference in cluster size. The cluster size  $D_{\min}$  and  $D_{\max}$  corresponds respectively to the minimal and the maximal dimension of the circumscribed box among all the clusters. Clustering that employs the median split retains the attribute of uniformity in the number of elements per cluster. The ratio  $N_{\max}/N_{\min}$  consistently equals to 1. In contrast, this ratio increases with the depth  $l_m$  for both the geometric and K-means clustering, reaching approximately 18 and 15, respectively. Regarding the variation in

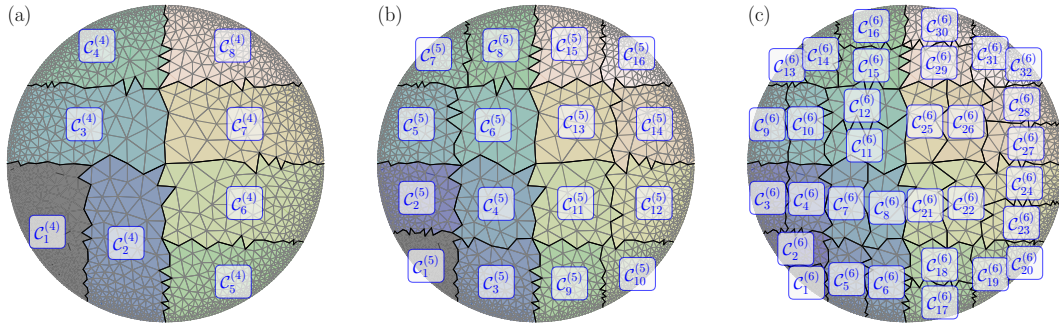


Figure 2.38: Clustering for a mesh of circular spot of  $N_e = 2984$  elements for geometric separation with (a)  $l_m = 4$ , (b)  $l_m = 5$ , (c)  $l_m = 6$

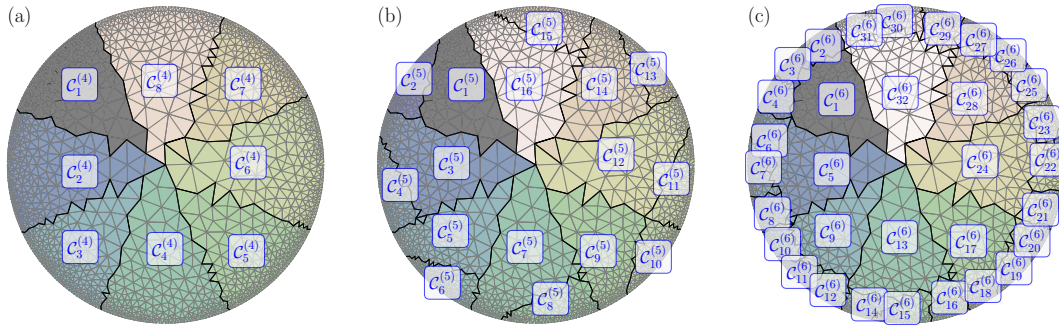


Figure 2.39: Clustering for a mesh of circular spot of  $N_e = 2984$  elements for maximal direction separation with (a)  $l_m = 4$ , (b)  $l_m = 5$ , (c)  $l_m = 6$

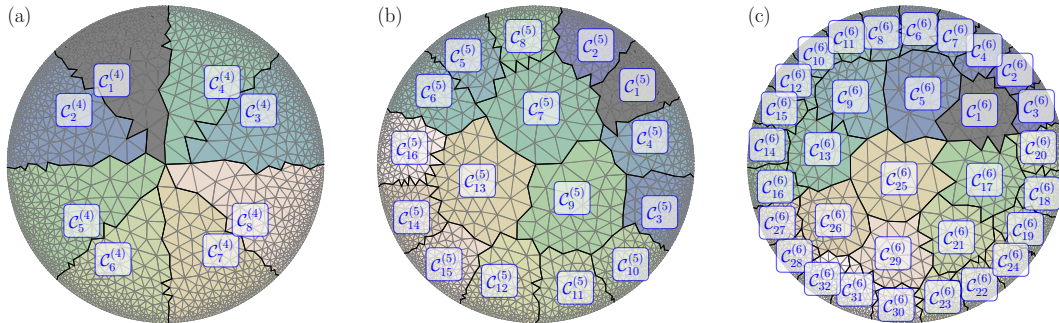


Figure 2.40: Clustering for a mesh of circular spot of  $N_e = 2984$  elements for K-means clustering with (a)  $l_m = 4$ , (b)  $l_m = 5$ , (c)  $l_m = 6$

cluster size, the geometric split is comparatively more stable than the other methods. Nonetheless, this trait might be less important within the context of approximation, than the criteria in number of elements. Indeed, it is more crucial to maintain uniform cluster sizes, aiming to get  $\text{rank}(\tilde{M}) \ll \min(m, n)$ , with  $\tilde{M}$  a sub-block approximation.

### 2.3.4 Application of the approximations

#### Hierarchical admissibility

For an optimal approximation, the integration process is hierarchically structured as well. When the clusters meet the condition of admissibility, the corresponding sub-block might be approximated; if not, the process continues, incrementing the level to assess the admissibility of the branch's cluster pairs. This approach appeals to recursive algorithm,

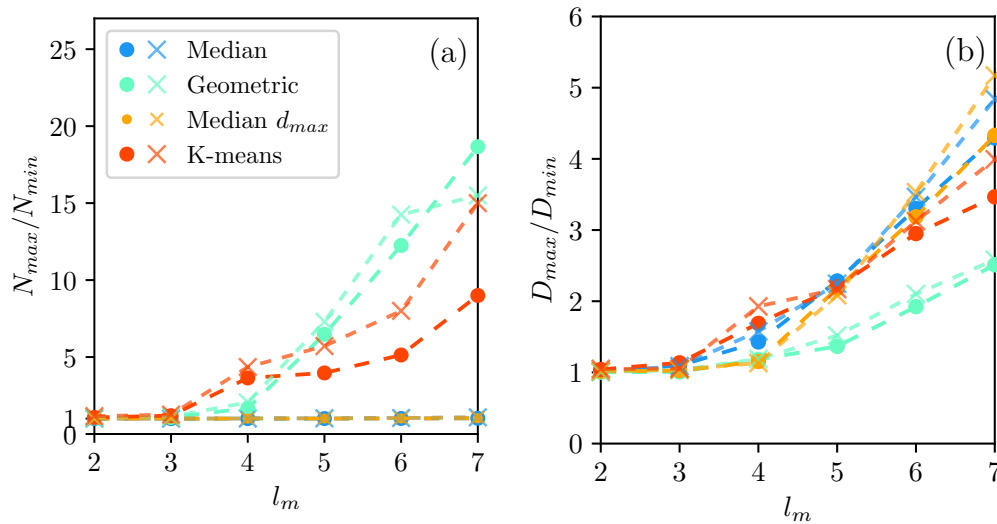


Figure 2.41: Performances of the clustering in function of the cluster depth

which relies on the assessment of cluster admissibility. At the final stage, when the algorithm has deepened to the depth  $l_m$ , the algorithm will simply reassess the condition of admissibility between leaf nodes. A cluster in relation to itself will invariably be inadmissible, similar to a cluster adjacent to another. For the non-admissible leaves, the corresponding sub-blocks are completely computed, i.e. no low rank approximation is used.

The methodology for constructing the  $\mathcal{H}$  admissibility matrix is outlined in Algorithm.5. It is presupposed that cluster construction has been completed in advance and the details are retained in memory. The H-Admi function thus references these clusters when invoked with  $C$ . The H-Admi function considers only the indices of the two clusters under scrutiny,  $i$  and  $j$ , along with the level  $l$ , and the global parameter  $\eta$  which governs the admissibility condition. The indices  $i$ ,  $j$ , and  $l$  are utilized to retrieve the clusters  $C_i^{(l)}$  and  $C_j^{(l)}$ . The  $\eta$  parameter is identical to the one in the Adm function, as delineated in Algorithm.5. This function verifies the admissibility condition and returns True when clusters are admissible, or False if they are not. The functions  $d$  and  $size$ , compute the separative distance between clusters and their sizes, respectively. These functions rely on the definition of the bounding boxes, as presented on the right side of Fig. 2.31.

The condition of admissibility is always assessed for cluster of an identical level  $l$ . At the final level  $l = l_m$ , the clusters are leaves; otherwise it is possible to get their nodes the couples  $(C_{2i-1}^{(l+1)}, C_{2i}^{(l+1)})$ , and  $(C_{2j-1}^{(l+1)}, C_{2j}^{(l+1)})$ , for  $(C_i^{(l)}, C_j^{(l)})$  respectively. This constitutes 4 of recursive calls to the next level. All recursive calls returns  $\mathcal{H}$ -matrix, or boolean variable referring to the result of the condition of admissibility. Their structures are thus built recursively.

**Example** Two examples of the condition of admissibility are presented in Fig. 2.42 giving insights into the assessment of this condition and the influence of  $\eta$ . Non-admissible clusters are shaded in white, while admissible ones are marked in green. The red cluster signifies the cluster currently under consideration. This example is using the mesh of a circular contact spot made of  $N_e = 2984$  elements, established through median separation at a tree depth of  $l_m = 6$ . These maps are generated by validating the admissibility of all clusters at each hierarchical level, commencing with the cluster indexed first. Should the admissibility condition be satisfied between this initial cluster and another at a given level, the cluster's geometry is recorded and colored green; if not, investigation proceeds to the subsequent level.

**Algorithm 5:** Implementation of the  $\mathcal{H}$ -admissibility

---

**Data:**  $\eta, l_m, C, \text{Global}$

```

1 Function Admi ( $l, i, j$ ):
2   if  $\max(\text{size}(C_i^{(l)}), \text{size}(C_j^{(l)})) \leq \eta d(C_i^{(l)}, C_j^{(l)})$  then
3     return True
4   end
5   return False
6 Function H-Admi ( $l, i, j$ ):
7   if  $l == l_m$  then
8     return True
9   end
10   $H_{11} \leftarrow \text{H-Admi}(l + 1, 2i - 1, 2j - 1)$ 
11   $H_{12} \leftarrow \text{H-Admi}(l + 1, 2i - 1, 2j)$ 
12   $H_{21} \leftarrow \text{H-Admi}(l + 1, 2i, 2j - 1)$ 
13   $H_{22} \leftarrow \text{H-Admi}(l + 1, 2i, 2j)$ 
14  return  $[[H_{11}, H_{12}], [H_{21}, H_{22}]]$ 

```

---

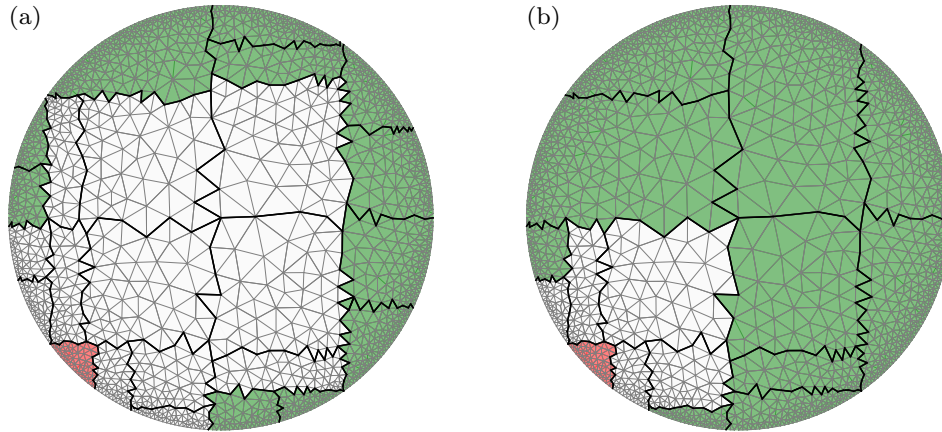


Figure 2.42: Examples of map of admissible (green) and non-admissible (blank) with respect to the red cluster  $\eta = 1$  (a) and  $\eta = 3$  (b)

**$\mathcal{H}$ -matrix of admissibility** Examples of  $\mathcal{H}$ -matrix of admissibility are represented in Fig. 2.43, using the mesh geometry in Fig. 2.42. Two different values of  $\eta = 1$ , and 3 were used. These matrices exhibit symmetry due to the symmetric nature of the admissibility condition. Empty sub-blocks denote non-admissible clusters, in contrast to the green sub-blocks, which signify admissibility. Non-admissible blocks invariably occur between two leaf clusters. Diagonal sub-blocks are tinted red when a set of source points lies within a set of integration elements. For all these diagonal coefficients, the integral is inherently singular. The physical is presumed constant for the sake of simplicity.

As indicated by the maps in Fig. 2.42, the count of non-admissible clusters depends on the  $\eta$  parameter. When  $\eta$  decreases, the condition of admissibility is more stringent, necessitating a careful selection of this parameter to align with the anticipated numerical efficacy. The matrices presented in Fig. 2.43 provide an alternative visualization of the interactions among clusters, akin to the maps in Fig. 2.42, and are designated as  *$\mathcal{H}$ -Admissible Matrix*. The maps presented in Fig. 2.42 can be inferred from the first row or column of these matrices. The green sub-matrices correspond to *BEM*-sub-matrices between clusters deemed admissible. As illustrated in Fig. 2.42 the condition of admissibility can be established prior to reaching the leaf level, which results in larger sub-blocks.

This results in the construction of larger sub-blocks than those of the last step. Thus all the sub-blocks have not the same dimension referring to different level in the  $\mathcal{H}$ -tree. In the opposite white sub-blocks illustrate non-admissible cluster, while the red sub-blocks along the diagonal depict self-interacting cluster segments, always found at the maximal depth. Diagonal entries in these red matrices are associated with singular integrals when the source point resides within the element.

For the recall, the nature of condition of admissibility is rooted in the interaction kernel function. The sub-block deemed admissible relates to clusters relatively close to each other. This leads to the rearrangement in the index of element.

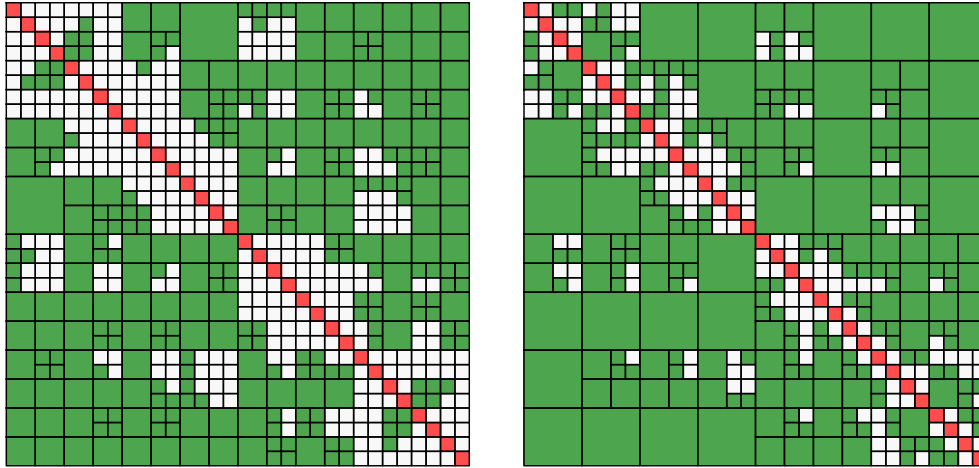


Figure 2.43: Examples of  $\mathcal{H}$ -matrix for admissible (green) and non-admissible (blank) clusters with  $\eta = 1$  (left) and  $\eta = 3$  (right)

As we can see by those two examples, the number of sub-block which are admissible decreases with the parameter  $\eta$ . This parameter also makes change the overall structure of the  $\mathcal{H}$ -Admissible matrix. Subsequently, we can define a rate of admissibility as the cumulative number of coefficients in the admissible block  $N_{Admi}$ , related to the number of coefficient in the fully populated matrix  $N_e^2$ , as follows,

$$\tau_{Admi} = \frac{N_{Admi}}{N_e^2}$$

The rate of admissibility is presented in Fig. 2.44. This rate is displayed for different values of  $\eta$ , and different depth of  $\mathcal{H}$ -tree,  $l_m$ . We consider again the two meshes of circular contact spot, with 804, and 2894 elements.

As expected, the rate of admissibility increases with the parameter  $\eta$ , and with the depth  $l_m$ , i.e, the number of approximated coefficients increases with the rate of admissibility. Nevertheless, the rate of admissibility for the two meshes seems identical. Ultimately the admissibility rate reaches a plateau at  $\eta = 3$ , for any depth  $l_m$ , and across both meshes, because we rapidly reach geometrically connected clusters for these particular examples.

### $\mathcal{H}$ -approximation

The construction of  $\mathcal{H}$ -Admi provides an approximation of the BEM matrix shaped as  $\mathcal{H}$ -matrix. The admissible sub-blocks are subject to approximation via one of the approximation methods, while the non-admissible sub-blocks undergo complete computation. A range of approximation approaches was discussed in Section 2.3.1. For the advantages in terms of reliability and time-saving, we have opted for the ACA+ technique. This section delves into the problem of hierarchical approximation and aims to assess its efficiency in terms of computer requirements.

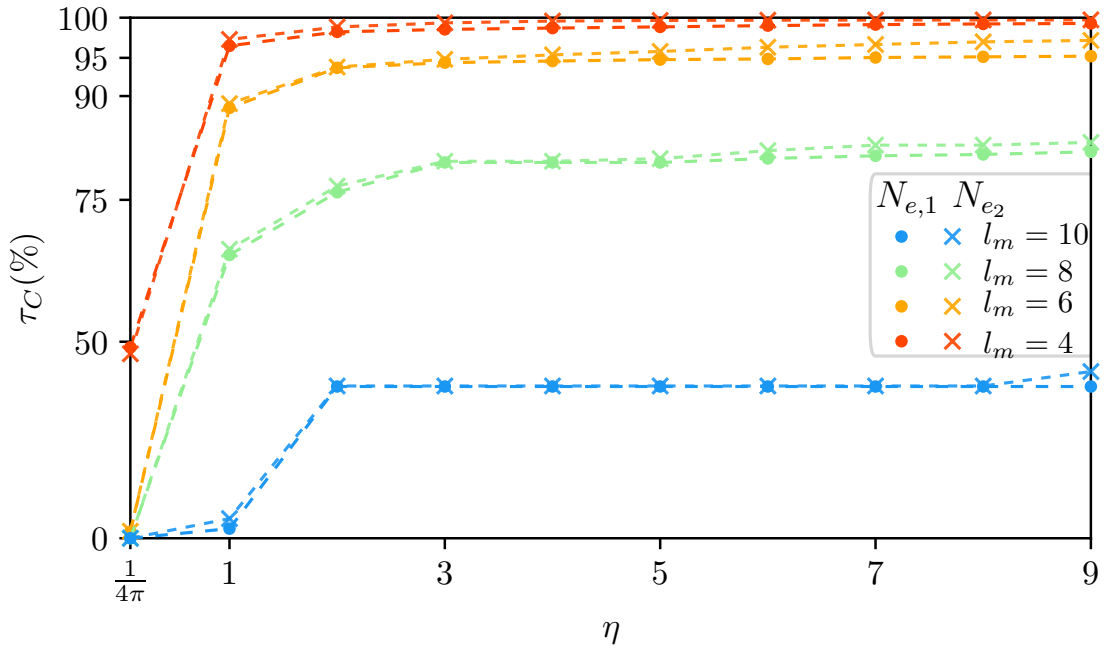


Figure 2.44: Rate of admissibility in function of  $\eta$  and  $l_m$

**Algorithm** The assembly of the approximation matrix leverages the implementation of  $\mathcal{H}$ -Admissibility, as detailed in Alg.6. This algorithm receives the  $\mathcal{H}$ -tree level  $l$ , cluster indices  $i$  and  $j$ , the parameter  $\eta$ , and the error parameter  $\epsilon$  as inputs. It does not require the preconstruction the  $\mathcal{H}$ -Admi since it enables to assess the condition of admissibility in the meantime.

The assembly of the approximation matrix can leverage the same foundations as those used for the  $\mathcal{H}$ -Admissibility, as detailed in Algorithm.6. This algorithm receives the  $\mathcal{H}$ -tree level  $l$ , cluster indices  $i$  and  $j$ , and the error threshold  $\epsilon$  as inputs. It obviates the necessity of preconstructing the  $\mathcal{H}$ -Admi since the condition of admissibility can be checked as well on fly during the integration process. During a recursive call, the level parameter is incremented by 1. The clusters inherently explored, are referred with the indices  $(2i - 1, 2i)$  for the cluster of observation point, and  $(2j - 1, 2j)$  for those of element of integration. This accounts for 4 recursive calls in total. The returned  $\mathcal{H}$ -matrices, computed by H-Appro with these recursive calls, are then combined in  $A_{\text{sup}}$ ,  $B_{\text{sup}}$ , and  $k_{\text{sup}}$ , and return.

**Rank Matrice** The approximation of the sub-block appeals to the definition of a compressibility ratio. This parameter might be defined as the ratio between the number of computed coefficients, denoted by  $N_c$  and the total coefficient number in the sub-matrix,  $n \times m$ . This compressibility ratio is defined for each sub-block.

$$\tau_C = 1 - \frac{N_C}{nm}, \quad n = |\mathcal{C}_i^{(l)}|, \quad m = |\mathcal{C}_j^{(l)}|$$

Or over the entire matrix,

$$\tau_C = 1 - \frac{N_C}{N_e^2} \quad (2.78)$$

The number of saved coefficients relates to the rank of a sub-block matrix, with  $N_c = k(m + n)$ . This compressibility ratio pertains to the memory-saving performance allowed by the approximation. The higher the compressibility ratio is, the more effective the approximation is in terms of memory. Some examples of compressibility ratio insight are presented in Fig. 2.45, still using a mesh geometry built with  $N_e = 2984$  elements, and using the parameters  $\eta = 3$  and  $l_m = 6$ .

**Algorithm 6:** Implementation of the  $\mathcal{H}$ -approximation

---

**Data:**  $\eta$ , Global

```

1 Function H-Appro ( $l, i, j, \epsilon$ ):
2   if Admi ( $l, i, j$ ) is True then
3      $A, B, k \leftarrow \text{Aca+} (C_i^{(l)}, C_j^{(l)}, \epsilon)$ 
4     return  $A, B, k$ 
5   else if  $l == l_m \cup$ , Admi ( $l, i, j$ ) is False then
6      $m, n \leftarrow |C_i^{(l)}|, |C_j^{(l)}|$ 
7      $M_{i,j}^{(l)} \leftarrow \text{BEM-integ} (C_i^{(l)}, C_j^{(l)})$ 
8     return  $M_{i,j}^{(l)}, [], \min(m, n)$ 
9    $A_{11}, B_{11}, k_{11} \leftarrow \text{H-Appro} (l + 1, 2i - 1, 2j - 1, \epsilon)$ 
10   $A_{12}, B_{12}, k_{12} \leftarrow \text{H-Appro} (l + 1, 2i - 1, 2j, \epsilon)$ 
11   $A_{21}, B_{21}, k_{21} \leftarrow \text{H-Appro} (l + 1, 2i, 2j - 1, \epsilon)$ 
12   $A_{22}, B_{22}, k_{22} \leftarrow \text{H-Appro} (l + 1, 2i, 2j, \epsilon)$ 
13   $A_{sup} \leftarrow \text{H-Sup} (A_{11}, A_{12}, A_{21}, A_{22})$ 
14   $B_{sup} \leftarrow \text{H-Sup} (B_{11}, B_{12}, B_{21}, B_{22})$ 
15   $k_{sup} \leftarrow \text{H-Sup} (k_{11}, k_{12}, k_{21}, k_{22})$ 
16  return  $A_{sup}, B_{sup}, k_{sup}$ 

```

---

The structure of these  $\mathcal{H}$ -matrices does not change with the error parameter  $\epsilon$ . It solely influences the ratio value in the admissible sub-blocks. The compressibility ratio in each sub-block decreases as the error factor  $\epsilon$  decreases. For example, for  $\epsilon = 10^{-4}$ , the compressibility ratio is about 73.5%, while for  $\epsilon = 10^{-6}$ , it decreases to  $\tau_c = 68.8\%$ . In the meantime, the compressibility ratio for the non-admissible sub-blocks is always equal to 0, not subjected to approximation.

**Error in matrix** The approximation will lead to error on coefficients. This yields the definition of a global error rate, denoted by  $\epsilon_{tot}$ , as follows,

$$\epsilon_{tot} = \frac{\|M - \tilde{M}\|_F}{\|M\|_F}$$

With  $M$  the reference matrix, and  $\tilde{M}$  its approximation using ACA+ and sub-matrix product. The reference BEM matrix was fully computed for this purpose. Some examples are presented in Fig. 2.46 giving insight of the error for all components.

The total error decreases with the increasing error factor  $\epsilon$ . It is noteworthy that the total error is lower than  $\epsilon$  prescribed in the left-hand side case, but higher for the right-hand side matrix. This comes from the fact that the measure of the error is only known a priori with the function ACA+, as detailed in algorithm.11 (in Appendix B.5.2), and that the incremental error can differ from the real one, see Fig. 2.30. Despite this fact, the relative error on each coefficient decreases in compliance with the parameter  $\epsilon$ , uniformly over the sub-blocks.

**Performance of compressibility** To assess of the performances review, related to the approximation is conducted for the resolution of circular contact spot problem made of  $N_e = 12208$  elements. The outcomes are represented in Fig. 2.47, and reported in terms of the rate of compressibility and the time of the integration, respectively on the left and the right hand side, for different error factor  $\epsilon$  and varying depth  $l_m$ . The time factor is defined as the ratio between the time for the construction of the approximation, and the time reference initially needed for the full assembly of the matrix.

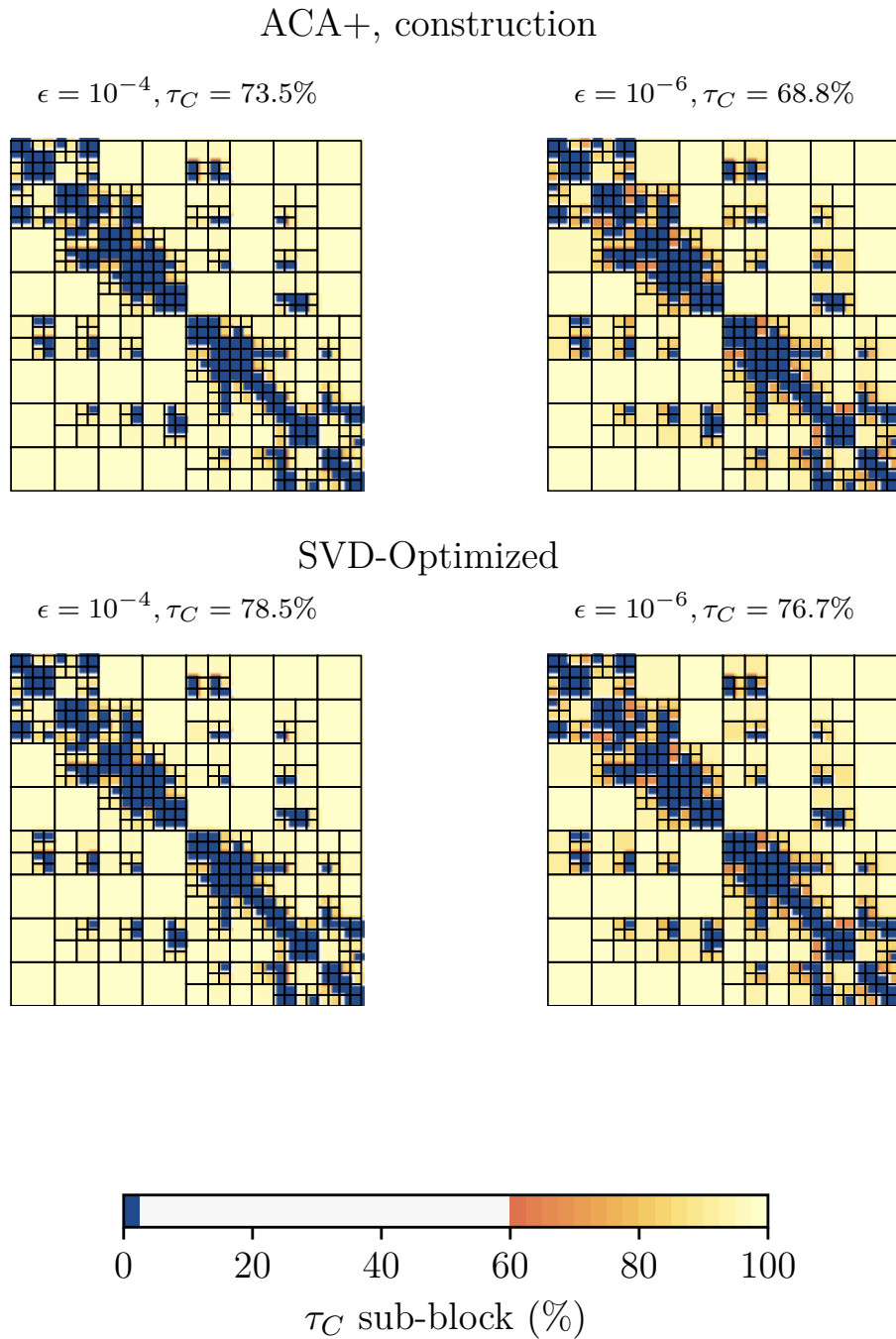


Figure 2.45:  $\mathcal{H}$ -matrices of rate of compressibility in sub-block using ACA method for a mesh of circular contact spot composed of  $N_e = 2984$  elements, using  $\eta = 3$  and  $l_m = 6$

The compressibility rate of the hierarchical approximations decreases with the error factor  $\epsilon$ , as higher accuracy requires a larger number of modes. In the opposite, the rate of compressibility is improved as the depth  $l_m$  increases. The rate of compressibility seems to converge to an upper bound when the prescribed error factor increases and also when the depth increases. Different mesh sizes have been tested, the rate of compressibility does not seem to depend on the number of element. However, as the rate of complexity is lowered in the *Fast-BEM* implementation, the *Fast-BEM* would become more advantageous as the size of the problem grows. The time parameter  $t/t_{ref}$  increases proportionally to  $\log(\epsilon)$ , as the rank  $k \sim \log(\epsilon)$ . In addition by an increasing rate of compression, the computer requirements is reduced. The *Fast-BEM* becomes advantageous in terms of time integration, when  $N_e \geq 10000$ . This limit is due to the subsequent operation that entails



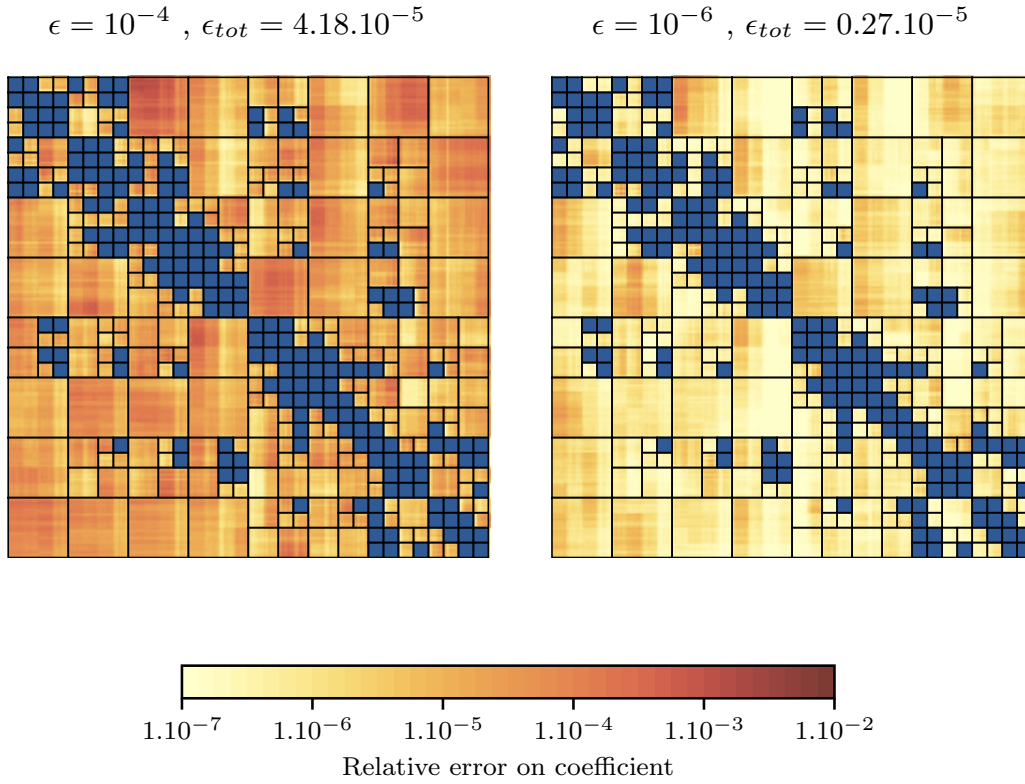


Figure 2.46: Matrix of relative error on coefficient of interaction using ACA process for a mesh of circular contact spot composed of  $N_e = 2984$  elements, using  $\eta = 3$ , with  $\epsilon = 10^{-4}$  (left), and  $\epsilon = 10^{-6}$  (right)

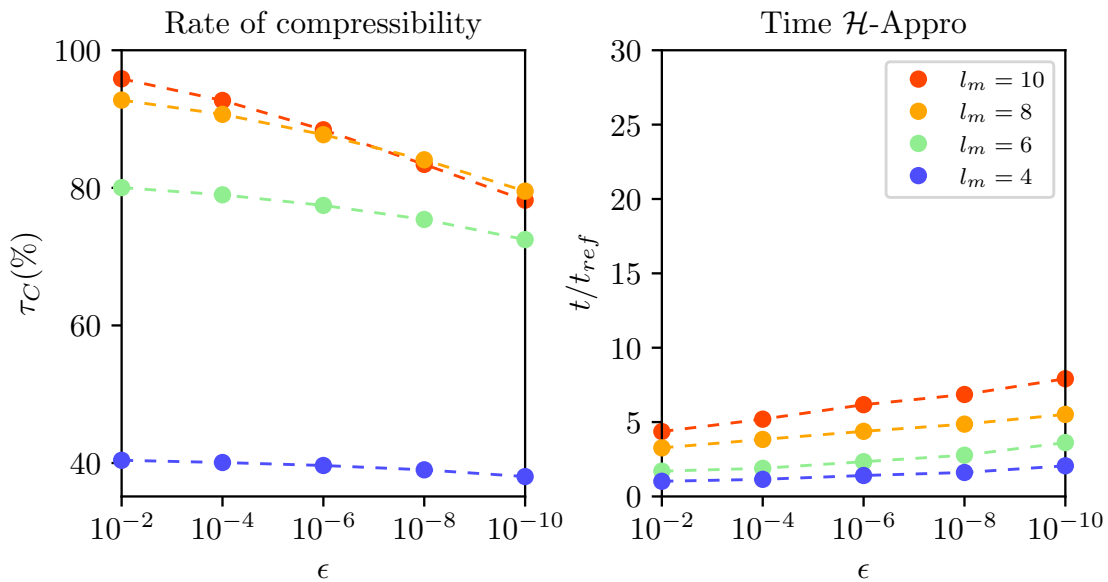


Figure 2.47: Rate of compression and time for approximation in function of  $\epsilon$  and depth level  $l_m$  for mesh of  $N_e = 12208$  elements

the use of  $\mathcal{H}$ -matrix. In summary, the  $\mathcal{H}$ -approximations enhance memory efficiency, but the improvement of the time integration might be harder to notice for small problems. The equilibrium between accuracy, memory, and computation time remains a crucial consideration when selecting the appropriate approximation method for a given problem.

**Resulting error** An additional error value might be defined, which relies on the definition on the overall flux emitted by the contact spot. This flux error, denoted as  $\epsilon_J$ , is defined as the absolute difference between the flux resulting from the entire construction of the matrix, with the flux yielding from the approximation denoted as  $\tilde{J}$ . We assume constant interpolation within the normal flux field, as given by Eq. (2.64), the total flux is given by the scalar product between the vector of normal flux solution,  $J$ , and the area of the element  $A$ . Consequently, the error  $\epsilon_J$  can be expressed in the context of this approximation, as follows:

$$\epsilon_J = \frac{\|(J - \tilde{J})A\|_F}{\|JA\|_F}$$

The error values measured on the approximated matrix, and on the flux results, are both represented Fig. 2.48, as a function of the error factor  $\epsilon$  used in ACA+. Those two errors are computed over different values of depth,  $l_m$ .

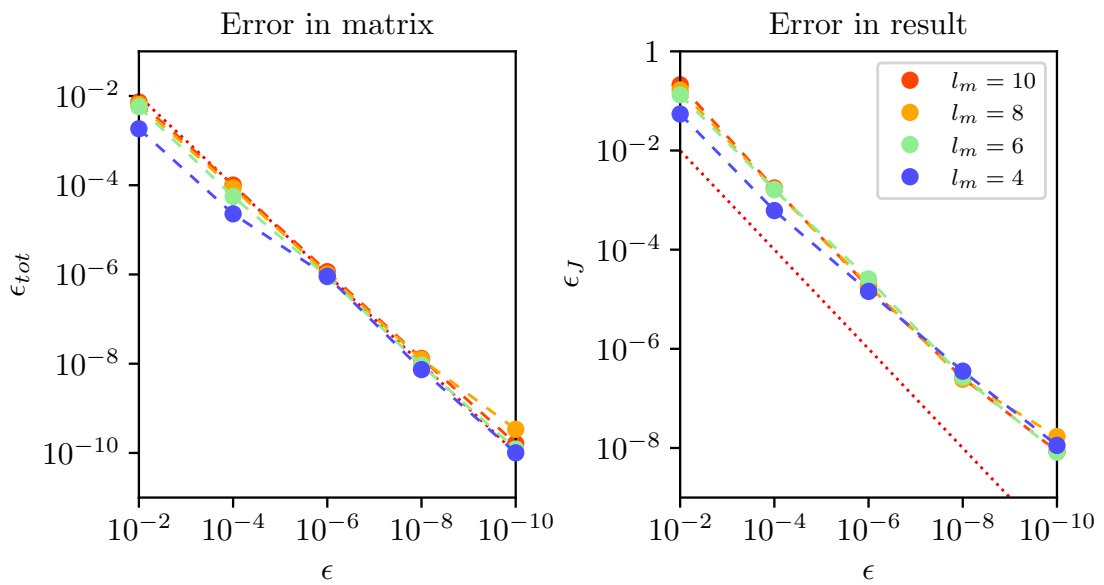


Figure 2.48: Error on the matrix components (left), and on the result of flux (right) for different error factor,  $\epsilon$  and depth  $l_m$ , for a mesh of circular contact spot composed of  $N_e = 12208$  elements

The errors are both exhibiting the same tendency with respect to the error factor  $\epsilon$ . This error factor appears to be an effective measure of the desired precision for both the matrix and the flux. The error associated with the matrix approximation is found to be lower than the  $\epsilon$  parameter, but for  $\epsilon_J$ , it is higher to this latter, up to in a magnitude of one order. Nevertheless its decrease is consistent with the behavior of the error parameter, affecting both the matrix and flux results.

### Optimization

As remarked in Section 2.3.1, the low-rank approximation does not provide the optimal number of modes. However, this could be enhanced by employing in addition a Singular Value Decomposition (SVD), which would enable a reduction in the number of modes required. Additionally, the approximation and the construction of the  $\mathcal{H}$ -matrix are dependent on the form mandated by the admissibility condition. But its form could be enhanced as well. Such modifications could lead to potential optimization in line with the initial error parameter  $\epsilon$ . An example of this approach is detailed in Algorithm 7, in agreement with [Grasedyck, 2005, Bebendorf and Kunis, 2009].

**Algorithm 7:** Implementation of the  $\mathcal{H}$ -optimization

---

```

1 Function H-Opti ( $A, B, \epsilon, k, i, j, l$ ):
2   if  $B$  is empty then
3     return  $A, B, k, \text{False}$ 
4   else if  $B$  is a matrix then
5      $A', B', k' \leftarrow \text{SVD}(A \cdot B, \epsilon)$ 
6     return  $A', B', k', \text{True}$ 
7    $A'_{11}, B'_{11}, k'_{11}, \text{adm}'_{11} = \text{H-Opti}(A_{11}, B_{11}, k_{11}, 2i - 1, 2j - 1, l + 1)$ 
8    $A'_{12}, B'_{12}, k'_{12}, \text{adm}'_{12} = \text{H-Opti}(A_{12}, B_{12}, k_{12}, 2i - 1, 2j, l + 1)$ 
9    $A'_{21}, B'_{21}, k'_{21}, \text{adm}'_{21} = \text{H-Opti}(A_{21}, B_{21}, k_{21}, 2i, 2j - 1, l + 1)$ 
10   $A'_{22}, B'_{22}, k'_{22}, \text{adm}'_{22} = \text{H-Opti}(A_{22}, B_{22}, k_{22}, 2i, 2j, l + 1)$ 
11   $A'_{sup} \leftarrow \text{H-Sup}(A'_{11}, A'_{12}, A'_{21}, A'_{22})$ 
12   $B'_{sup} \leftarrow \text{H-Sup}(B'_{11}, B'_{12}, B'_{21}, B'_{22})$ 
13   $k'_{sup} \leftarrow \text{H-Sup}(k'_{11}, k'_{12}, k'_{21}, k'_{22})$ 
14  if Any ( $\text{adm}'_{11}, \text{adm}'_{12}, \text{adm}'_{21}, \text{adm}'_{22}$ ) is False then
15    return  $A'_{sup}, B'_{sup}, k'_{sup}, \text{False}$ 
16   $M'_{sup} \leftarrow \text{H-Sup}(A'_{11} \cdot B'_{11}, A'_{12} \cdot B'_{12}, A'_{21} \cdot B'_{21}, A'_{22} \cdot B'_{22})$ 
17   $A''_{sup}, B''_{sup}, k''_{sup} \leftarrow \text{SVD}(M'_{sup}, \epsilon)$ 
18  else if  $k''_{sup} < \min(k'_{11} + k'_{12}, k'_{21} + k'_{22})$  then
19    return  $A''_{sup}, B''_{sup}, k''_{sup}, \text{True}$ 
20  return  $A'_{sup}, B'_{sup}, k'_{sup}, \text{False}$ 

```

---

**Algorithm** This optimization aims to modify the structure of  $\mathcal{H}$ -matrices  $A, B$ , and the variable  $k$ . The algorithm solely accounts for the results of the already known  $\mathcal{H}$ -matrices  $A, B$ . It takes into account the indices  $i, j$ , and the level  $l$ . It outputs optimized versions of  $A, B$ , and  $k$ , and a fourth boolean variable,  $adm$ , which indicates the admissibility of the sub-blocks.

Similarly to the previous algorithm, it features four recursive calls. If all branches are deemed admissible, it attempts to synthesize the entire sub-block. If not, the existing structure is preserved. As previously mentioned, Singular Value Decomposition (SVD) is employed to decrease the rank of a sub-block within an admissible matrix, discarding modes with an eigenvalue exceeding  $\epsilon$ . Additionally, SVD may be applied to a collection of admissible sub-blocks to further reduce the rank of the assembled sub-matrix.

**Result of compressibility and error** Examples of  $\mathcal{H}$ -matrices optimized are displayed in Fig. 2.45. The rate of compressibility initially of 73.5% for  $\epsilon = 10^{-4}$ , and of 68.8% for  $\epsilon = 10^{-6}$  are increased to 78.5% and 76.7%, respectively. The compressibility increases, and the structure is improved, resulting in the assembly of admissible sub-blocks.

The error outcomes are also presented in Fig. 2.49. This study takes backs the last case study presented in Fig. 2.46. The total error could be compared to the prior ones. Initially, the approximation accounts for  $e_{tot} = 4.18 \cdot 10^{-5}$ , with  $\epsilon = 10^{-4}$  and  $e_{tot} = 2.7 \cdot 10^{-6}$ , with  $\epsilon = 10^{-6}$ , and after optimization those increase to  $5.26 \cdot 10^{-5}$  and  $2.7 \cdot 10^{-6}$ , respectively. Hopefully, the approximation does not seem to be deprecated in both case. The rate of compressibility still accounts for the entire matrix number of components, as given by Eq. (2.78).

**Performances review** Results in terms of rate of compressibility and time needed for optimization are reported Fig. 2.50, employing two meshes  $N_e = \{824, 2984\}$  of a circular contact spot, and different values of depth.

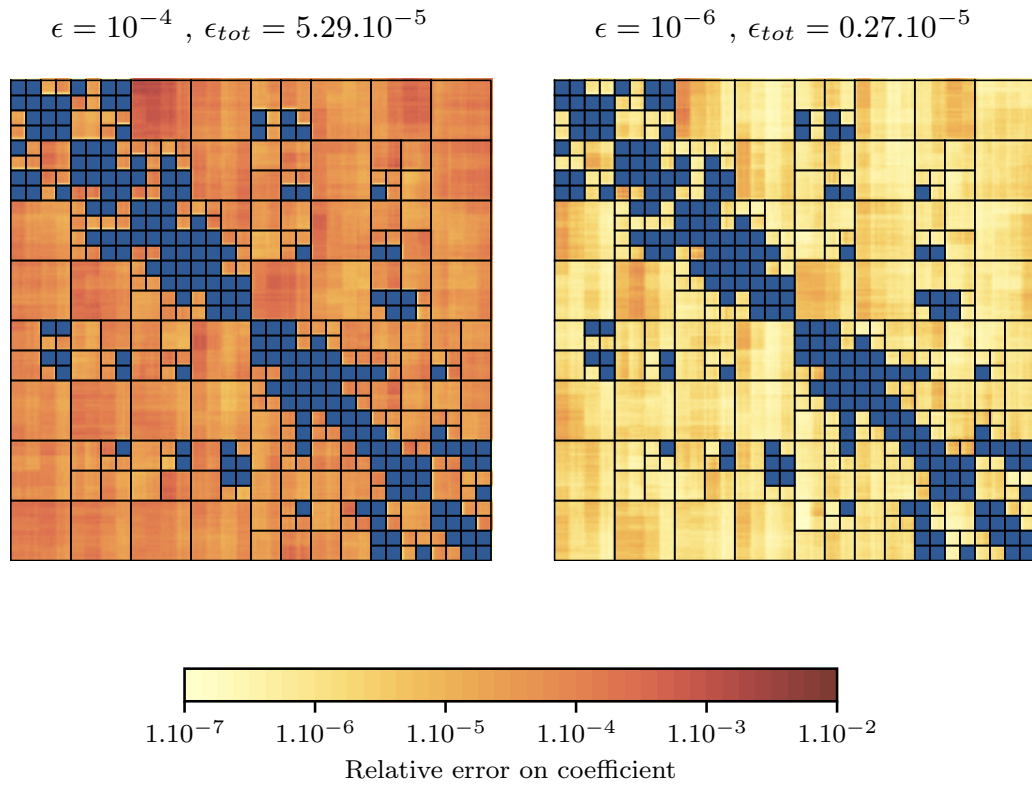


Figure 2.49: Matrix of relative error on coefficient of interaction using ACA and optimization process for a mesh of circular contact spot composed of  $N_e = 2984$  elements, using  $\eta = 3$ ,  $\epsilon = 10^{-4}$  (left), and  $\epsilon = 10^{-6}$  (right)

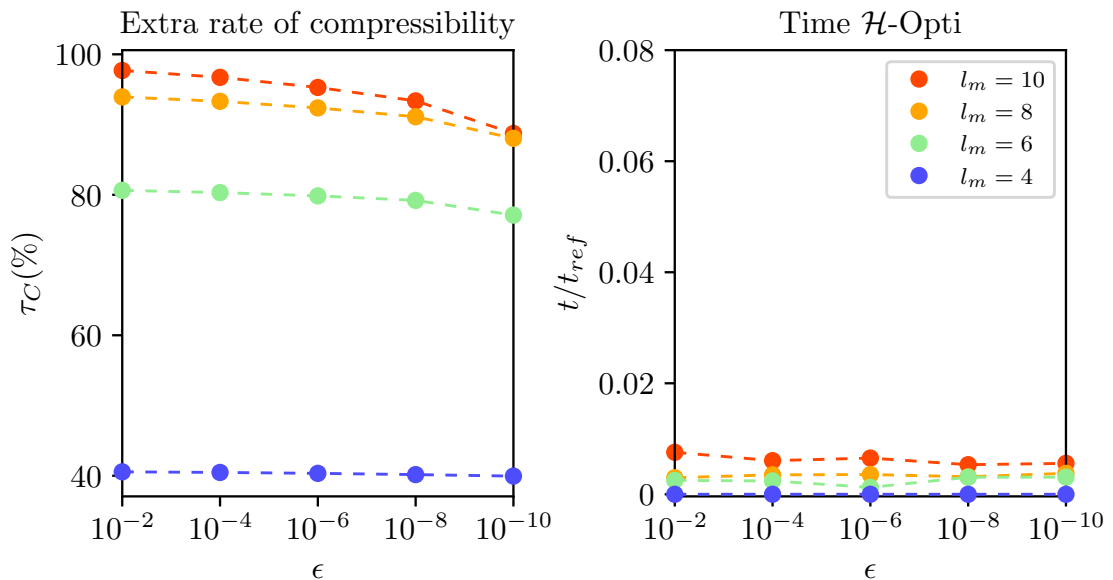


Figure 2.50: Matrix of relative error on coefficient of interaction using ACA and optimization process for a mesh of circular contact spot composed of  $N_e = 2984$  elements, using  $\eta = 3$ ,  $\epsilon = 10^{-4}$  (left), and  $\epsilon = 10^{-6}$  (right)

The optimization process using low-rank SVD appears to be computationally efficient and effective in increasing the rate of compressibility of the  $\mathcal{H}$ -matrix. By reducing the number of modes in each sub-block, the memory efficiency of the  $\mathcal{H}$ -matrix is improved, leading to higher rates of compressibility. The complexity of the SVD relates to the rank

of the approximated sub-block,  $k$ , and arises to an order of  $O(k(m+n))$ . The increase in the rate of compressibility achieved through the optimization process indicates that the low-rank SVD successfully identifies and retains the most important modes, while discarding the less significant ones. The rate of compressibility is subsequently increased up to 90.1% for the mesh of 804 elements, and up to 95.6% in the second case for 2894 elements, while initially those rates of compressibility were about 76.2% and 88.2% respectively. With the optimization process, the  $\mathcal{H}$ -matrix can achieve higher levels of compression, leading to more memory savings while maintaining a desired level of accuracy. In addition it appears really affordable, and scalable to problems with much higher size.

### 2.3.5 $\mathcal{H}$ -solver

The processes involved in constructing and integrating the BEM matrix have been thoroughly explained. The benefits of using  $\mathcal{H}$ -matrix approximation have already been demonstrated through savings in the computation of coefficients and memory. Now, we will demonstrate how solving the linear system can benefit from the  $\mathcal{H}$ -matrix definition.

This section is designed to introduce some specialized algebraic tools for  $\mathcal{H}$ -matrices, following some implementation proposed in [Bebendorf, 2008]. These tools are designed to expedite certain operations without necessitating reassembly, thereby maintaining the memory efficiency. For solving the linear system, it may be necessary to tailor operations such as addition and matrix-vector multiplication to the  $\mathcal{H}$ -matrix context. Consequently, the iterative solver is set to leverage methods specific to iterative solving.

#### $\mathcal{H}$ -matrix-vector product

Let consider  $M$  as  $\mathcal{H}$ -matrix. The vector-matrix product, with  $x$  and  $b$ , as follows,

$$b = Mx \quad (2.79)$$

A naive method would be to first reassemble  $M$ , losing the memory-saving allowed  $\mathcal{H}$ -matrix. To overcome this problem, one might implement this operation, tailored for  $M$  defined as  $\mathcal{H}$ -matrix see Algorithm 8.

---

#### Algorithm 8: Implementation of the $\mathcal{H}$ -matrix-vector-product

---

```

1 Function HVectMatProduct ( $M, x, b, i, j, l$ ):
2   if  $M$  is a matrix then
3     return  $M.x + b$ 
4    $m, n \leftarrow |C_{2i}^{(l+1)}|, |C_{2j}^{(l+1)}|$ 
5    $b_1, b_2 \leftarrow b[\leq m], b[m \geq]$ 
6    $x_1, x_2 \leftarrow x[n \geq], x[n \geq]$ 
7    $b_1 \leftarrow$  HVectMatProduct ( $M_{11}, x_1, b_1, 2i, 2j, l + 1$ )
8    $b_1 \leftarrow$  HVectMatProduct ( $M_{12}, x_2, b_1, 2i, 2j + 1, l + 1$ )
9    $b_2 \leftarrow$  HVectMatProduct ( $M_{21}, x_1, b_2, 2i + 1, 2j, l + 1$ )
10   $b_2 \leftarrow$  HVectMatProduct ( $M_{22}, x_2, b_2, 2i + 1, 2j + 1, l + 1$ )
11  return HVectCombine  $b_1, b_2$ 

```

---

**Algorithm** One possible implementation of this process is presented in Algorithm 8, which initiates the function HVectMatProduct. This function takes the indices  $i, j$ , and the level  $l$  as inputs. This implementation follows the one proposed for the  $H$ -matrix-vector product in [Bebendorf, 2008]. Initially, the vector  $b$  is established as a null vector corresponding to the size of the linear system. If the *if* condition is satisfied,  $b$  is augmented by the product  $Mx$ , where  $M$  represents a sub-block of the original  $\mathcal{H}$ -matrix.

When this condition is not met, the matrix  $M$  is further divisible into sub-blocks, prompting the unwrapping of another  $\mathcal{H}$  matrix at the subsequent level  $l + 1$ . Consequently, the branch groups of  $C_i^{(l)}$  and  $C_j^{(l)}$ , as well as the pairs  $(C_{2i}^{(l+1)}, C_{2i+1}^{(l+1)})$  and  $(C_{2j}^{(l+1)}, C_{2j+1}^{(l+1)})$ , are invoked. This results in the 4 recursive calls of the function `HVectMatProduct`. The vectors  $x$  and  $b$  are then partitioned according to the dimensions of the branch clusters. The scalars  $m$  and  $n$  stands for the dimensions of the clusters  $C_{2i}^{(l+1)}$  and  $C_{2j}^{(l+1)}$ , respectively. The vectors  $b_1$  and  $b_2$  are employed to construct and adapt the output vector on fly. They are subsequently merged using the function `HVectCombine`.

The outlined algorithm, which solely accounts for the  $\mathcal{H}$  matrix  $M$ , does not inherently diminish the count of coefficients in the product. Specifically, if  $M$  is pre-assembled yet retains the  $\mathcal{H}$  structure, it would possess an equivalent quantity of coefficients within each sub-block. Nevertheless, this approach could be expanded within the framework of low-rank approximation, with  $M$  represented by the product  $A.B$ . Instead of  $m.n$  computations, the number might be curtailed to  $k.(m + n)$ , thereby potentially enhancing the complexity akin to the compressibility rate. The process is partially illustrated in Fig. 2.51. On the example, the  $\mathcal{H}$ -matrix aligns with a cluster tree spanning three levels. The yellow blocks correspond to the second level, while the blue blocks on the diagonal are indicative of the third level. The entire matrix is denoted by the first level.

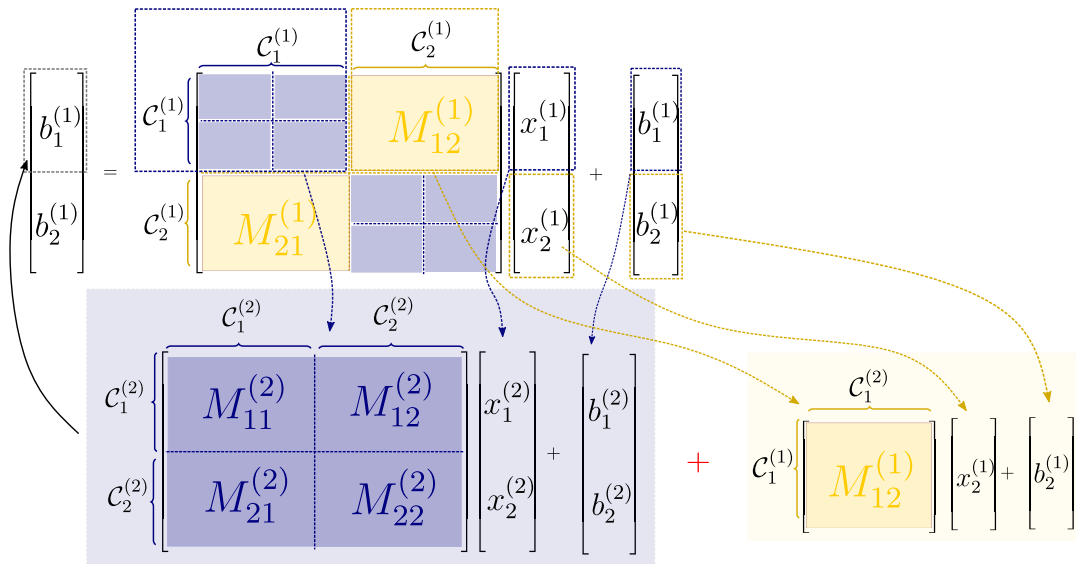


Figure 2.51: Diagram on the procedure of the  $\mathcal{H}$ -matrix-vector-product

This diagram aims to focus on the computation of first part of the output vector  $b_1$ . This involves the product on the second stage of  $M_{12}$  with the sub-block vector  $x_1$ . This product will involve 4 matrix-vector product in turns. The vectors  $x_1, x_2$ , are the two-part of the vector  $x_1$  at the second level, related to the cluster  $C_1^{(2)}$ .

### $\mathcal{H}$ -matrix-vector-product & $\mathcal{Z}$ -curve

Despite the reduction in memory for multiplication, the advantage in terms of calculation time is not obvious compared with the original procedure, referred as *full product*. Indeed, the addition of recursive call steps would introduce extra computation and preparation steps, which cancel out the advantages of performing operations on smaller sub-blocks. Nonetheless, it is anticipated that for larger scale problems, being  $N > 10^4$ , this method will show asymptotic benefits, although this is also dependent of the depth of the tree.

In efforts to streamline the access to hierarchical sub-blocks, a subsequent approaches has been developed to eliminate the recursive calls. The strategy aims to *flatten* the  $\mathcal{H}$ -matrix to enable direct access to sub-blocks via a standard container object. There are several approaches to matrix flattening; our consideration involves  $\mathcal{Z}$ -curves across the hierarchical structure and its sub-blocks, inspired from [Bebendorf, 2008]. This flattening procedure is illustrated Fig. 2.52 for three distinct  $\mathcal{H}$ -matrix structures, where the hierarchical tree depths are either 2 or 3.

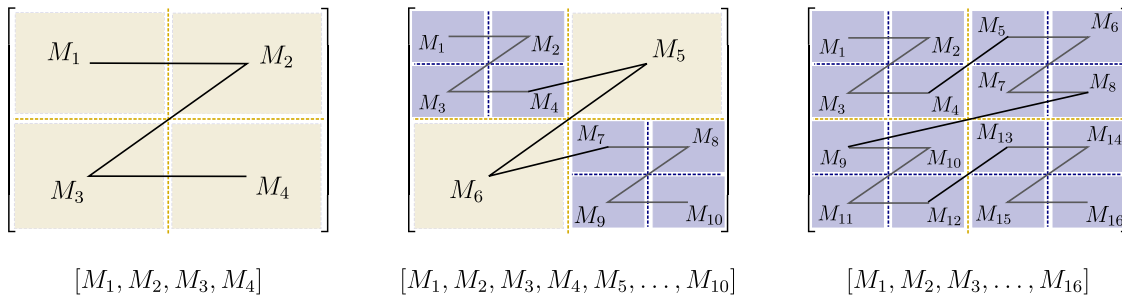


Figure 2.52: Presentation of  $\mathcal{Z}$ -curve and of the construction of flat  $\mathcal{H}$ -matrix

The structure of the  $M$  matrix is streamlined, but it would require the definition of an object like  $SLevel$ , which contains all the absolute positions of each sub-block and their dimensions. The matrix-vector product can then follow the process described Fig. 2.53. The positions  $m, n$  and dimensions  $d, e$ , got from  $SLevel$ , are used to define the partition  $x_k$  and  $b_k$  of the global vectors  $x$  and  $b$ , respectively. The  $b$  vector continues to be built incrementally, along the travel of the series of sub-blocks  $M_k$ .

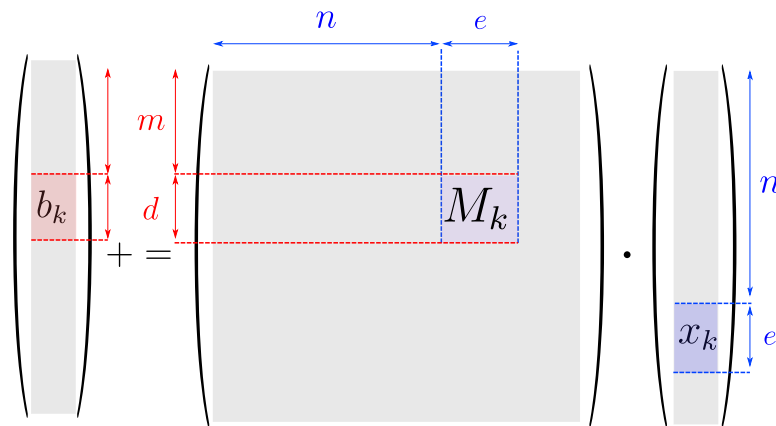


Figure 2.53: Diagram of  $\mathcal{H}$ -matrix-vector product with a flat structure

The sub-block vector product can be completed via a looping process. An instance of this algorithmic implementation for low-rank approximations is provided in Algorithm 9. In this context, the sub-block  $M_k$  is represented by the product  $A_k \cdot B_k$  when the sub-block is admissible, or by  $A_k$  alone in cases where the sub-block is not admissible.

### $\mathcal{H}$ -resolution performance

Let consider again the linear system.(2.79), with  $M$  a matrix of shape  $(N \times N)$ . The complexity of the inverse of  $M$  varies in order of  $\mathcal{O}(N^3)$ . This appeals to the resolution by iterative solver, especially for fully-populated matrix and this type of problem, which aim to reduce the complexity to  $\mathcal{O}(N^2)$ .

Those methods could account for many different methods and use. One of the best-indicated method for the iterative resolution is *Generalized Minimal Residual* (GMRES)

**Algorithm 9:** Implementation of the  $\mathcal{H}$ -product &  $\mathcal{Z}$ -curve

---

```

1 Function HMatVectProductFlat ( $A, B, x, b, SLevel$ ):
2   for  $k$  in range( $|A|$ ) do
3      $A_k \leftarrow A[k]$ 
4      $B_k \leftarrow B[k]$ 
5      $m, n, d, e \leftarrow \text{UnWrap}(SLevel[k])$ 
6     if  $B_k$  is empty then
7        $b[m : m + d] += A_k \cdot x[n : n + e]$ 
8     else
9        $b[m : m + d] += A_k \cdot (B_k \cdot x[n : n + e])$ 
10  return  $b$ 

```

---

method introduced by Saad and Schultz. [Saad and Schultz, 1986].

**GMRES** This method allows to approximate a vector solution for  $x$  accounting for the definition of a *Krylov's sub-space*, based on *Arnoldi's algorithm* for the iterative process. The Krylov's sub-space is defined as a span of vectors,

$$K_n = \text{Span}\{\mathbf{b}, M\mathbf{b}, M^2\mathbf{b}, \dots, M^{n-1}\mathbf{b}\}$$

Krylov methods can leverage the  $\mathcal{H}$ -product implementation tailored for  $\mathcal{H}$ -matrices. The convergence properties of such methods have been investigated by the work of Kandler-Schröder [Kandler and Schröder, 2014].

Both the  $\mathcal{H}$ -product and the  $\mathcal{H}$ -product & flat methods offer a memory-efficient strategy when operating with  $\mathcal{H}$ -matrices. Consequently, the Krylov subspace could be constructed with these methods in mind. To evaluate the performance of the iterative solver, we take the example of circular meshes with various number of elements. The outcomes in times are presented in Fig. 2.54. The results employing  $\mathcal{H}$ -product and  $\mathcal{H}$ -product &  $\mathcal{Z}$ -curve methods are both depicted in greenish colors, while the blue line represents the results computed by GMRES using the full-matrix assembled.

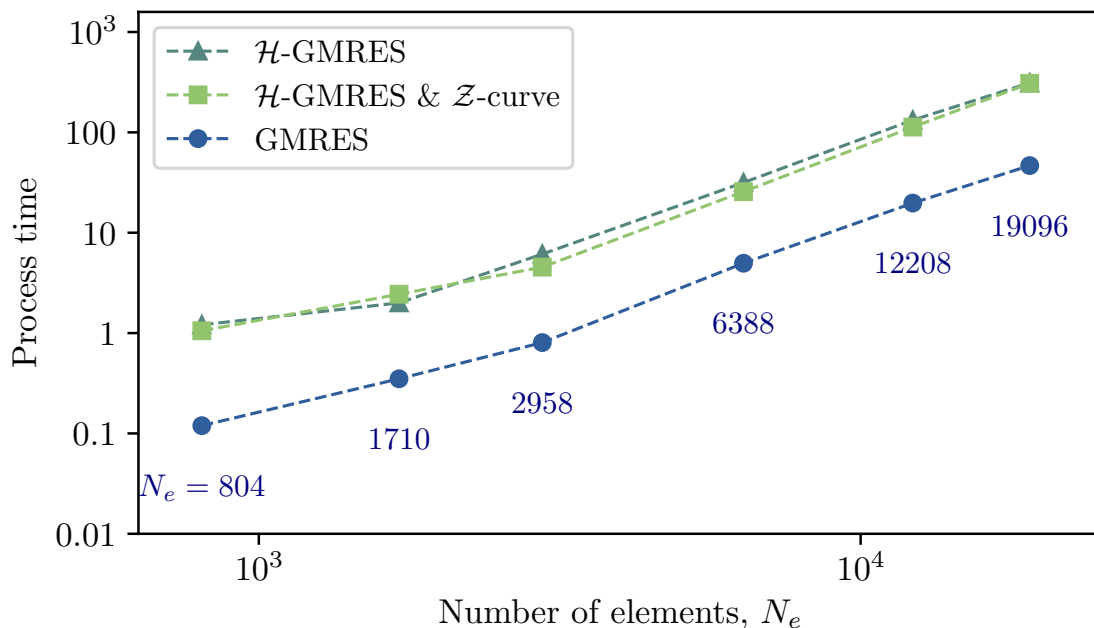


Figure 2.54: Time for resolution of linear system, according to different mesh size problem



The problem size variation depicted in Fig. 2.54 spans roughly one order of magnitude in terms of the number of elements. This scale range in size of problem is restrictive. The experiment is carried out on a computer equipped with a 1.30GHz Intel Core i7 processor and 15 GB of RAM memory. The resolution using the fully-assembled matrix is still faster than those employing  $\mathcal{H}$ -matrices. In reality, it relies on the efficiency of the vector-matrix operations and the specific implementation. Since this problem utilizes a Python implementation, it is less efficient compared to optimized vector-matrix operators. Therefore, at this stage, solving with  $\mathcal{H}$ -matrix operators takes 10 about times longer than operations on the full matrix. Nevertheless, this implementation already reduces the memory requirement. For the largest problem illustrated in Fig. 2.54, with  $N_e = 19096$  elements, a compression rate of 79.9% is achieved.

## Conclusion

Throughout this section, we delved into the problem of conduction generated by real contact interface. This endeavor combines an appropriate physical formulation with numerical development. It begins with the establishment of an integral equation, and follows by the construction of numerical methods to solve it. It has conducted us to the implementation of the Boundary Element Method, culminating in numerical enhancements leading to a Fast-BEM version.

Section 2.2 is dedicated to the formulation of the linear problem to solved by the Boundary Element Method. We have endeavored to maintain this formulation as general as possible, accounting for different shape elements and interpolation functions. Every step of our numerical development has been thoroughly detailed and illustrated, offering deeper insight into our technical choices. For the sake of precision, this formulation has led us to concentrate the presentation on the most fundamental issues, such as:

- *Numerical Integration:* It has been highlighted that traditional Gaussian quadrature techniques are not suitable for integrating the Green function. To evaluate precision, we suggest various parametrization methods, particularly for *Singular* and *Quasi Singular* integrals.
- *Numerical Precision:* In order to thoroughly assess precision, different interpolations and element types have been analyzed. The precision benefits from the benchmark scenario of a circular contact spot, utilizing its analytical solution. Ultimately, this has led us to choose constant interpolation, coupled with triangular-shaped elements.

The third Section 2.3 is dedicated to the implementation of the  $\mathcal{H}$ -matrix, constructed to enhance the capabilities of the classical BEM. For this part we have solely accounted for triangular elements and constant interpolation, in regard of the precision results at Section 2.2. The use of  $\mathcal{H}$ -matrix may be seen as a granted heuristic method, but similar to Section 2.2, we have endeavored to justify its implementation. These discussions have raised critical questions about:

- *The Clustering Consistency:* We have considered different clustering methods. This step could incorporate various approaches, enhancing the cluster's geometries. In evaluating alternative methods, the *median* technique continues to prove its effectiveness, in terms of time efficiency and  $\mathcal{H}$ -tree consistency.
- *Precision on Final Results:* The efficacy of the low-rank approximation, and its ACA+ implementation, has been also evaluated in terms of result precision. Errors in both matrix components and final outcomes have been documented. The influence of both maximal hierarchical level  $l_m$  and precision of ACA+ construction  $\epsilon$  have been carefully examined, in comparison with classical BEM.

- *Performance Review:* The application of the  $\mathcal{H}$ -matrix leads to considerable savings in both memory and time, reducing the asymptotic complexity to  $\mathcal{O}(N \log N)$ . These benefits have been analyzed based on the parameters  $(l_m, \epsilon)$ , proving their effectiveness in handling realistic problems. Additionally, a consistent matrix-vector product implementation has been implemented to leverage the structure of the  $\mathcal{H}$ -matrix for the iterative linear solver, GMRES; various implementations of the  $\mathcal{H}$ -matrix have also been considered, further enhancing performance, notably by the flattening using the  $\mathcal{Z}$ -curve.

This work was structured into three sections. The numerical methods employed have been thoroughly documented and illustrated through particular examples. This section may serve as a guideline for BEM and Fast-BEM implementations.

We believe that the conductivity problem formulation makes BEM a particularly good choice. Indeed, the integral equation established here exclusively considers the conductive area, without the need for bulk modeling or even non-conductive surface. This method enables to define consistently the geometry of contact spots and properly refine the mesh near edges. In the following section the methods developed in this part will allow us to deal with contact spot of very complex geometries.



---

 Conductivity of Complex-Shaped Contact Spots
 

---

**Contents**


---

<b>3.1</b>	<b>Introduction</b> . . . . .	<b>115</b>
<b>3.2</b>	<b>Conductivity of not simply connected spot</b> . . . . .	<b>116</b>
3.2.1	Analytic result . . . . .	116
3.2.2	Finite element results . . . . .	117
<b>3.3</b>	<b>Conductivity of flower-shaped spots</b> . . . . .	<b>120</b>
3.3.1	Geometrical reduction . . . . .	122
3.3.2	Conductivity results . . . . .	124
3.3.3	Other "multi-petal" spots . . . . .	126
<b>3.4</b>	<b>Conductivity of self-affine spots</b> . . . . .	<b>130</b>
3.4.1	Geometry of spots . . . . .	130
3.4.2	Geometrical characteristics . . . . .	132
<b>3.5</b>	<b>Two-mode spots</b> . . . . .	<b>146</b>
3.5.1	Results and modeling . . . . .	148
<b>3.6</b>	<b>Koch snowflake</b> . . . . .	<b>149</b>
<b>3.7</b>	<b>Conclusion</b> . . . . .	<b>152</b>
3.7.1	Flower-shaped spots and other simple forms . . . . .	152
3.7.2	Conductivity of self-affine spots . . . . .	152
3.7.3	Contact spots between rough surfaces . . . . .	153
3.7.4	Supplementary work, two-modes spots, and Koch snowflake . . .	153
3.7.5	Conclusion . . . . .	153

---

### ■ ■ Résumé du Chapitre III

Depuis les premières observations d'aire réelle de contact, nous savons que celles-ci sont composées de taches de contact distinctes, regroupées en cluster. Souvent, dans les modèles de résistance de constriction, les formes de ces taches sont réduites au cas circulaire, alors que l'étude de surfaces rugueuses en contact fait apparaître des taches à géométrie plus complexes. Cette partie plonge ainsi dans le problème de la conduction pour ces taches, tirant partie de notre modèle BEM. Cette partie sera donc divisée en plusieurs sous-parties, chacune dédiée à une forme de tache particulière. Sans être tout à fait exhaustif, nous avons cherché à être le plus complet possible dans la variété des géométries traitées. La première étude est associée à l'étude des *taches annulaires*. La deuxième sous-partie présentera l'étude des taches en forme de *fleur*, d'*étoile* et d'*engrenage*, dont la conductivité varie en fonction du nombre de pétal. Une troisième sous-partie vise à étudier des taches à contour rugueux de géométrie *auto-affine*, généralisant l'analyse des taches en forme de fleur. Une variante des taches en forme de fleur à *deux rangées de pétale* sera ensuite étudiée. Cette partie sera enfin conclue par l'étude de tache en forme de *flocon de Koch*. Chacune de ces études fera l'objet d'une *analyse phénoménologique*, permettant de mieux comprendre les résultats, et d'exhiber l'influence de certains paramètres. Pour les taches auto-affines l'analyse fera notamment intervenir des paramètres tels que le rayon moyen, l'écart type du contour, la largeur du contenu spectral, ou la dimension fractale.

### 🇬🇧 Abstract for Chapter III

Since the early observations of real contact area, we know that those are composed of distinct contact spots, grouped into clusters. However, in some models of constriction resistance, often the shapes of the spots are reduced to circles for which an analytical solution exists. In general case, the conductivity of spots of more complex shape is difficult to relate to their shape and to a particular geometric parameter. This chapter thus delves into the problem of conduction for an isolated spot of complex shape, taking advantage of our BEM solver. This chapter is divided into several sections, each dedicated to a particular shape family. Without being entirely exhaustive, we have sought to be as comprehensive as possible in the variety of geometries treated. The first study is associated with the study of an *annular spot*, which is the simplest non-simply connected shape. The second section will present the study of spots shaped like *flowers*, *stars*, and *gears*, whose conductivity varies with the number of "petals". The third section aims to study spots with rough contours of *self-affine* geometry, generalizing the analysis of flower-shaped spots. A variant of flower-shaped spots with *two sets of petals* will then be studied along with a simplified superposition model handling two modes as if they could be summed up. This part will end with the study of spots in the shape of a *Koch snowflake*. Each of these families benefit from a *phenomenological analysis*, allowing a better understanding of the results and geometrical parameters. For self-affine spots, the analysis will particularly involve parameters such as the average radius, the standard deviation of the contour, the width of the spectral content, and the fractal dimension. The constructed phenomenological models permit to estimate the asymptotic conductivity in the fractal limit.

### 3.1 Introduction

The primary motivation for the study of conductivity of non-convex contact spot stems from the observation of contact spot geometry formed between model rough surfaces (self-affine random geometry). Figure 3.1(a) illustrates how individual contact spots evolve under increasing load [Yastrebov et al., 2015a], while in (b) three separate contact spots obtained from similar simulations demonstrate high complexity both in terms of connectedness and boundary shape. Even under relatively small loads, very complex contact spots can be formed if the spectral content of roughness is sufficiently rich. However, basic models of contact resistance assume that individual contact spots distributed over the nominal contact area possess simple shapes: elliptical or circular.

In contrast, the depicted contact shapes can be non-simply connected (having holes) and exhibit highly complex boundaries, which can be characterized by the ratio of the square root of the area to its perimeter, also known as compactness. In this study, we investigate the impact of connectedness and compactness of individual contact spots on their conductive properties. Instead of studying contact spots obtained in direct numerical simulations, as shown in Fig. 3.1, we construct relatively simple models that capture the primary features of such spots: (1) connectedness, and (2) low compactness. The first effect is represented by an annulus shape with a varying ratio of inner to outer radius. Compactness, as a first approximation, is modeled through a flower-shaped spot with varying numbers of petals and their lengths. Further, some additional relatively simple "multi-petal" shapes are considered. Moreover, the self-affine aspect of contact spot geometry is considered by modeling a flower with multi-scale petals: paraphrasing Archard, we envision "petals on top of petals on top of petals." The objective of the study is to propose a relatively simple model enabling to predict thermal and electrical resistance using geometrical parameters of the conductive spot.

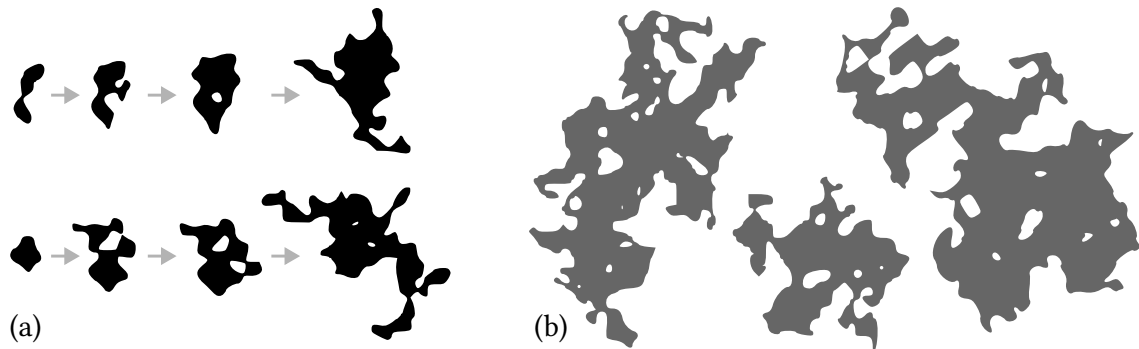


Figure 3.1: Simulation results of the true contact-area between self-affine random rough surfaces taken from [Yastrebov et al., 2015a]: (a) evolution of separate contact spots under increasing load, (b) snapshots of separate clusters highlighting the complexity of the shape.

This aims to study the effects of the topology and the shape of contact spots on simplified examples: in Section 3.2 we briefly study the effect of not simple connectedness on an example of the flux through an annulus spot; the effect of shape irregularity on a simplified example of a flower-shaped spot (and similar shapes) with equally spaced petals of the same size, in Section 3.3; in Section 3.4, the same effect is studied on self-affine spots which could be seen as flower-shaped spots with polydisperse petals following a self-affine distribution. Furthermore in Section 3.5, some relevant results are obtained for two-mode flower-shaped spots highlighting the evolution of the flux for vanishing amplitude of high-frequency mode; ultimately in Section 3.6, the conductivity related to the fractality is studied in the modeling on contact spot shaped like Koch snowflake.

### 3.2 Conductivity of not simply connected spot

This section aims to study the total flux through an annulus spot of different internal radius. The question is to which extent the flux is altered by the presence of small internal holes in not simply connected spots. The internal radius is  $r = b$ , the external one  $r = a$ , their ratio is denoted  $\xi = b/a < 1$ . The boundary conditions remain the same as for circular spot: the potential is set constant  $U = U_0$  at the annulus ( $b \leq r \leq a$ ) the zero flux is set elsewhere ( $r > a$  and  $r < b$ ), at infinity the potential is set to  $U = 0$ . The geometry is shown in Fig. 3.2 for three different values of  $\xi$ . We are mainly interested by the asymptotic evolution of the total flux  $Q(\xi)$  in the limit of  $k \ll 1$ .

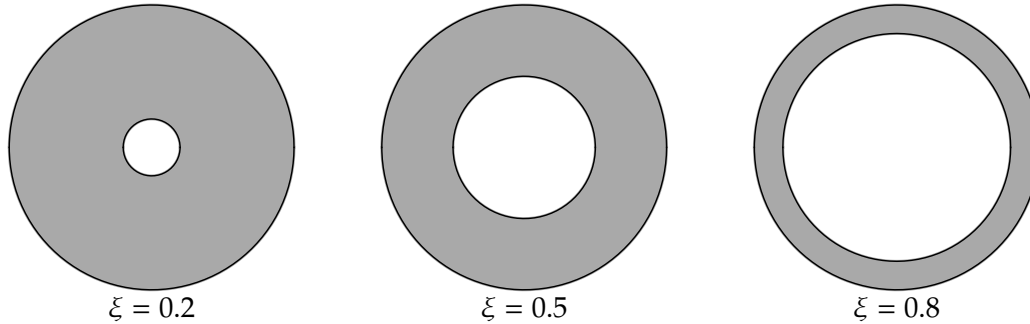


Figure 3.2: Geometry of the annular contact spot for various ratios of the internal to external radii  $\xi = \{0.2, 0.5, 0.8\}$ .

The flux diverges at borders of the annulus, however the total flux should be continuous and decreasing with respect to the relative hole radius  $\xi$ . As  $\xi \rightarrow 0$ , the total flux should tend to  $Q_0$ , whereas for  $\xi \rightarrow 1$ , the flux should vanish  $Q \rightarrow 0$ . We could also conjecture, from a physical point of view, that the flux should be a concave function of  $\xi$  meaning that small holes should not affect considerably the flux. Subsequently, the local singularity on the inner edge should be less pronounced than on the outer edge being regularized to some extent by the interaction with the whole inner border especially for small size holes.

#### 3.2.1 Analytic result

The problem of annulus contact spot was first subjected to analytical study. We can especially recall the work attempted by Smythe [Smythe, 1951], who solves this by superposition method, and establishes a law for the flux with different geometries, and provides tabulated results. Other authors [Cooke, 1963, Collins, 1963, Fabrikant, 1993] expanded Smythe's work by reformulating the problem as a triple integral or as a Fredholm's integral equations of second kind. However, those solutions do not provide closed form formulas for the flux; the influence of the effect of the hole cannot be easily deduced. Fabrikant [Fabrikant, 1993] proposed an iterative method for the resolution of the integral system. And Love's solution [Love, 1976] based on constructing upper and lower limits series provided the following closed form solution:

$$\frac{Q_{\text{Love}}}{Q_0} = 1 - \frac{4}{3\pi^2}\xi^3 - \frac{8}{15\pi^2}\xi^5 - \frac{16}{27\pi^4}\xi^6 - \frac{92}{315\pi^2}\xi^7 - \frac{416}{675\pi^4}\xi^8 + o(\xi^8) \quad (3.1)$$

When  $\xi$  is small the flux decrease induced by the annulus, is in order of  $\xi^3$ . This means that the decrease in flux is lower in magnitude than the decrease in perimeter of magnitude  $\xi$ , or even in area of magnitude  $\xi^2$ .

### 3.2.2 Finite element results

#### Geometry definition

The solution validation is sought using numerical simulation, in this case using the Finite Element Method (FEM). Thanks to the axial symmetry, the problem can be reduced to a square plane of length and width  $R \gg a$ . Considering width and height of the square section large enough, we could assume the FEM well-defining the infinite geometry of this problem. We need to control mesh definition near the inner and outer edges of the annulus where the imposed boundary conditions make diverge the normal flux. The Gmsh software [Geuzaine and Remacle, 2009] enables to set specific mesh sizes at the constructing points.

#### Method: Annulus mesh construction

To capture accurately the singularities at the vicinity of the inner and the outer edges of the annulus, two semi-circular shapes of radius  $r_e$  are constructed near the singularity points. The element size at the annulus's edge is set to  $h_{\min}$ , considering  $h_{\min}/a \ll 1$ . The mesh size is set to a coarser value far from the annulus  $h_{\max}$ , as  $h_{\max}/h_{\min} \gg 1$ . Supplementing the mesh refinement near the annulus' edge, the mesh size is set to  $h_e$ , at the edge of the semi-circular object setting  $h_e = 10h_{\min}$ . All the mesh size parameters are related to  $h_{\min}$ , to ensure a consistent refinement.

Mesh setting parameters :

- Dimension of the square geometry,  $R/a \geq 5$ ,
- Radius of the surrounding circle,  $r_e/a = 0.1$ ,
- Mesh parameters,  $h_{\min}/a \leq 0.01$ ,

An example for the annulus mesh geometry is represented in Fig. 3.3, using triangular elements for  $\xi = 0.5$ . The surrounding circle at the edges of the singularities are depicted in a darker color than the rest of the mesh. The boundary conditions are the following: within the annulus the potential is set to  $U_0$ , zero normal flux to  $j_n = 0$  is set on the free-surface out of the annulus and for the outward boundary when  $r = R$ . This is complemented by the potential value of  $U^\infty = 0$  at  $z = R$ . Using FEM, we can obtain the potential (or temperature) distribution corresponding to these boundary conditions. The problem geometry described in the previous section, as shown in Fig. 3.3, is utilized, and the results are presented in Fig. 3.4. In response to the potential field, we can determine the flux field at Gauss points and extrapolate it to surface nodes. Selected results for various annular geometries are presented in Fig. 3.5, plotted against the normalized radial position, defined as  $r = r/a$ . As anticipated, the normal flux exhibits divergences at both edges. But the singularity at the hole (inner edge) is less pronounced than at the outer edge, with the flux decreasing more rapidly near the hole compared to its decline at the outer edge.

#### Convergence with respect to geometry and mesh

The total flux through the annulus spot can be evaluated by summing up nodal "reactions" over the contact area. By employing different mesh definitions and different square sizes, we can construct an extrapolation technique. First, it is well known that the mesh convergence for linear elements is of order  $h/a$ , so we can find coefficients of the affine function for the flux  $Q(\xi, h) = Q^*(\xi) + m(\xi)h$ . On the other hand, the convergence with respect to the geometrical parameter  $a/R$  can be also established as  $Q(\xi, a/R) = Q^*(\xi, a/R) + n(\xi)a/R$ . These relation of proportionality can be expressed as

$$Q(\xi) = Q^*(\xi) + m(\xi)\frac{h}{a} + n(\xi)\frac{a}{R} \quad (3.2)$$



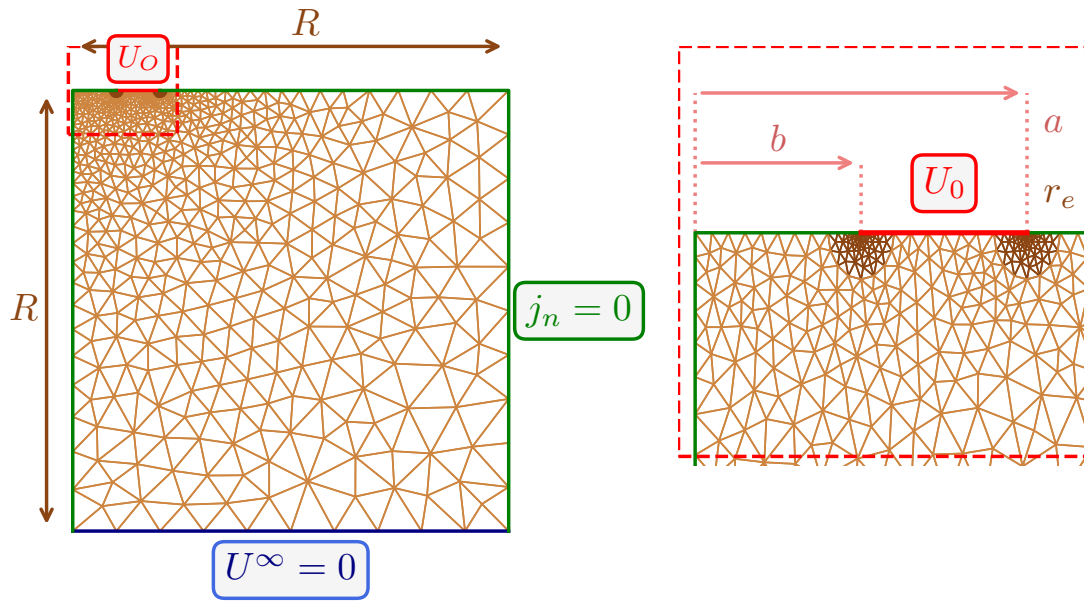


Figure 3.3: Mesh definition and boundary conditions for modeling of an annulus contact spot, using the parameters  $\xi = 0.5$ ,  $h_{\min}/r_0 = 0.005$  and  $R/a = 5$

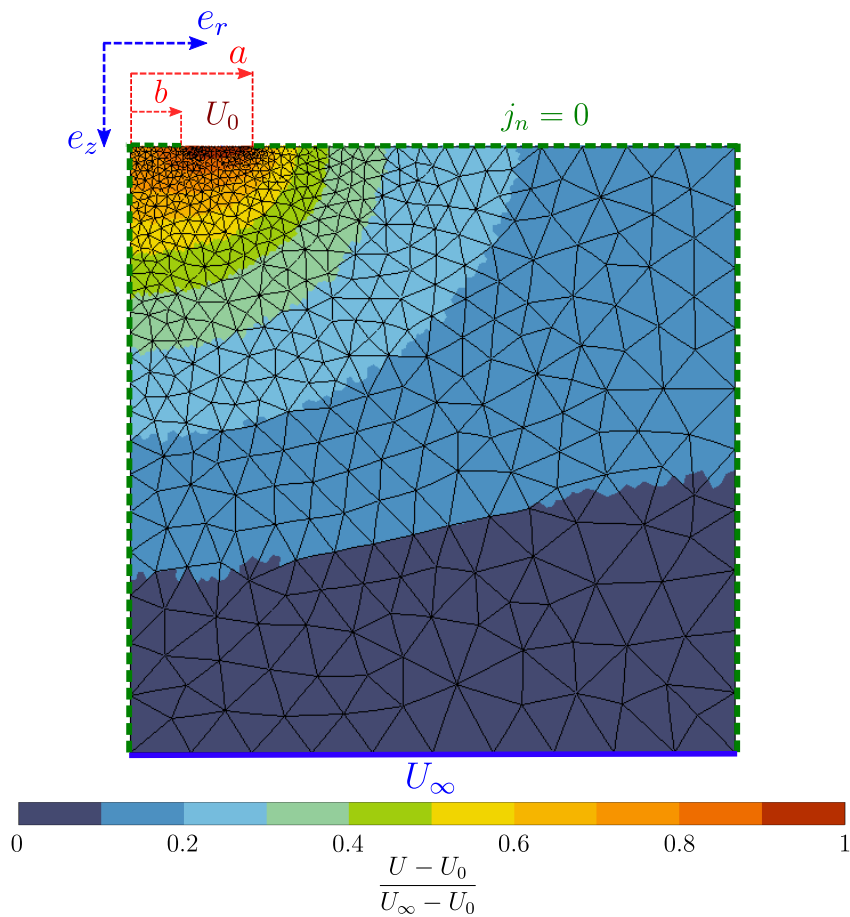


Figure 3.4: Result in temperature field computed by FEM, for an annulus of  $\xi = 0.5$ , using a cylinder size of  $R/a = 5$  and a mesh size of  $h_{\min}/a = 0.005$

Where  $Q^*(\xi)$ ,  $m$  and  $n$  are coefficients, which depend on the annular geometry with  $\xi$  and could be determined by least mean squares fit as presented for the annulus

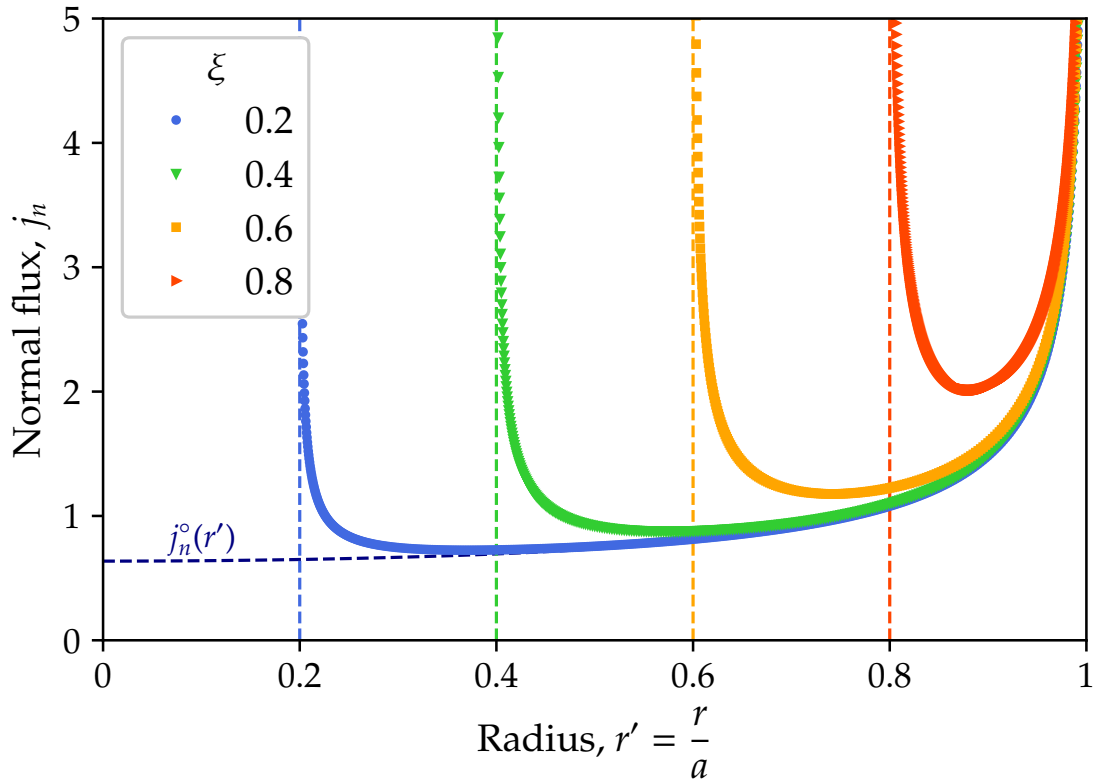


Figure 3.5: Finite element results of the normal flux distribution for annulus spot for different values of  $\xi$ , dashed line represents the normal flux of a circular spot.

problem with  $\xi = b/a = 0.5$  in Fig. 3.6. This problem was addressed for various cylinder sizes with values of  $R/a = 5, 10, 15, 20, 25, 50$ , and for different mesh sizes  $h/a = 0.001, 0.00075, 0.0005, 0.00025, 0.0001$ . It accounts for a total of 30 simulations. The fitting process allows us to identify the coefficients in eq.(3.2):  $Q^*/Q_o = 0.98$ ,  $m/Q_o = 0.15$ , and  $n/Q_o = 0.12$ . The limit  $Q^*$  could be reported as the best approximation for the flux for a half-space geometry  $a/R \rightarrow 0$  taking into account mesh convergence  $h/a \rightarrow 0$ .

This extrapolation procedure agrees with the extrapolation process proposed by Richardson [Richardson, 1911]. Aiming to improve the precision of the results, those are extrapolated using 2 different mesh sizes ( $h_1$  and  $h_2$ ) and 2 different dimensions of cylinder  $R_1$  and  $R_2$ , with  $R_1 > R_2$  and  $h_1 < h_2$ . So to find an accurate estimation for the flux, we solve the problem for three different configurations ( $h_1, R_2$ ), ( $h_1, R_2$ ), and ( $h_1, R_2$ ). Simulation results for the *total flux* are shown in Fig. 3.7 with the flux normalized by the one of a circular spot  $Q_o$ . The asymptotic results for small holes is identified by least mean square fit using a power-law of  $\xi$  as detailed in the frame below.

#### Model: Total flux for annular contact spot

An asymptotic result for the flux through an annulus with small holes  $\xi \ll 1$  could be properly fitted as

$$Q_{\text{fit}} = Q_o (1 - \alpha \xi^\beta), \quad (3.3)$$

where  $\alpha, \beta$  are positive parameters.

The parameters  $\alpha, \beta$  were identified by least squares method as  $\alpha \approx 0.1435$  and  $\beta \approx 3.028$  in the interval  $\xi < \xi_{\text{lim}} = 0.2$ , which are very close to analytical results of [Love, 1976, Fabrikant, 1993],  $\alpha = 4/(3\pi^2) \approx 0.1351$  and  $\beta = 3$  (see Eq.(3.1)). Nakamura's results [Nakamura, 1993] calculated by the BEM are also displayed for comparison, however, because of the lack of Richardson type extrapolation and convergence

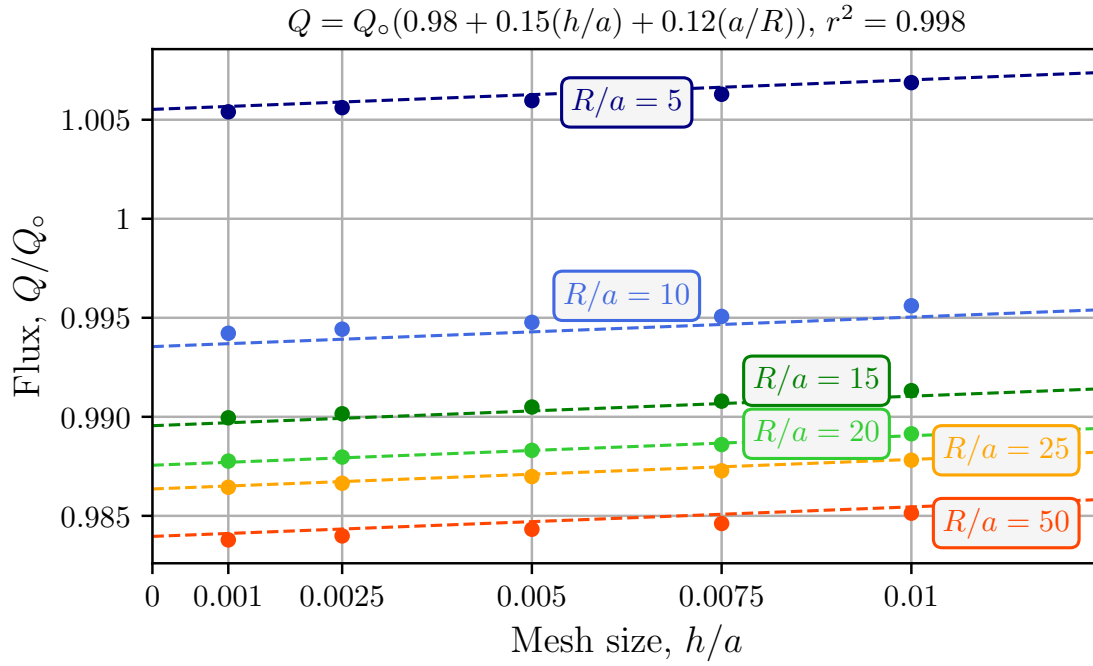


Figure 3.6: Linear dependency on the cylinder dimension and the mesh size for an annular contact spot with hole dimension  $\xi = 0.5$

study, they underestimate the flux value. The Love's solution slightly overestimates the flux for higher values of  $\xi$ , but this could be readily improved by including a larger number of terms in his series. In fact, all polynomial coefficients of  $\xi$  for the series expansion of the flux function are negative and adding new terms will slightly reduce the flux. Nevertheless, the first terms in Eq. (3.1) are in very good agreement with the numerical results at least for small values of  $\xi$ .

Expectedly, we conclude that the total flux is very weakly dependent on the presence of small holes in annulus spots because the corrective term is of order  $\xi^3$  with a small factor  $\sim 0.1$ . Therefore, the not simply connected spots, at least for holes located far from the outer boundary, conduct almost as well as simply connected spots with the same outer boundary. In addition to this axisymmetric study, one could conduct a similar study but with a hole placed with some excentricity with respect to the center. Such a study would provide an even stronger argument on the effect of such holes in conductivity problems, however, this study is not included in the scope of the current paper.

### 3.3 Conductivity of flower-shaped spots

To mimic complex shapes formed by contact between random rough surface, we first consider a simple geometrical model which we call *flower-shaped* spot parametrized a radius function  $r(\theta)$ , with  $\theta$  the polar coordinate.

#### Definition: Geometry of the flower-shaped spot

The radius of the flower-shaped contact spot, is defined as a circular contact spot enclosing a sine profile, as:

$$r(\theta) = r_0 + r_1 \cos(n\theta), \quad r_1 < r_0 \quad (3.4)$$

where  $r_0$  is the mean radius,  $r_1$  is the half-length of petals and  $n$  is their number.

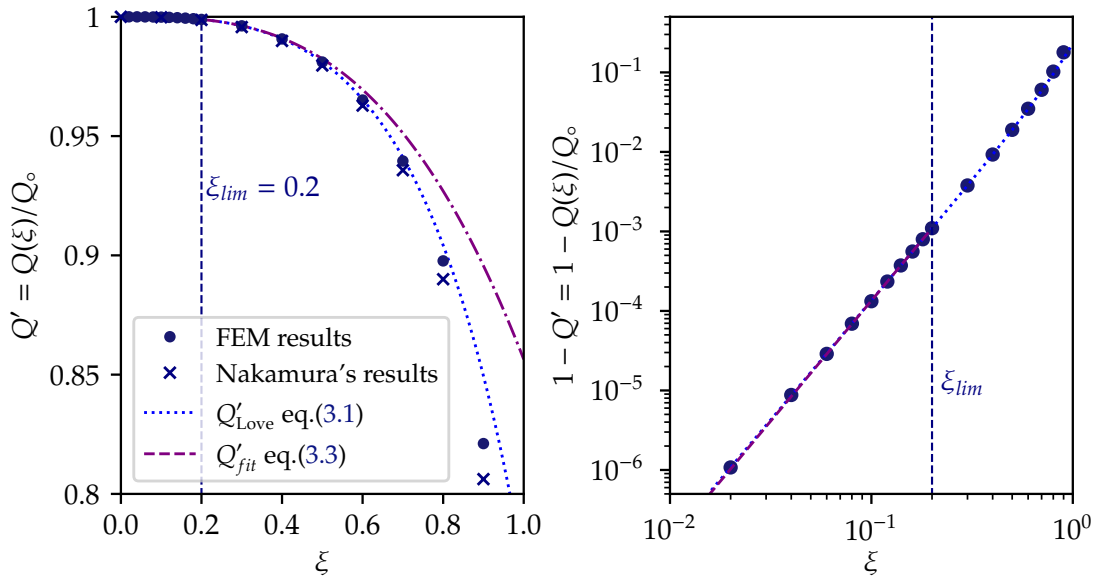


Figure 3.7: Total flux of an annulus as a function of internal to external radius ratio  $\xi$ : shown the finite element results (circles), least squares fit of an offsetted power-law for the asymptotic solution  $Q'_{fit}$  for  $\xi < 0.2$  and an approximate analytical solutions by [Love, 1976]  $Q'_{Love}/Q_0$ . (a) – normalized total flux  $Q'(k) = Q(k)/Q_0$ ; (b) – normalized flux difference compared to the circular flux  $(Q_0 - Q(k))/Q_0$  in log-log scale highlighting the power-law flux evolution.

So the two positive dimensionless parameters describing the shape are  $\xi = r_1/r_0 < 1$  and  $n$ . Different flower-shaped spots are presented in the Fig. 3.8. Note that the average radius does not change with the number of petals nor with their length and is equal to  $\langle r \rangle = r_0$ . Circles of radius  $r_0$  and  $r_0(1 + \xi) = r_0 + r_1$  are also shown in the figure; corresponding to minimal and maximal limits for the resulting flux  $Q_{min}(r_0) = Q_0 = 4kr_0U_0$ ,  $Q_{max} = Q_0(r_0 + r_1) = 4kr_0(1 + \xi)U_0$ ,

$$1 \leq \frac{Q(r_0, \xi, n)}{Q_{min}} \leq 1 + \xi$$

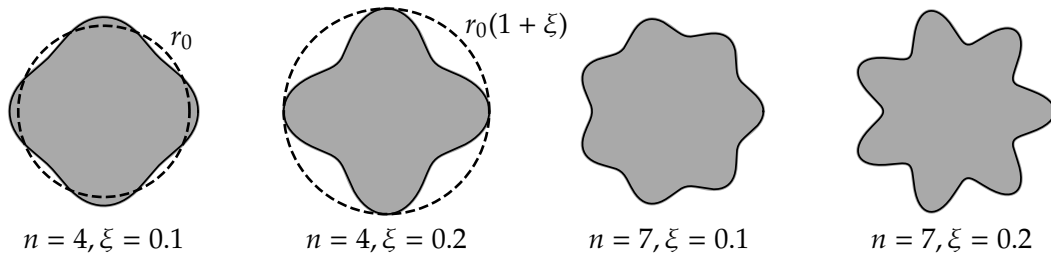


Figure 3.8: Examples of flower-shaped spots with  $\xi = \{0.1, 0.2\}$  and the number of petals  $n = \{4, 7\}$ .

The particularity of these flower-shaped spots is that the perimeter increases with the number of petals whereas the area remains constant. They are given by the following equations

**Property: Area and perimeter for flower-shaped contact spot**

The area and the perimeter of flower-shaped contact spot is given by

$$A = \pi r_0^2 \left(1 + \frac{\xi^2}{2}\right), \quad (3.5a)$$

$$P = r_0 \int_0^{2\pi} \sqrt{1 + (n\xi \sin(\theta))^2} d\theta, \quad (3.5b)$$

We can notice that the integrand depends on the dimensionless parameter  $n' = n\xi \in \mathbb{R}$  which is continuous contrary to the number of petals  $n \in \mathbb{N}$ . To characterize the shape of the flower-shaped spot, we could also use compactness  $C$  being the ratio of the square root of the area to the perimeter:

$$C(n') = \frac{\sqrt{A}}{P} = \sqrt{\pi} \frac{1 + \xi^2/2}{4E(in')}, \quad (3.6)$$

where  $E(x) = \int_0^{\pi/2} \sqrt{1 - x^2 \sin^2(\theta)} d\theta$  is the complete elliptic integral of the second kind and  $i$  is imaginary unit. For small values of  $\xi$ , we could assume that the compactness depends on  $n'$  only, for  $n' \rightarrow 0$ ,  $E(in') \rightarrow \pi/2$  and the compactness tends to the maximal value, i.e. the compactness of a circle  $C \rightarrow C_o = 1/(2\sqrt{\pi}) \approx 0.282$ .

**3.3.1 Geometrical reduction**

The flower shape presents a dihedral symmetry  $D_m$  which allows us to reduce the geometry problem for FEM. BEM could exploit this property in turns. A flower-shaped contact spot, made of  $n$  petals, enclose  $m = 2n$  identical section. Each petal section can be divided in two; the whole geometry is rebuilt by one reflection and a series of  $n$  rotation. An example of dihedral symmetry is presented Fig.3.9, for a flower-shape with the petal height of  $\xi = 0.1$ , and with a number of petals of  $n = 32$ . In the case of flower with 32 petals, there is Initially 64 identical sections. However in the example displayed Fig. 3.9, the division is limited to 16 sections.

As mentioned the dihedral symmetry enables to reduce the size of the BEM problem. In fact the problem can be reformulated as detailed in the blue frame below.

**Definition: Dihedral symmetry**

For a set of  $\{D_1, \dots, D_m\}$ , referring to set of elements, the BEM linear system can be decomposed according to these sets of :

$$\begin{pmatrix} G_{11} & G_{12} & \cdots & G_{1m} \\ G_{21} & G_{22} & \cdots & G_{2m} \\ \vdots & \vdots & \ddots & \vdots \\ G_{m1} & G_{m2} & \cdots & G_{mm} \end{pmatrix} \begin{pmatrix} \{J_1\} \\ \{J_2\} \\ \cdots \\ \{J_n\} \end{pmatrix} = \begin{pmatrix} \{U_{1,0}/2\} \\ \{U_{2,0}/2\} \\ \cdots \\ \{U_{m,0}/2\} \end{pmatrix} \quad (3.7)$$

Where the global matrix  $G$  is divided in sub-blocks,  $G_{i,j}$ . The subindex  $i$  refers to the set  $D_i$ , set of physical nodes for the potential. And the subindex  $j$  refers to the set of physical nodes for the flux.

This development is supplemented by assuming that the solution for the normal flux is the same of all sectors  $J_1 = J_2 = \dots = J_m$ . The linear system can be condensed to its first line: substituting all vectors  $J_i$  by  $J_1$ , the problem can be reformulated as follows :

$$\left(\sum_{i=1}^m G_{1,i}\right) \{J_1\} = \left\{\frac{U_0}{2}\right\} \quad (3.8)$$

The  $\mathcal{H}$ -addition helps to preserve the hierarchical structure. The problem can be still solved using  $\mathcal{H}$  – GMRES tool given Section 2.3.5.

### Mesh definition

The normal flux is supposed singular on the edges, still requiring special refinement. An example of mesh definition is presented Fig. 3.10. In the problem, an angular section of  $\theta_s = 2\pi/16$  is meshed, standing for the 16-th of the whole geometry, referring to the darker section in Fig. 3.9. This section avoids element discrepancy at the tip of the geometry, and so avoids degradation in the solution. Practically, BEM result shows sensitivity to the geometry of the tip element, which bounds the number of section division.

#### Method: Mesh construction for flower shape

The geometry is decomposed in two parts. The darker region ensures consistent refinement at the edge. In the opposite, within the lighter one the mesh is coarsened. The mesh parameters are tailored to follow the max edge's curvature,  $\alpha_{\max}$ , as:

$$h_{\min} = \frac{h}{\log_{10}(\alpha_{\max})}$$

Where  $h$  is the initial value for the mesh size, and  $h_{\min}$  represents the mesh size so-defined of the contour edge. Conversely the mesh size is set to a value of  $h_0$  at the tip of the geometry, i.e. in the flower's center. The edge's curvature increases as the number of petals or the ratio  $\xi$  increase.

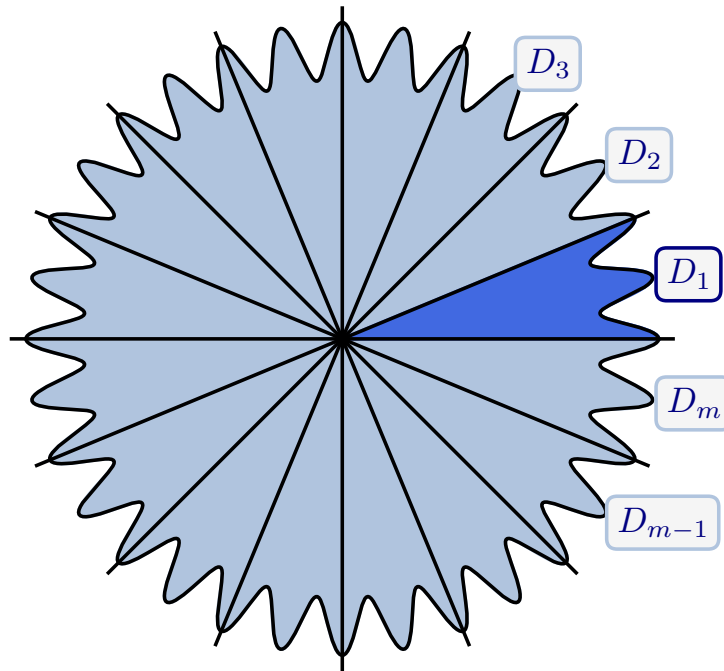


Figure 3.9: Symmetrical division for a flower shape with ratio  $\xi = 0.1$  and  $n = 32$  petals.

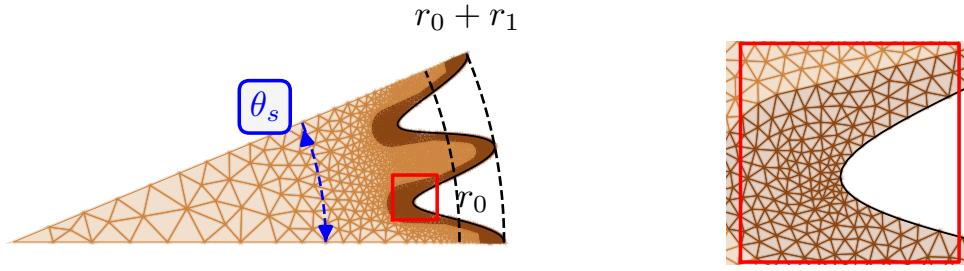


Figure 3.10: Mesh definition of the 16-th section of the flower contact spot  $\xi = 0.1$  and  $n = 32$ , with element parameters  $h_{min}/h_0 = 0.2$ , and  $h_0/r_0 = 0.1$

### 3.3.2 Conductivity results

This study was conducted using both FEM and BEM. Despite the fact that the BEM is more appropriate for half-space approximation, the comparison of two methods with an extrapolation in terms of the size of simulated domain used in the FEM assess the validity of the latter. The same geometric reduction used in the BEM is also applied in defining the FEM mesh using dihedral symmetry. The physical definition for the FEM problem, includes extra boundary condition of the edge of the geometry. The normal flux is equal zero, as no-flux is exchanged.

Some results for the normal flux are presented in Fig. 3.11 for  $n = \{4, 7, 10\}$  petals and for  $\xi = 0.1$ , obtained from BEM. For the first two cases, the symmetry is fully exploited whereas for  $n = 10$  the angle is limited to  $\pi/5$  to preserve good mesh quality in the center. Meshes are refined near the outer edges where the flux is singular. For  $n = 4$  the total flux is  $Q \approx 1.0084Q_{min}$ , for  $n = 7$  the total flux is  $Q \approx 1.015Q_{min}$ , and for  $n = 10$  the total flux is  $Q \approx 1.0209Q_{min}$ . So there is a trend to increase the total flux with the increasing number of petals. Visually we can also observe that the singularity in the trough (petal's root) is weaker than the one near the crest (petal's extremity). The more petals we have, the weaker the flux intensity in the trough because of the increasing interaction of the neighboring petals; a similar trend was observed for the annular spot for small internal radii.

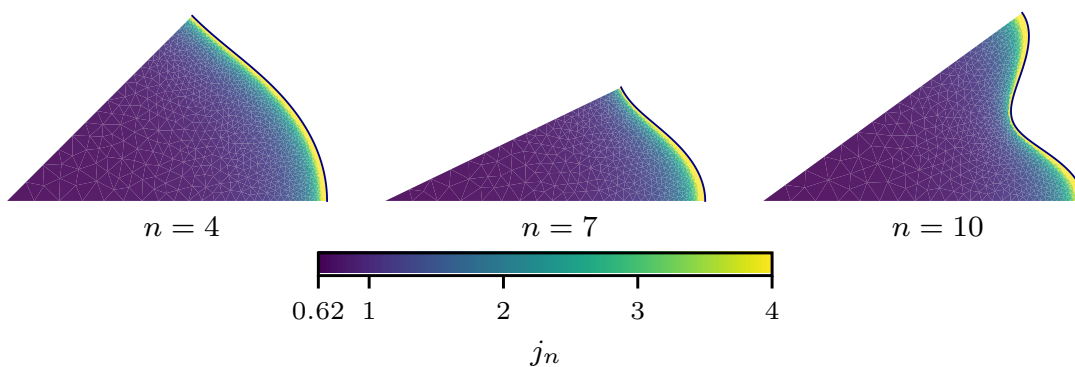


Figure 3.11: Simulation results for the normal flux for flower-shaped spots with  $n = 4, 7, 10$  and  $\xi = 0.1$ .

In total, 97 simulations<sup>1</sup> were carried out for  $\xi = 0.1$  and  $n \in (2, 150)$  as well as for  $\xi = 0.2$  and  $n \in (2, 100)$ . The resulting total flux with respect to the normalized number of petals  $n'$  is presented in Fig. 3.12. Those results are computed with Richardson extrapolation obtained by two meshes of different density for FEM and BEM and using a similar extrapolation for domain's dimensions in case of FEM simulations. The total

<sup>1</sup>Without counting simulations used to use Richardson extrapolation.

flux, offset by the minimal flux  $Q - Q_o$  could be normalized by the difference between the maximal and the minimal theoretical fluxes, corresponding to circular spots of radii  $r_0(1 + \xi)$  and  $r_0$ , respectively, i.e. we get in the denominator  $Q_{up} - Q_o = 4kr_0\xi U_0 = \xi Q_o$ . A normalization is defined for the total flux of the flower-shaped contact spot, encompassing the geometrical consideration, as presented in the blue-frame below.

#### Definition: Flux normalization & flower-shaped contact spots

This normalization results in a universal curve for the total normalized flux for any  $r_0$  and  $\xi$ :

$$Q' = \frac{Q - Q_o}{Q_{up} - Q_o} = \frac{Q - Q_o}{\xi Q_o} \quad (3.9)$$

The normalized flux evolution seems to be logarithmic, but from the physical point of view, the flux cannot overpass  $Q_{up}$ , therefore  $0 \leq Q' \leq 1$  for any  $n'$ . The resulting flux is well fitted by a two-parameter function which, however, was found empirically, as presented below:

#### Model: Total flux for flower-shaped contact spots

The results of normalized flux transmitted by flower-shaped contact spot is identified by a law of  $n'$ , as formulated:

$$Q'_{fit}(n') = a \left( 1 - \frac{1}{bn' + 1} \right), \quad 0 < a \leq 1. \quad (3.10)$$

Where  $n'$  is the normalized number of petals, and  $a, b$  are two positive parameters.

This fit function is also shown in Fig. 3.12 along with FEM and BEM simulation results. The coefficients determined by least squares fit are presented in Table 3.1. The slope at  $n' = 0+$  is equal to the product  $ab$ . Even if the coefficients  $a$  and  $b$  are slightly different for different sets, the slopes remain close for all three independent fits, and roughly equal to 0.3. Combining Eqs. (3.9) and (3.10), we obtain the following phenomenological equation for the total flow of a flower-shaped spot:

$$Q = Q_o \left( 1 + a\xi \left( 1 - \frac{1}{bn\xi + 1} \right) \right) \approx Q_o \left( 1 + 0.923\xi \left( 1 - \frac{1}{0.326n\xi + 1} \right) \right), \quad (3.11)$$

where  $Q_o = 4kr_0U_0$ . For the infinite number of petals  $n$  of finite half-length factor  $\xi$ , there is a limit flux given by this fit,  $\lim_{n' \rightarrow \infty} (Q'_{fit}) = a \approx 0.923$  and this limit is independent of  $\xi$ . However, the validity of the suggested fit beyond the studied interval of  $n'$  cannot be taken for granted. An argument in favor of such a limit  $a < 1$ , i.e. that the total flux for the infinite number of petals remains below the flux of a circular shape of radius  $r_0(1 + \xi)$ , could be made based on the area of the conductive spot. Indeed, the area of the full circular spot is considerably bigger than this of the flower-shaped spot  $\pi r_0^2(1 + \xi)^2 > \pi r_0^2(1 + \xi^2/2)$ . On the other hand, the small features (infinitely thin petals) should not strongly affect the conductivity of the spot, thus suggesting that possibly the flux should simply tend to 1. However, the current fit function could not be properly approximate the data if one sets  $a = 1$ . The question of a rigorous definition of the limit flux for the infinite number of petals *remains open*. But our initial guess, for the fitted parameters is given by the following limit flux:

$$\lim_{n\xi \rightarrow \infty} Q \approx Q_o(1 + 0.923\xi) < Q_{up} = Q_o(1 + \xi). \quad (3.12)$$

Even though such a flower-shaped geometry, especially in the limit of infinite number of petals, is not very relevant to contact problems between isotropic surfaces, which was at the origin for this study, this limit value presents an interesting by-product of this



study. Among other results one can deduce a relation between  $n$  and  $\xi$  which ensures  $x$  fraction conductivity in the interval  $Q_o$  and  $Q_{up} = (1 + \xi)Q_o$ , with  $Q = Q_o$  for  $x = 0$  and  $Q = Q_o(1 + \xi/2)$  for  $x = 0.5$ :

$$x = a \left( 1 - \frac{1}{bn\xi + 1} \right) \Leftrightarrow n' = n\xi = \left[ \frac{x}{b(a-x)} \right] \Rightarrow n\xi \approx \left[ \frac{x}{0.326(0.923-x)} \right], \quad (3.13)$$

Therefore, to reach the mean flux between two limits, i.e. for  $x = 0.5$ , one would need a spot with  $n\xi \approx 3.61$ , i.e. for  $\xi = 0.2$  one would need approximately 18 petals and for  $\xi = 0.1$  a double of that. However, to reach 75% ( $x = 0.75$ ), for  $\xi = 0.1$ , one would need a spot with approximately 130 petals.

Simulation	Parameters		Coefficients		
	$\xi$	$n \in$	$a$	$b$	$ab$
FEM	0.1	[1, 150]	0.928	0.327	0.304
FEM	0.2	[1, 100]	0.923	0.326	0.301
BEM	0.1	[1, 256]	0.923	0.326	0.301

Table 3.1: Least squares fit for coefficients of Eq. (3.10) for the sets of results of flower-shaped spot obtained using FEM and BEM simulations.

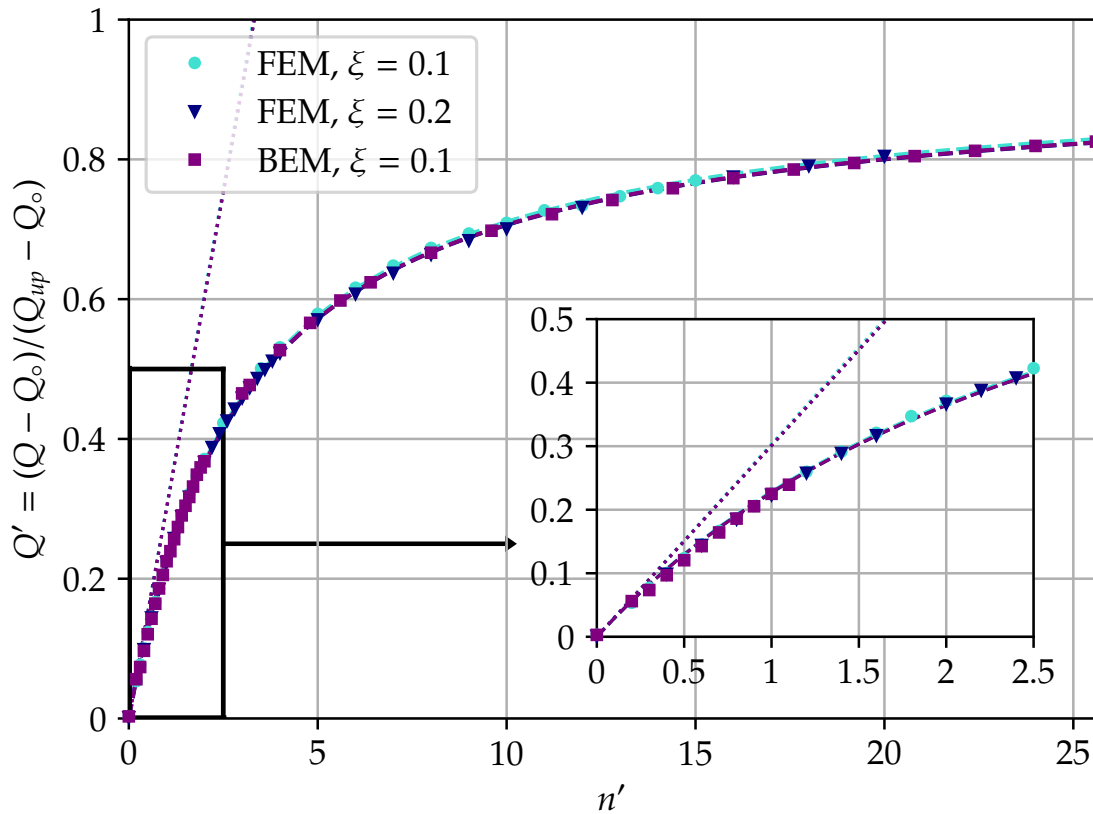


Figure 3.12: Simulation results for the normalized total conductivity for the flower-shaped spot as a function of normalized petal's parameter  $n'$  for different  $\xi$ , three independent least squares fit of function (3.10) are also plotted; the three corresponding tangents at the origin are also plotted.

### 3.3.3 Other "multi-petal" spots

The same conductivity study could be conducted on other simple forms possessing a single-scale petal-like structures with the same symmetry properties. Specifically we

identified the following shapes: star-shaped and gear-shaped spots shown in Fig. 3.13 and Fig. 3.14, respectively. For "stars", each petal is made up by straight lines connecting the roots and extremities of "petals", i.e. points with radial coordinates  $r_0(1 - \xi)$ ,  $r_0(1 + \xi)$ . The number of "petals" (or "rays") as previously is denoted by  $n$ , and the half-petal length  $r_1$  is again determined by the ratio  $r_1 = \xi r_0$ . The gear-shaped spots are made of circular arcs with constant  $r = r_0(1 - \xi)$  and  $r = r_0(1 + \xi)$  over equal angular segments. Contrary to  $C^\infty$  flower-shaped spots, star-shaped ones are only of class  $C^0$  with respect to  $\theta$  whereas gear-shaped spots represent multivalued mapping, so they are not even injective even for a single "petal" or "tooth".

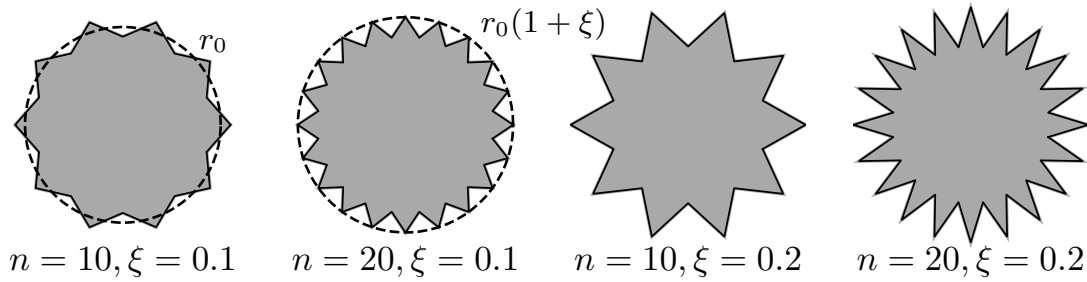


Figure 3.13: Examples of star-shaped spots with  $n \in \{10, 20\}$  petals, and half-petal length defined by  $\xi \in \{0.1, 0.2\}$ .

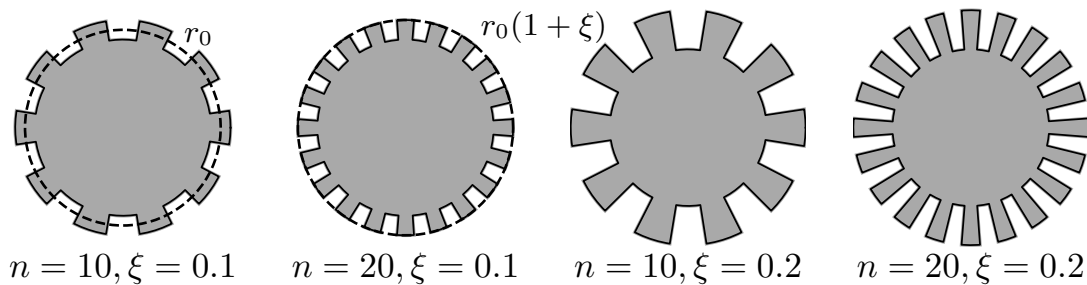


Figure 3.14: Examples of gear-shaped spots with  $n \in \{10, 20\}$  petals, and half-petal length defined by  $\xi \in \{0.1, 0.2\}$ .

The area of these shapes can be readily expressed by an elementary sum of triangles and a regular polygon for the stars, or circular sectors for the gears. Area, perimeter and compactness can be readily developed for these shapes contact spot as presented in the blue-frame below.

#### Definition: geometric properties for star & gear shapes

Star-shaped contact spot :

$$\begin{aligned}
 P_{\text{star}} &= 2\sqrt{2}nr_0\sqrt{1 + \xi^2 - (1 - \xi^2)\cos(\pi/n)}, \\
 A_{\text{star}} &= nr_0^2(1 - \xi^2)\sin(\pi/n), \\
 C_{\text{star}} &= \frac{\sqrt{(1 - \xi^2)\sin(\pi/n)}}{2\sqrt{2n}\sqrt{1 + \xi^2 - (1 - \xi^2)\cos(\pi/n)}}.
 \end{aligned}
 \tag{3.14}$$

**Gear-shaped** contact spot :

$$\begin{aligned} P_{\text{gear}} &= 2\pi r_0(1 + 2n'/\pi), \\ A_{\text{gear}} &= \pi r_0^2(1 + \xi^2), \\ C_{\text{gear}} &= \frac{\sqrt{(1 + \xi^2)}}{2\sqrt{\pi}(1 + 2n'/\pi)}. \end{aligned} \quad (3.15)$$

All those geometric features are summarized in Fig. 3.15. In summary, the star-shaped area converges to

$$A_{\text{star}} \xrightarrow{n \rightarrow \infty} \pi r_0^2(1 - \xi^2),$$

but for all  $n$  it is always smaller than the area of gear- and flower-shaped spots:

$$A_{\text{star}} < A_{\text{flower}} < A_{\text{gear}}.$$

The gear-shaped spots also have a bigger perimeter than the one of flower and star for a given number of petals:

$$P_{\text{flower}} \approx P_{\text{star}} < P_{\text{gear}}.$$

Finally, the gear-shaped spots appear to be the least compact shape, while the flower shape is as compact as the star

$$C_{\text{gear}} < C_{\text{flower}} \approx C_{\text{star}}.$$

All these results are illustrated in Fig. 3.15.

### Mesh definition

Similar to the problem with flower-shaped contact spots, simulations for these shapes were conducted using BEM. The star- and gear-shaped spots present the same dihedral symmetry  $D_m$  as for the flower-shaped, which allows us again to reduce the problem geometry. The mesh is divided in two region ensuring the consistent refinement on the edge, and in opposite the coarsening at the tip. The mesh size parameter is set to  $h_1$  on the edge, and is defined by  $h_0$  at the tip element. Those two mesh size parameters relates as  $h_1 = h_0/20$ . Examples of meshes are represented in Fig. 3.16 and Fig. 3.17, respectively for star and gear shape contact spot both with 32 dents, and height of  $\xi = 0.1$ . These meshes are both built with mesh sizes  $h_0/r_0 = 0.1$ .

### Flux results

Qualitatively, all three types of shapes show the same trend in the total flux evolution with the number of "petals": an initial steep increase and further saturation to a more or less constant value. The thermal conductivity of the gears is higher than that of the flowers, while the star-shaped configuration displays a lower conductivity. We could attribute this ordering to the only basic geometric parameter which significantly differs for all three of them, namely the area. Another consideration is the amount of area located closer to the outward boundary, which of course is higher for the gear like geometry than those of flower and star. In the limit of the infinite number of petals, the following result (initial guess obtained by extrapolation) is obtained (see parameter  $a$  in Table 3.2):

$$Q_{\text{star}}^{\text{lim}} \approx 0.903 < Q_{\text{flower}}^{\text{lim}} = 0.923 < Q_{\text{gear}}^{\text{lim}} = 0.978.$$

However, we would like to highlight once again that these values must be seen as a first guess, and a more rigorous assessment (e.g., using an accurate asymptotic analysis) is needed.

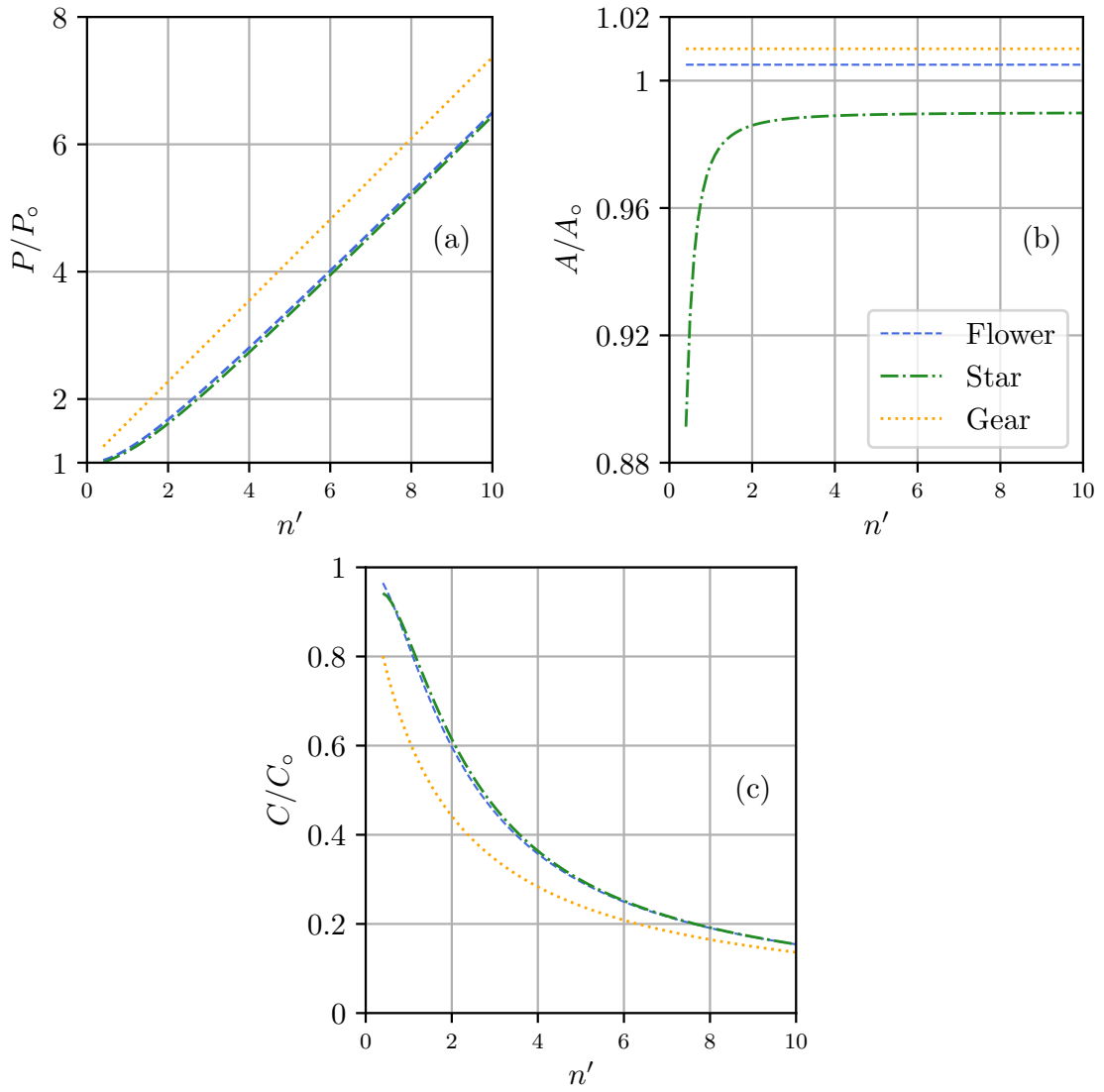


Figure 3.15: Comparison for perimeters (a), areas (b) and compactness (c) between the different shapes of contact spot

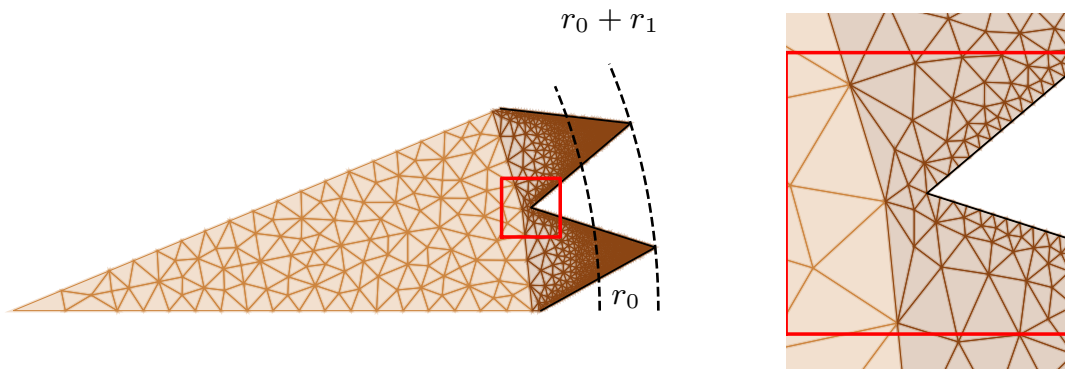


Figure 3.16: Mesh geometry for a star contact spot, with a number of ray  $n = 32$ , and height of  $\xi = 0.1$ , and with mesh size parameter of  $h_0/r_0 = 0.1$

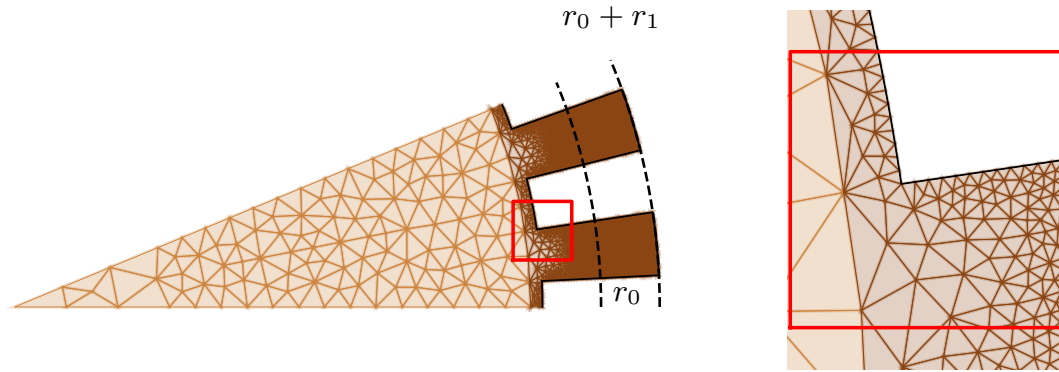


Figure 3.17: Mesh geometry for a gear contact spot, with a number of dent  $n = 32$ , and height of  $\xi = 0.1$ , and with mesh size parameter of  $h_0/r_0 = 0.1$

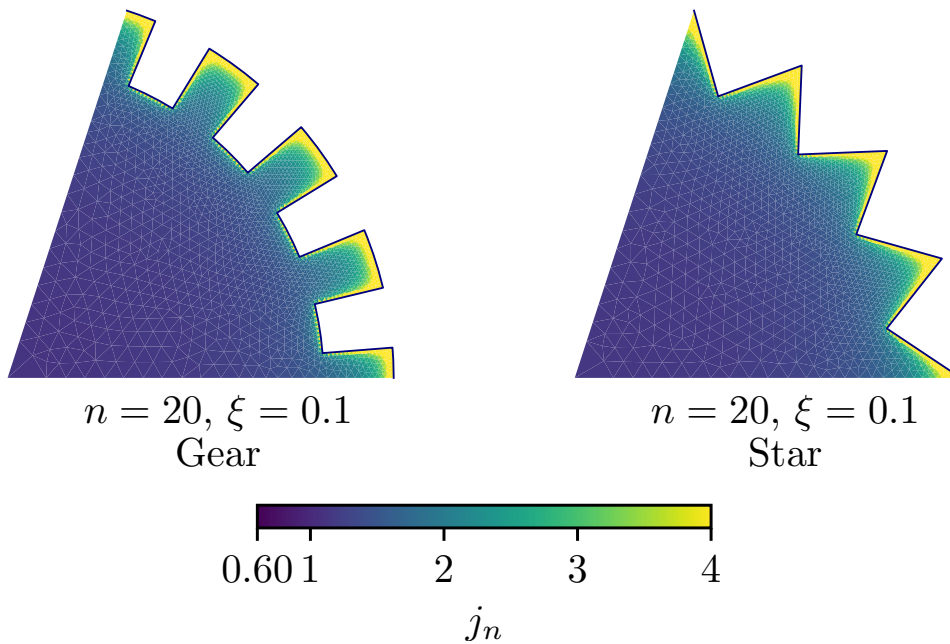


Figure 3.18: BEM result of the flux through a gear- and star-shaped spots of 20 petals and  $\xi = 0.1$ .

## 3.4 Conductivity of self-affine spots

### 3.4.1 Geometry of spots

Being inspired by shapes of contact clusters occurring in contact of random rough surfaces (see Fig. 3.1), in this section we study contact spots of model complex shapes presenting some randomness. The shapes under study (see Fig. 3.21) are modeled to be similar to coffee or ink stains. To take up the Archard's image of "protuberances on protuberances on protuberances" [Archard, 1957], we constructed contact-spots in a self-affine fashion by summing-up multiple harmonics. The goal is to imitate (to some extent) realistic contact spots occurring for surfaces with a rich spectral content and to expand the results obtained for single-harmonic flower-shaped spots to more complex forms.

The first step to generate a spot with self-affine boundary is to introduce a periodic perturbation function  $h(\theta)$  (3.16a) as a superposition of cosines which individually could be seen as flower-shaped spots. The summed up harmonics include all integer modes from a fixed interval  $k \in (k_l, k_s)$  with amplitudes equal to  $\xi_k$  (3.16b) which decay as a power-law

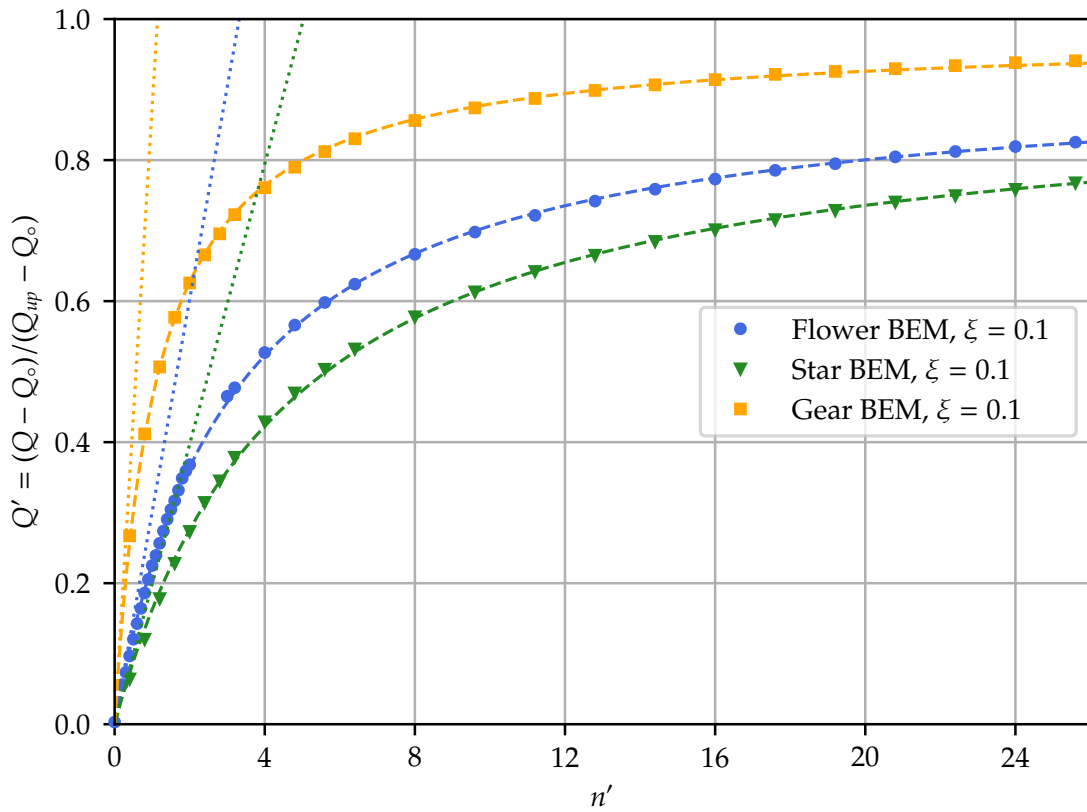


Figure 3.19: Results of the normalized flux for star-, gear- and flower-shaped spots with respect to the normalized "petal" parameter  $n' = \xi n$ . Least squares fit of Eq.(3.10) is also shown.

Simulation	Parameters		Coefficients		
	$\xi$	$n \in$	$a$	$b$	$ab$
Gear	0.1	[4, 256]	0.978	0.894	0.875
Flower	0.1	[1, 256]	0.923	0.326	0.301
Star	0.1	[4, 256]	0.903	0.220	0.199

Table 3.2: Fit parameters for Eq. (3.10) for the total flux of different multi-petal shapes.

of the mode number with an exponent involving the Hurst exponent  $H \in [0, 1]$  ensuring a self-affinity of the boundary. The height perturbation can be defined following these properties as detailed in the blue-frame below:

#### Definition: Self-affine height perturbation

Self-affine height perturbation,  $h$ , can be defined as a continuous function of polar coordinate  $\theta$ , as:

$$h(\theta) = \sum_{k=k_l}^{k_s} \xi_k \cos(k\theta + \theta_k^0), \quad h(\theta) = h(\theta + 2\pi), \quad \langle h \rangle = 0 \quad (3.16a)$$

$$\xi_k = \xi \left( \frac{k}{k_l} \right)^{-(0.5+H)}, \quad (3.16b)$$

The randomness is provided by the phase  $\theta_k^0$  which follows a uniform distribution on  $\theta_k^0 \in [-\pi, \pi)$ ; the average of this perturbation is zero. The perturbation  $h(\theta)$  thus

constructed follows a Gaussian distribution.

The power spectral density (PSD) decays as a power law of the wavenumber with the exponent  $-(1 + 2H)$ . This PSD function appeals the definition of the spectral breadth also known as Nayak parameter [Nayak, 1971], which is related to the "magnification" parameter presenting the ratio of the highest to lowest wavenumbers  $\zeta = k_s/k_l$  [Persson, 2001b].

The radius of a contact spot in polar coordinates  $r(\theta)$  can be readily defined with the perturbation  $h(\theta)$  by simply adding it up to one  $1 + h(\theta)$  and multiplying by a factor of the nominal contact spot radius  $r_0$  (3.17); naturally  $\langle r \rangle = r_0$ .

$$r(\theta) = r_0(1 + h(\theta)) \quad (3.17)$$

However, for such a construction, even if  $\xi < 1$  is imposed,  $r(\theta)$  can become negative. To overcome this problem, a regularization should be used, as presented in the blue frame below.

#### Definition: Radius definition of self-affine spot

The contour of the self-affine contact spot derives from the height perturbation  $h$ , as :

$$r(\theta) = r_0 \exp(h(\theta)), \quad (3.18)$$

with  $r_0$  is a positive radial parameter.

The two first terms of Taylor expansion is equivalent to (3.17), but the transformation (3.18) keeps the final shape well defined without self-intersections: even for  $h \rightarrow -\infty$ ,  $r \rightarrow 0$ . However, this transformation does not preserve the mean radius at  $r_0$ ; the radius will change with  $H$ ,  $\xi$ ,  $k_l$  and  $\zeta$  and could be characterized by  $\bar{r} = \langle r(\theta) \rangle / r_0$ . Within this formulation the parameter  $\xi$  plays the same role as in the study of flower-shaped spots: here, to the first order it presents the ratio between the amplitude of the first mode to the nominal radius. An example of two transformations (3.17),(3.18) is provided by Fig. 3.20 highlighting an example, where for transformation (3.17), the radius becomes negative. Therefore, for this study we adopt the exponential transformation (3.18). Several examples of complex shapes generated using the presented algorithm are shown in Figs. 3.21 for different values of  $k_l$ ,  $k_s$  and  $H$  but with the same set of random phases  $\theta_k^0$ . Naturally, for increasing Hurst exponent, the spot becomes smoother.

### 3.4.2 Geometrical characteristics

The initial height perturbation  $h$  follows normal distribution with zero mean and standard deviation  $\sigma_h$ , but it is not preserved by the exponential transformation (3.18). The obtained radius follows a *log-normal* distribution

$$P(r) = \frac{1}{r\sigma_h\sqrt{2\pi}} \exp\left(-\frac{\ln^2(r)}{2\sigma_h^2}\right). \quad (3.19)$$

Histograms shown in Fig. 3.22 present the probability density of the spot radius constructed for  $H = 0.25$ ,  $k_l = 8$ ,  $k_s = 16$  and two values of  $\xi = \{0.05, 0.1\}$  and computed over 1000 generated spots, the least squares fitted normal and log-normal densities are also plotted. For small values of  $\xi$ , the distribution is very close to the normal one, whereas for a higher value, it clearly follows the log-normal one.

The standard deviation  $\sigma_h$  or the variance  $\sigma_h^2$  of the height perturbation  $h(\theta)$  can be computed taking into account the orthogonality of cosine functions:

$$\sigma_h^2 = \frac{\xi^2}{2} \sum_{k=k_l}^{k_s} \left(\frac{k}{k_l}\right)^{-(1+2H)} \quad (3.20)$$

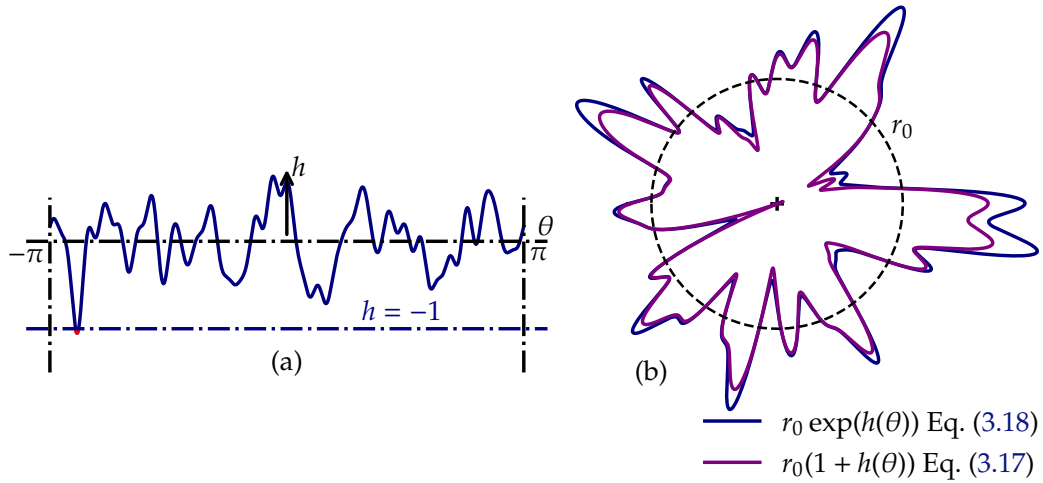


Figure 3.20: Example of self-affine spot construction for  $\xi = 0.25$ ,  $k_l = 4$ ,  $k_s = 32$  and  $H = 0.5$ : (a) height perturbation  $h(\theta)$  and (b) resulting spot radius for linear (3.17) and exponential (3.18) transformations.

After the transformation, the mean radius  $\langle r \rangle$  and the variance of the height distribution  $\sigma_r^2$  can be found as

$$\langle r \rangle = r_0 \exp(\sigma_h^2/2), \quad (3.21a)$$

$$\sigma_r^2 = [\exp(\sigma_h^2) - 1] \exp(\sigma_h^2), \quad (3.21b)$$

The mean value of the radius is no longer equal to  $r_0$ , but it tends to  $\langle r \rangle \rightarrow r_0$  as  $\sigma_h \rightarrow 0$ . Note that the variance could be expressed through the first terms of the Taylor expansion as  $\sigma_r^2 \approx \sigma_h^2 + 1.5\sigma_h^4 + 7/6\sigma_h^6 + O(\sigma_h^8)$ , which demonstrates that for small values of  $\sigma_h$ ,  $\sigma_r \approx \sigma_h$  with a high accuracy. The comparison of the analytical expression of the variance Eq. (3.21b) with numerically evaluated standard deviation is presented in Appendix C.1.

The standard deviation of radius is an important geometric characteristic of the spot. However, the standard deviation of the gradient and laplacian of the radius as well as Nayak parameter [Nayak, 1971] could also have an effect on the conductivity of the spot. These geometrical characteristics are related to spectral moments  $m_0$ ,  $m_2$  and  $m_4$  undergoes slight change in definition, recalling the initial definition.

#### Definition: Spectral moments for rough contour

Considering a surjective function for the radius of a contact spot,  $r$ , spectral moments can be namely defined as:

$$m_0 = \sigma^2, \quad (3.22a)$$

$$m_2 = \langle |\nabla r|^2 \rangle = \frac{1}{2\pi} \int_0^{2\pi} \left( \frac{1}{r(\theta)} \frac{\partial r}{\partial \theta} \right)^2 d\theta, \quad (3.22b)$$

$$m_4 = \frac{1}{2\pi} \langle |\Delta r|^2 \rangle = \int_0^{2\pi} \left( \frac{1}{r^2(\theta)} \frac{\partial^2 r}{\partial \theta^2} \right)^2 d\theta, \quad (3.22c)$$

In the limit of infinitesimal perturbations  $\xi \ll 1$ , we can use the following analytical equations for the 2nd and 4th spectral moments (the 0th moment is nothing but the



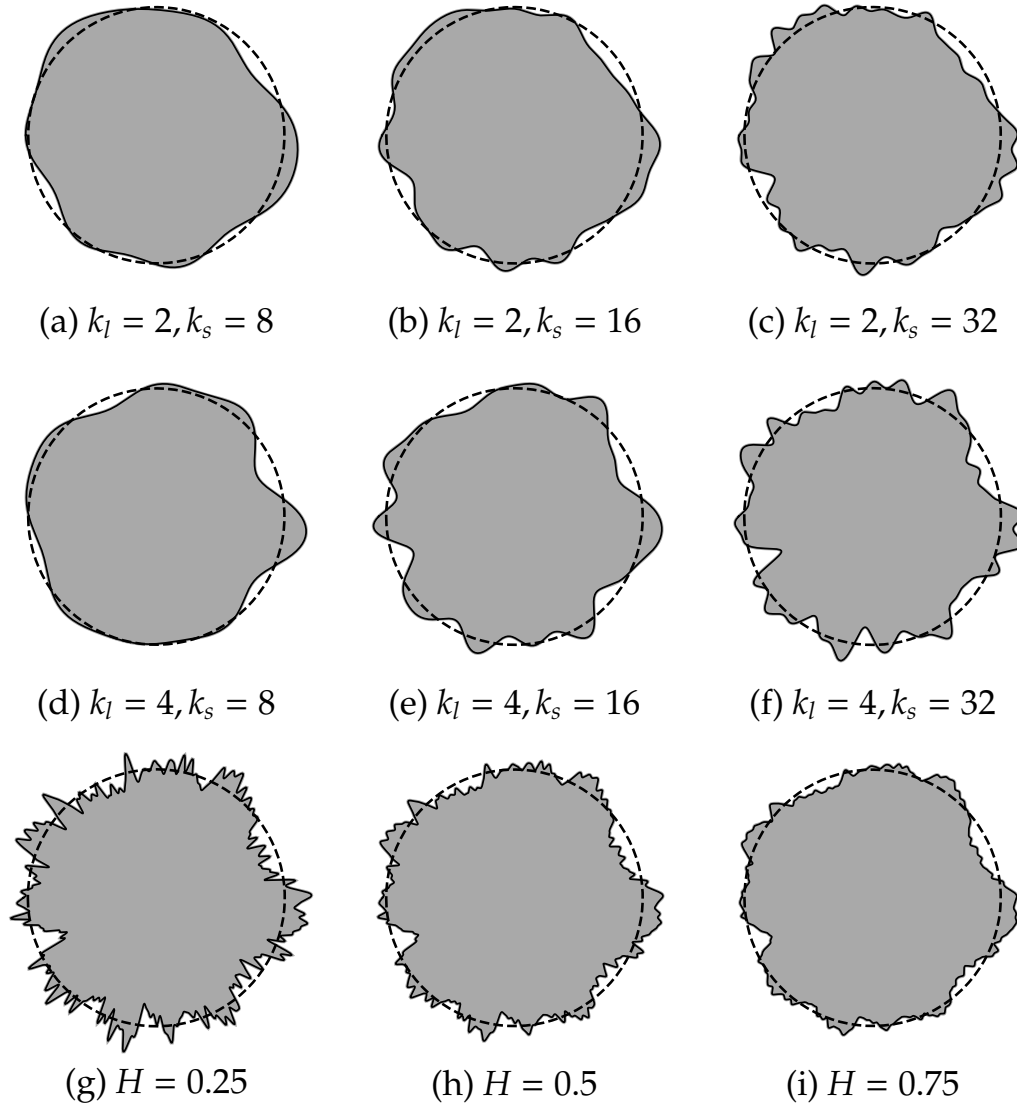


Figure 3.21: Examples of self-affine spots and their geometrical characteristics for  $\xi = 0.1$ ,  $k_l = 2$ ,  $k_s = \{8, 16, 32\}$ ,  $H = 0.25$  (a,b,c) (a)  $\bar{r} = 1.0017$ ,  $\sigma = 0.057$ , (b)  $\bar{r} = 1.0020$ ,  $\sigma = 0.063$ , (c)  $\bar{r} = 1.0023$ ,  $\sigma = 0.067$ ; for  $\xi = 0.1$ ,  $k_l = 4$ ,  $k_s = \{8, 16, 32\}$ ,  $H = 0.25$  for (d,e,f) (d)  $\bar{r} = 1.0019$ ,  $\sigma = 0.062$ , (e)  $\bar{r} = 1.0029$ ,  $\sigma = 0.075$ , (f)  $\bar{r} = 1.0036$ ,  $\sigma = 0.084$ ; for  $\xi = 0.1$ ,  $k_l = 4$ ,  $k_s = 128$ ,  $H = \{0.25, 0.5, 0.75\}$  for (g,h,i) (g)  $\bar{r} = 1.0044$ ,  $\sigma = 0.094$ , (h)  $\bar{r} = 1.0028$ ,  $\sigma = 0.074$ , (i)  $\bar{r} = 1.0020$ ,  $\sigma = 0.063$

variance of radius computed in (3.21b)):

$$m_2 = \frac{\xi^2}{2} \sum_{k_l}^{k_s} k^2 \left(\frac{k}{k_l}\right)^{-(1+2H)}, \quad m_4 = \frac{\xi^4}{2r_0^2} \sum_{k_l}^{k_s} k^4 \left(\frac{k}{k_l}\right)^{-(1+2H)} \quad (3.23)$$

The comparison of Eq. (3.23) with numerically evaluated moments is presented in Appendix C.1. For flower-shaped spots, the spectral moments simplify to the following forms:

$$m_0^f = \frac{r_1^2}{2} = \frac{\xi^2 r_0^2}{2}, \quad m_2^f = \frac{r_1^2 n^2}{2r_0^2} = \frac{\xi^2 n^2}{2} = \frac{n'^2}{2}, \quad m_4^f = \frac{r_1^2 n^4}{2r_0^4} = \frac{\xi^2 n^4}{2r_0^2} = \frac{n'^2 n^2}{2r_0^2} \quad (3.24)$$

Since the normalized conductivity for flower-shaped spots was shown to depend exclusively on  $n' = \xi n$  (see Eq. (3.10)), we could suggest that for a similar normalization, the

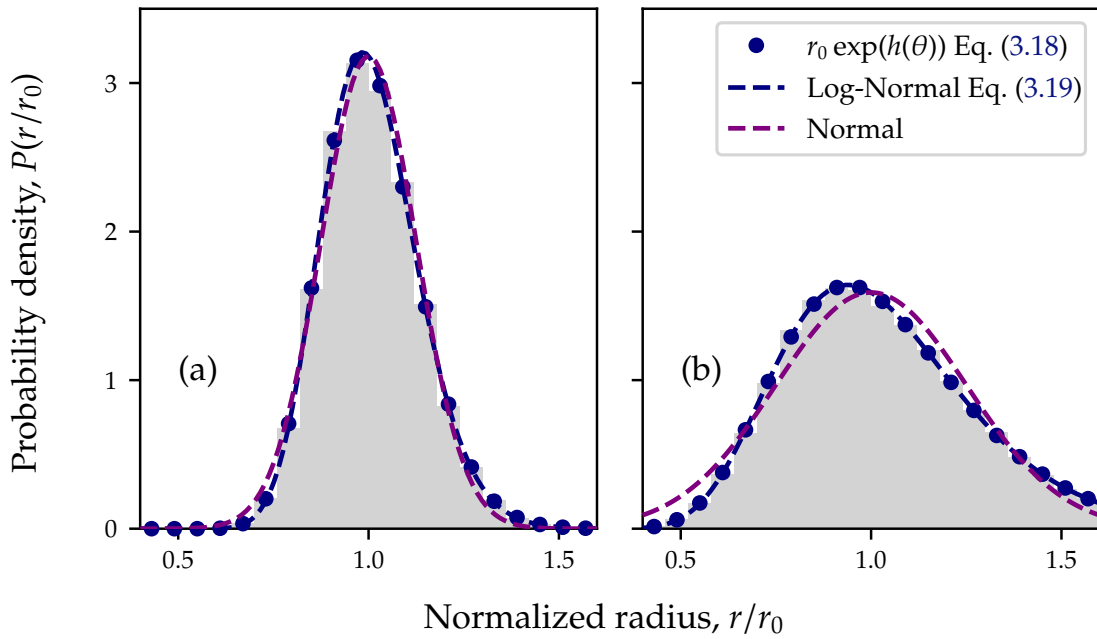


Figure 3.22: Distribution of the radius for constructed self-affine spots for  $H = 0.25, k_l = 8, k_s = 16$  and (a)  $\xi = 0.05$  and (b)  $\xi = 0.1$ . Least squares fit of the normal and log-normal distributions is also presented.

main characteristic affecting the conductivity of self-affine spots will be the standard deviation of the gradient  $\sqrt{\langle |\nabla r|^2 \rangle} = \sqrt{m_2}$ . In addition, it could be shown that the area of a spot is an affine function of  $m_0$ :  $A \approx \pi r_0^2(1 + am_0)$ , and its perimeter is an affine function of  $\sqrt{m_2}$ :  $P \approx 2\pi r(1 + b\sqrt{m_2})$ , where  $a, b$  are positive constants.

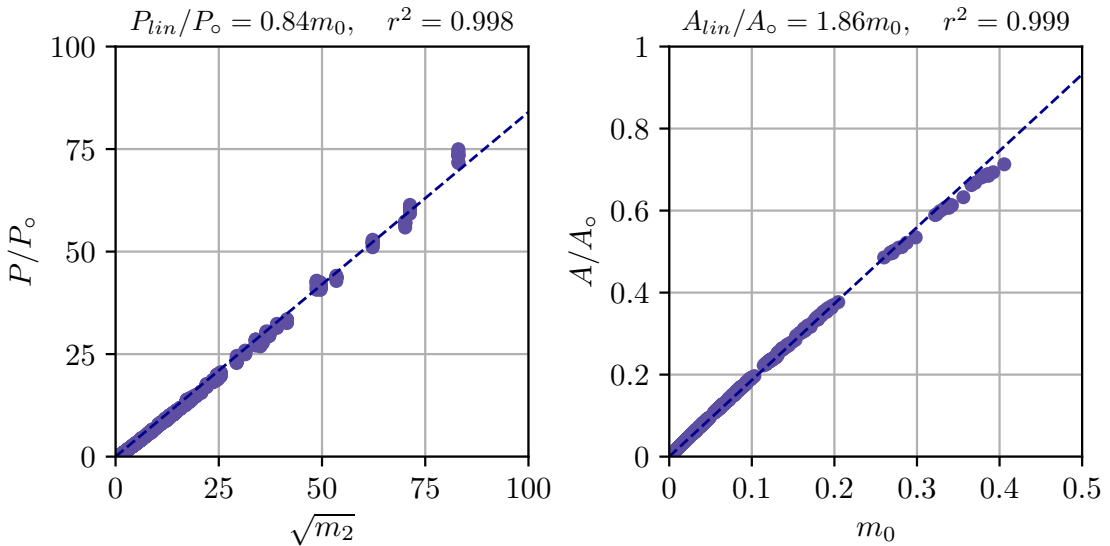


Figure 3.23: Perimeter and area's growth in function of rough moment  $m_2$  and  $m_0$  respectively

### Self-affine property

Following the definition given by Meakin [Meakin, 1998], the self-affine property pertains to the relation between the height of the perturbation and the zooming scale. In this case,

the contour is parametrized by the angular position  $\theta$ . The zooming scale can be resumed by a phase change  $\delta\theta$ . The self-affine property can be formulated as follows,

$$\langle |r(\theta) - r(\theta + \delta\theta)| \rangle \sim \delta\theta^H \quad (3.25)$$

This property is experimented in Fig. 3.24, for various values of  $H$ . To evaluate the height perturbation for a decreasing  $\delta\theta$ , we need to dispense with the upper-cutoff wavenumber  $k_s$ , to ensure that we still get height perturbation beyond any zooming scale. The mean absolute distance between contour radius is measured over 10 random distribution, using  $k_l = 8$  and  $\xi = 0.05$ . Then the results can be identified using a law  $a\delta\theta^b$ , with  $a, b$  two positive parameters. The low-cutoff wavenumber needs to be high enough, avoiding the dominant macroscale results, resulting in some inconsistencies. The results of the fitting process are represented in legend in Fig. 3.24, and we are interested in the exponent.

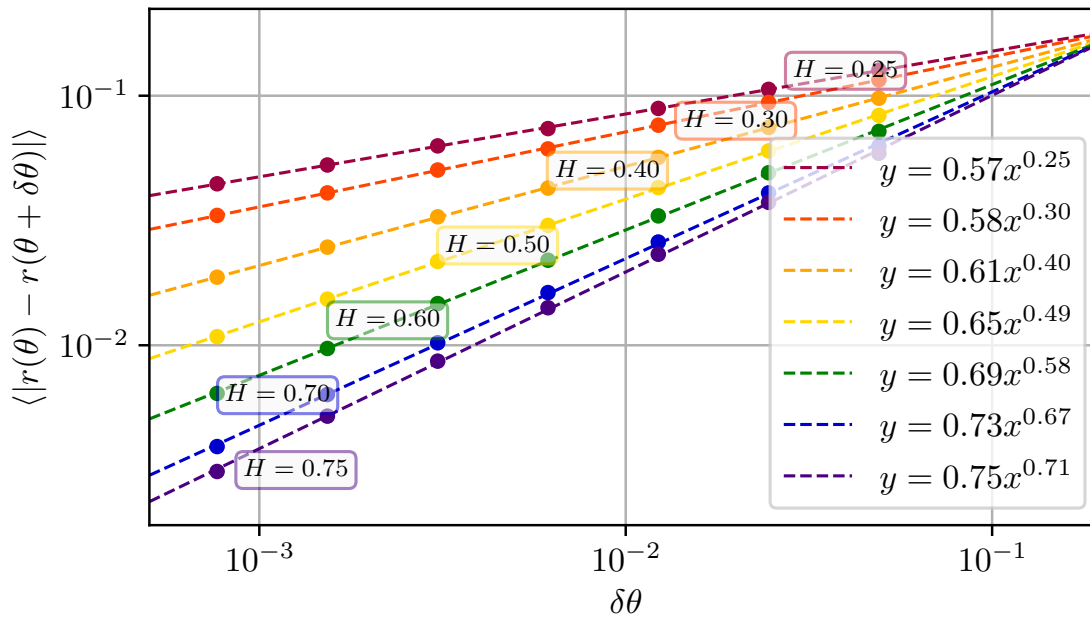


Figure 3.24: Self affine property in zooming of ink-shaped contact spot

The exponent values of  $\delta\theta$  are consistent with the Meakin's definition Eq. (3.25) for low value of  $H$ . This condition is more challenging to meet for higher value of  $H$  due to the asymptotic nature of the definition. Surprisingly, more consistent value of exponent are obtained by only using the two lowest values of  $\delta\theta$  displayed in Fig. 3.24. The Hurst parameter relates to the fractal dimension of the object, like for the Weierstrass function in which  $H = 2 - D$ .

### Mesh definition

To ensure a gradual mesh coarsening towards the center of the contact patch, a geometrical point is added in the center with a mesh parameter of  $h_0/r_0$ . In practice  $h_1$  is set to  $0.1h_0$ . Two mesh examples can be seen in Fig. 3.25 and Fig. 3.26, having  $h_1/r_0$  values of 0.02 and 0.012, respectively. The refinement of the mesh at the edges aligns well with the geometry, successfully preventing element degradation, whether at peak points or within contour recesses, as depicted in Fig. 3.26. The number of elements increases with the length of the contour and the inverse of the mesh size at the edge  $h_1$ . The contour is first discretized linearly in  $P/h$ . This number of segments increases as the second moment  $m_2$  grows, inducing a total number of elements of 6212 for the first case Fig. 3.25, and of 34340 elements for the second geometry Fig. 3.25, consistent with the roughness growth.

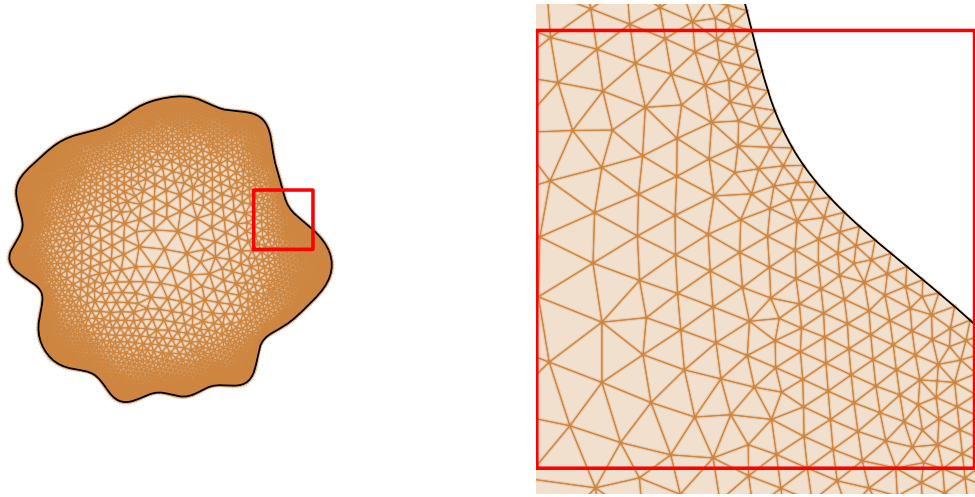


Figure 3.25: Mesh definition of a self-affine shaped contact spot with  $k_l = 4$ ,  $k_s = 16$ , and  $H = 0.75$ , with a mesh size parameter of  $h_0/r_0 = 0.2$

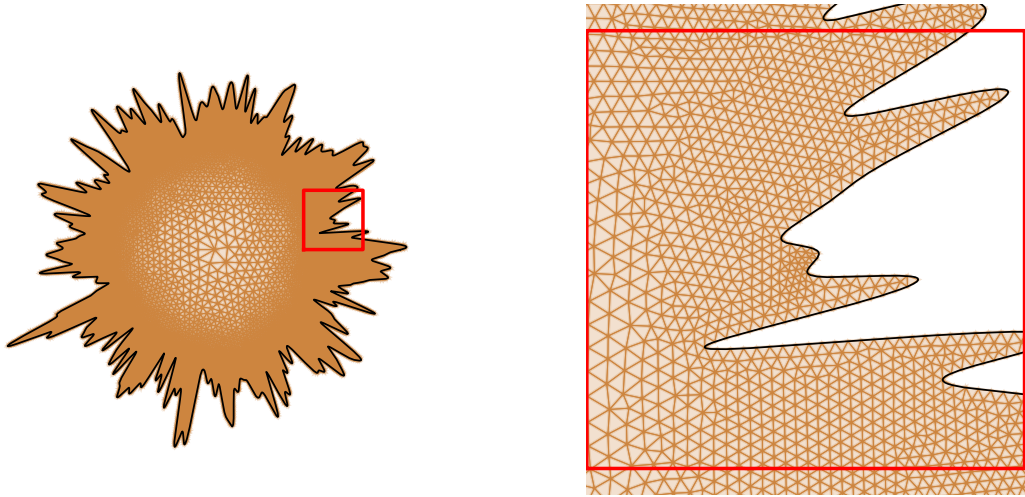


Figure 3.26: Mesh definition of a self-affine shaped contact spot with  $k_l = 8$ ,  $k_s = 128$ , and  $H = 0.25$ , with a mesh size parameter of  $h_0/r_0 = 0.12$

### Normalization and result

In contrast to the study of flower-shaped spots, this study is no-longer deterministic and requires to take into account the randomness of the studied geometries. The total flux for a given geometry  $Q_i$ , defined as an independent event, is assumed to have a consistent average value  $\mu(Q)$  and a standard deviation  $\sigma(Q)$  across the same set of spot-generative parameters. This section aims to understand the average behavior based on these parameters. To achieve this, we compute average values for numerous realizations of spot geometries. However, this yields only an approximate value for  $\langle Q \rangle$ , which depends on the number of realizations  $n$ . In practice, the standard deviation of the mean value scales as  $\sigma(\langle Q \rangle) = \sigma(Q)/\sqrt{n}$ . The Bienaymé-Chebyshev inequality aids in establishing a confidence interval implying a parameter  $\gamma \in (0, 1)$ : the probability to find the mean value  $\langle Q \rangle$  outside the interval  $\pm\sigma(Q)/\sqrt{n\gamma}$  around its theoretical value  $\mu(Q)$  is smaller than  $\gamma$  whatever the true underlying distribution, i.e.

$$P\left(|\mu(Q) - \langle Q \rangle| \geq \frac{\sigma(Q)}{\sqrt{n\gamma}}\right) \leq \gamma, \quad (3.26)$$

Equivalently, the probability is  $(1 - \gamma)$  to find the mean value in the confidence interval  $\pm\sigma(Q)/\sqrt{n\gamma}$ . When there are 11 simulations, the interval of confidence spans approximately  $\pm 3\sigma(Q)$  with the probability of 99%, effectively encapsulating the mean value  $\langle Q \rangle$ . In order to reduce the interval to one standard deviation with the same accuracy, i.e.  $\sqrt{n\gamma} = 1$  for  $\gamma = 0.01$  one would need to carry out  $n = 100$  simulations. For  $n = 11$  the probability to find the mean value in one standard deviation interval, i.e.  $\sqrt{11\gamma} = 1$  is higher than  $\approx 9\%$ . While the Bienaymé-Chebyshev inequality provides a rigorous lower bound, the actual accuracy of our results can overpass this conservative limit. To balance the computational efforts and the accuracy, the number of BEM simulation results per combination of parameters was set to  $n = 11$ , and this dataset was utilized to estimate the mean value and the confidence interval obtained from the measurement of the standard deviation.

An example of flux distribution obtained by fast-BEM is displayed in Fig. 3.27 for  $\xi = 0.05$ ,  $k_l = 8$ ,  $k_s = 128$  and  $H = 0.25$ . The normal flux remains singular at the edge but less pronounced at troughs than at crests as shown previously for the flower-shaped contact spot. Compared to the latter, it appears more difficult to construct a good mesh for self-affine spots efficiently (fine mesh near the border and coarse far from border). The mesh size was prescribed as a function of the edge curvature and as a function of the shortest distance to the border. See zoom in Fig. 3.27, the finest used mesh reach  $N_e = 34\,340$  elements. As previously, to employ the Richardson extrapolation, two meshes of different density were used to obtain accurate results.

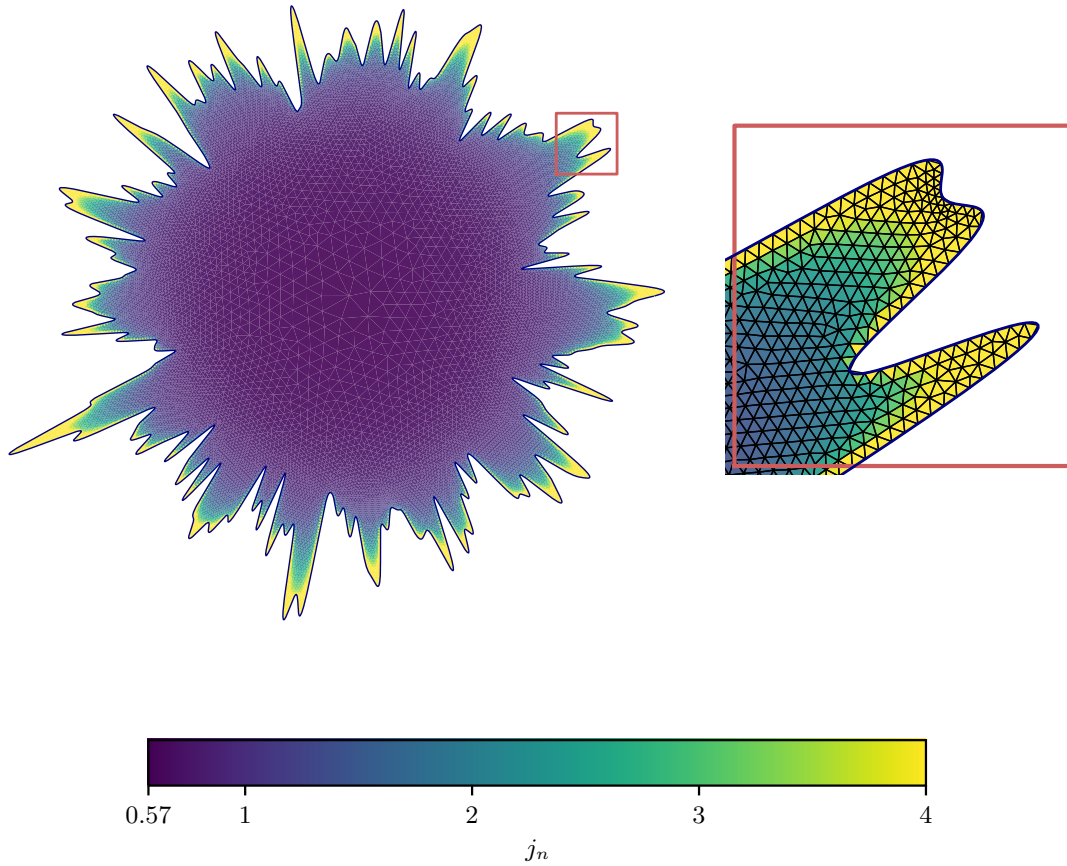


Figure 3.27: Example of simulation results representing the flux distribution for a self-affine spot with  $\xi = 0.05$ ,  $k_l = 8$ ,  $k_s = 128$  and  $H = 0.25$ .

For the global flux analysis, geometrical characteristics  $\mathcal{A} = \{\langle r \rangle, \sqrt{m_0}, \sqrt{m_2}, \sqrt{m_4}, H\}$ :

(1) the mean radius  $\langle r \rangle$ , (2) the standard deviation of the radius  $\sqrt{m_0}$ , (3) of its gradient  $\sqrt{m_2}$ , (4) of its laplacian  $\sqrt{m_4}$  and (5) the Hurst exponent describe sufficiently well the geometry. The initial set of independent generative parameters is  $\mathcal{I} = \{r_0, \xi, k_l, k_s, H\}$  and contains (I) radius  $r_0$ , (II) amplitude of perturbation  $\xi$ , (III) lower  $k_l$  and (IV) upper  $k_s$  cutoffs, and (V) the Hurst exponent  $H$ . The set  $\mathcal{A}$  is easy to measure for any spot and it allows to separate their effects on the total flux; the generative set  $\mathcal{I}$  is complete and dimensionless. Therefore, as soon as results are presented, we will carry out a sensitivity analysis.

The first task is to normalize the total flux  $Q$  produced by self-affine spots. There are two main options: it can be normalized by the flux of an equivalent circular contact spot (a) of the same mean radius  $Q_o = 4kU_0\langle r \rangle$  or (b) of the same area. The first option was selected since the mean radius also enters in the set of parameters, moreover  $Q_o$  is equivalent to the definition of  $Q_{\min}$  used for the flower-shaped contact spot. The normalized total flux is thus defined by

$$Q' = \frac{Q}{Q_o} = \frac{Q}{4kU_0\langle r \rangle} \quad (3.27)$$

Therefore, since the problem does not have an internal length, we can exclude the mean radius  $\langle r \rangle$  from the set of parameters defining the total flux  $Q'$  and consider two sets of dimensionless parameters:

- Geometrical set of parameters  $\mathcal{A}' := \{\sqrt{m_0}/\langle r \rangle, m_2/\langle r \rangle \sqrt{m_4}, H\}$
- Generative set of parameters  $\mathcal{I}' = \{\xi, k_l, k_s, H\}$

By analogy with the maximal total flux  $Q_{\text{up}}$  defined for flower-shaped spots, we could define an equivalent upper limit for self-affine spots. It is not a good idea to define it as the maximal radius of the self-affine spot as it could tend to infinity for very high number of modes. However, the variance of the flower-shaped spot  $m_0^f$ , Eq. (3.24), provides us with a hint getting back the half-petal length  $r_1$  in another way, i.e. using this equation we can express it as  $r_1 = (2m_0^f)^{1/2}$ ; therefore, the limit characteristic radius could be expressed as  $\langle r \rangle + \sqrt{2m_0}$ . Thus, the difference between two flows used for normalization takes the following form:

$$Q_{\text{up}} - Q_o = 4kU_0 \sqrt{2m_0}$$

This term entails the definition of a normalization for rough contact spot, such as self-affine contact spot.

### Model: Normalization for self-affine spot

Recalling the renormalization between zero and one as was used for the flower-shaped spots, we could define the renormalized flux as:

$$Q'' = \frac{Q - Q_o}{Q_{\text{up}} - Q_o} = \frac{Q}{4kU_0 \sqrt{2m_0}} - \frac{\langle r \rangle}{\sqrt{2m_0}} \quad (3.28)$$

The total flux normalized according to Eq. (3.27) is presented in Fig.3.28 for all simulated self-affine spots. These spots are constructed by changing the lower cutoff  $k_l = \{2, 4, 8\}$  and for four values of the upper cutoff  $k_s = \zeta k_l$  with the magnification  $\zeta = \{4, 8, 16, 32\}$ . The Hurst parameter  $H$  takes the values  $H = \{0.25, 0.3, 0.4, 0.5, 0.6, 0.7, 0.75\}$ . The colors are used to distinguish the 3 sets of the results according to different  $k_l$ . In each color set, the results are distinguished by their marker style according to values of magnification  $\zeta$ , moreover, the higher the  $\zeta$ , the darker the color. Along every result-curve the Hurst exponent  $H$  changes as shown by the arrow: the smaller the  $H$ , the higher the flux. The curves are entwined together, but they seem to follow the same trend. Plotting the data with respect to geometrical parameters  $\mathcal{A}'$  offers a better representation than the

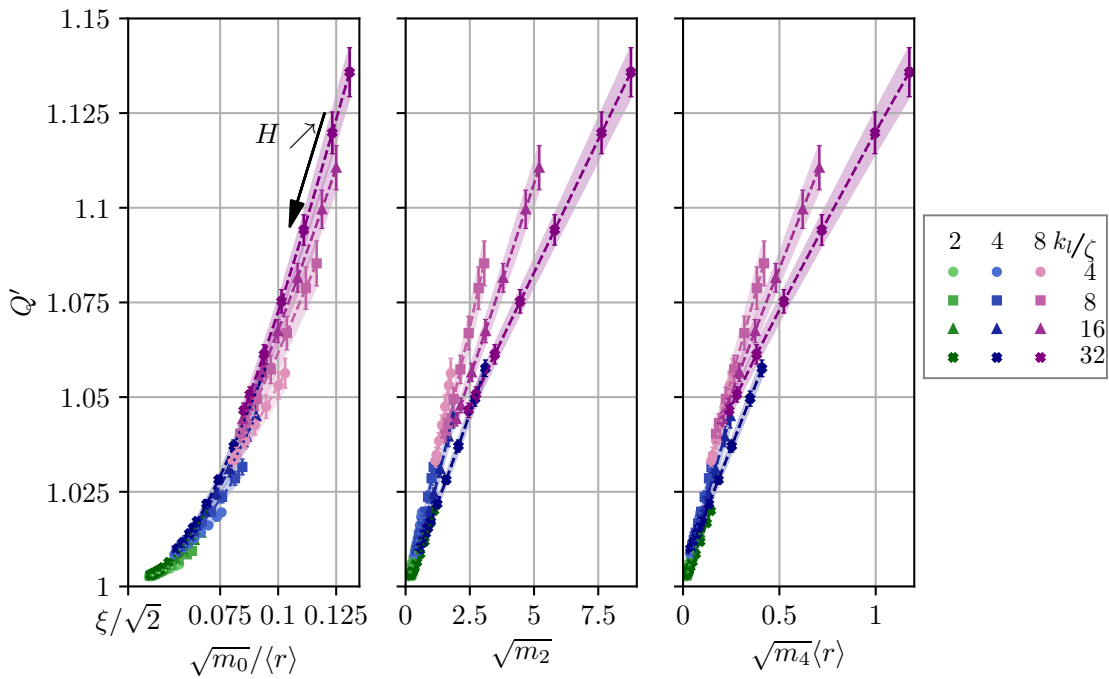


Figure 3.28: Normalized flux (3.27) of self-affines spots: for  $k_l = \{2, 4, 8\}$ ,  $\zeta = \{4, 8, 16, 32\}$ ,  $H = \{0.25, 0.3, 0.4, 0.5, 0.6, 0.7, 0.75\}$ . The mean normalized flux is plotted with a marker and shaded around according to the confidence interval defined for  $\gamma = 0.05$  (with a rate of confidence of 95% ).

use of the generative set of parameters  $I'$ . The variation in slope seems to be controlled by parameter  $\zeta = k_s/k_l$ : increasing  $\zeta$  increases the average slope with respect to  $\sqrt{m_2}/\langle r \rangle$  and decreases the average slope with respect to  $\sqrt{m_2}$  and  $\langle r \rangle \sqrt{m_4}$ .

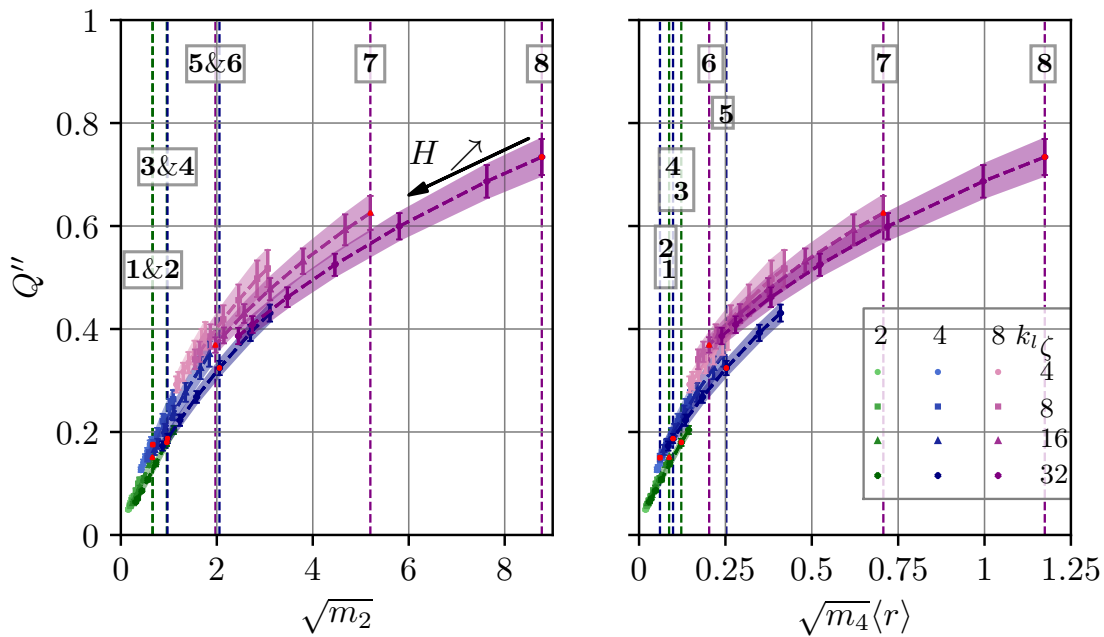


Figure 3.29: Renormalized flux, Eq. (3.28) of self-affine spots: for  $k_l = \{2, 4, 8\}$ ,  $\zeta = \{4, 8, 16, 32\}$ ,  $H = \{0.25, 0.3, 0.4, 0.5, 0.6, 0.7, 0.75\}$ . The mean normalized flux is plotted with a marker and shaded around according to the confidence interval width of  $\pm 1.34\sigma$  and of 95% of accuracy; vertical lines and numbers correspond to spots shown in Fig. 3.30.

The results of the renormalized flux Eq.(3.28) with respect to  $\sqrt{m_2}$  and  $\langle r \rangle \sqrt{m_4}$  are presented in Fig.3.29. However, the role of the fourth moment in the form  $\langle r \rangle \sqrt{m_4}$  seems to be strongly correlated with  $\sqrt{m_2}$  and does not bring much additional information. The lack of simple dependency of the normalized flux with respect to geometrical characteristics pushes us to suggest an alternative normalization. The shown results seem to depend strongly on  $k_l$  parameter. By exploring a wider spreading of  $\sqrt{m_2}$  for different  $k_l$ , we hope to easily identify their influence, which is the objective of the following sections.

To provide a visual geometrical interpretation in the flux variation (see Fig. 3.30) related to geometrical characteristics of self-affine spots, we present particular shapes along with the values of corresponding geometrical characteristics and of the total flux in Table 3.3, the location of these particular spots is also highlighted in Fig. 3.29. The pairs  $\{S_1, S_2\}$ ,  $\{S_3, S_4\}$  and  $\{S_5, S_6\}$  have close values of  $\sqrt{m_2}$ . The difference between the flux of spots  $S_5$  and  $S_6$  highlights the fact that the flux does not depend only on the second moment. Nevertheless, this could be seen as a second order effect compared to that of  $\sqrt{m_2}$ . Spots  $S_7$  and  $S_8$  are among the "roughest" spots and possess the highest flux.

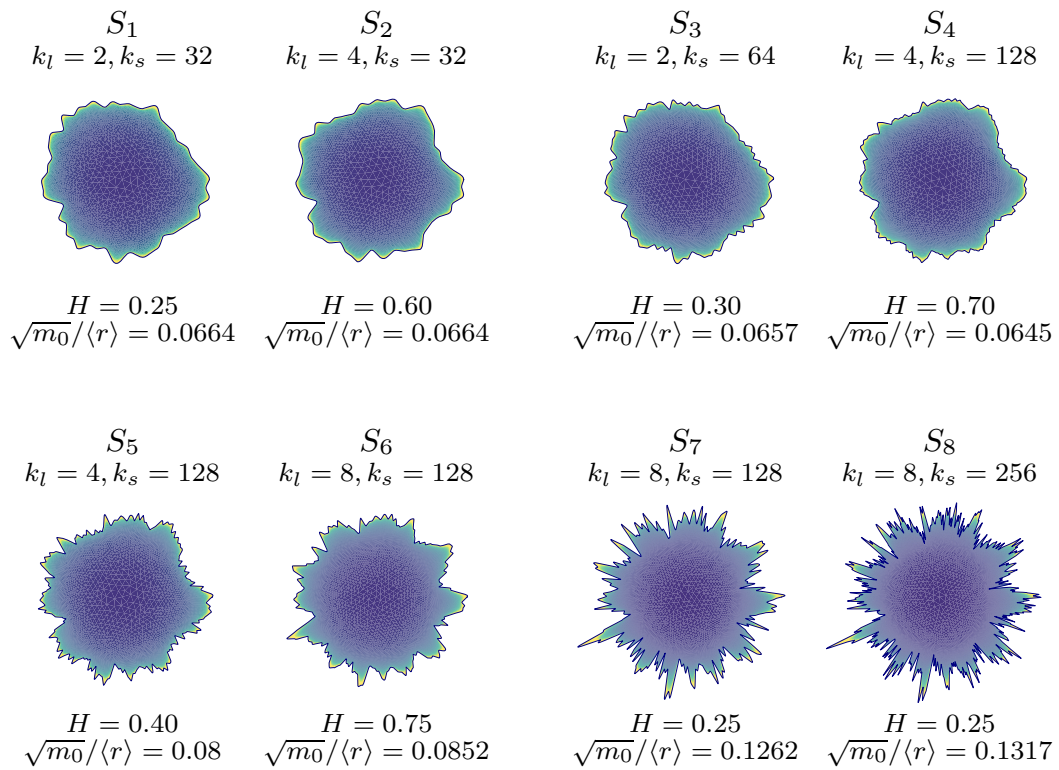


Figure 3.30: Examples of self-affine spots with corresponding geometrical characteristics and resulting total flux; the corresponding data points are highlighted in Fig. 3.29.

### Results with renormalized standard deviation

As presented in Figs. 3.28 and 3.29, the results are clustered with respect to  $k_l$ . To have more control on geometrical characteristics, we renormalize the generative function  $h(\theta)$  in order to prescribe its dimensionless standard deviation  $\sigma_h = \sqrt{m_{0,h}}$  (see Eq. (3.20)):

$$h(\theta) = \sqrt{\frac{2m_{0,h}}{s}} \sum_{k=k_l}^{k_s} \xi_k \cos(k\theta + \theta_k^0), \quad s = \sum_{k=k_l}^{k_s} \xi_k^2 \quad (3.29)$$

with  $\xi_k$  defined by Eq. (3.16b). The exponential transformation from  $h(\theta)$  to radius  $r(\theta)$  (3.18) remains intact. Then, for the normalized generative parameters we have:



Spot #	$Q''$	Parameters $\mathcal{A}'$			Parameters $\mathcal{I}'$			
		$\sqrt{m_0}/\langle r \rangle$	$\sqrt{m_2}$	$\sqrt{m_4}\langle r \rangle$	$\xi$	$k_l$	$k_s$	$H$
$S_1$	0.151	0.0664	0.658	14	0.05	2	32	0.25
$S_2$	0.172	0.0664	0.666	12.7	0.05	4	32	0.6
$S_3$	0.173	0.0657	0.958	39.8	0.05	2	64	0.3
$S_4$	0.184	0.0645	0.972	63.8	0.05	4	128	0.7
$S_5$	0.317	0.0800	2.06	163	0.05	4	128	0.4
$S_6$	0.380	0.0852	1.97	130	0.05	8	128	0.75
$S_7$	0.644	0.126	5.12	446	0.05	8	128	0.25
$S_8$	0.749	0.182	8.77	1493	0.05	8	256	0.25

Table 3.3: Parameters for spots shown in Fig. 3.30 and the resulting total flux.

$\mathcal{I}'' = \{\sqrt{m_{0,h}}, k_l, k_s, H\}$  and for the geometrical ones we still have  $\mathcal{A}'$ . The main goal for such a choice is to uncorrelate  $\sqrt{m_0}/\langle r \rangle$  and  $\sqrt{m_2}$  and thus to level down  $m_0$  for  $k_l = 8$ , and to level it up for  $k_l = 2$ . Note also that  $\sqrt{m_0}/\langle r \rangle \approx \sqrt{m_{0,h}}$  for small values of the latter, see (3.21b) and its Taylor expansion.

The results of this set of simulations for the renormalized flux (3.28) are presented in Fig. 3.31 with respect to the standard deviation of the radius gradient  $\sqrt{m_2}$ ; lower cutoffs  $k_l = 2$  (orange circles and red squares) and  $k_l = 8$  (green crosses and cyan triangles) were used. In addition, different colors correspond to different magnifications:  $\zeta = 4$  for red squares and cyan triangles,  $\zeta = 8$  for orange circles and green crosses. The Hurst exponent takes three values  $H = \{0.25, 0.50, 0.75\}$ . For the same value of  $\sqrt{m_{0,h}} \approx \sqrt{m_0}/\langle r \rangle$ , thanks to the variation of the Hurst exponent, the value of  $\sqrt{m_2}$  varies within a certain interval, such data points are connected by a line. Every set of such lines (of the same shade) align along their master curve. Such results demonstrate that even though the standard deviation  $\sqrt{m_0}/\langle r \rangle$  controls the thermal flux to a large extent, the standard deviation of the gradient  $\sqrt{m_2}$  also influences the result. This conclusion is possible since  $\sqrt{m_2}$  does not enter in the flux normalization (3.28). The flux increases with respect to both  $\sqrt{m_0}/\langle r \rangle$  and  $\sqrt{m_2}$  as well as with respect to  $\langle r \rangle \sqrt{m_4}$  because of the strong correlation of the latter with the second moment. For an equivalent  $\sqrt{m_2}$ , the flux is higher for spots with a lower magnification  $\zeta$ .

To provide a geometrical meaning to these results, a coupled pairs of self-affine spots  $\{S_1, S_2\}$ ,  $\{S_3, S_4\}$ ,  $\{S_5, S_6\}$  with different spectral content but similar value of  $m_2$  are displayed in Fig. 3.32 and are highlighted in Fig. 3.31 and in Table 3.4. Remarkably, the three foremost right lines (d) in the figure seem to continue each other. The spots  $\{S_5, S_6\}$  well illustrate this link: they in fact have the same number of modes, but different  $H$  and  $m_{0,h}$ .

Spot #	$Q''$	Parameters $\mathcal{A}'$			Parameters $\mathcal{I}''$			
		$\sqrt{m_0}/\langle r \rangle$	$\sqrt{m_2}$	$\sqrt{m_4}\langle r \rangle$	$\sqrt{m_{0,h}}$	$k_l$	$k_s$	$H$
$S_1$	0.189	0.100	0.507	5.10	0.100	2	16	0.5
$S_2$	0.213	0.143	0.515	2.84	0.141	2	8	0.5
$S_3$	0.510	0.0995	1.56	33.6	0.100	8	32	0.5
$S_4$	0.476	0.0705	1.56	61.9	0.005	8	64	0.5
$S_5$	0.665	0.0997	2.62	114	0.100	8	64	0.25
$S_6$	0.666	0.141	2.61	94.1	0.141	8	64	0.75

Table 3.4: Parameters for spots shown in Fig. 3.32 and the resulting total flux. The spots are ordered according to increasing  $\sqrt{m_0}$ .

Finally, we would like to point out that (1) the influence of  $\sqrt{m_0}$  is ultimately handled by normalization; (2) the results are rather well clustered along a simple trend line in

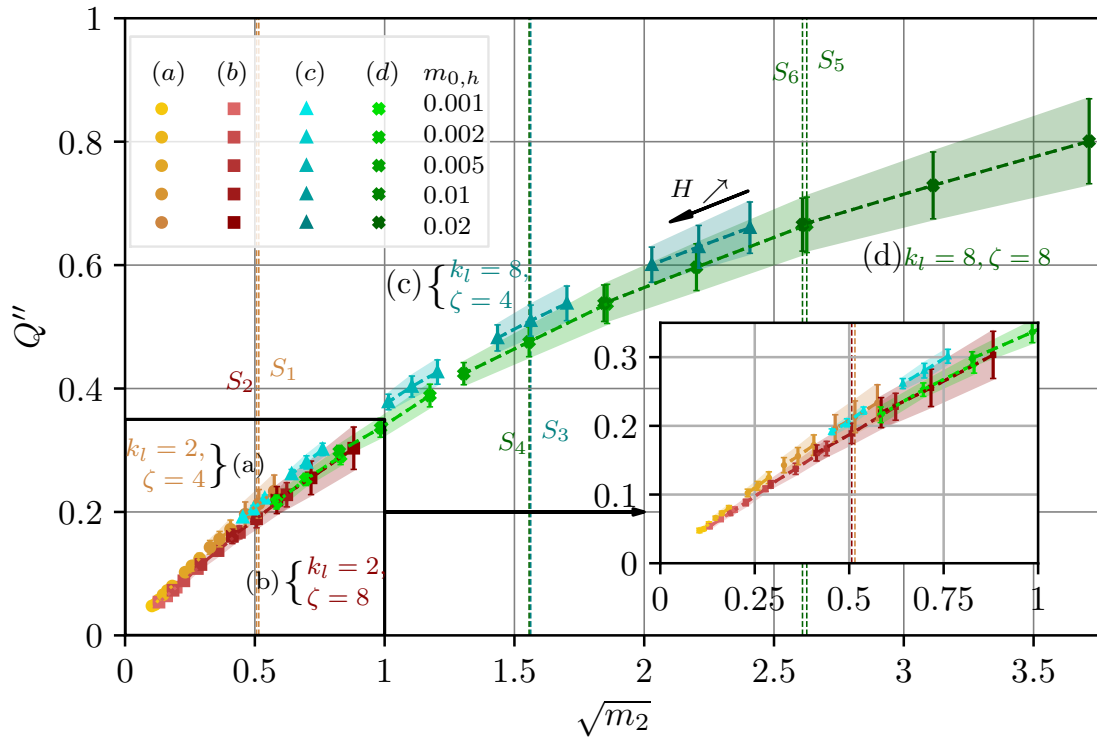


Figure 3.31: Results for the renormalized total flux eq. (3.28) of self-affine spots with respect to standard deviation of the radius gradient  $\sqrt{m_2}$  obtained with controlled standard deviation  $\sqrt{m_{0,h}} \approx \sqrt{m_0}/\langle r \rangle$ .

terms of  $m_2$ , (3) but clearly there is a dependence on  $\zeta$ . At the same time, the shape of the trend is very similar to what was observed for multi-petal spots and we recall that  $\sqrt{m_2}$  is an analogous parameter to  $n'$  used there. Qualitatively the slope of the normalized total flux with respect to  $\sqrt{m_2}$  decreases suggesting an ultimate saturation as in multi-petal shapes (see Figs. 3.12 and 3.19). For the extra generative parameter  $\zeta \in \mathcal{I}''$  to which some dependence is observed, it should be expressed through spectral moments which could be easily measured for arbitrary shape, it will be handled in the following subsection.

### Conductivity model

This study aims to quantify the flux transmitted through a spot of complex shape. While the numerical results encompass a broad parametric space, they are not readily comprehensible in their full scope and pose challenges for generalization. We thus make an attempt to construct a general phenomenological model relying on geometrical characteristics and inspired from the model used for flower-shaped spots.

**Covariance matrix** The first simple step is the construction of a covariance  $C_{ij}$  matrix of the normalized flux and all available normalized parameters  $\tilde{x}_i$ :

$$C_{ij} = \langle \tilde{x}_i \tilde{x}_j \rangle, \quad \tilde{x}_i = \frac{x_i - \langle x_i \rangle}{\sigma(x_i)}, \quad (3.30)$$

where, as previously  $\langle x_i \rangle$  denotes the average value, and  $\sigma(x_i)$  denotes its standard deviation. The covariance matrix constructed based on all available simulation data is provided in Table 3.5. There is a strong correlation between  $\tilde{Q}'$ ,  $\tilde{Q}''$  and parameters  $\tilde{k}_l$ ,  $\sqrt{\tilde{m}_0}/\langle r \rangle$ ,  $\sqrt{\tilde{m}_2}$  and  $\sqrt{\tilde{m}_4}/\langle r \rangle$ . However, because of the strong correlation, the effect of the moment  $m_4$  is hard to isolate from the effect of  $m_2$ . Very small correlation of the flux is found with  $\tilde{\xi}$ ,  $\tilde{H}$  and  $\tilde{a}$ ; slightly more correlation exists with  $\tilde{\zeta}$ . According to the covariance matrix,

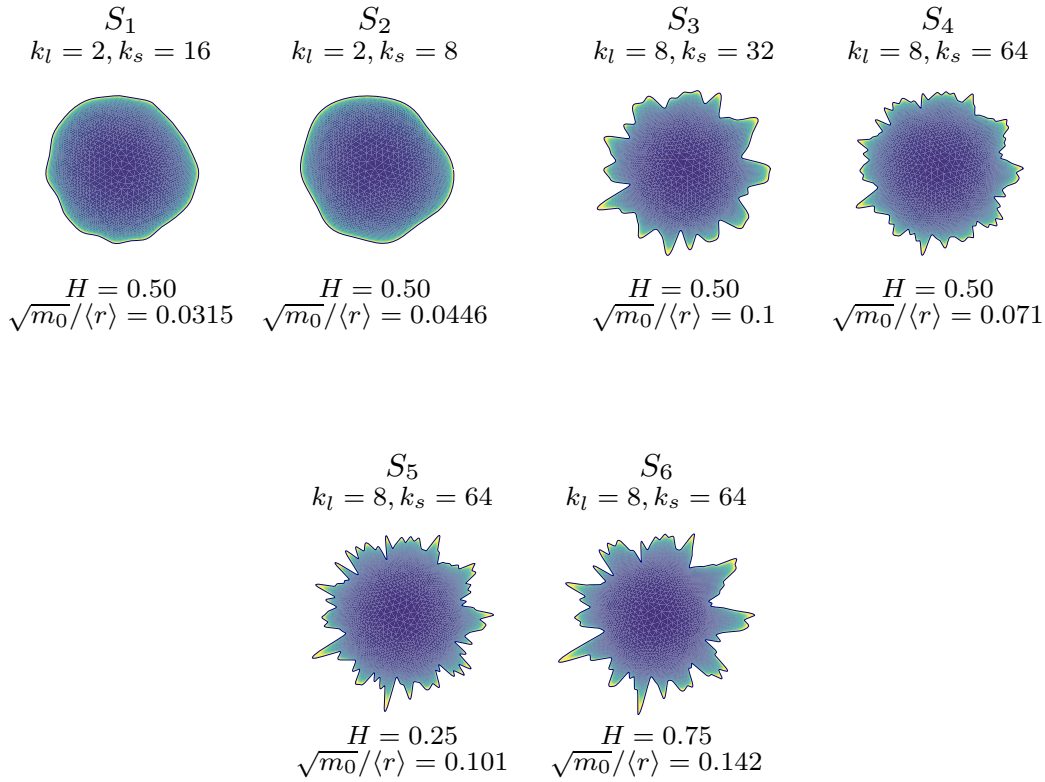


Figure 3.32: Comparison of pairs of self-affine spots for the same  $\sqrt{m_2}$  and for different values of  $\sqrt{m_0}/\langle r \rangle$ . To simplify the reading of the parameters, they are equivalently displayed in Table 3.4.

the Hurst exponent seems to be negligible, which is surprising in the light of our previous results. In conclusion, we could confirm that the covariance matrix and eventual Principal Component Analysis, which access only first order correlations, present too coarse tools to determine subtle non-linear correlations. Finally, since generative parameters  $\mathcal{I}$  are strongly linked to the method of spot generation, in constructing our model we will focus exclusively on geometrical parameters  $\mathcal{A}$  which could be measured for an arbitrary shape.

**Phenomenological model** Analyzing the obtained results, we noticed a weak logarithmic dependence of the total normalized flux on the magnification parameter  $\zeta = k_s/k_l$ . A relatively simple phenomenological model including this parameter could be constructed, but since this parameter is generative, it is of no help for a general case. Nevertheless, it is clear that the magnification  $\zeta$  is intimately related to another geometrical parameter, known as Nayak parameter [Nayak, 1971, Yastrebov et al., 2017b]  $\alpha = m_0 m_4 / m_2^2$  (see covariance matrix in Table 3.5). Remark that from Eqs. (3.24) for the flower-shaped spot, the Nayak parameter is simply 1 so, consistently it does not enter the phenomenological equation for the conductivity of such simple forms Eq. (3.10). A rigorous link between the generative parameter  $\zeta$  and the geometrical parameter  $\alpha$  can be provided, see Appendix C.1. The concrete form of this link was not used but we could notice that another geometrical characteristic, namely the Hurst exponent  $H$  is involved, regardless the results of the covariance analysis. So, the ultimate set of geometrical dimensionless parameters is chosen to be:

$$\mathcal{A}^f = \left\{ \sqrt{m_0}/\langle r \rangle, \sqrt{m_2}, H, \alpha \right\} \equiv \left\{ \sigma/\langle r \rangle, \sqrt{\langle (\nabla r)^2 \rangle}, H, \alpha \right\} \quad (3.31)$$

	$\tilde{Q}'$	$\tilde{Q}''$	$\tilde{\xi}$	$\tilde{k}_l$	$\tilde{\zeta}$	$\tilde{H}$	$\sqrt{\tilde{m}_0}/\langle r \rangle$	$\sqrt{\tilde{m}_2}$	$\sqrt{\tilde{m}_4}/\langle r \rangle$	$\tilde{\alpha}$
$\tilde{Q}'$	1	0.9	0.1	0.7	0.3	-0.2	0.7	0.9	0.7	0.06
$\tilde{Q}''$	-	1	-0.04	0.8	0.4	-0.2	0.7	0.9	0.7	0.1
$\tilde{\xi}$	-	-	1	-0.2	-0.2	0.1	0.7	-0.06	-0.07	-0.08
$\tilde{k}_l$	-	-	-	1	0.06	0.0	0.4	0.7	0.4	-0.03
$\tilde{\zeta}$	-	-	-	-	1	0.0	0.06	0.5	0.5	0.9
$\tilde{H}$	-	-	-	-	-	1	-0.2	-0.2	0.3	0.2
$\sqrt{\tilde{m}_0}/\langle r \rangle$	-	-	-	-	-	-	1	0.6	0.4	-0.05
$\sqrt{\tilde{m}_2}$	-	-	-	-	-	-	-	1	0.9	0.2
$\sqrt{\tilde{m}_4}/\langle r \rangle$	-	-	-	-	-	-	-	-	1	0.3
$\tilde{\alpha}$	-	-	-	-	-	-	-	-	-	1

Table 3.5: Covariance matrix of normalized flux and all normalized parameters according to Eq. (3.30).

### Model: Interpolation of self-affine contact spot

The results in flux are identified by the following phenomenological model, encompassing the effects of  $m_2$ ,  $H$  and  $\alpha$  :

$$Q'' = a \left[ 1 - \frac{1}{b \sqrt{m_2} + 1} \right] (1 + cH) \left\{ 1 + \frac{d}{e\alpha^f + 1} \right\} \quad (3.32)$$

With  $a, b, c, d, e, f$  five positives parameters.

The core term in square brackets in Eq.(3.32), is equivalent to the phenomenological law obtained for multi-petal spots, see Eq. (3.10).

In addition, the effects of  $H$  and  $\alpha$  enter in the equation through the product of linear and non-linear functions, respectively (normal and curly brackets). The former is the increasing function of  $H$  and the latter is a decreasing function of  $\alpha$ . Both terms provide a slight factor adjustment: in the interval  $(1, 1+c)$  for  $H \in (0, 1)$ , and in the interval  $(1+d/(1+e), 1)$  for  $\alpha \in (1, \infty)$ . Due to a weak dependence on the Nayak parameter, we made an attempt to integrate it through a logarithmic dependence, like in [Yastrebov et al., 2017b], but the constructed model could not fulfill the physical consistency, i.e. ensure always positive normalized flux  $Q''$  which increases monotonically for increasing  $\alpha$  and  $\zeta$  (see Appendix C.2). This physical consistency could be formulated as an inequality for the exponent parameter  $f$ :

$$f \geq \frac{1-H}{2H}.$$

The issue with this bound is that it diverges for  $H \rightarrow 0$ . Therefore, we deliberately fixed the minimal value of the Hurst exponent that we took into consideration  $H \geq 0.25$ , providing the following condition for the exponent  $f \geq 1.5$ . A further study should be carried out to formulate a physically consistent phenomenological model for the flux for spots with lower values of the Hurst exponent.

Combining Eqs.(3.32) and (3.28), the final equation for the flux is obtained as:

$$Q = Q_o \left( 1 + a \frac{\sqrt{2m_0}}{\langle r \rangle} \left[ 1 - \frac{1}{b \sqrt{m_2} + 1} \right] (1 + cH) \left\{ 1 + \frac{d}{e\alpha^f + 1} \right\} \right) \quad (3.33)$$

The coefficients are found by the least square fit of all simulation results, see Table 3.6. Results of the fitting law are shown in Fig. 3.33 separately for two sets of simulation data: in Fig. 3.33(a) for the set of contact spots parametrized by Eq.(3.16a), and in Fig. 3.33(b)

for those defined by Eq. (3.29). A relative error could be defined as:

$$E = \frac{1}{N} \sum_{i=1}^N \frac{|Q_i - Q_i^{\text{fit}}|}{Q_i}, \quad (3.34)$$

and for the fit coefficients the error reduces to  $E = 4.3\%$ . The Pearson's correlation factor for the set of identified parameters is equal to  $\rho = 0.9976$ .

Parameter	$a$	$b$	$c$	$d$	$e$	$f$
Value	0.968	0.255	0.0867	4.38	5.49	1.50

Table 3.6: Parameters of the phenomenological model (3.32),(3.33) optimized through least square fit and resulting in relative error  $E = 4.3\%$  and Pearson's correlation factor  $\rho = 0.9976$ .

The high concentration of data for low  $\sqrt{m_2}$  might have introduced biases during the fitting process. Nonetheless, the obtained model captures well all the trends observed in our simulation results, notably, it represents well the flux of the roughest contact spots with highest values of  $\sqrt{m_2}$  and  $\alpha$ . In summary, the obtained model could be seen as a generalization of the initial model formulated for multi-petal shapes (flower-, star- and gear-like). The ultimate model integrates the combined effects not only of standard deviation  $\sigma = \sqrt{\langle (r - \langle r \rangle)^2 \rangle} = \sqrt{m_0}$  and  $\sqrt{\langle (\nabla r)^2 \rangle} = \sqrt{m_2}$  but also of more subtle shape parameters such as the Nayak parameter  $\alpha$  and the Hurst exponent  $H$ , which are related to bandwidth length and fractal dimension, respectively.

As a by product, the form of the phenomenological model (3.33) permits us to access the fractal limit of the self-affine spots, when the magnification  $\zeta = k_s/k_l \rightarrow \infty$ , then a very simple form for the limit flux could be obtained, depending only on the standard deviation of the spot and its Hurst exponent:

$$\lim_{\zeta \rightarrow \infty} (Q) = Q_0 \left( 1 + a \frac{\sqrt{2m_0}}{\langle r \rangle} (1 + cH) \right) = 4kU_0 \left( \langle r \rangle + a \sqrt{2m_0} (1 + cH) \right). \quad (3.35)$$

As a first order approximation, one could use the following value  $4kU_0 \left( \langle r \rangle + \sqrt{2m_0} \right)$  which remains relatively accurate due to the factor  $a(1 + cH)$  having minimal variation, remaining within the range (0.968, 1.052). In general, this fractal limit remains speculative and could be seen as our conjecture as for the case of multi-petal shapes.

### 3.5 Two-mode spots

In the previous section, the influence of the spectral content on the flux of self-affine spots was identified extending the study of multi-petal geometries. In this section, we aim to give additional insights into this aspect, constructing a two-mode geometry. Our goal is to explore, from a deterministic perspective, the interplay between these modes.

#### Definition: Radius of flower-shaped with two modes

The radius function of a flower-shaped contact spot with two modes is constructed by applying two cosine profiles upon a circular contact spot, as follows:

$$r(\theta) = r_0 + r_1 \cos(n_1\theta) + r_1 \left( \frac{n_1}{n_2} \right)^{H+0.5} \cos(n_2\theta) \quad (3.36)$$

With  $n_1, n_2$  two integer parameters, denoting the number of petals related to the first and the second mode, respectively.

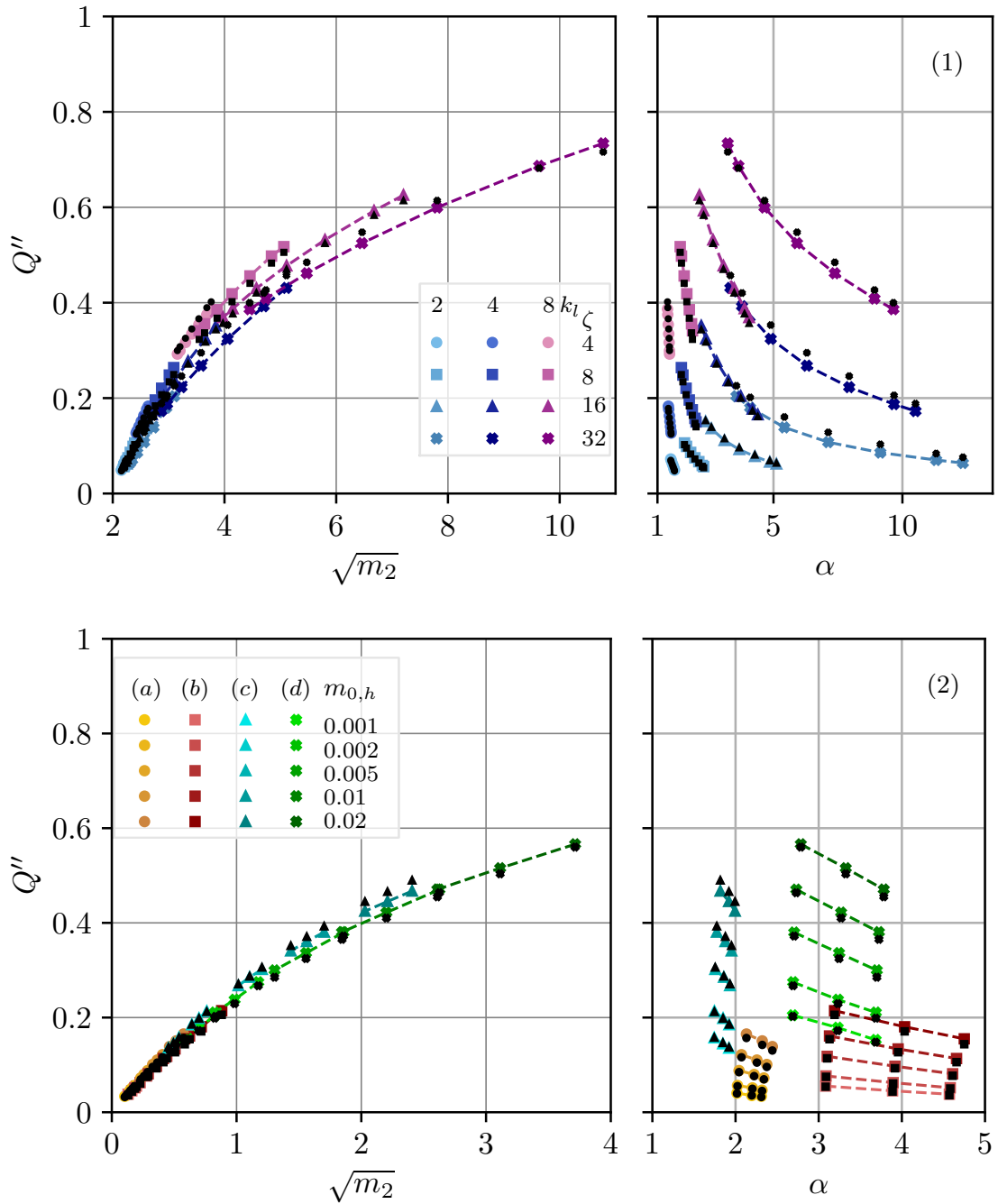


Figure 3.33: Simulation results for the normalized flux through self-affine spots (color markers and interpolation lines) and phenomenological prediction (smaller black markers of the same type). Upper row: initial set of data (1), lower row: data with controlled standard deviation (2). The letters in the second series refer to those defined in Fig. 3.31.

The mean radius is equal to  $r_0$ , the petal’s length parameter  $\xi = r_1/r_0$ . This incorporates two sets of parameters that describe the height and number of petals:  $(r_1, n_1)$  and  $(r_2, n_2)$ . The height of the second mode  $r_2$  is defined by the Hurst parameter  $H$ , as  $r_2 = r_1(n_1/n_2)^{H+0.5}$ . The magnification-like parameter is defined as the ratio of the number of petals of these two modes  $\zeta = n_2/n_1$ . Examples of such a two-mode shapes are presented in Fig. 3.34 for different values of  $\zeta$ , but constant parameters  $n_1 = 4$  and  $H = 0.75$ . Note that  $r_2$  experience a power-law decrease as  $n_2$  grows: the bigger the Hurst exponent the more pronounced this decrease is.

The expressions for the standard deviation  $\sigma$  and the second moment  $m_2$  are derived

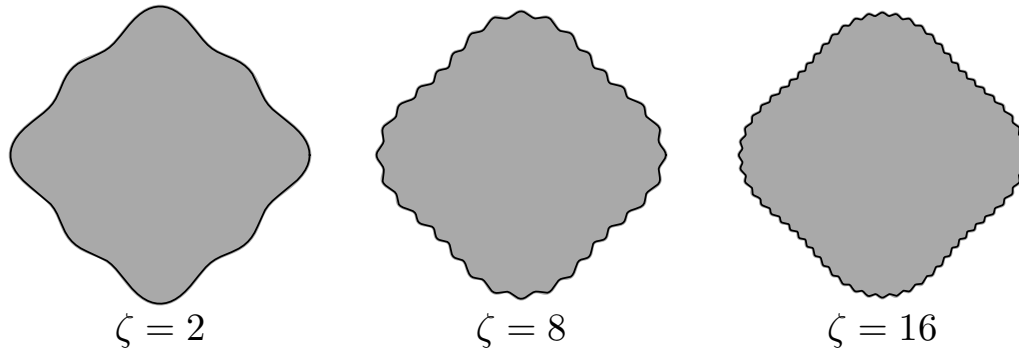


Figure 3.34: Profiles of contact spots with  $n_1 = 4$ , and  $r_1/r_0 = 0.1$ , for  $\zeta \in \{2, 8, 16\}$ , with  $H = 0.75$

as follows:

$$\sigma^2 = m_0 = \frac{r_1^2}{2} (1 + \zeta^{-(2H+1)}), \quad m_2 = \frac{r_1^2 n_1^2}{2r_0^2} (1 + \zeta^{-(2H-1)}) \quad (3.37)$$

The standard deviation decreases with  $H$  and  $\zeta$ . The second moment may increase for increasing  $\zeta$  only for  $H \leq 0.5$ .

### 3.5.1 Results and modeling

The resolution of this two-mode problem was carried out by BEM. Some examples of the normal flux result are presented in Fig. 3.35, simulating a 1/8th of the contact spot. Once again the final result in flux are computed by extrapolation and then normalized following the expression given by Eq. (3.9). An approximate model can be constructed for the normalized flux, assembling the normalization induced separately by every mode even though rigorously speaking the superposition principle does not hold in this situation.

#### Model: "Superposition" of two-mode fluxes

The normalized flux is modeled as if it would result from a superposition of two modes with normalized number of petals  $n'_1$  and  $n'_2$ , as follows

$$Q'_{f,2} = Q'_f(n'_1) + Q'_f(n'_2) \quad (3.38)$$

This model aims to provide a comparison with numerical results. The function  $Q'_f$  reuses the model define by Eq. 3.10, with parameters found by BEM fitting, see Table. 3.1. Of course, it is clear that the model is non-linear and  $Q'_f(2n') \neq 2Q'_f(n')$ . However, surprisingly, the comparison between numerical results and this simplified model reveals to be a very good fit as shown in Fig.3.36 for three Hurst exponents  $H = \{0.25, 0.5, 0.75\}$ . Note that the flux decays surprisingly slowly to the limit  $\zeta \rightarrow \infty$  especially for lower values of  $H$ , shown as a thick blue dashed line.

Initially, for  $n_2$  close to  $n_1$ , there is a slight difference between the numerical results and the model Eq. 3.38. However, as  $n_2$  increases, this difference diminishes since the shape perturbation induced by the second mode diminishes too. Overall, the two sets of results follow the same tendency, even capturing the growth for  $H = 0.25$  for small values of  $n_2$ . However, we have no clue about the peak found in numerical results for  $n_2 = 8$ . This could possibly arise from the exact superposition of the second mode over the first, leading to a more pronounced shape perturbation.

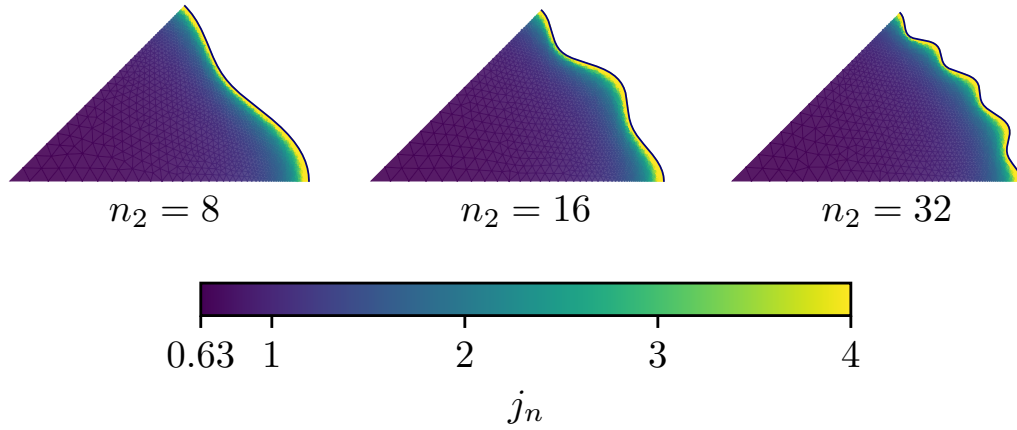


Figure 3.35: The simulated normal flux in two-mode spot with  $n_1 = 4$  and  $\xi = 0.1$  and  $n_2 \in \{8, 16, 32\}$ .

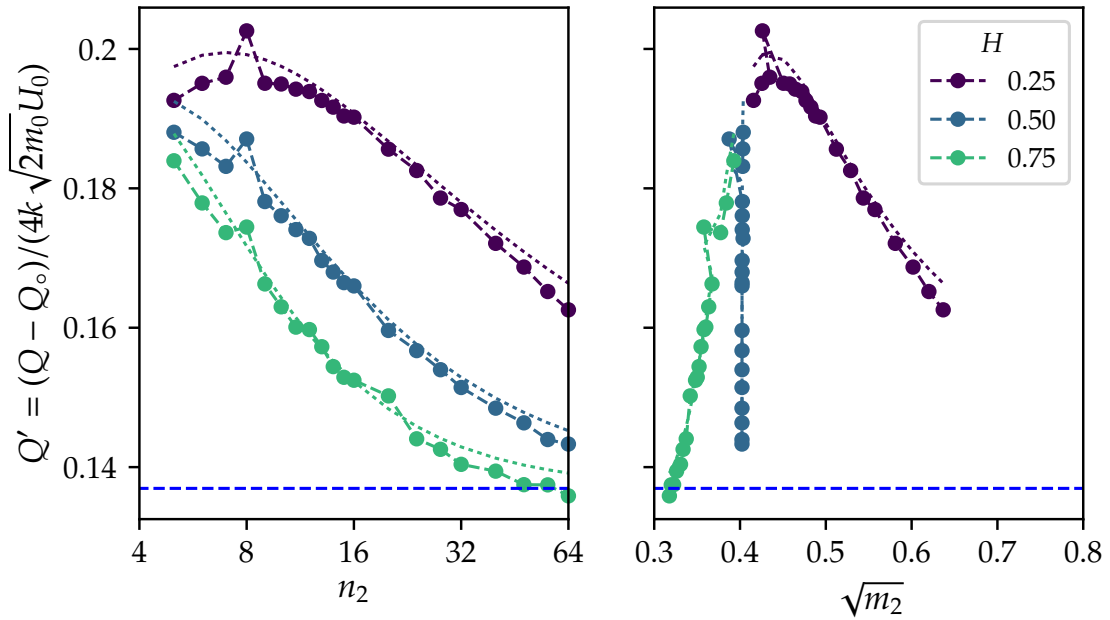


Figure 3.36: Normalized flux for two-mode spot: BEM results (circles) compared with a simplified superposition model (3.38) (dashed lines) with  $n_1 = 4$  and  $\xi = 0.1$  for  $H$  parameter  $\{0.25, 0.5, 0.75\}$ . The thick dashed line represents the normalized flux for the low mode  $n_1 = 4, \xi = 0.1$ .

This simplistic model offers a new insight from the geometric decomposition of complex shapes. It provides a relatively good approximation even for a *square contact spot*, experiencing an infinite spectral content. If the square shape is decomposed into a finite number of modes  $N = 128$  the sum of contributions from every mode results in an overestimation of the numerically computed flux by 7.98%. Such an overestimation arises from the lack of interaction between modal flux perturbations, which is the source of the nonlinearity.

### 3.6 Koch snowflake

The effect of the fractal dimension has motivated us to undertake a brief study on a *Koch snowflake*. This shape is a truly fractal deterministic shape, constructed iteratively through



a series of stages  $N$ . The initial stage is an equilateral triangle. With each subsequent stage, every side of the shape from the previous stage is divided, and an outward triangle is added in the center of each side, see Fig. 3.37.

The perimeter of the snowflake increases by a factor of  $4/3$  by every increment of stage, describing an unbounded sequence. Conversely, the area describes a bounded increasing sequence converging to a limit of  $8/5A_0$ , with  $A_0$  the area of the initial equilateral triangle. Some examples for such geometry are presented Fig. 3.37 for various stages. All these snowflakes are enclosed within a circle. Subsequently to these geometric features, the fractal dimension can be defined using the homothety dimension, which pertains to  $D = \log(4)/\log(3) \approx 1.26$ .

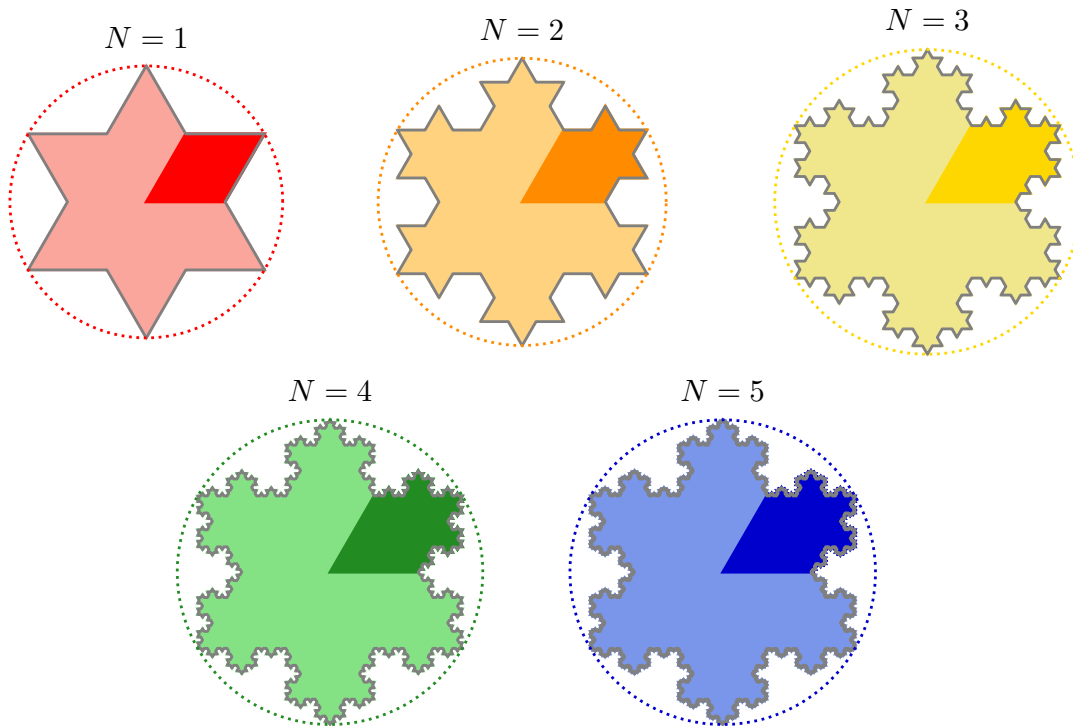


Figure 3.37: Collection of Koch snowflake, at different stage  $n = \{1, 2, 3, 4, 5\}$

### Mesh geometry

The Koch snowflake-shaped spot is modeled only by a  $1/6$ -th of its section, as presented in Fig. 3.37. One example of such mesh definition is presented in Fig. 3.38, at the fifth stage. Similarly to all the previous contact spots, the mesh is refined on the edge. Even though the element size diminishes rapidly with fractal stages, the triangular tessellation aligns well with the contour's shape. The mesh example presented in Fig. 3.38 is built both using  $h_0/r_0 = 0.05$  and  $h_1/r_0 = 0.005$ , for the mesh parameters set at the tip element, and at contour edge, respectively.

### Flux

The solution to the conduction problem for these shapes is carried out by BEM. Recalling the study of star, gear-shaped contact spot, one can establish a normalization similar to Eq. (3.9). The radius for the circular contact spot, defining the flux  $Q_o$ , is set equal to the mean radius  $\bar{r}$ . For the definition of  $Q_{up}$ , the radius is given by the surrounding circle. The total flux is then extrapolated using two distinct mesh sizes:  $h_0/r_0 = \{0.1, 0.05\}$  with a consistent refinement on the edge. With the finest mesh size, it ensures multiple elements

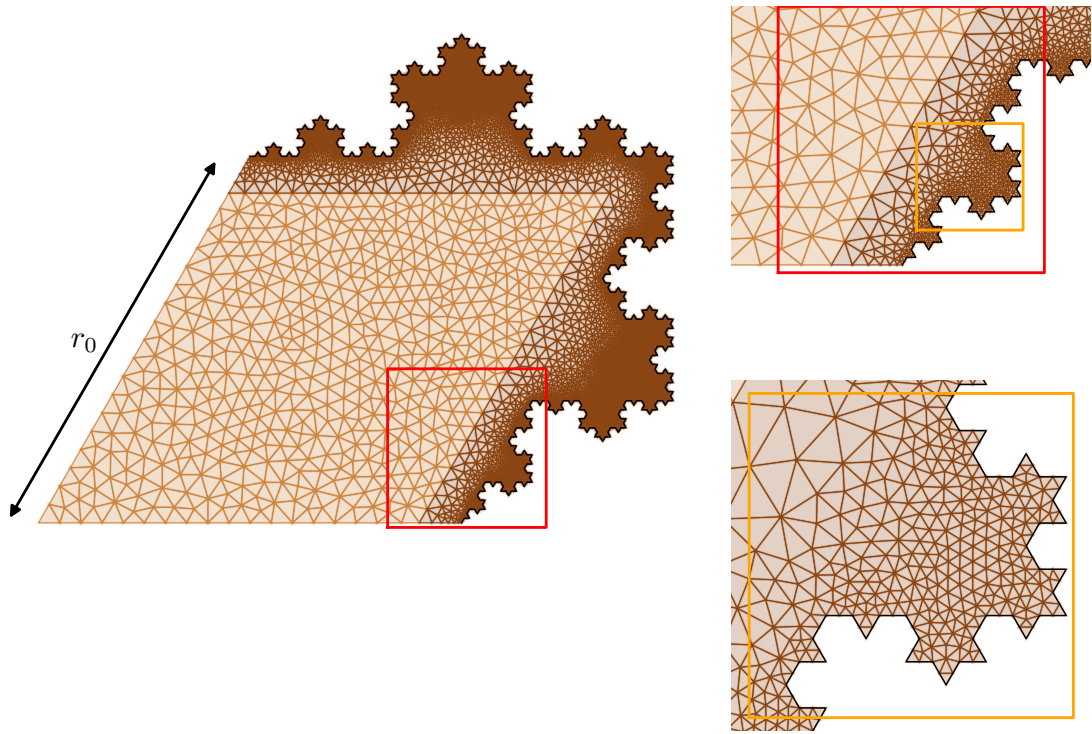


Figure 3.38: Mesh definition for a Koch snowflake at the stage 5, with  $h_0/r_0 = 0.05$

within the smallest triangular boundary pattern, at the ultimate considered fractal stage. The results are presented in Fig. 3.39 for different fractal stages.

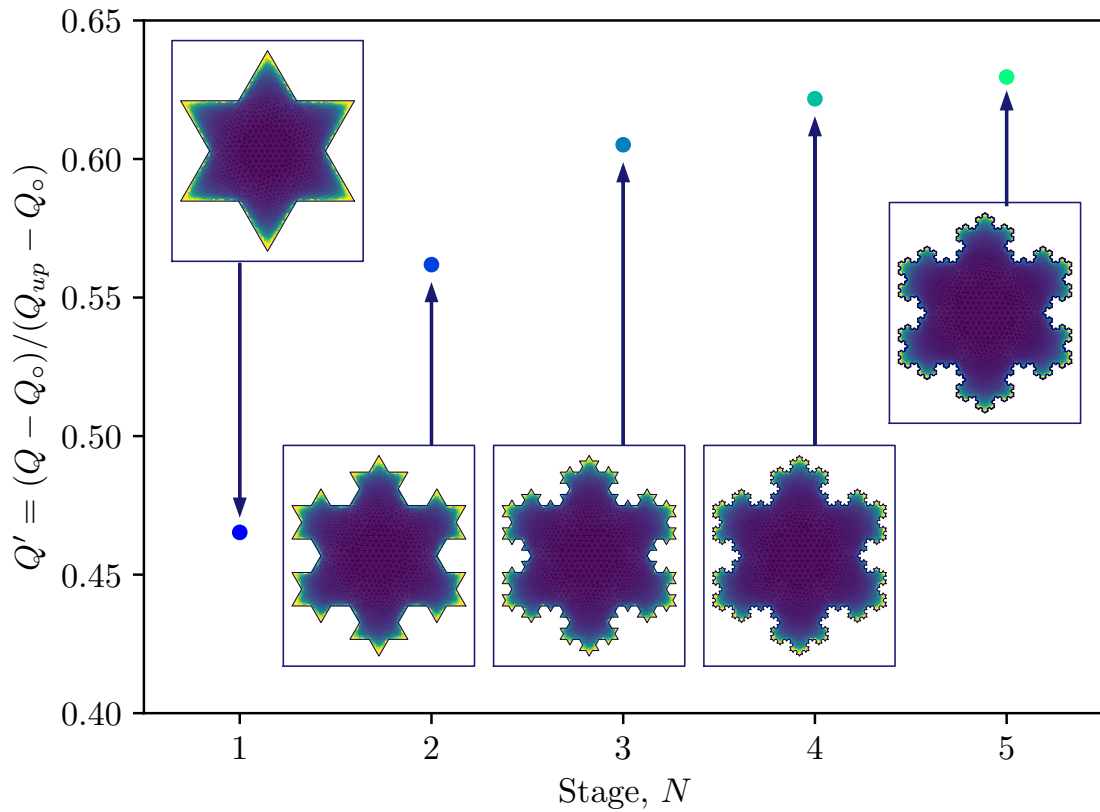


Figure 3.39: The total normalized flux for Koch snowflake spots, for various fractal stages  $N = \{1, 2, 3, 4, 5\}$

As seen in Fig.3.39, the normalized flux converges to an upper limit, akin to what was observed for the multi-petal contact spots. Clearly, the stage number is not analogous to the  $m_2$  parameter seen with the flower shape. However, the similarity is clear since the compactness of the shape diminishes with fractal stages. The method of constructing this fractal shape highlights that the minor shape alterations to the boundary does not really affect the overall flux and we anticipate that in the fractal limit, the flux will converge to some value:

$$\lim_{N \rightarrow \infty} Q' = \lim_{N \rightarrow \infty} \frac{Q - Q_o}{Q_{up} - Q_o} \approx 0.65.$$

### 3.7 Conclusion

In establishing the bounds on the conductivity of rough contacts [Barber, 2003], Barber argued that "its greatest potential probably lies in establishing the maximum effect of neglected microscales of roughness in a solution of the contact problem for bodies with multiscale or fractal roughness." In our contribution, we focus on these "microscales" and make an attempt to assess their quantitative effect on the conductivity. If we repeat after Samuel Karlin that "the purpose of models is not to fit the data but to sharpen the questions", this study indeed permitted to sharpen few of them.

#### 3.7.1 Flower-shaped spots and other simple forms

For simple multi-petal shapes: flower-, star- and gear-like conductive spots we could obtain the following results. In the limit of the infinite number of petals, rays, and teeth, the conductivity seems to converge to different finite limits. The bigger the area, the higher its limit, therefore the gear-like shapes have the highest and star-like shapes the lowest conductivity. We determined these limits by an extrapolation of a constructed phenomenological model, and these results should be interpreted as a first guess. Hence, the *first question* is whether a conductivity of such spots could be determined analytically in the limit of infinite number of petals, rays or teeth? Expectedly, these limits are bounded between the conductivity of a circle with the average radius  $r_0$  and a circle with the radius equal to the maximal extent of these spots  $r_0(1 + \xi)$ . On the other hand, in this limit, the boundary of the conducting spot could be seen as fuzzy, with the same geometrical bounds but different "fuzziness" types, which surprisingly significantly affects the limit. The physical and mathematical limits could be different here because of radiative and eventually convective heat exchanges or because of tunneling effects. The physical conductivity should probably hit the upper limit  $Q_{up}$  defined by the conductivity of a circular spot of radius  $r_0(1 + \xi)$ .

#### 3.7.2 Conductivity of self-affine spots

In terms of conductivity of self-affine random spots, based on numerous simulation results and being inspired by the phenomenological model constructed for a flower-shaped spot, we suggested a phenomenological model including four parameters: (1) mean radius, (2) its standard deviation (or the square root of the zero-th spectral moment), (3) its gradient's standard deviation (or the square root of the second spectral moment), (4) its Hurst exponent and (5) its Nayak parameter. The model is applicable in a relatively large interval of parameters and properly describes the change in flux with these geometrical parameters. It is worth noting that the model shows an interplay between the second spectral moment and a specific combination of the Hurst exponent and the Nayak parameter. The conductivity increases with the former and decreases with the latter. In the generative model employed in this study, under increasing magnification, the second spectral moment and the Nayak parameter increase in such a way that the flux is always a monotonically increasing function (by construction). Nonetheless, it is conceivable to

design shapes where these two parameters are independently controlled. Consequently, the *second question* arises: could an increase in the Nayak parameter actually lead to a reduction in flux in practical scenarios? An affirmative response would intriguingly imply the existence of an optimal Nayak parameter (linked to an ideal shape) that maximizes conductivity. However, such a scenario seems rather unlikely.

Similar to our analysis of simple multi-petal shapes, the phenomenological model enabled us to determine the ultimate fractal limit for the conductivity of self-affine shapes as the magnification  $\zeta$  approaches infinity. This limit depends solely on the mean radius, standard deviation, and only weakly on the Hurst exponent. However, as in our earlier findings, this identified limit should be regarded as a preliminary estimate. The mathematical *question of the conductivity of self-affine shapes in the fractal limit* remains open for further exploration. From a physical perspective, similarly to observations with flower-shaped spots, the diffusive nature of the boundary could provide a more practical approach to determining this limit.

### 3.7.3 Contact spots between rough surfaces

Concerning the conductivity of contact spots formed between randomly rough surfaces in contact, we can highlight several pertinent findings. The non-simple connectedness of these spots, characterized by non-contact areas surrounded by contact ones, does not appear to significantly affect overall conductivity. However, the complexity of their shapes undoubtedly influences this conductivity. Drawing from our analyses of relatively simpler cases, a set of parameters proves effective for estimating conductivity using the developed phenomenological models (Eqs. (3.32) and (3.33)). These parameters include (1) average radius, (2) standard deviation, (3) second spectral moment, (4) Hurst exponent, and (5) Nayak's parameter of the outer contour. But this model should be applied to realistic contact spots with caution. In most cases, such spots cannot be parametrized through a function in polar coordinates  $r(\theta)$  and, in general, polar coordinates do not make much sense for complex spots (see Fig. 3.1). Instead, a more general parametrization using convective coordinates defined along the outer boundary is needed. In this study, by limiting ourselves to relatively simple geometrical models, we left more realistic contact shapes for future research.

### 3.7.4 Supplementary work, two-modes spots, and Koch snowflake

In order to confirm the observation made on self-affine shapes, we expanded our research on other simple shapes, such as the two-mode spot. Ultimately, this study gives new insights on the interplay of the modes, and yields a new model for the normalized flux. However this model tends to overestimate the flux, which aligns with our previous observations regarding the Nayak's parameter influence.

In the meantime, to bolster our findings on the fractal limit, we study spot shaped like Koch snowflake. These spots, bearing a resemblance to star-shaped spots, reinforce the idea of a fractal limit for the conductivity, even as the perimeter undergoes continued expansion.

### 3.7.5 Conclusion

The conductivity of contact spots formed between randomly rough surfaces in contact, we could argue that their non-simple connectedness (presence of non-contact areas surrounded by contact ones) should not noticeably affect the overall conductivity. However, the complexity of the shape of contact spots should necessarily affect this conductivity. Following our development for relatively simple cases: (1) the average radius, (2) its standard deviation, (3) the second spectral moment and (4) Nayak's parameter of the outer

contour of the spot serve a good set of parameters to estimate the conductivity following the developed phenomenological model (3.32), and to sustain a model for fractal limit.

---

Multi-Spot Conductivity and the Effect of Oxides

---

**Contents**

---

<b>4.1</b>	<b>Introduction</b>	<b>157</b>
<b>4.2</b>	<b>Multi-spot contact</b>	<b>157</b>
4.2.1	Geometrical construction	157
4.2.2	Greenwood's Model	159
4.2.3	Comparison with BEM and conclusion	160
<b>4.3</b>	<b>FFT-BEM for conductivity problem</b>	<b>162</b>
4.3.1	Circular contact spot	164
4.3.2	Comparison with BEM	166
4.3.3	Flower-shaped contact spots	167
<b>4.4</b>	<b>Elastic contact of rough oxidized spheres</b>	<b>168</b>
4.4.1	Real contact area	168
4.4.2	Conductivity of a clean rough contact	173
4.4.3	Oxidation analysis and results	178
4.4.4	Comparison with BEM results	181
<b>4.5</b>	<b>Conclusion</b>	<b>186</b>
4.5.1	Multi-spots area	187
4.5.2	Results on real contact area with oxidation	187
4.5.3	Conclusion	187

---

## ■ ■ Résumé du Chapitre IV

Dans cette dernière partie le problème de la résistance de constriction est élargi au cas des aires réelles de contact. Cette étude vise à étudier l'influence de la morphologie des aires réelles de contact sur la résistance de constriction. Cette partie sera divisée en deux sous-parties, avec une première étude consacrée à la résistance produites par des aires multi-taches. Les calculs seront conduit par BEM, et comparés aux resultats du modèle de Greenwood de la *résistance de constriction*. Dans un second temps, l'étude se portera sur l'étude de la résistance de constriction is-sus d'aire réelle de contact impliquant le contact entre surfaces rugueuses. Nos résultats BEM seront comparés à ceux issus de l'utilisation d'une implémentation *spectrale* des Éléments de Frontière (nommé FFT-BEM). Ce dernier outil nous permettra de résoudre le problème mécanique des surfaces rugueuses en contact. La présence d'oxide sera également considérée, réduisant la surface de conduction, et augmentant la résistance de constriction. Les calculs FFT-BEM sont réalisé avec l'utilisation du code Tamaas.

## 🇬🇧 Abstract for Chapter IV

In this final chapter, the problem of constriction resistance is expanded to include real contact areas. This study aims to investigate the influence of the morphology of real contact areas on constriction resistance. It contains two main parts, the first one is dedicated to the resistance produced by multi-spot areas. BEM simulations compared with the results of an extended constriction resistance Greenwood model. In the second part, the study focuses on the resistance arising from real contact areas produced by the contact between rough surfaces. Our BEM results will be compared with those obtained with *FFT-BEM* (Tamaas library), whose accuracy for conductivity problem is also assessed here. *FFT-BEM* allows us to solve the mechanical problem of rough surfaces in contact. The presence of insulating oxide films in the contact interface is also considered. They reduce the conduction surface and increase the constriction resistance. A preliminary version of a phenomenological conductivity model is derived and a new definition for the Holm's effective radius is proposed.

## 4.1 Introduction

The growth of the real contact area between rough surfaces results in a complex morphology of contact cluster, as could be seen in Fig. 3.1 adapted from [Yastrebov et al., 2015a]. At light loads, the real contact area yields the formation of small separated contact spots, which aligns well with the assumption made by Holm [Holm, 1967] and Greenwood [Greenwood, 1966], based on the observation by Dyson [Dyson and Hirst, 1954]. The constriction resistance arises from conduction through these sparsely distributed contact spots. In the light of the equivalence between conductivity and elasticity rigorously established by Barber [Barber, 2003], the results obtained for the elastic rough contact has been substantially studied giving insights into the problem of conduction [Pastewka et al., 2013, Papangelo et al., 2017, Joe et al., 2022]. Different numerical methods have been successively used to study the elastic problem between rough surfaces in contact: FEM [Hyun et al., 2004, Pei et al., 2005], FFT-BEM [Yastrebov et al., 2015a, Monti et al., 2022] or using molecular simulation [Pastewka and Robbins, 2016].

This section delves into the problem of constriction resistance arising due in contact between rough surfaces. This study begins with the study of constriction resistance due to multi-spots contact of relatively simple shapes, where BEM results will be compared with Greenwood model (Section 4.2). In the second part, the study focuses on constriction resistance of more complex conductive geometries produces by accurate simulations of the mechanical contact. In addition, we will take into consideration the effect of a contaminant agent or fully isolating oxide clusters randomly distributed in the contact interface. For the majority of this oxide-study we used Tamaas software [Frérot et al., 2020], an efficient FFT-BEM implementation for contact problems. In addition, the FFT-BEM and our fast-BEM implementations will be compared on several academic examples and in the study of the oxide-contaminated rough surface in contact.

## 4.2 Multi-spot contact

Generally, the roughness is superposed on an average shape of the body, therefore when brought in contact, the contact area is localized and separate contact spots gather within a single or several macro-clusters. Considering, for example, a roughness on a parabolic profile, the density of contact spots aligns with the pressure solution of the Hertzian contact [Greenwood and Tripp, 1967, Pastewka and Robbins, 2016, Yastrebov, 2019]. However, beyond a certain load, or for small enough separation distance, Greenwood [Greenwood, 2007] reasonably pointed out that the coalescence of initially separate contact spots must be taken into account. And since near the coalescence of contact spots their shapes loose convexity [Yastrebov et al., 2014], simple elliptic shapes cannot serve a good representation of contact areas. Nevertheless, assuming separated contact spots, Greenwood proposed a simple formula for the constriction resistance [Greenwood, 1966]. This section aims to assess the accuracy of this formula for the conductivity problem involving non-circular contact spot.

### 4.2.1 Geometrical construction

We will mimic the growth of the real contact area under load, using separated flower-shaped contact spots which were explored in detail in the previous chapter. Some examples are presented Fig. 4.1. Constructed contact spots will be randomly spread within a nominal radius following the picture drawn in [Greenwood, 1966] but not the one from [Greenwood and Tripp, 1967]. The spots have random radii following a truncated normal distribution with the mean radius parameter  $r_o$  and a standard deviation  $\sigma$ . For the flower-shaped spots both the number and the height of petals are defined proportionally to the spot's size. The spots are included in a macro-cluster of radius  $R_o$ , so the



contact is characterized by the ratio of this macro-cluster to the average radius of the spot:  $R = R_o/r_o$ . The methodology for creating these multi-spot clusters is explained in detail in the colored box provided below.

#### Method: Construction of multi-spot clusters

The spots with a random radius  $r$  (truncated normal distribution  $r > r_{\min}$ ) are distributed randomly (Matérn hard-core point processes) within a circular zone of radius  $R_o$ . The number of petals is proportional to  $r$ , following  $n^f = \lceil \eta^f r/r_o \rceil$ , but bounded at a maximum number of petals  $n_{\max}^f$ . In a similar manner, the petal's height is also proportional to the radius as  $r_1^f = \rho^f r/r_o$ . A check is performed to measure the gap distance between the new spot and the existing others, to maintain the non-overlapping criterion. If this gap is smaller than  $\delta$  parameter, the spot is discarded, and the procedure is repeated until reaching the desired density of contact spots. The density of these spots is defined by  $d = A_c/A_o$ , where  $A_c$  is the total area of contact spots and  $A_o$  represents the area of the nominal contact radius.

Three distinct types of contact clusters are defined  $\mathcal{A}_1, \mathcal{A}_2$  and  $\mathcal{A}_3$ , presented in Fig. 4.1. They correspond to the following ratios of cluster radius to the most probable spot radius:  $R_o/r_o = 5, R_o/r_o = 10$  and  $R_o/r_o = 20$ , respectively. It implies that for the same density, the number of spots for  $\mathcal{A}_3$ -type cluster will be higher than for  $\mathcal{A}_2$  cluster and so on. All the construction parameters are summarized in Table. 4.1.

Cluster name	$R_o/r_o$	Spot characteristics			Flower parameters		
		$r_{\min}/r_o$	$\sigma/r_o$	$\delta/r_o$	$n_{\max}^f$	$\eta^f$	$\rho^f$
$\mathcal{A}_1$	5	0.25	0.25	0.5	0.04	40	6
$\mathcal{A}_2$	10	0.5	0.5	0.5	0.04	40	6
$\mathcal{A}_3$	20	0.5	0.5	0.5	0.04	40	6

Table 4.1: Parameters of the geometrical construction of multi-spot areas.

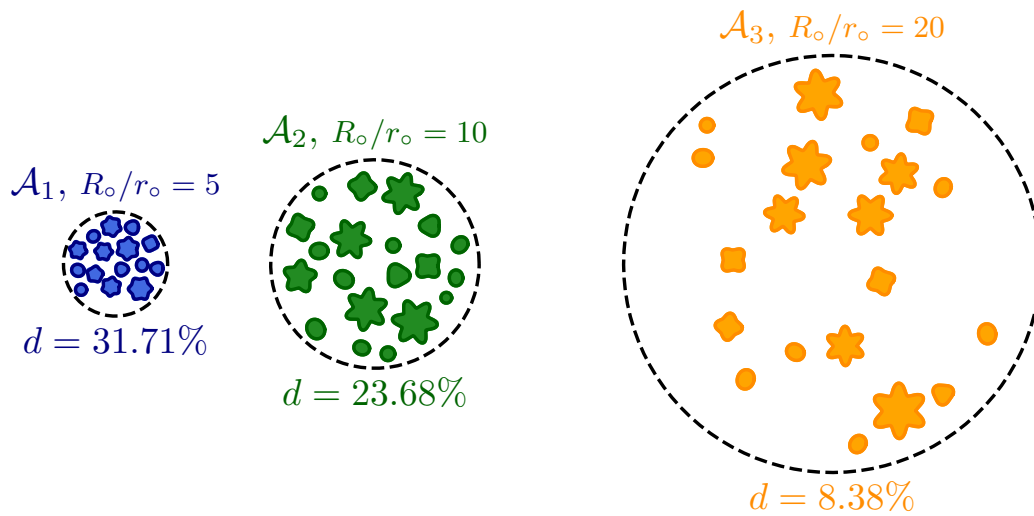


Figure 4.1: Random clusters of contact spots used for multi-spot simulations with  $r_o = 1$ :  $\mathcal{A}_1, \mathcal{A}_2, \mathcal{A}_3$

### 4.2.2 Greenwood's Model

In its original presentation, the Greenwood model deals with constriction resistance of circular contact spots. These contact spots are assumed punctual and are gathered together within a cluster. It assumes a constant potential across all contact points, set uniformly at  $U_0$ . The problem takes on the problem of conduction between half-spaces, as we studied before. The flux at each spot is denoted by  $j_i$  for the  $i$ -th contact spot. The definition of the potential at  $l$ -th spot leads to the definition of the following equation

$$U_0 = j_l r_{l,l} + \sum_{i \neq l} j_i r_{i,l}, \quad (4.1)$$

where  $r_{i,l}$  represents the resistance between the  $i$ -th and  $l$ -th spots,  $r_{l,l}$  is inherently the *self-resistance* term, i.e. the constriction resistance produced by an isolated contact spot  $l$ . This self resistance is equal to  $1/4Ka_l$  for a circular spot of radius  $a_l$ , with  $K$  being the conductivity of the half-space. The resistance term  $r_{i,l}$ , with  $i \neq l$  decays inversely proportionally to the distance  $d_{i,l}$  between the centers of the spots, in summary we get

$$r_{i,l} = \begin{cases} \frac{1}{4Ka_l}, & \text{if } i = l, \\ \frac{1}{2\pi K d_{i,l}}, & \text{if } i \neq l \end{cases} \quad (4.2)$$

Equation (4.1) can be turned into a linear system of equations

$$[R] \{j\} = \{\Phi_0\} \quad (4.3)$$

with the *matrix resistance*, denoted  $[R]$  and  $\{j\}$  being the vector of flux transmitted at the contact spots. The Greenwood resistance formula yields an approximation for the constriction resistance of the whole contact area  $R_{tot}$  as:

$$R_{tot} = \frac{\{\mathbf{c}\}^T [R] \{\mathbf{c}\}}{\|\mathbf{c}\|_F^2}, \quad (4.4)$$

where the vector  $\{\mathbf{c}\} = 4K\{a_1, a_2, \dots, a_N\}^T$  is the inverse of the diagonal of the matrix  $[R]$ . Equivalently, the Greenwood's constriction resistance could be expressed as a double summation:

$$R_{tot} = \left( \sum_{i,j} a_i a_j r_{i,j} \right) / \left( \sum_i a_i^2 \right) \quad (4.5)$$

In addition, Greenwood proposed a further simplification assuming all contact spots are equal to a mean radius,  $\bar{a}$ . The total flux  $Q$ , relates to the potential  $\Phi_0$  by the constriction resistance  $R_{tot} = \Phi_0/Q$ . Note that the matrix  $[R]$  is diagonal dominant if one assumes that  $\forall i, j, i \neq j, a_i \ll d_{i,j}$ . The definition in Greenwood's formula for the self-resistance allows to use any shape of spot as was remarked in [Boyer, 2001b], where the author considered contact spot shaped like square or triangle. This adapted Greenwood's resistance will mix cross resistance terms  $r_{i,l}$  and the self-resistance which could be obtained through our phenomenological models based on BEM results (see previous Chapter, Eq. 3.10 and Table 3.1). Hence, the self-resistance  $r_{i,i}$  will be defined by the spot's mean radius  $r_{o,i}$  and its normalized number of petals  $n'_i = n_i^f \xi_i$  with  $\xi = l_i/a_{o,i}$  and  $l_i$  is the half-length of petals of the  $i$ -th spot:

$$r_{i,i} = \frac{U_0}{Q^f(r_{o,i}, n'_i)}. \quad (4.6)$$

In other words, for every spot instead of assuming  $r_{i,i} = 1/(4Ka_i)$  we will use the resistance

$$r_{i,i} = \frac{U_0}{Q_{oi} \left( 1 + p_1 \xi_i \left( 1 - \frac{1}{p_2 n_i^f \xi_i + 1} \right) \right)}, \quad Q_{oi} = 4KU_0 a_i,$$

where  $p_1, p_2$  are the model parameters analogous to  $a, b$  in Eq. 3.10. Simplifying this expression we get the inverse self-resistance as

$$\frac{1}{r_{i,i}} = 4Ka_i \gamma_i, \quad \gamma_i = 1 + p_1 \xi_i \left( 1 - \frac{1}{p_2 n_i^f \xi_i + 1} \right) \geq 1,$$

where  $\gamma_i$  is the shape corrective factor depending on  $\xi_i$  and  $n_i^f$ . This enhanced model could be simply seen as Greenwood model for bigger spots. Then the vector  $\{c\}$  takes the form:

$$\{c\} = 4K\{a_1 \gamma_1, a_2 \gamma_2, \dots, a_n \gamma_n\}^T$$

and the total resistance can be computed from Eq. (4.7) as:

$$R_{tot} = \frac{1}{4K \sum_i^n (\gamma_i a_i)^2} \left( \sum_i^n \gamma_i a_i + \frac{2}{\pi} \sum_{i,j,i \neq j}^n \frac{\gamma_i a_i \gamma_j a_j}{d_{i,j}} \right), \quad (4.7)$$

where the first term is simply the sum of self-resistances and the second one takes into account the resistance due to mutual arrangement of contact-spots. It is quite clear from this equation that since  $\gamma_i \geq 1$  and  $d_{i,j} > \langle a_i \rangle$ , the resulting resistance which takes into account flower-shaped clusters will be smaller than the one found for circular spots of the same average radius  $\langle a_i \rangle$ . This model can be seen as an extended Greenwood model for constriction resistance.

### Testing the extended Greenwood model

In this short section we perform a series of simple tests to demonstrate how the total contact resistance is affected by the shape factor  $\gamma_i$  aiming to model more realistic contact clusters. We consider two models: the first one assumes that the shape factor is the same for all contact spots  $\gamma_i = \gamma \geq 1$ , which we refer to as *constant shape factor*. The second model adjusts the size of cluster accordingly to its size  $\gamma_i = 1 + \gamma' a_i \geq 1$ , this model is referred as *proportional shape factor*. We generate a sample distribution of contact spots with parameters listed in Table 4.2 (see Fig. 4.2) and compute the reference resistance  $R_{tot}$  according to Eq. 4.7. Further, all contact spots are expanded according to a constant or proportional shape factor and the resistance is recomputed providing us with a ratio  $R(\gamma)/R_{tot}$  which is shown in Fig. 4.3. This primitive simulation is repeated for different contact densities  $d = \{0.025, 0.05, 0.1\}$ . The results demonstrate a stronger resistance decay for proportionally adjusted shape factor (see Fig. 4.3(b)) for which bigger contact spots, which ensure the higher flux, become proportionally bigger. These results are quite straightforward and we can go for our slightly more advanced model which takes true change in shape factor and the resulting conductivity.

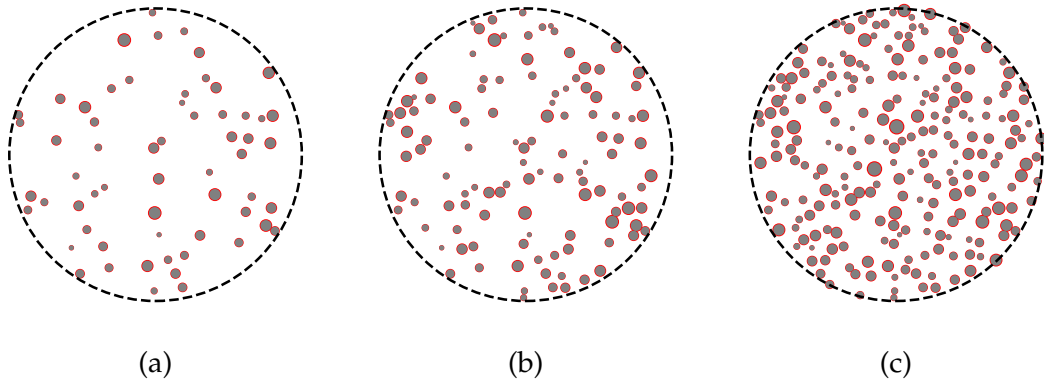
### 4.2.3 Comparison with BEM and conclusion

Here we compare Greenwood's resistance for different configurations of different density (like those shown in Fig. 4.1) with accurate simulations carried out by our BEM implementation. An example of BEM results in normal flux is presented in Fig. 4.4 for configuration  $\mathcal{A}_1$ . In contrast to the study of individual flower-shaped spots, the normal flux does not follow the symmetry of the geometry. With naked eye we see higher

Table 4.2: Simulation Parameters

Parameter	Notation	Value
Average Radius	$\langle a \rangle$	1 (l.u.)
Minimum Radius	$a_{\min}$	$0.1\langle a \rangle$
Standard Deviation	$\sigma/\langle a \rangle$	0.3
Minimum Distance between circles	$\delta$	$3\sigma$
Cluster Radius	$R_o/\langle a \rangle$	50
Spot Densities	$d$	$\{0.025, 0.05, 0.1\}$
Uniform shape factor	–	$\gamma_i = \gamma \in [1, 1.2]$
Proportional shape factor	–	$\gamma_i = 1 + \gamma' a_i, \gamma' \in [0, 0.2]$

Constant shape factor  $\gamma_i = \gamma$



Proportional shape factor  $\gamma_i = 1 + \gamma' a_i$

Figure 4.2: A sample configuration of circular spots with a density  $d = \{0.025, 0.05, 0.1\}$  for (a,b,c) with a constant shape factor  $\gamma = 1.2$  and (d,e,f) with a proportional shape factor  $\gamma' = 0.2$ . Grey circles on the foreground represent the original distribution of spots and background red circles represent the expanded ones for  $\gamma = 1.2$  or  $\gamma' = 0.2$ .

values of the flux near the outer border of the cluster but lowered with the vicinity of the interacting spots. Note that BEM simulation results do not make an assumption of point-like spots and properly compute all interaction terms contrary to the Greenwood model. Nevertheless, the comparison between these two models presented in Fig. 4.5 for different contact densities reveals that the extended Greenwood model is very accurate and the finite-size interaction captured by the BEM is negligible for the total contact resistance. The relative error between two models is presented in Fig. 4.6. In this study we demonstrate that the error is correlated with the number of contact spots, rather than with the density of contact. The Greenwood resistance appears to be very accurate in estimation of the constriction resistance for a cluster of localized contact spots.

It is important to remark that such a Matérn hard-core point process does not re-

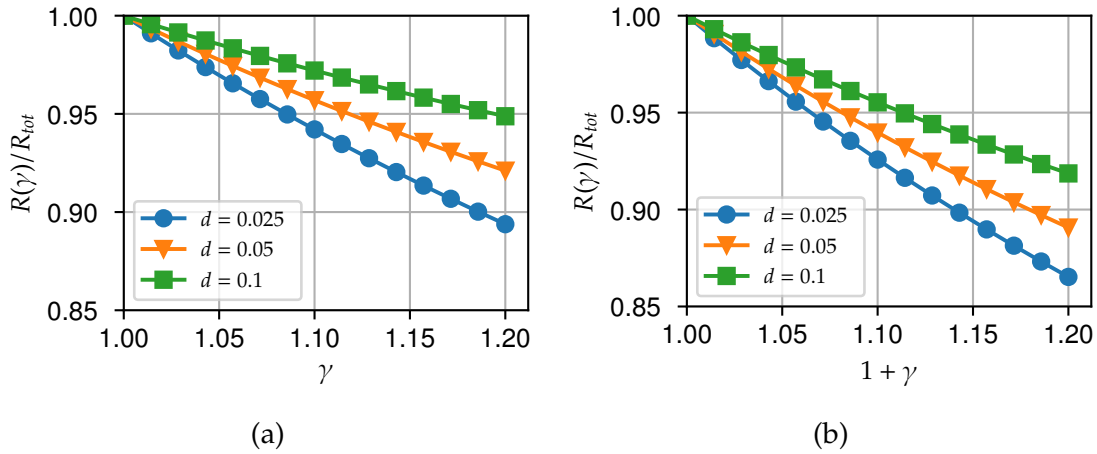


Figure 4.3: Resistance ratio between the original spots and modified with (a) a constant shape factor or (b) proportional shape factor.

sult in a physics-motivated distribution of contact spots, which should not be evenly distributed within a circular region. A much more accurate vision was constructed in [Greenwood and Tripp, 1967] or more recent works [Pastewka and Robbins, 2016, Yastrebov, 2019] accounting for elastic interactions. In contact of rough spheres, which represent a rather general case for solids with revolution symmetry, at small loads, the Hertzian theory does not provide an accurate assessment of contact area distribution, i.e. the classical top-down multi-scale approach does not work [Greenwood et al., 1984]. So, following Greenwood-Tripp model [Greenwood and Tripp, 1967], one could measure the probability of having asperity within every location of the Hertzian area and outside which would allow to smartly distribute contact spots according to this probability. This work, however, is left for the future. In Section 4.4 we will adopt a more direct and free of assumption approach enabling us to obtain realistic contact clusters for a localized contact case.

### 4.3 FFT-BEM for conductivity problem

The previous section has allowed to delve into the problem of conduction of a simplified multi-spot model of contact interfaces. However, such models, even if equipped with long range elastic interactions and physics-based spot distributions, cannot properly take into account the coalescence of spots (even though such attempts were already undertaken in the first approximation [Afferrante et al., 2012]). This section aims to present a methodology tailored for studying conductivity of more realistic contact clusters obtained by accurate contact simulations. This study encompasses both non-oxidized (clean) and oxidized surfaces.

The computations are carried out using an FFT-BEM<sup>1</sup> (external open-source) and fast-BEM (in-house) methods. First, both methods are compared on a benchmark problem of a circular contact spot conductivity. Due to the similarity between elastic contact and conductivity problem [Barber, 2003] there are two ways how the FFT-BEM (optimized for contact problems) could be used to solve the conductivity problem. The first option is to solve the contact problem for flat punch, then the resulting pressure would be analogous to heat flux. Another approach is to use a parabolic indenter and evaluate the contact stiffness when the contact extend reaches the needed value.

In a subsequent part, we will focus on the problem of conduction with oxidized conductive interface, for which we will use a simple geometric strategy to mimic localized

<sup>1</sup>We use a high-performance library for periodic and non-periodic rough surface contact called Tamaas [Frérot et al., 2019].

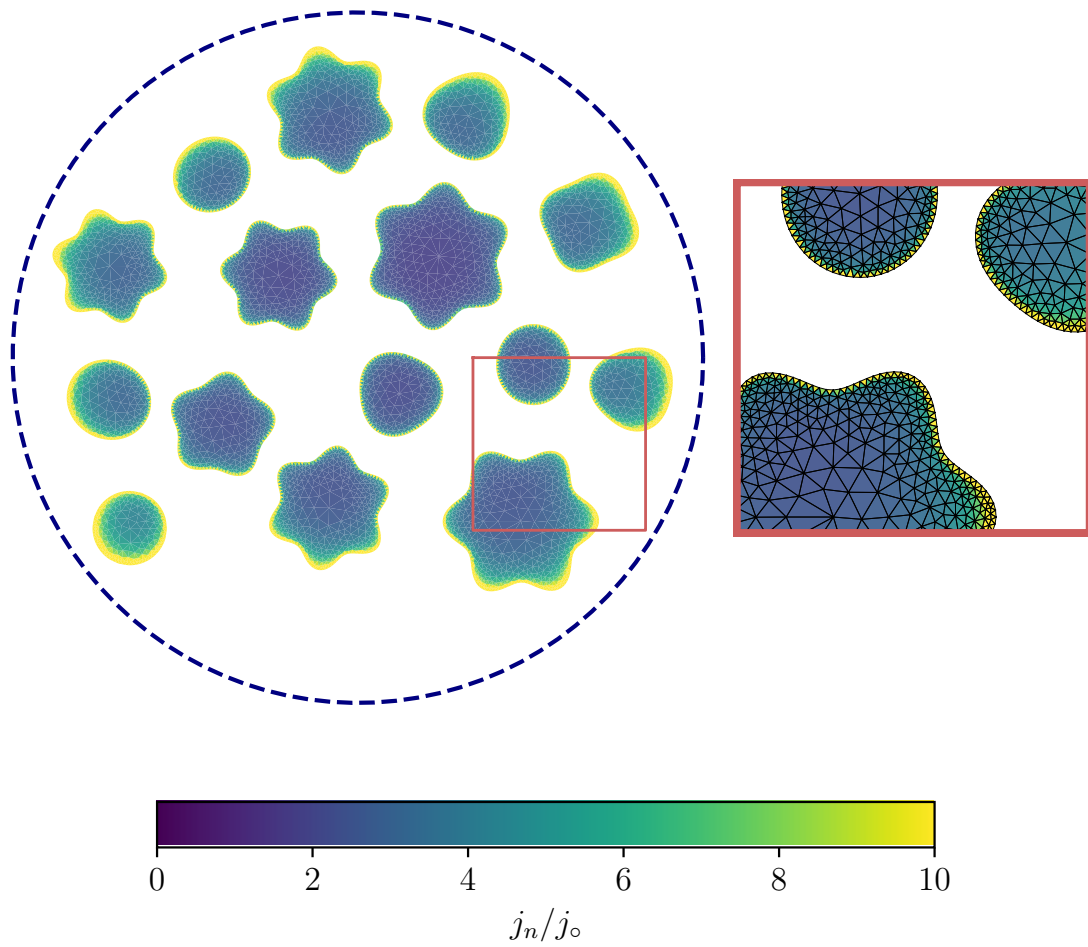


Figure 4.4: Results for  $\mathcal{A}^1$  illustrating the normal flux computed by BEM.

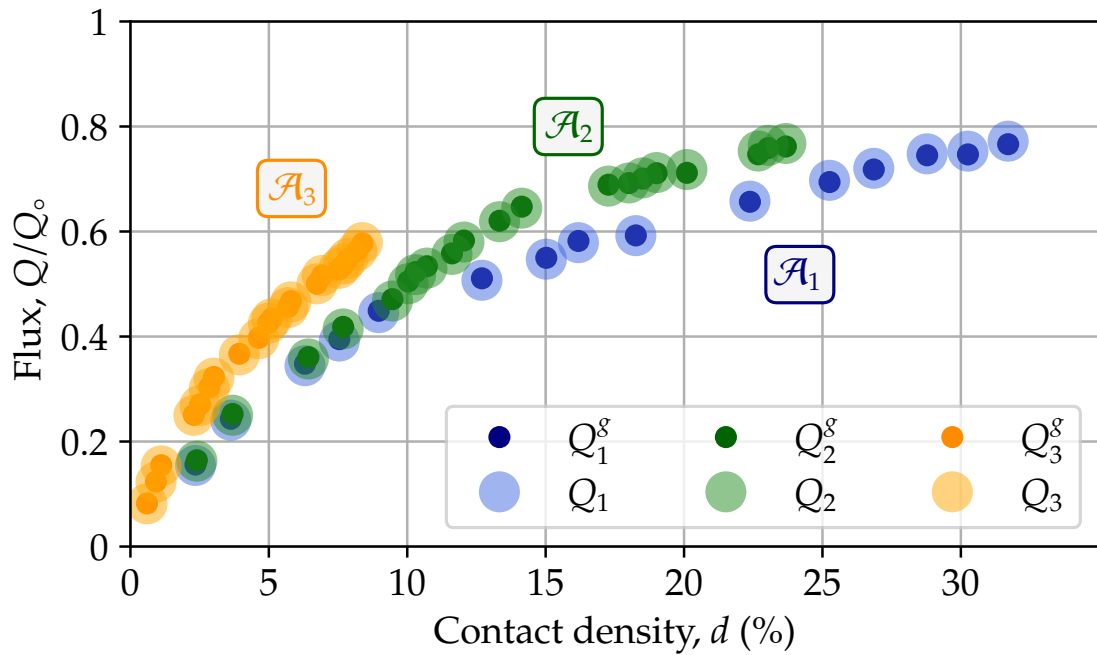


Figure 4.5: Comparison of the total flux computed by BEM and by extended Greenwood model for various multi-spot area.

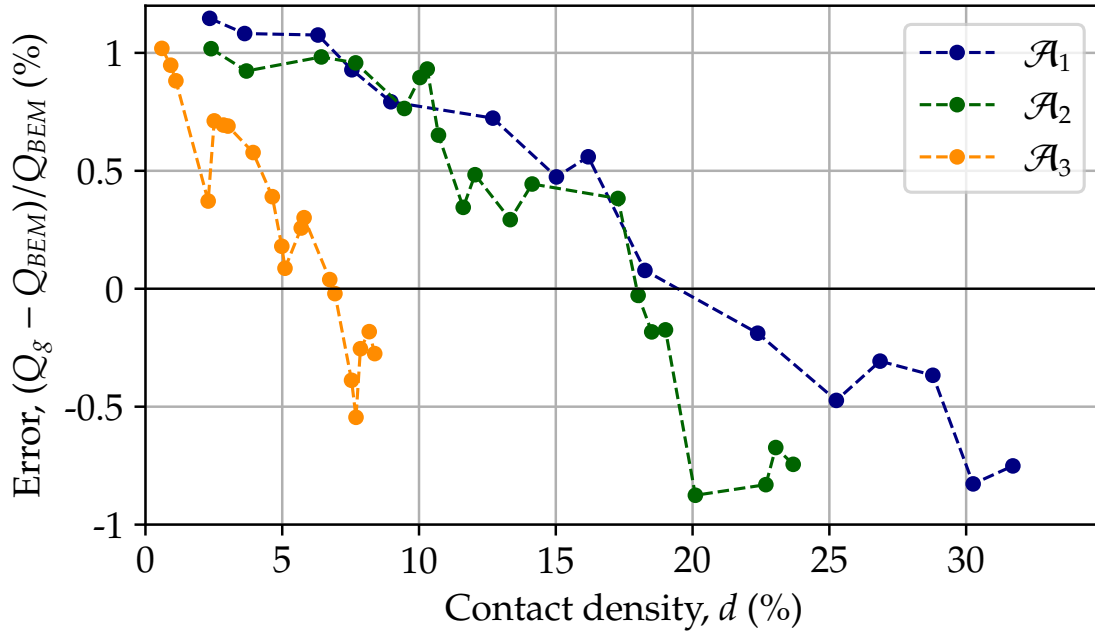


Figure 4.6: Relative error between the BEM results and Greenwood model for various multi-spot densities.

oxide films. In presence of such films, the conductive area is reduced in comparison to the initial contact area and the simple contact stiffness cannot capture this change thus appealing for a detailed study of the conductivity at the interface. The objective of this study is to develop a methodology and carry out numerous simulations to obtain some insights into the influence of the oxidation on the conductivity of rough contact.

### 4.3.1 Circular contact spot

This section aims to introduce the FFT-BEM for the conduction problem on a half-space. As precision is crucial, we will reuse the circular contact spot problem as a benchmark for FFT-BEM. Similarly to the classical BEM, the FFT-BEM is based on an integral equation, but uses a Fourier transform, and subsequently benefits from the use of convolution products. However, this relies on a regular mesh or a grid. Originally, FFT-BEM methods were designed for periodic problems, owing to the application of Fourier transform. But in Tamaas [Frérot et al., 2019] library, which is used throughout our study, a non-periodic option is available, i.e. the Green kernel for half-space without periodicity constraints can be used. This implementation uses the same method as those detailed in [Liu et al., 2000, Monti et al., 2021] and relies on an expanded pressure representation in Fourier space, which is subsequently truncated to yield a non-periodic displacement field.

### FFT-BEM and a flat punch

Flat punch indenting an elastic half-space is equivalent to a uniform potential set on the same area of contact. The framework for the geometrical setup is illustrated in Fig. 4.7 following the grid discretization. The contacting cells are defined by the set  $\mathcal{A}_{\text{flat}}$ , as presented in the color frame below.

### Method: Set of contact cells for a circular spot

The pixels are indexed by  $i$  and  $j$ , denoted by  $c_{i,j}$ . The coordinates of its centroid point, denoted by coordinates  $\{x_i, y_j\}$  for the cell  $c_{i,j}$  are both situated within the interval  $[-L/2, L/2]$ . The set of contacting cells  $\mathcal{A}_{\text{flat}}$  is defined by a set of cells  $c_{i,j}$  such that

$$\mathcal{A}_{\text{flat}} = \{c_{i,j} \mid x_i^2 + y_j^2 \leq R_o^2\}$$

With  $R_o$  the radius of the circular contact spot.

All the height of pixel in  $\mathcal{A}_{\text{flat}}$  is assigned the same value, greater than the height of non-contacting cells. Practically, the height of cells in  $\mathcal{A}_{\text{flat}}$  is set to 1, while the non-conductive cells are assigned a value of  $-1$ . Within the FFT-BEM framework, as utilized in Tamaas, the contact problem can be driven in terms of mean pressure,  $p_m$ . The convergence loop stops when the mean pressure is reached and contact constraints are respected. For  $p_m > 0$ , this ensures the contact on  $\mathcal{A}_{\text{flat}}$ . The numerical procedure is illustrated in Fig. 4.10(a).

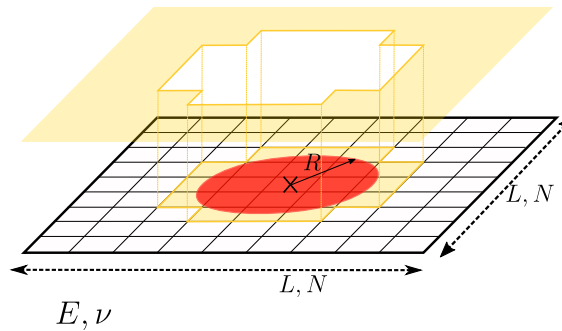


Figure 4.7: Problem geometry for a circular flat indenter in contact with an elastic half-space.

Contact pressure and displacement fields obtained by FFT-BEM are displayed in Figs. 4.8 and 4.9, respectively. The displacement field  $u_z$  is normalized by the penetration parameter  $\omega$ , which is the displacement measured at the flat punch. Note that it is uniformly consistent for every "pixel" under the flat punch. Different grid sizes,  $N$ , were used, as the accuracy of course depends on the size of pixel,  $\delta x = L/N$ . In contrast to classical BEM, the FFT grid definition does not allow special refinement at the indenter's edge and requires to solve the problem on a square domain. Therefore, the problem size accounts for  $N^2$  pixels. Integrating contact pressure and converting elastic effective modulus constant in conductivity would provide us with the total flux.

### Incremental stiffness of a parabolic indenter

The constriction resistance might be deduced from the equivalence with the contact stiffness [Barber, 2003] for a parabolic indenter. However, this requires to compute the derivative of the applied load in regard of the increment of penetration  $\delta\omega$ . Two computations are therefore needed as schematized in Fig. 4.10(b). An equivalent Hertzian contact problem might be considered to evaluate the circular contact spot conduction.

For the sake of precision, the largest circular contact spot should be considered, with radii  $R = L/2 - \delta$  and  $R = L/2$  at two subsequent load increments, where  $\delta/L \ll 1$ . The two computations should result in a negligible difference in the contact area: therefore we assumed  $\delta = \delta x/8$  or  $\delta/L = 1/(8N)$ . This permits the final calculation of the constriction



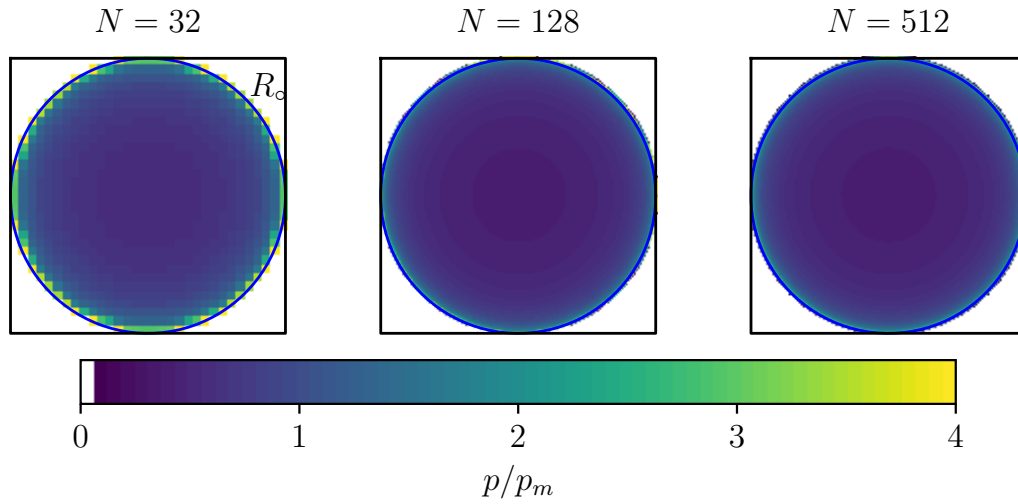


Figure 4.8: Maps of contact pressure computed with FFT-BEM for a circular flat punch with radius of  $R_o/L = 1/2$  in contact with a grid of various size  $N = \{32, 128, 512\}$

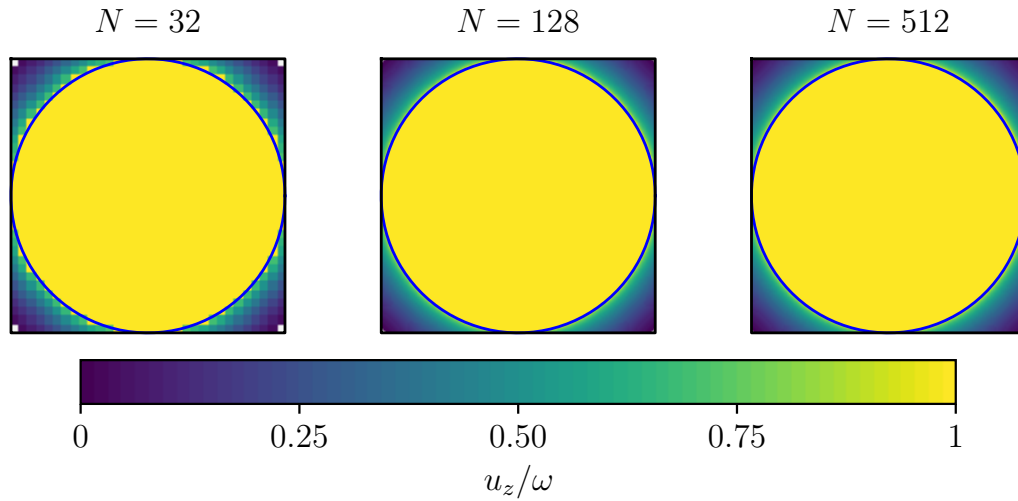


Figure 4.9: Maps of normal displacement computed with FFT-BEM, for circular flat punch with radius of  $R_o/L = 1/2$  in contact with a grid of various size  $N = \{32, 128, 512\}$

resistance with the normal stiffness expressed by the finite difference, as:

$$R = \frac{E^*}{2KA} \left( \frac{dp}{d\omega} \right)^{-1} \approx \frac{E^*}{2KA} \left( \frac{\delta p}{\delta \omega} \right)^{-1},$$

where  $A = \pi a^2$  is the contact area.

### 4.3.2 Comparison with BEM

For FFT-BEM we used grid with  $N_{\text{FFT}} = 32^2, 64^2, 128^2, 256^2, 512^2$  DOFs. The fast-BEM version uses triangular mesh element and constant interpolation, the ACA and SVD is performed with precision  $\epsilon = 1.10^{-6}$ . The circular contact spot is defined by 4 different meshes with  $N_{\text{BEM}} = 1192, 4428, 7804, 16746$  DOFs (see Fig. 4.11). Despite the lack of alignment of the FFT grid with the geometry, the FFT-BEM demonstrates a very good precision. The relative error between the analytical solution and the three methods is presented in Fig. 4.12: fast-BEM, flat punch FFT and incremental stiffness FFT. The fast-BEM thanks to its flexibility in mesh arrangement expectedly shows a better accuracy

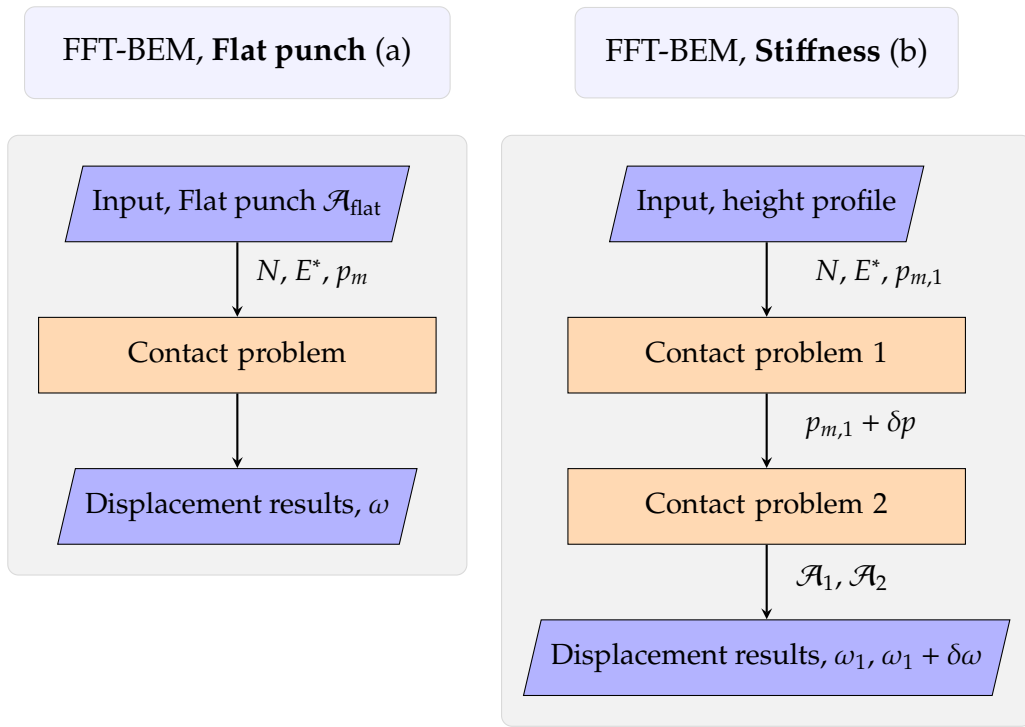


Figure 4.10: Diagram illustrating the numerical procedure for the computation of conductivity with Flat-punch (a), with the Stiffness equivalence (b)

than the FFT-BEM and the average convergence slope looks better for the fast-BEM but this aspect is possibly due to non-homogeneous mesh refinement. Note also that we did not use Richardson extrapolation here to achieve more accuracy. Nevertheless, the FFT demonstrates a very good accuracy especially when used with the incremental stiffness approach. We have to remark that such an approach requires two subsequent nonlinear computations, whereas only one computation is required for the flat punch approach which is at the same time is a much simpler linear problem.

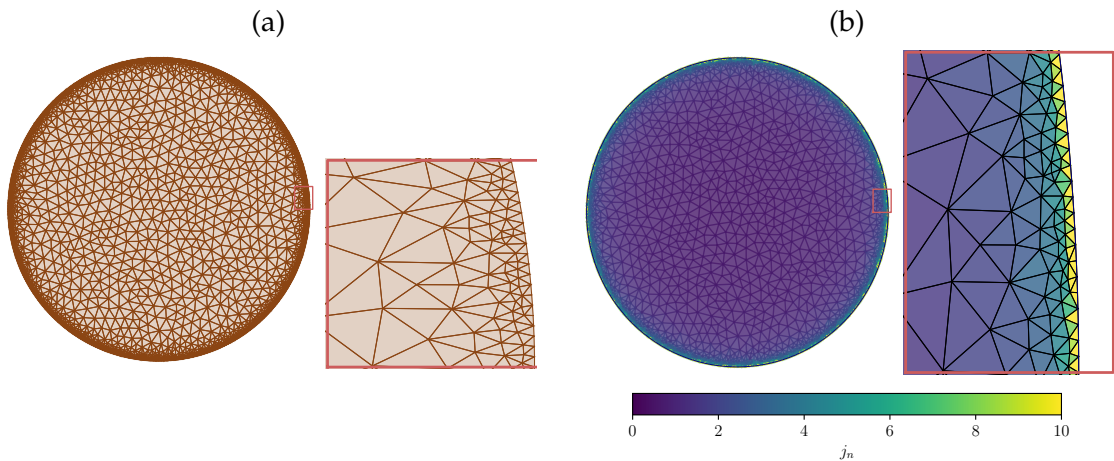


Figure 4.11: (a) The boundary element mesh example containing  $N_e = 7804$  elements used for comparison with the FFT-BEM and (b) the resulting flux.

### 4.3.3 Flower-shaped contact spots

The FFT-BEM could be also probed on more complex geometries, like the flower-shaped contact spot. The approach with the incremental stiffness computation would be too tedious to implement, but the flat-punch approach with the flower-shaped contour is still

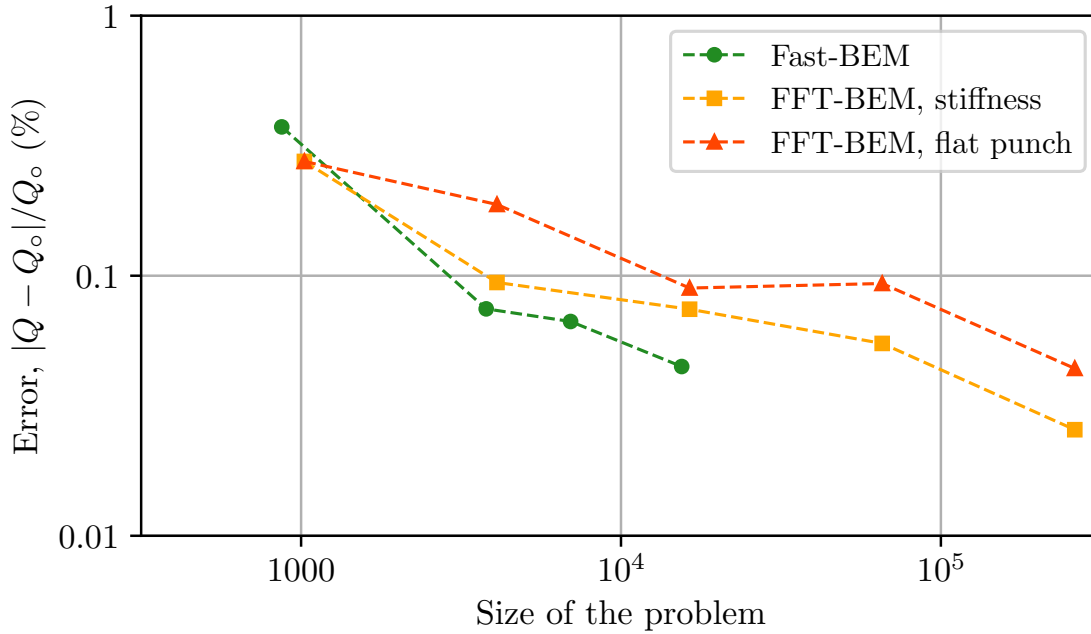


Figure 4.12: Error in flux for a circular contact spot for different sizes of the problem for fast-BEM and FFT-BEM.

feasible. To increase the precision, the smallest possible extension of the grid is used so that  $r_o + r_1 = L/2$ . An example of pressure field is presented in Fig. 4.13, for a flower with 100 petals, and a height petal ratio of  $r_1/r_o = 0.1$ , using a grid of  $(256 \times 256)$  pixels. The results shown Fig. 4.13 also illustrate the difficulty for a grid, to follow a complex contour shape.

A consistent study of the flower-shaped results are displayed Fig. 4.14 using different grid size, and different flower geometry. The total flux transmitted is normalized as in the previous chapter. The flux values obtained with FFT-BEM align well with those computed by BEM but slightly underestimate it. A convergence tendency is however quite clear: with the increasing grid size, FFT-BEM results converge towards Richardson extrapolation of BEM results, which could be seen as the reference value. The consistency of the results is checked with the least-square fitting with coefficients summarized in Table 4.3. The coefficients  $a$  and  $b$  determined for FFT-BEM results and related to the phenomenological model Eq.(3.10), tend to our reference values when  $N$  increases. In conclusion, the FFT-BEM method presents a good alternative to solve both contact problem and conductivity problem.

Method & discretization	LMS fitted coefficients			Pearson correlation $r^2$	
	$a$	$b$	$ab$		
FFT	$256 \times 256$	0.863	0.348	0.300	0.9985
	$512 \times 512$	0.898	0.334	0.300	0.9995
	$1024 \times 1025$	0.916	0.328	0.300	0.9997
BEM-Richardson	0.923	0.326	0.301	0.9997	

Table 4.3: Least squares fit for coefficients of Eq. (3.10) for flower-shaped spot obtained using FFT-BEM and Richardson extrapolation of BEM results.

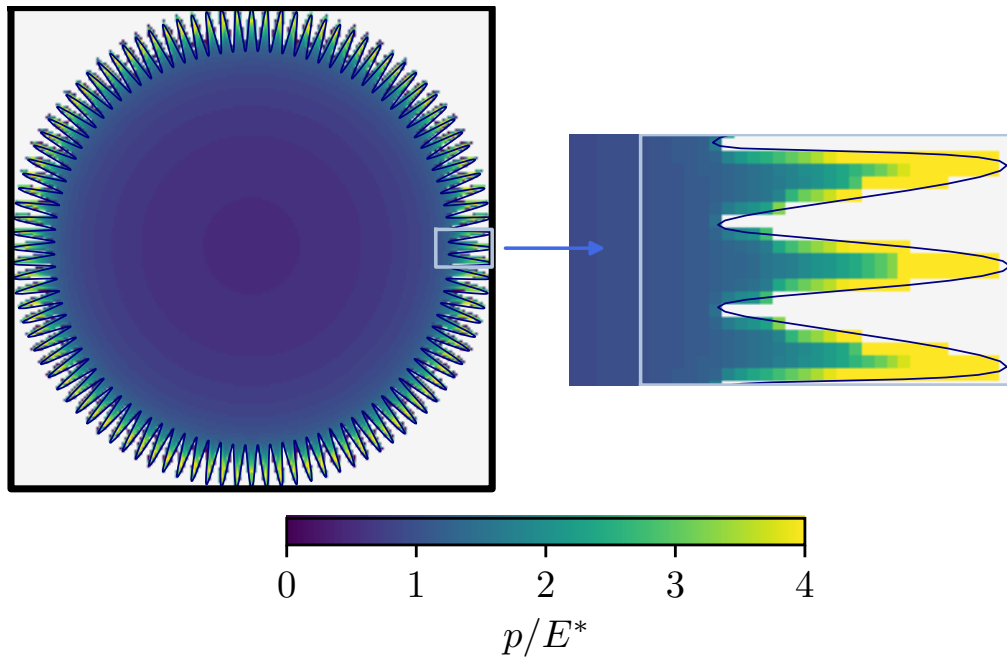


Figure 4.13: Illustration of the FFT-BEM contact pressure (or normal flux) for a flower-shaped punch with a grid of  $256 \times 256$  pixels:  $r_1/r_o = 0.1$ ,  $(r_1 + r_o)/L = 1/2$ , and  $n = 100$  petals.

## 4.4 Elastic contact of rough oxidized spheres

### 4.4.1 Real contact area

This section explores the influence of oxidation, which results in an additional constriction resistance. Oxidation often occurs due to exposure to oxidizing agents, commonly found in the surrounding air, like dioxygen. Such a phenomenon leads to the creation of non-conductive or weakly conductive films on the contact. As oxidation expands, the real conductive area decreases compared to a clean non-oxidized conductive area. Therefore, the established equivalence between contact stiffness and constriction resistance is no longer valid anymore and one needs to delve into the joint contact/oxide morphology in the contact interface. The analysis starts with the conduction problem for an oxide-free rough surface in contact simulated in FFT-BEM adapted for this purpose. Assuming weak unilateral contact between contact and conduction problems, the latter is solved either with FFT-BEM or with our fast-BEM permitting mesh refinement near the borders of contacting clusters. Our contribution focuses on constructing oxide model and studying its role. To pass from the contact area defined on a regular grid in FFT-BEM, we constructed an algorithm transforming a stair-like FFT boundary into a smooth spline, which is further used to solve the problem using fast-BEM.

### Rough surface generation

The computation of the real contact area, start with the generation of rough surfaces. To generate those, we opt for a self-affine description of roughness, which employs a white noise filtering in Fourier space [Hu and Tonder, 1992] and implemented in Tamaas. Four parameters are required, similar to those already employed in the generation of self-affine contact spots and summarized by the set  $\mathcal{I}$

- $\mathcal{I} = \{\sigma, k_l, k_s, H\}$ ,

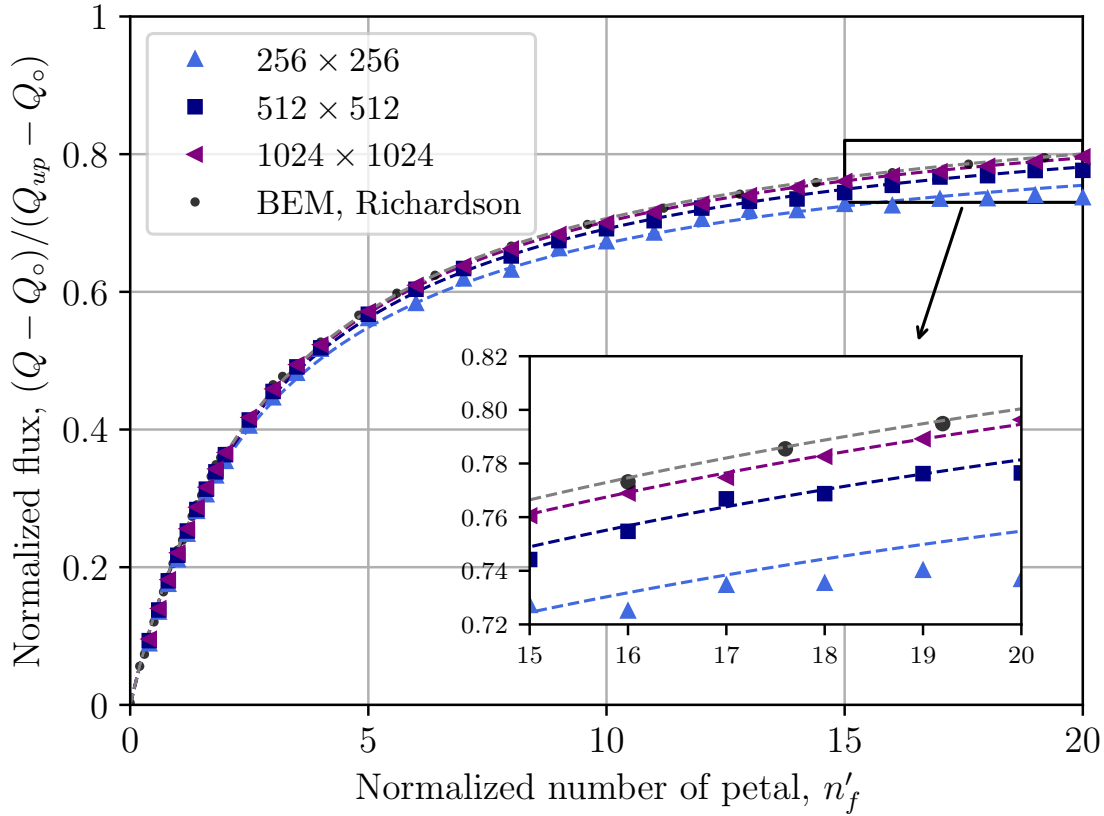


Figure 4.14: Evolution of the normalized flux for the flower-shaped contact with the normalized number of petals. The FFT-BEM results were obtained on 3 grid sizes  $N = \{256, 512, 1024\}$ , black circles represent extrapolated fast-BEM results. Dashed lines of the associated color represent the least-square fit of the phenomenological model, see Table 4.3.

where  $\sigma$  represents the standard deviation of the roughness height,  $k_l$  and  $k_s$  are the low and high cut-off wavenumbers, respectively, and  $H$  denotes the Hurst exponent, which governs the decay of the spectrum of the roughness. The use of the Fourier transform leads to the definition of the PSD function,  $\Phi$ , which follows a power law decay with respect to the wavenumber  $\sqrt{k_x^2 + k_y^2}$  with the exponent  $-2(H+1)$ . Here, the presence of a plateau in the PSD is neglected. As in the study of self-affine spots, because of the random aspect of such surfaces, several experiments must be conducted for each configuration, seeking for a mean behavior. The rough surface definition via the Fourier-transform appears very convenient for FFT relying on the same grid. To localize the contact cluster to a central region of the surface, we superpose the rough surface onto a parabolic one. The height profile definition follows the method detailed in the box below.

#### Method: Parabolic rough surface

The contacting rough surface is defined as a scalar function  $z$  of the planar coordinates  $\{x, y\}$ . This contacting surface represents a superposition of a self-affine surface  $z_s$  and a parabolic body-shape  $z_p$  as defined below:

$$z_s(x, y) = Z(\sigma, k_l, k_s, H), \quad (4.8a)$$

$$z_p(x, y) = -\frac{1}{2R} (x^2 + y^2), \quad (4.8b)$$

$$z(x, y) = z_s + z_p, \quad (4.8c)$$

where  $R$  is the curvature of the parabolic surface across both the  $x$ -axis and  $y$ -axis. The parabolic surface is a close approximation for a spherical one if the curvature  $R$  is considerably larger than the average contact radius  $a$ ; in practice we set  $R = 10L$  and  $a \ll L$ .

An illustration of the three stages of the algorithm is presented in Fig. 4.15, utilizing exaggerated parameters  $\sigma/L = 0.1$ ,  $k_l = 8$ ,  $k_s = 16$ , and  $H = 0.5$ , across a grid of size  $N = 512$ . The standard deviation is set to 0.1 to keep the height of the rough surface below the height of the parabolic profile.

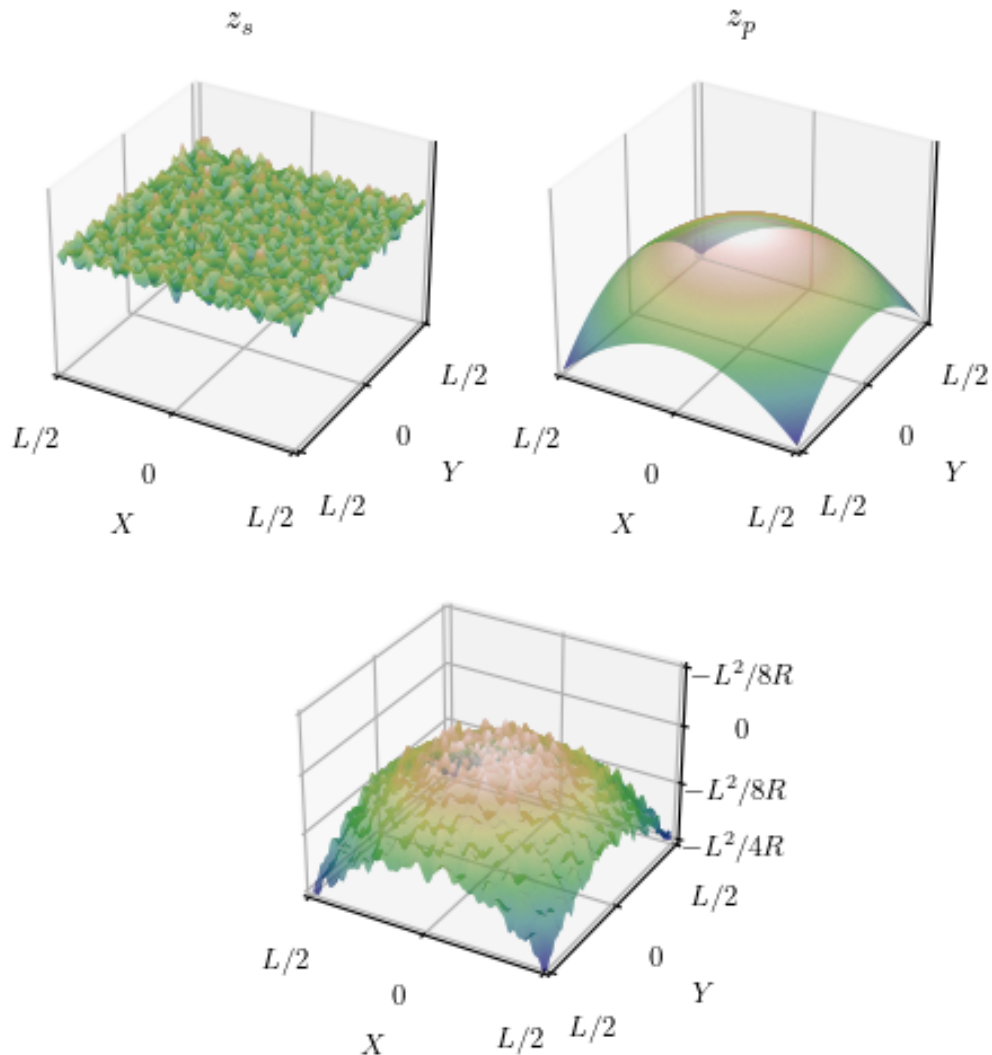


Figure 4.15: Rough surface with nominal parabolic surface using  $k_l = 8$ ,  $k_s = 32$ ,  $H = 0.5$  and the parabolic radius  $R = 2$

### Contact and conductivity results

The contact problem is first solved, followed by the problem of conduction imposing flat punch indenter over the area of conduction. An example of the results of conduction is displayed in Fig 4.16, with the set of parameters:  $k_l = 8$ ,  $k_s = 16$ , and  $H = 0.5$ , as those employed for the rough surface generation in Fig. 4.15. The mean pressure is determined for a prescribed contact radius as for a smooth parabolic surface  $a_{\text{Hertz}}$ , but must be defined over the grid of geometric dimension  $(L \times L)$ . The radius derives from the load in Hertzian

problem. Thus the mean pressure is define by the following expression,

$$p_m = \frac{4E^*}{3RL^2} a_{\text{Hertz}}^3, \quad (4.9)$$

where  $E^*$  represents the effective elastic modulus.

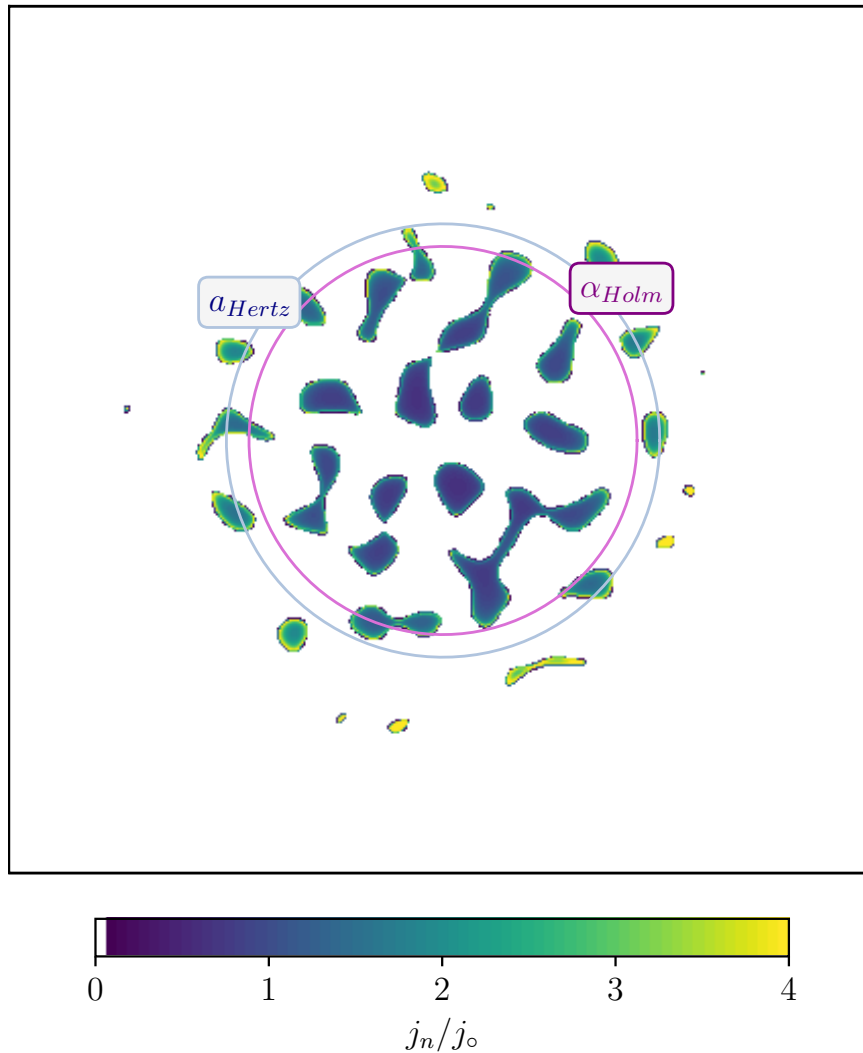


Figure 4.16: Result map for the normal flux through the contact area induced by the pressure equivalent to  $a_{\text{Hertz}}/L = 0.25$ .

The contact area consists of nominally circular contact area crossed by furrows and stripes. At the beginning, for a low contact regime, the contact spots are distinctly separate, for increasing load they expand and coalesce. The contact area seems to be well localized within a circular cluster. This cluster size could be defined in term of the *Holm's radius*, denoted by  $\alpha_{\text{Holm}}$ , as represented in Fig. 4.16. This radius based on the interaction term in Greenwood model Eq.(4.7), can be reformulated for the discretized problem in which every contacting pixel could be seen as individual contact spot as defined in the box below.

**Definition: Holm's radius: discrete and continuous definitions.**

For a conductive map  $C$  composed of pixels  $\{i, j\} \in C$ , the Holm's conductive radius

can be defined from interactive term in Eq. (4.7) where spot radii are all set to be equal:

$$R_i = \frac{1}{4K\alpha_{\text{Holm}}} = \frac{1}{2\pi KN_c} \sum_{i,j,i \neq j}^n \sum_{\{i,j\} \in C, i \neq j} \frac{1}{\|x_i - x_j\|}$$

where  $N_c$  is the number of "pixels" in the set  $C$  and  $x_i$  is the centroid coordinates of the  $i$ -th pixel. From this expression we readily get the Holm's radius,

$$\alpha_{\text{Holm}} = \frac{\pi N_c}{2} \left[ \sum_{\{i,j\} \in C, i \neq j} \frac{1}{\|x_i - x_j\|} \right]^{-1} \quad (4.10)$$

Note that this radius is defined using the whole span of pixel, some are touching themselves, in contrast to the original definition considering separated contact spots. Equivalently, the Holm's radius can be interpreted as an average distance of interaction, reformulated by the Green function and the Riemann integral. Indeed, the expression on the right-hand side in Eq. (4.10) could be derived from a continuous framework, where the double summation is replaced by integrals

$$\frac{1}{2\alpha_{\text{Holm}}} \approx \frac{2}{A_c} \left\langle \int_{A_c} G(x, y) dS_y \right\rangle_{\forall x \in A_c},$$

where  $A_c$  is the contact area and the average  $\langle \bullet \rangle$  is taken for all points  $x \in A_c$ .

Visually the Holm's radius appears to be consistent with the cluster size, the contact area widely spread beyond the radius of  $a_{\text{Hertz}}$ , due to the roughness. The result, in general, demonstrate a particular sensitivity to the low wavenumber parameter  $k_l$ . Other examples are depicted in Fig. 4.17 and 4.18, for different roughness parameters and for different mean pressure applied, using  $a_{\text{Hertz}}/L = 0.1$  and  $a_{\text{Hertz}}/L = 0.35$ , respectively. The contact size area better aligns with the Hertzian contact spot, as  $a_{\text{Hertz}}, k_l$  increase, in agreement with [Greenwood and Tripp, 1967]. To limit the size of contact area, and ensure that it does not spread beyond the grid limit, the low cut off parameter is set higher than 8. Some test have demonstrated, it is hard to set a contact area with  $a_{\text{Hertz}}/L < 0.05$ , as for a grid using  $N = 512$  pixel on its length, the contact area set is equivalent to the pixel size.

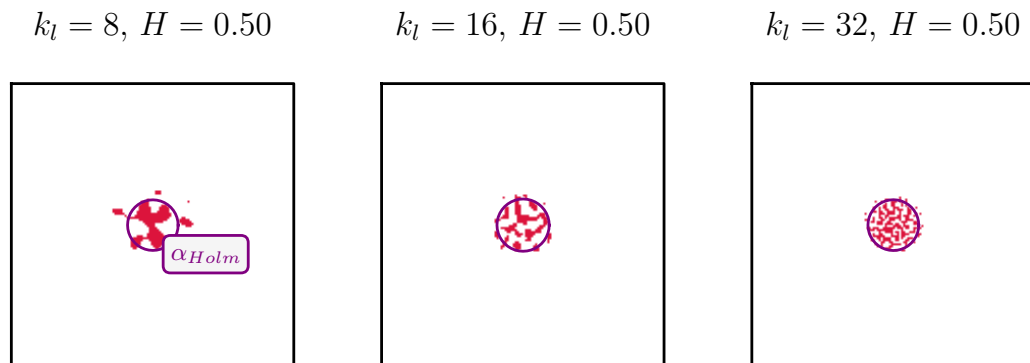


Figure 4.17: Real contact area for contact with a rough sphere for with Hurst parameter  $H = 0.5$ , with different low cutoff wavenumber  $k_l = \{8, 16, 32\}$  and with a prescribed Hertzian radius of  $a/L = 0.1$ .

The real contact area grows as the mean pressure increases. Consequently, individual contact spots expand and coalesce resulting in a more "monolithic" unified contact area.



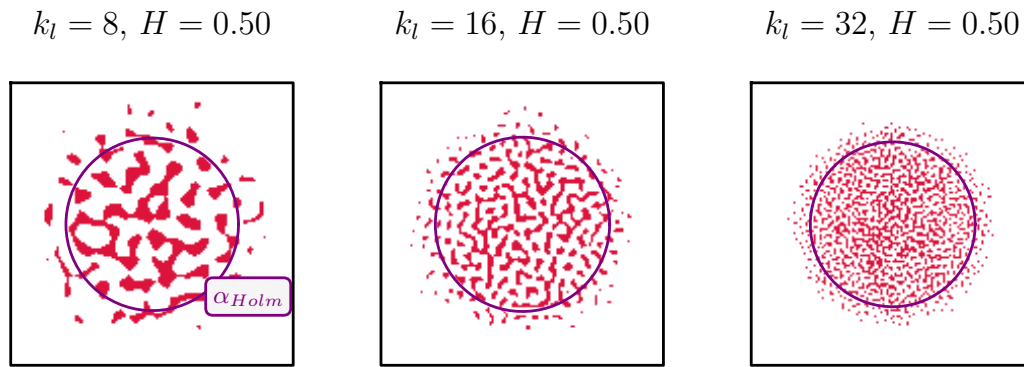


Figure 4.18: Real contact area for contact with a rough sphere for with Hurst parameter  $H = 0.5$ , with different low cutoff wavenumber  $k_l = \{8, 16, 32\}$  and with a prescribed Hertzian radius of  $a/L = 0.35$ .

The coalescence of the contact spots is prompted by an increase of  $k_l$ . This phenomenon is consistent with the multi-asperity based model [Bush et al., 1975], which leads to the relation  $A \sim F/\sqrt{m_2}$ . The contact area  $A$  decreases with an increasing  $m_2$  value when  $k_l$  is raised, maintaining a steady load  $F$ .

#### 4.4.2 Conductivity of a clean rough contact

For the resolution of the conductivity problem, we consider the real contact area obtained by the FFT-BEM simulations as the conductive contact area, disregarding any oxidation factors at this stage. To solve the conductivity problem, the contact area could be transformed in a flat punch of the same contour, so solving the indentation problem by analogy results in the flux within the contact area. Of course, for oxide-free surface, an incremental stiffness could be also used to evaluate the conductivity. However, since the aim of this study is mainly to investigate the effect of oxide, so throughout the study we use the flat punch analogy. The low cut-off wavenumber  $k_l$  varies in the span  $\{8, 16, 32\}$ , the Hurst parameter  $H$  in  $\{0.25, 0.5, 0.75\}$  while the magnification is set equal to  $\zeta = k_s/k_l = 2$ . 10 simulations are conducted for every set of parameters, referred by a *seed* index. The mean imposed pressure is driven by the contact radius  $a_{\text{Hertz}}/L$  ranging from 0.05 to 0.35 by increments of 0.05, all these parameters are summarized in the box below. This set-up leads the determination of the average behavior, surrounded by a confidence interval. The width of the interval is given by *Bienaymé-Tchebychev* formula, similar to analysis of self-affine contact spots. In Fig. 4.19 we show the evolution of the flux for the normalized force  $F' = F/(AE^*)$ . This normalized force is still almost constant, compared to the flux evolution, agreeing to [Yastrebov, 2019]. It is interesting to note that the normalized flux seems to be proportional to this normalized force. However, the variation related to the wavenumber  $k_l$  is not monolithic.

##### Method: Set of parameters

- Cutoff wavenumber (3 values):  $k_l = \{8, 16, 32\}$ ,  $k_s = 2k_l$ .
- Hurst parameters (3 values):  $H = \{0.25, 0.5, 0.75\}$ .
- Contact load (7 values):  $a_{\text{Hertz}} = [0.05 : 0.35]$  with step of 0.05.
- Seed index (10 values):  $[1 : 10]$ .

Cumulatively, this leads to a total of 630 simulations.

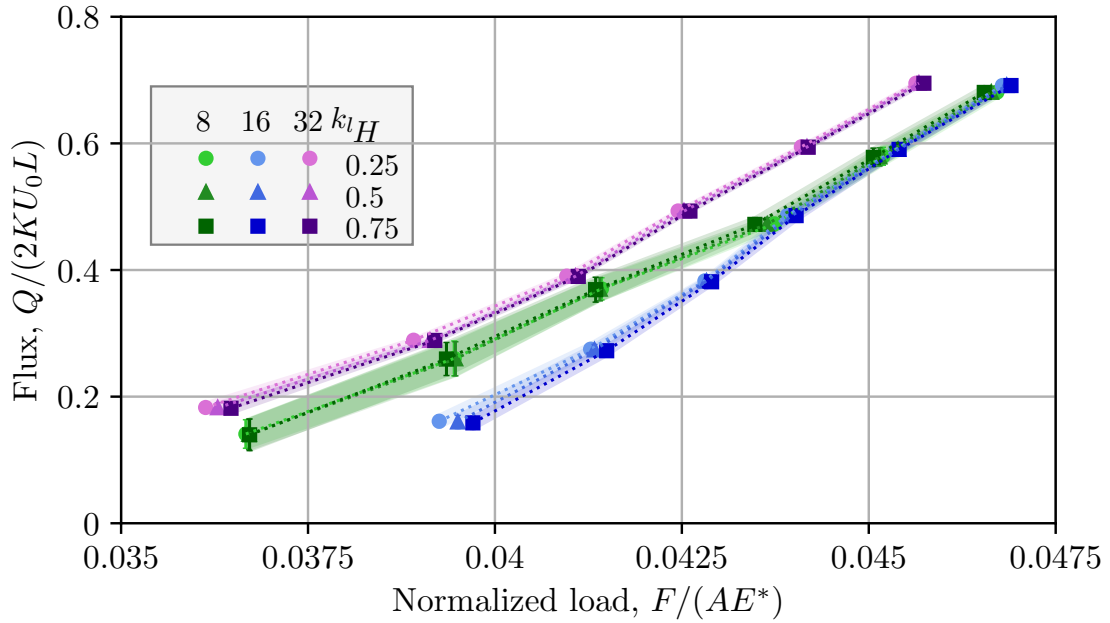


Figure 4.19: Evolution of the total flux with the normalized force for different rough surfaces. The flux is normalized by  $2KU_0L$ , equal to the flux for a circular contact spot with a radius of  $L/2$

The normalized results of the flux are presented in Fig. 4.20 for the different roughness configurations. This flux is normalized by  $Q_{\text{Holm}}$ , which stands for the total flux transmitted by a circular contact spot with a radius of  $a_{\text{Holm}}$ ,

$$Q_{\text{Holm}} = 4KU_0\alpha_{\text{Holm}}$$

As seen, the total flux through the contact area is lower than the reference flux through a circular spot with Holm's radius  $Q_{\text{Holm}}$ . The ratio between these two fluxes remains relatively stable, which is due to a rather compact geometry of the contact area cluster. The most significant differentiation in these results can be attributed to the parameter  $k_l$  controlling representativity of the roughness. Moreover, as  $k_l$  increases, it entails a subsequent increase in compactness in the contact area. At the same time the Hurst parameter  $H$  seems to have a weaker influence as could be anticipated from the study of self-affine spots.

The discrepancy between the computed flux and Holm's flux  $Q_{\text{Holm}}$  inherits from the non-connectedness of the contact area within the radius of  $a_{\text{Holm}}$  which could be eventually amplified by numerical errors, whose analysis we skip in this section. The comparison between associated contact areas (true one and Holm's radius defined ones) is presented in Fig. 4.21 for increasing contact area. At light contact regime stage, the real contact area would appear less compact, manifesting larger non-conductive space within a radius of  $a_{\text{Holm}}$ , as illustrated in Fig. 4.16. Interestingly, the ratio tends to a certain limit which depends solely on the parameter  $k_l$  indicating that it is probably affected by a numerical error as in [Yastrebov et al., 2015b, Yastrebov et al., 2017b]. The limit for  $k_l = 32$  appears to be upper one, exhibiting contact spot even well beyond the Holm's cluster radius. The compactness of the real conductive area increases, as the mean pressure rises, akin to the representation in Fig. 4.18. The contact area expands as the load increases, overtaking the area defined by the Holm's radius.

### Oxide film model

To handle the problem for oxidized contact, we need to construct a model for surface oxides. Such films, present in contact, increase the resistance which

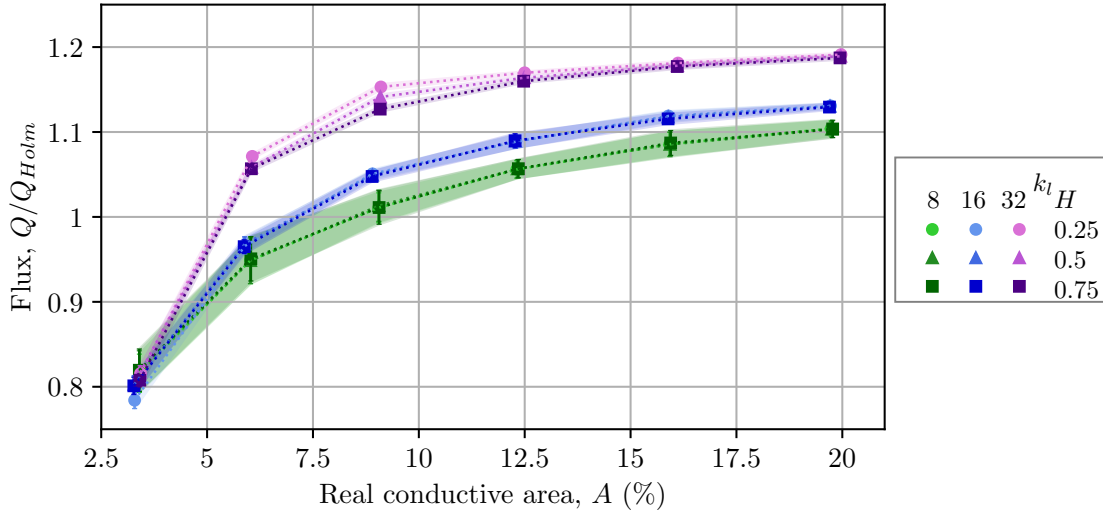


Figure 4.20: Normalized flux change with the (conductive) contact area in absence of oxide for different roughness parameters  $k_l = \{8, 16, 32\}$ ,  $H = \{0.25, 0.5, 0.75\}$ : mean value  $Q/Q_{HoIm}$  and the confidence interval are reported.

can no longer be predicted by the Holm's radius or more advanced models [Yastrebov et al., 2015c]. The problem of oxide growth has been extensively studied [Lawless, 1974, Thomas and Probert, 1970, Jeurgens et al., 2002] showing the complexity of oxidation which depends on many different factor, but could be formulated in term of an activation energy. One of the crucial parameters is the temperature playing a role of a source of energy. On another hand, the energy of activation can be lowered by the increase of the pressure of oxidant component. The oxidation starts on the metal surface, and continues with the growth of the oxide layers over the surface, and inward the bulk. The very stage of oxidation at low temperatures cannot be explained by temperature activated diffusion, so a different model was developed by *Cabrera-Mott* model [Cabrera and Mott, 1949]. Since the initial oxide films are very thin the curvature of the surface does not play a big role, however, at the nano-scale there is a correlation between the oxidation kinetics and the curvature, see e.g. [Ermoline and Dreizin, 2011]. The morphology of oxide films depends also on the material. For copper, oxidation first occurs in formation of island of oxide as was reported in [Yang et al., 1998, Lampimäki et al., 2007]. As a result, oxidation follows the crystal orientation of the grain underneath, yielding the formation of rather polygonal shape for oxide film islands.

Even though some models have proven their capabilities to simulate the oxidation [Huin et al., 2005, Pillai et al., 2021], we opt here for a simple geometrical model. The oxide film morphology is constructed as cut through a random self-affine field. A set of parameters  $\mathcal{I}_O$  used for this construction includes a similar (but uncorrelated) set as for the roughness construction but with an additional parameter indicating oxide surface fraction  $\phi^o = A_o/A_0$ :

$$\bullet \mathcal{I}_o = \{\sigma^o, k_l^o, k_s^o, H^o, \phi^o\},$$

where  $\sigma^o$  is the standard deviation of the random distribution,  $k_l^o, k_s^o$  are the lower and upper cut-off wavenumbers, respectively, and  $H^o$  represents the Hurst parameter. These parameters lead the definition of first rough surface  $z^o$ , which employs a self-affine generation model like for  $z_s$  in Eq.(4.8a). Then, the oxide patches are delineated, to correspond with a ratio of oxidation, set to  $A^o$ . The oxide region encloses a span of pixel,  $\mathcal{O}$ , as presented in the yellow frame below,

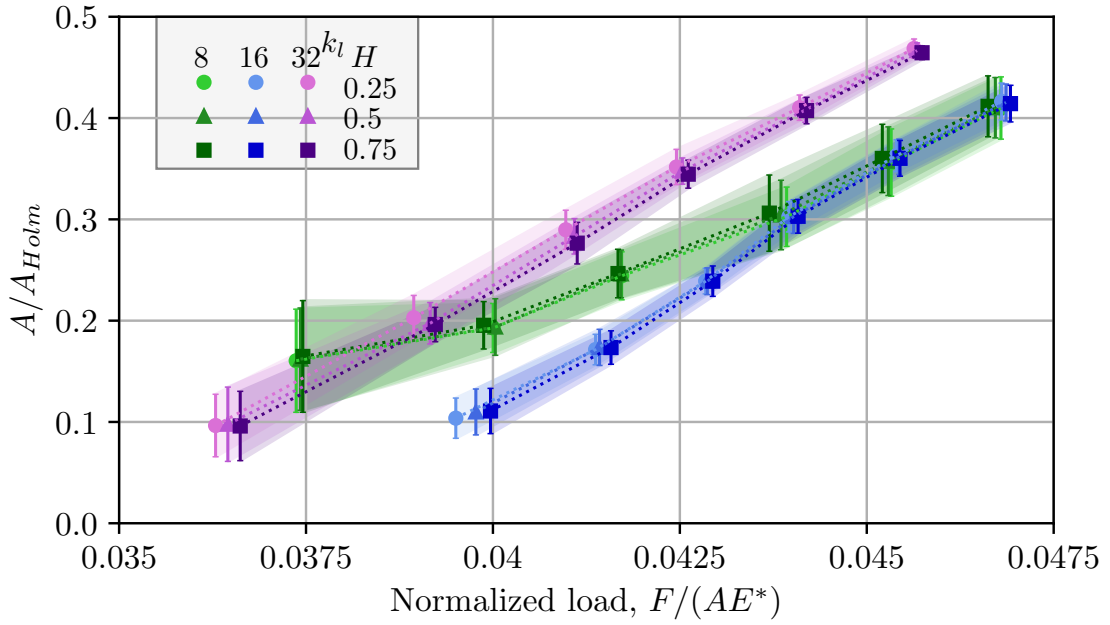


Figure 4.21: The ratio between the Holm's area to the true contact area for increasing normalized load and different roughness parameters. The mean value and confidence interval are reported.

#### Method: construction of oxide clusters

A spatial random field  $\Omega(x, y)$  is generated for the set of parameters  $\{\sigma^o, k_l^o, k_s^o, H^o\}$ . Now, to model the oxide film, we will consider zones  $\{x, y\} \in \mathcal{O}$  where  $\Omega(x, y) \geq l$ . Assuming that the surface fraction of the oxide is provided by the last parameter  $\phi^o = \mathcal{O}/A_0$ , one needs to find the corresponding  $l$ :

$$\text{Find } l \text{ such that for } \mathcal{O} = \{\{i, j\} \mid \Omega(x_i, x_j) \geq l\}, \quad \mathcal{O}/A_0 = \phi^o$$

This is a nonlinear problem and can be found, for example, by a bisection method or Newton method with a model Gaussian distribution. Nevertheless, a residual error may still persist due to the pixel-based discretization of the grid. Various tests have indicated a maximum error of around 0.5% in terms of the surface fraction of the oxide.

Examples of oxide films are depicted in Fig. 4.22 and 4.23, representing oxide fractions of  $\phi^o \approx 20\%$  and  $\phi^o \approx 40\%$ , respectively. In Fig. 4.22, the random field parameters are  $k_l^o = 8$ , and  $k_s^o = 128$  with different Hurst parameters  $\{0.4, 0.6, 0.8\}$  presented from left to right. This approach yields relatively dense and sparsely distributed oxide spots, which are clearly distinct from each other. The individual size of these oxide spots decreases as the Hurst parameter increases or for the low cut-off wavenumber increase  $k_l^o$  (not presented in these maps). In Fig. 4.23, the average size of oxide patches increases, but they remain well separated. In all our generations the higher cut-off wavenumber is always set as  $k_s^o = 32k_l^o$ .

#### Conductive area

To take into account the effect of the oxide film, we simple assume that areas covered by oxide become insulating. Since the film thickness is very small, we assume that homogeneous elastic model is still valid for the entire half-space. The conductive area, denoted by  $\mathcal{A}'$ , is a superposition of the conductive area (area without oxide films) and

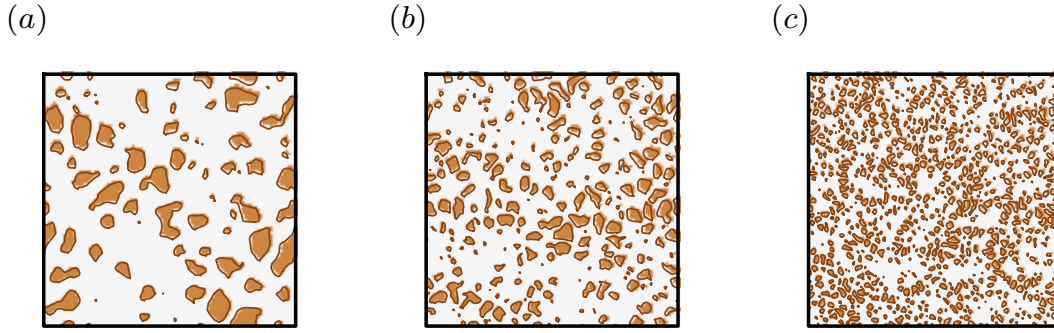


Figure 4.22: Generated oxide films with surface fraction  $\phi^o = 20\%$  using the following wavenumber parameters:  $k_l^o = 8$ ,  $k_s^o = 128$  on the grid ( $512 \times 512$ ) pixels presented for different Hurst exponents (a)  $H = 0.4$ , (b)  $H = 0.6$  and (c)  $H = 0.8$ .

the contact area:

$$\mathcal{A}' = \bar{\mathcal{O}} \cap \mathcal{A}.$$

Some examples of such a superposition are presented in Figs. 4.24 and Fig. 4.25 for the rough surface defined by the lower cut-off wavenumber  $k_l = \{8, 32\}$ , respectively. In these figures, three different lower cut-off parameters for the oxide layer are employed, illustrating the difference induced by this latter parameter. However, all oxide layers use the same Hurst parameter of  $H^o = 0.4$ . These figures emphasize the role of  $k_l^o/k_l$  ratio, controlling to some extent the size of oxide spots to contact spots. When  $k_l^o/k_l \approx 1$ , the size of the oxide defect appears to be similar to the size of the contact spot for an interval of oxide area fractions  $\phi^o$ . In the limit  $k_l^o/k_l \gg 1$ , such as  $k_l^o = 32, k_l = 8$ , the oxide defect is much smaller than average size of contact spots. Whereas in the limit  $k_l^o/k_l \ll 1$ , for example, for  $k_l^o = 8, k_l = 32$ , it entails the opposite size effect: oxide spots are much bigger than contact spots. Nevertheless, the Holm radius remains a good measurement of the conductive zone, even for a particular example of  $k_l = 32$  and  $k_l^o = 8$ .

### 4.4.3 Oxidation analysis and results

This study of conduction was carried out by FFT-BEM using flat-punch geometry with the contour defined by the conductive area  $\mathcal{A}'$ . The oxide layers and the contact area are both defined on the same grid, which results in a straightforward definition of conductive area. An example of the normal flux is displayed in Fig. 4.26 using surface roughness parameters as for Fig. 4.16 but this time with the superposition with the conductive area defined by oxide films, whose surface fraction reaches  $\phi^o = 40\%$ .

Adding the oxidation strongly increases the parametric space: first by 4 parameters for the random field and also by the oxide surface fraction  $\phi^o$ . This investigation is confined to the variation of  $k_l^o$  and  $\phi^o$  only since they are the most influential parameters. The Hurst parameter for the oxide random field is set to  $H^o = 0.4$ , and the high cutoff wavenumber is defined to be  $k_s^o = 2k_l^o$ . Three distinct values for the low cutoff wavenumber,  $k_l^o = \{8, 16, 32\}$  will be explored in combination with three different oxidation rates  $\phi^o = \{20\%, 30\%, 40\%\}$ . The parametric space for rough surfaces is reduced as well: the Hurst exponent is set to  $H = 0.5$ , and the lower cut-off wavenumber is set to  $k_l = \{8, 16, 32\}$ . Due to the stochastic nature of the surface of conduction, multiple simulations are needed: 10 experiments are conducted for every combination of parameters, see a summary in the box below.

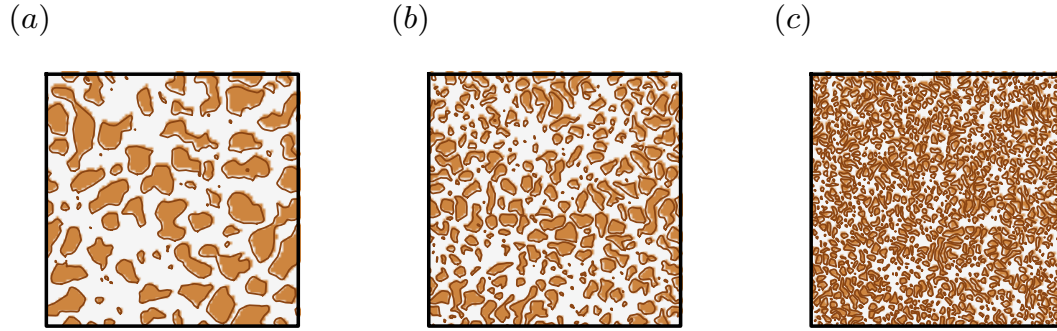


Figure 4.23: Generated oxide films with surface fraction  $\phi^o = 20\%$  using the following wavenumber parameters:  $k_l^o = 8$ ,  $k_s^o = 128$  on the grid ( $512 \times 512$ ) pixels presented for different Hurst exponents (a)  $H = 0.4$ , (b)  $H = 0.6$  and (c)  $H = 0.8$

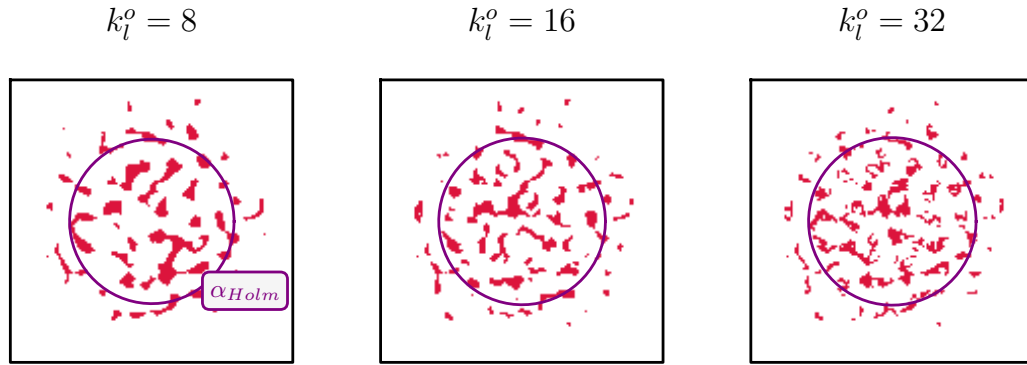


Figure 4.24: Maps of real conductive area, defined by intersection the real contact area using parameter of  $k_l = 8$ ,  $H = 0.5$ ,  $k_s = 16$  for a Hertzian radius parameter  $a_{\text{Hertz}}/L = 0.35$ , intersected by the oxide layers defined by different FFT parameter  $k_l$  of  $\{8, 16, 32\}$ , Hurst parameter of  $H = 0.4$ , and a set oxidation rate of 40%

#### Method: Set-up parameters for conductivity of oxidized rough contact

Parameters for the generation of the roughness,  $\mathcal{I}$ :

- Wavenumbers (3 values):  $k_l = \{8, 16, 32\}$ ,  $k_s = 2k_l$
- Hurst parameter :  $H = 0.5$ ,
- Load applied (10 values):  $a_{\text{Hertz}}/L = [0.05, 0.35]$  with step of 0.05.

Parameters for the generation of oxide films  $\mathcal{I}^o$ :

- Wavenumbers (3 values):  $k_l^o = \{8, 16, 32\}$ ,  $k_s^o = 2k_l^o$
- Hurst parameter :  $H^o = 0.4$ ,
- Surface fraction (3 values):  $\phi^o = \{0.2, 0.3, 0.4\}$

Seed index (10 values):  $[1, 10]$

This accounts for a total of 1890 simulations.

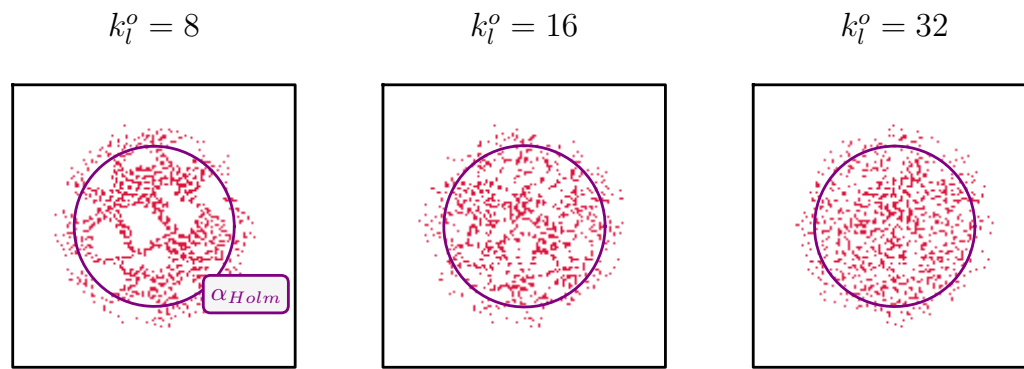


Figure 4.25: Maps of real conductive area, defined by intersection the real contact area using parameter of  $k_l = 32$ ,  $H = 0.5$ ,  $k_s = 64$  for a Hertzian radius parameter  $a_{Hertz}/L = 0.35$ , intersected by the oxide layers defined by different FFT parameter  $k_l$  of  $\{8, 16, 32\}$ , Hurst parameter of  $H = 0.4$ , and a set oxidation rate of 40%

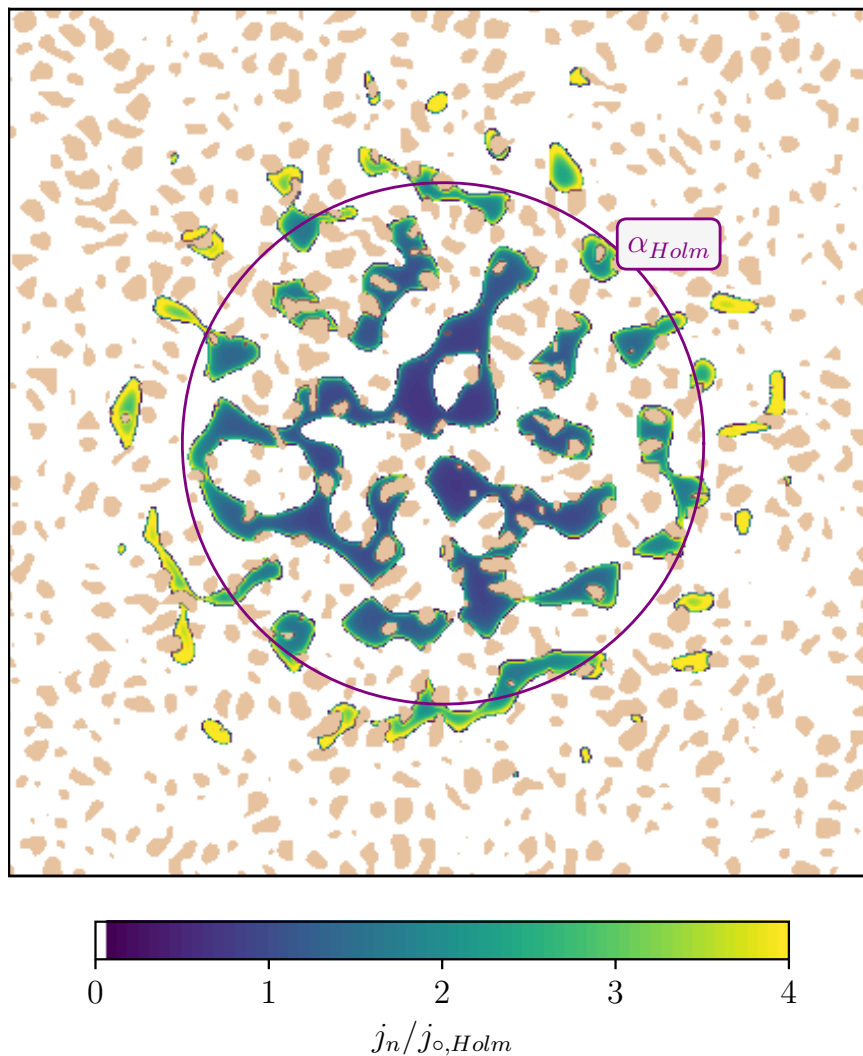


Figure 4.26: Map result of the normal flux with a rough surface defined by  $k_l = 8$ ,  $H = 0.5$ ,  $k_s = 16$  with the contacting pressure  $a_{Hertz}/L = 0.35$  interplaying with oxide films built with  $k_l^o = 32$ ,  $H = 0.4$

The results of simulations for  $k_l$  at 8, 16, and 32 are presented separately in Figs. 4.27, 4.28 and 4.29, respectively. Each figure depicts the total flux normalized by the flux through a non-oxidized surface  $Q/Q_{\text{clean}}$  for varying oxide patterns defined by  $k_l^o$  and  $\phi^o$ . We can see that the ratio  $k_l^o/k_l$  does indeed have a strong effect on the contact resistance. The confidence intervals or standard deviations of the results appear to be fairly wide, but they gradually decrease as the area of conduction increases. The dispersion of results is also reduced with the multiplication of oxide patterns, i.e. with the increase in  $k_l^o$  value. In fact, the average size of oxide spots decreases with  $k_l^o$ , similar to the annular contact spot problem. The proportion of oxide also reduces the flux compared to the flux of the non-oxidized surface. However, this loss is not proportional to the oxidation ratio, and appears to be more limited.

To better this non-linear influence of the ratio of oxidation, the drop in flux  $Q$ , compared with  $Q_{\text{clean}}$  generated by the non-oxidized surface, is identified with the law presented in the color frame below. It appears this drop depends on the contact area  $A$ , as well, decreasing as this latter increases.

#### Model: Interpolation result of $Q/Q_{\text{clean}}$

The results in flux are identified by the following phenomenological model, encompassing the effects of the oxidation ratio  $\phi^o$  and the growth of the contact area  $A$  :

$$\frac{Q}{Q_{\text{clean}}} = 1 - \frac{1 - a(\phi^o)^b}{1 + c(A/\phi^o)^d} \quad (4.11)$$

With  $a, b, c, d$  are four positive parameter

This law can be decomposed in two terms, one influenced by the ratio of oxidation,  $\phi^o$ , and a second term which account for the ratio  $A/\phi^o$ . When the rate of oxidation decreases to 0, this law tends to 1, i.e. the area of conduction is not perturbed by the oxidation. The coefficient values are found by least square fit on separated serie of data related to the different couples  $(k_l, k_l^o)$ . The results of interpolation are presented in black dots in Fig. 4.27, 4.28, and 4.29.

#### 4.4.4 Comparison with BEM results

To validate the FFT-BEM simulation results, we reproduce some simulations using our fast-BEM with and without oxide films. The surface roughness is defined by  $k_l = 32$ ,  $k_s = 64$ , and  $H = 0.5$ , a light loading is considered  $a_{\text{Hertz}}/L = 0.15$ . These parameters correspond to the smallest contact areas among the span of parameters considered so far. These parameters also reduce the variability of the results, as illustrated Fig. 4.29. All associated contact problems and oxide generation are conducted for a grid sized at  $(512 \times 512)$ . All parameters are summarized in a box below.

#### Method: Parameters for BEM simulations

Surface roughness parameters:  $\mathcal{I} = \{k_l = 32, k_s = 64, H = 0.5\}$  and  $a_{\text{Hertz}}/L = 0.15$

Oxide parameters  $\mathcal{I}^o$  :

- Wavenumbers (3 values):  $k_l^o = \{8, 16, 32\}$ ,
- Hurst parameters:  $H^o = 0.4$ ,
- Oxide surface fraction (3 values):  $\phi^o = A^o = \{20\%, 30\%, 40\%\}$ ,

This study is conducted on a single surface roughness and accounts for the total of 18 simulations. Each geometry of oxide layers area is computed for two different element sizes,  $h/L = 2/N$  and  $h/L = 1/N$ .



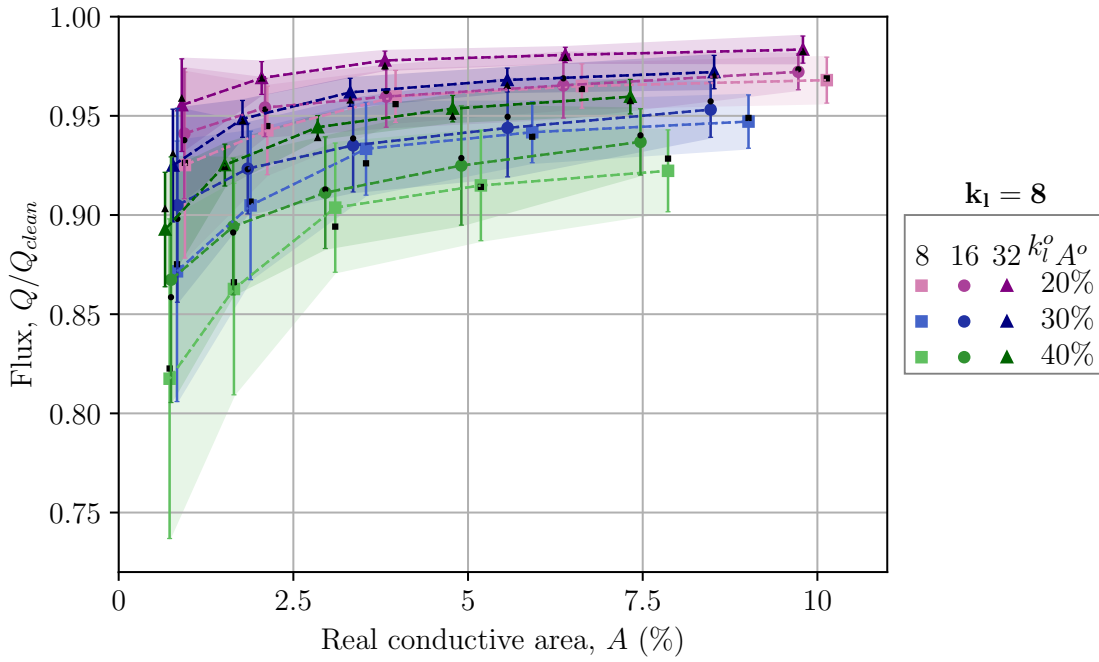


Figure 4.27: Normalized flux for oxidized surfaces evolving with the conductive contact area  $A_c$ : the rough surface constructed with  $k_l = 8$  with different oxide patterns constructed using  $k_l^o = \{8, 16, 32\}$  and oxide fraction of  $A^o = \phi^o = \{20\%, 30\%, 40\%\}$ .

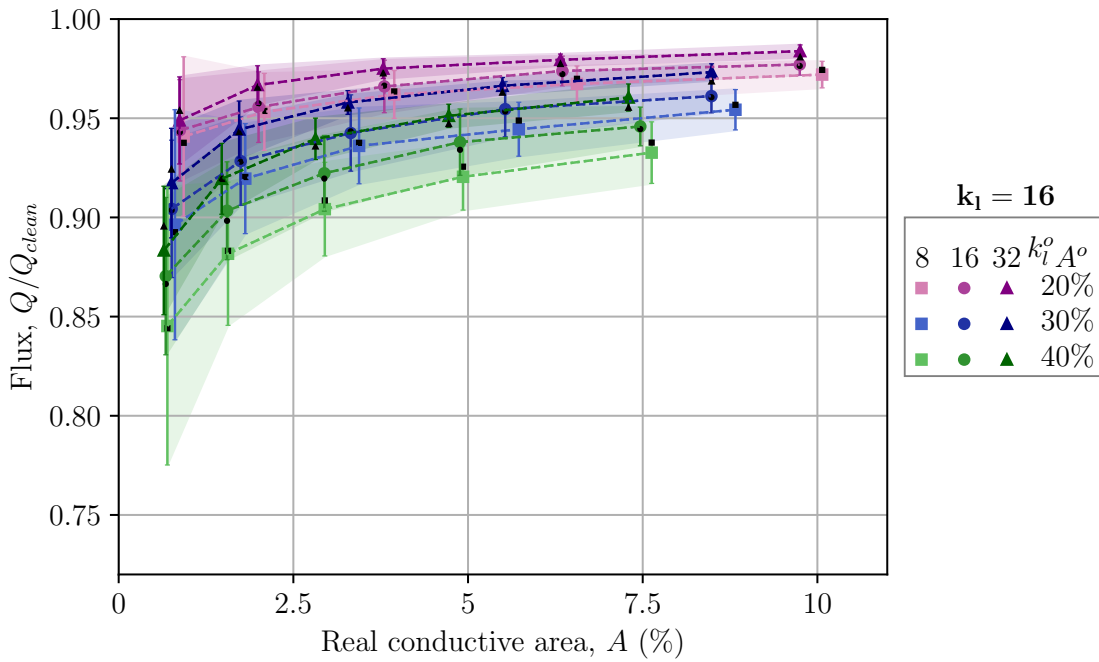


Figure 4.28: Normalized flux for oxidized surfaces evolving with the conductive contact area  $A_c$ : the rough surface constructed with  $k_l = 16$  with different oxide patterns constructed using  $k_l^o = \{8, 16, 32\}$  and oxide fraction of  $A^o = \phi^o = \{20\%, 30\%, 40\%\}$ .

### From FFT to BEM: from binary matrix to smooth surface

Through this final study, we aim to compare FFT-BEM and BEM results for oxidized conductive area. Employing BEM needs to redefine the boundaries of the conductive surface. We shift from a pixel-based description to a new paradigm, enabling the establishment of smoother outlines for related spots. Nevertheless our goal pertains to conservation of the

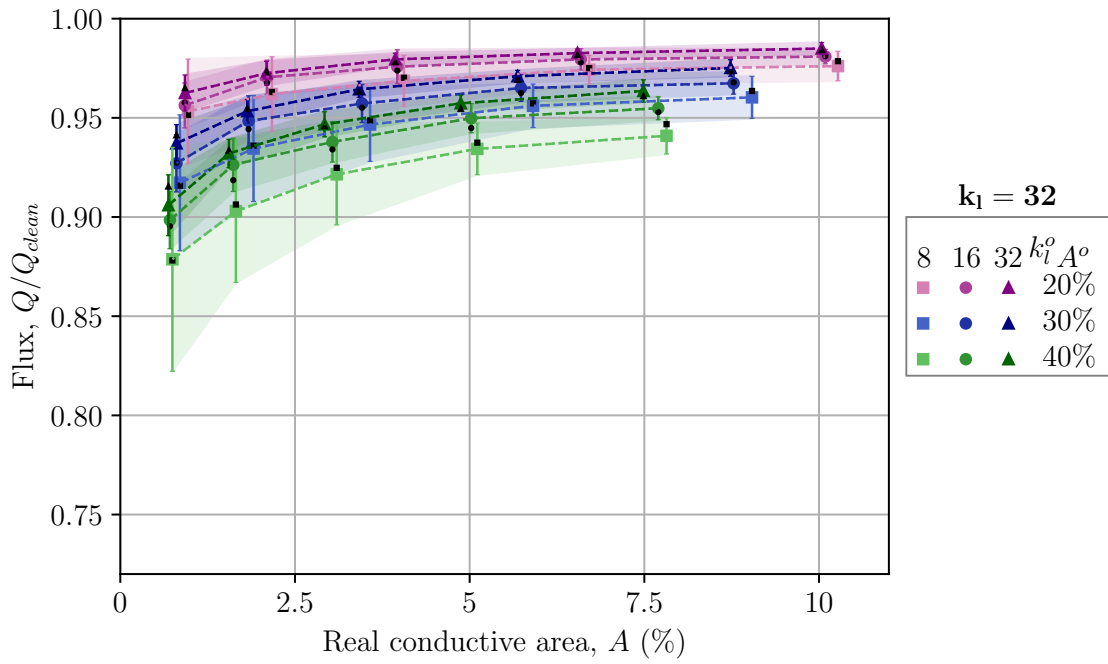


Figure 4.29: Normalized flux for oxidized surfaces evolving with the conductive contact area  $A_c$ : the rough surface constructed with  $k_l = 32$  with different oxide patterns constructed using  $k_l^o = \{8, 16, 32\}$  and oxide fraction of  $A^o = \phi^o = \{20\%, 30\%, 40\%\}$ .

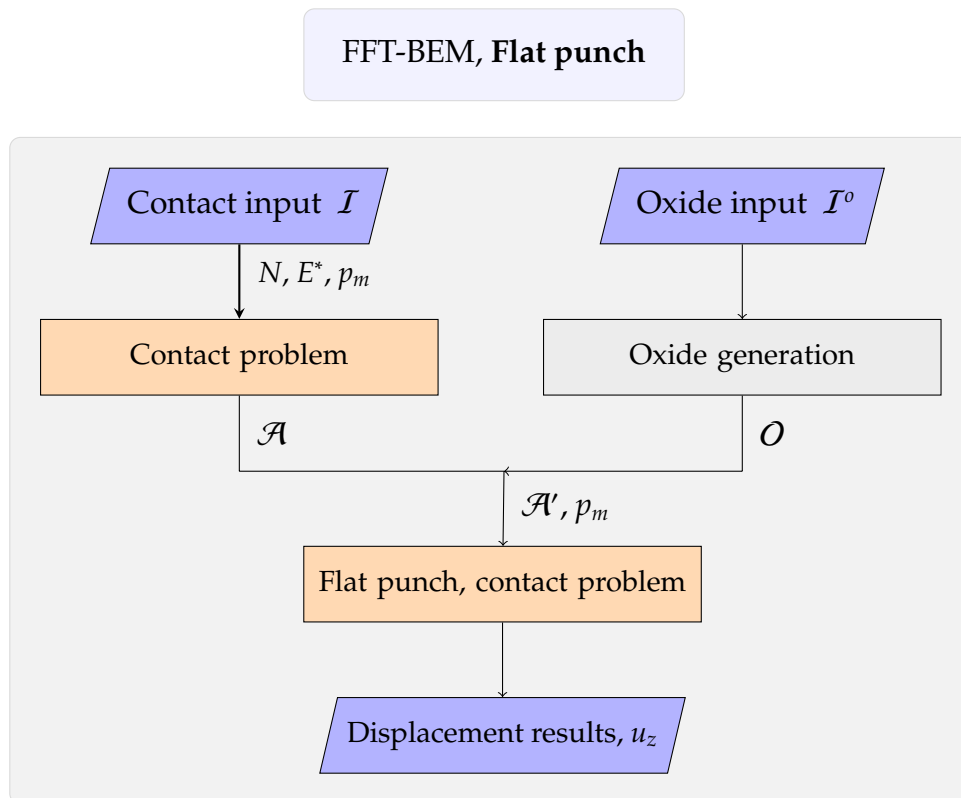


Figure 4.30: Diagram illustrating the numerical procedure for the computation of the conductivity for oxidized surface based on the flat-punch analogy.

initial pixelated contour as much as possible. For this task, the definition of the smooth curve takes advantage of *Bezier curve*.

FFT-BEM results are presented on a regular grid. The contact area is thus could

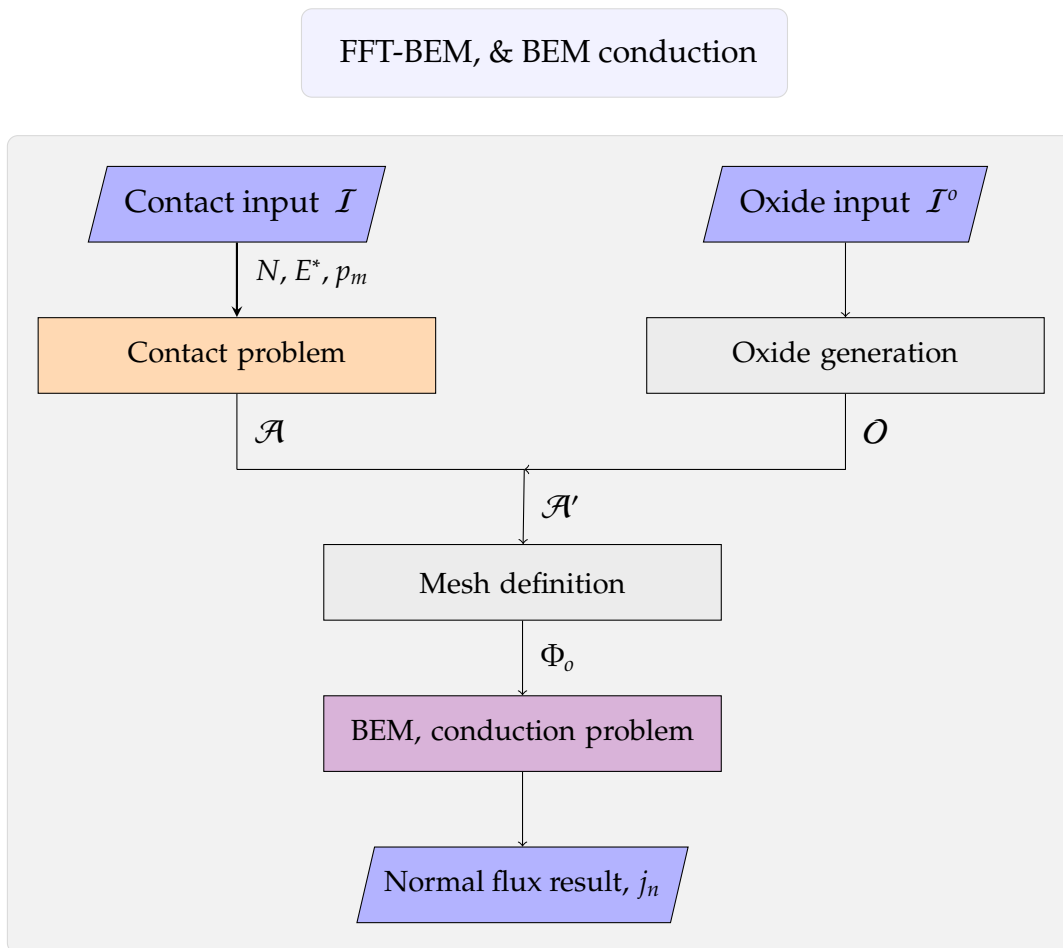


Figure 4.31: Diagram illustrating the numerical procedure for the calcul of conductivity based on Flat-punch

be seen as a binary matrix. To construct an adapted mesh for the BEM simulations, we need to extract non-connected regions and approximate their contours with closed smooth curves, for example, cubic Bezier splines. To this end, we have developed a computational approach to identify distinct contact regions and transform their contours into closed Bezier splines. This method not only facilitates a precise representation of the interface and the accurate use of the fast-BEM method but also potentially permits to increase the accuracy of the contact area representation. The contours are extracted via OpenCV's contour detection algorithm, and the resulting points are coarsened to eliminate redundant details. Subsequently, the script meticulously calculates control points for Bezier splines that closely emulate the contour while ensuring there are no self-intersections or excessively tight curvatures. It is shared along with our [fast-BEM code](#) as a tool [Beguin and Yastrebov, 2023]. The complete numerical chain is depicted in Fig. 4.31, where the FFT-BEM conduction resolution is replaced by the mesh generation and the Fast-BEM step.

A possible enhancement would be to formulated this problem as an optimization problem with some curvature and area constraints. Indeed, the contact area of pixel-based contact spot is typically overestimated compared to its asymptotic limit as the pixel size tends to zero. A numerical error for the asymptotic area denoted by  $A^*$ , as defined in the color frame below. An error compensation technique could be used for this purpose and could be integrated in the optimization problem.

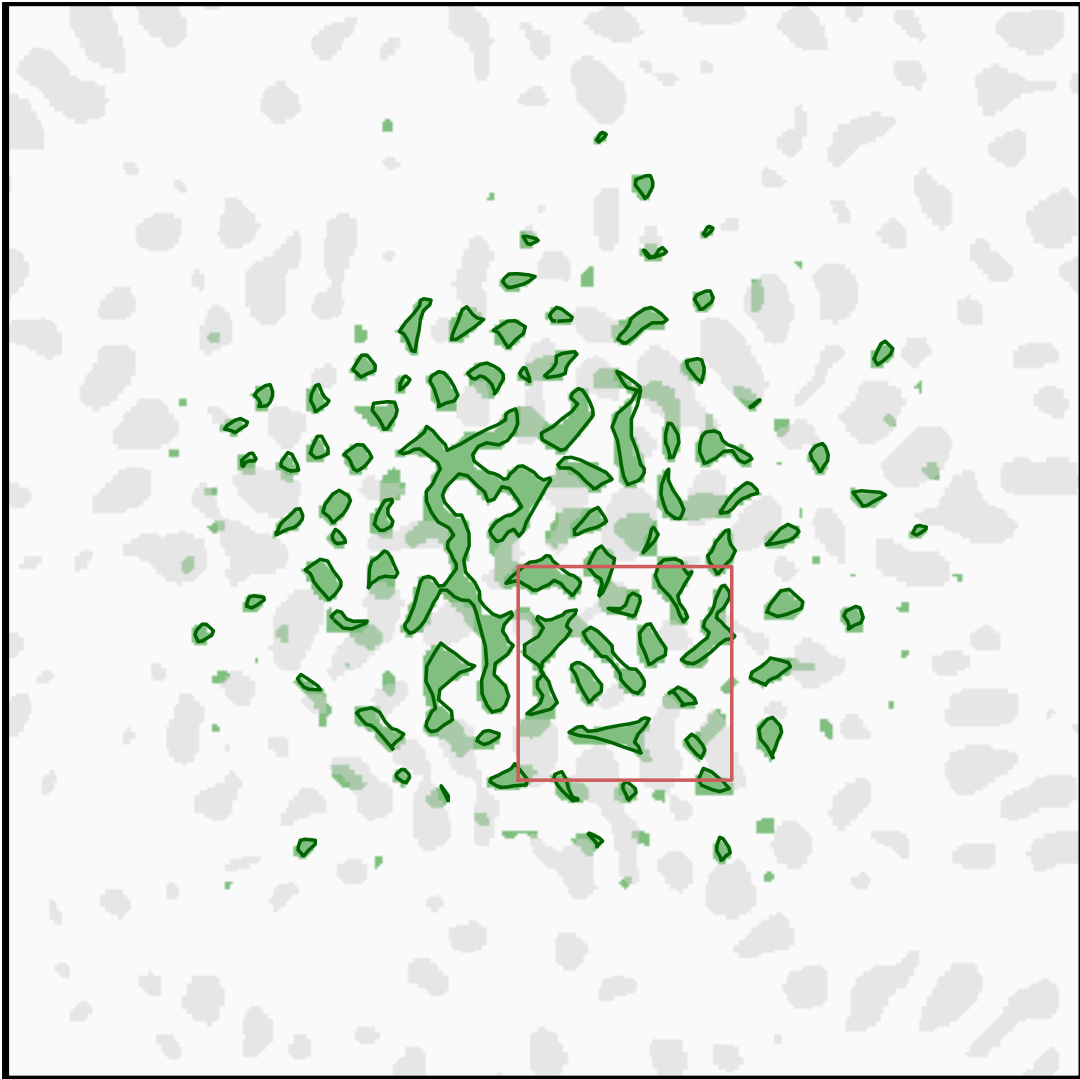


Figure 4.32: Representation of the mesh for a conductive layer.

#### Model: Accurate contact area computation

The area of pixelized contact spot depends on the grid size. This area tends to  $A^*$  when the pixel size  $\delta x$  tends to 0 and this convergence limit could be estimated as

$$A^* \approx A_d - \frac{\pi - 1 + \log 2}{24} S_d \Delta x, \quad (4.12)$$

where  $A_d$ ,  $S_d$  represent the area and the perimeter for pixelized contact spot, respectively. Here the coefficient  $(\pi - 1 + \log 2)/24 \approx 0.118$  indicates by how much the contact area measured on the border pixels is overestimated compared to its limit value [Yastrebov et al., 2017a].

An illustration of the mesh construction for an oxidized contact surface is presented Fig. 4.32 and 4.33. In Fig.4.32, the oxide patches are depicted in grey, while the green patches represents the real contact surfaces. The contours of conductive spots are plotted in green color. A zooming view is proposed in Fig.4.33 for the red frame, showcasing the mesh created with an edge mesh parameter of  $h/L = 1/512$ .

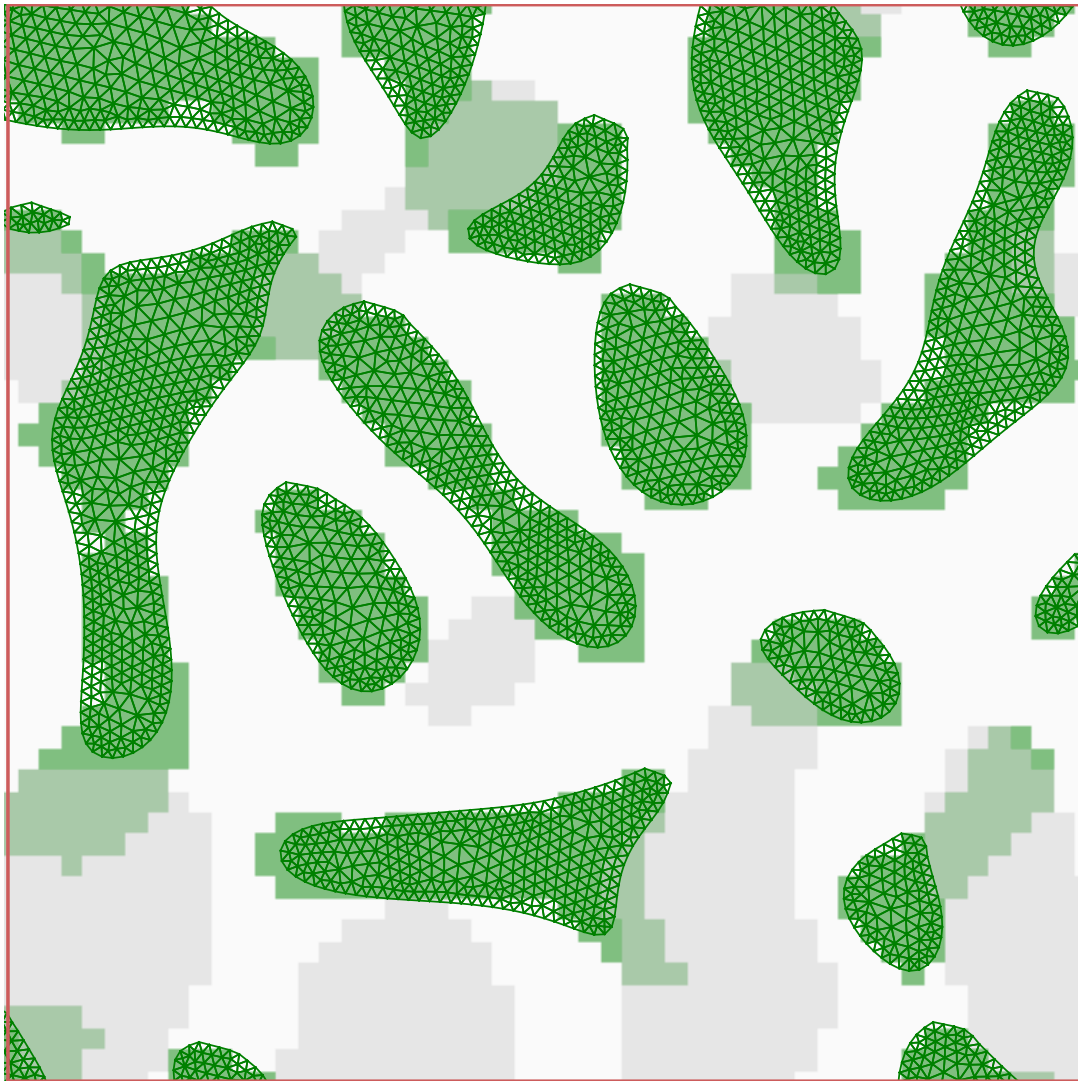


Figure 4.33: Representation of the mesh for a conductive layer.

### BEM results for contact area and oxide layers

The results of normal flux computed with BEM for the conductive area Fig. 4.32 are displayed in Fig.4.34. Other results are presented Fig.4.35, taking into account  $k_l^o = 32$  and an oxide fraction of  $\phi^o = 20\%$ . For both of these result maps, the flux is normalized to  $j_{o,Holm} = 2\Phi_o/(\pi K\alpha_{Holm})$ , which represents the flux at the center of a circular spot with a radius of  $\alpha_{Holm}$ .

The result maps demonstrate a rise in the flux in spots that are distanced from the others. The nominal size of these spots is less significant, although a singularity persists at the edges of the spots. In the map shown in Fig.4.35, the construction of the Bezier curves overlaps with the oxide spots. Conversely, in the scenario depicted in Fig.4.34, the Bezier curves appear to more accurately accommodate the oxide patches, owing to their larger nominal size. These two maps, initially based on identical contact area definitions, end up being significantly altered by the presence of oxide in conjunction with the construction of Bezier surfaces, particularly in the case of larger spots.

The analysis of these outcomes, along with the extrapolation of total fluxes, leads to a comparison with the results obtained from FFT-BEM. The flux values determined by BEM exhibit a variance of about 3% when compared to the outcomes from FFT-BEM computations. This variance is relatively minor, in regard of the differences in the

morphology of the conduction spots. BEM calculations are generally expected to yield higher flux estimation compared to the one obtained from FFT-BEM, especially after the extrapolation.

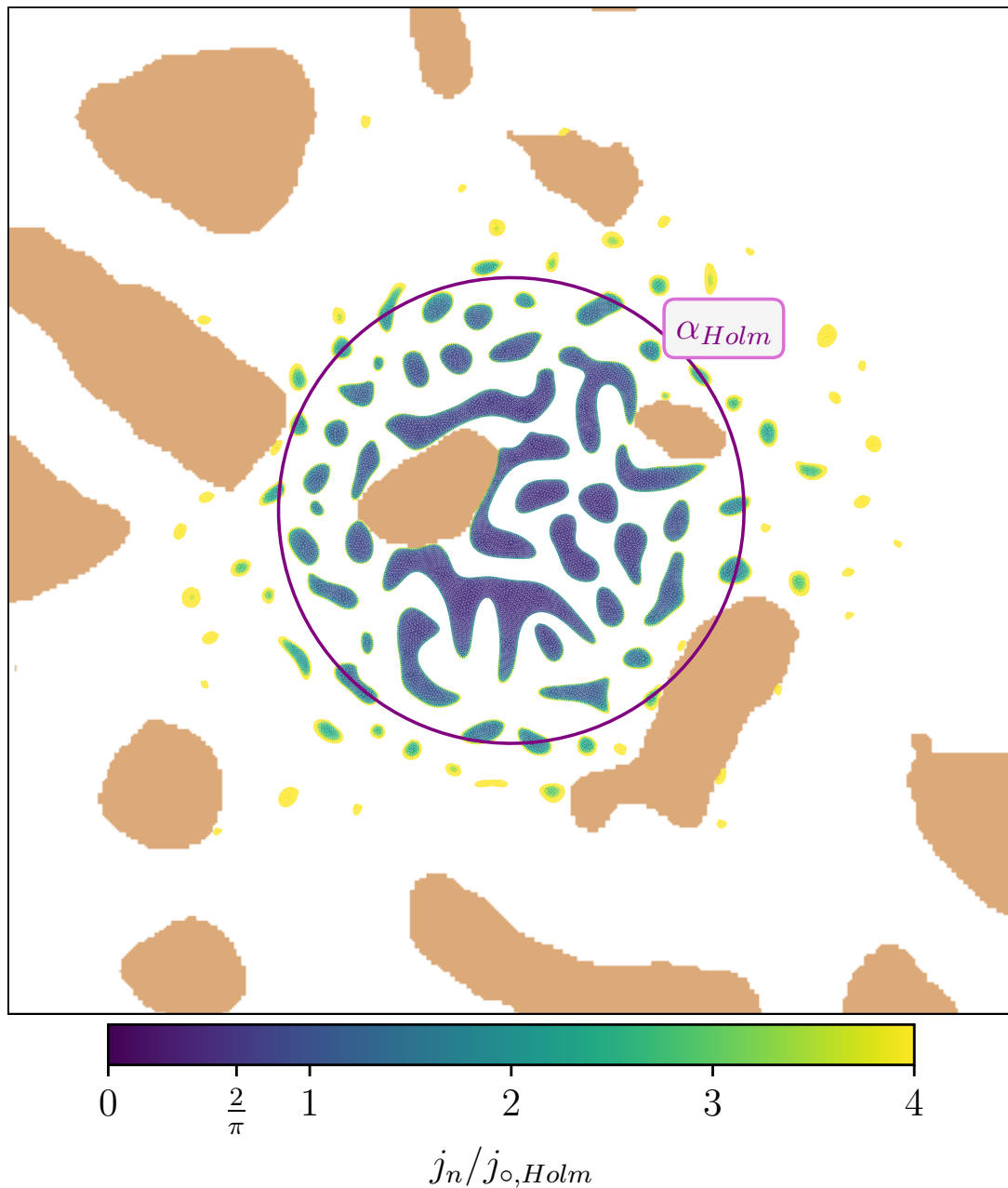


Figure 4.34: Representation of results for normal flux computed with BEM

## 4.5 Conclusion

This section focused on the contact problem originally conceived for the constriction resistance at real contact interfaces. This study has enabled us to slightly revisit the pioneering works by Holm and Greenwood and combine FFT-BEM with Fast-BEM to handle a weakly coupled problem between contact and conductivity between rough surfaces.

### 4.5.1 Multi-spots area

Aiming to describe more realistic contact area, the study has initially proposed to replace the circular spots with flower-shapes contact spots. Greenwood's model can be adapted by making modifications in the term of self-resistance. Compared to BEM results, it still demonstrates its accuracy. But the discrepancy from BEM-results depends more on the number of spots enclosed in the multi-spots area than on the density of contact. Further work is needed to testify of its precision for non-uniform density of contact, as described by [Greenwood and Tripp, 1967].

### 4.5.2 Results on real contact area with oxidation

In order to extend this study to realistic cases, we have finally studied conduction between rough surfaces in contact. The contact surfaces are defined as parabolic surfaces with additional roughness. The resulting contact areas are composed of close or already coalesced contact spots. This study allowed us to compare our Fast-BEM results with those obtained by FFT-BEM. Results obtained for a circular spot serve to attest the precision of two methods to obtain conductivity: incremental stiffness calculation or flat-punch indentation.

First, this study gave insights into conduction between rough surfaces in case of oxide-free surfaces, leading to a new definition of the Holm's radius. The study of conduction and the comparison with the results of oxidized surfaces have emphasized the influence of the ratio of oxidation. The conductivity discrepancy between oxide-free and oxidized surface is not proportional to the surface fraction of oxides, and also depends on the size of the contact surface. Comparing these FFT-BEM results with those obtained by Fast-BEM, by changing the geometric definition of the contact areas, confirms an error of few percent only. This error would be due to the change in morphology of the spots and more accurate accounting of complex spot boundaries captured by Fast-BEM. The unravel possibility of using Fast-BEM unravel new calculation and verification for the FFT-BEM results. Some study are still needed so far to better capture the difference between geometries, and to identify the causes of the flux difference.

### 4.5.3 Conclusion

This section has allowed us to study the effects of interaction between spots within real contact areas and the influence of oxidation on conduction. Conduction remains dominated by the size of the real contact area, which can be defined by the continuous Holm's radius. Conduction does not decrease proportionally to the oxidized surface, as the latter ultimately has little impact on the Holm's radius of the cluster.

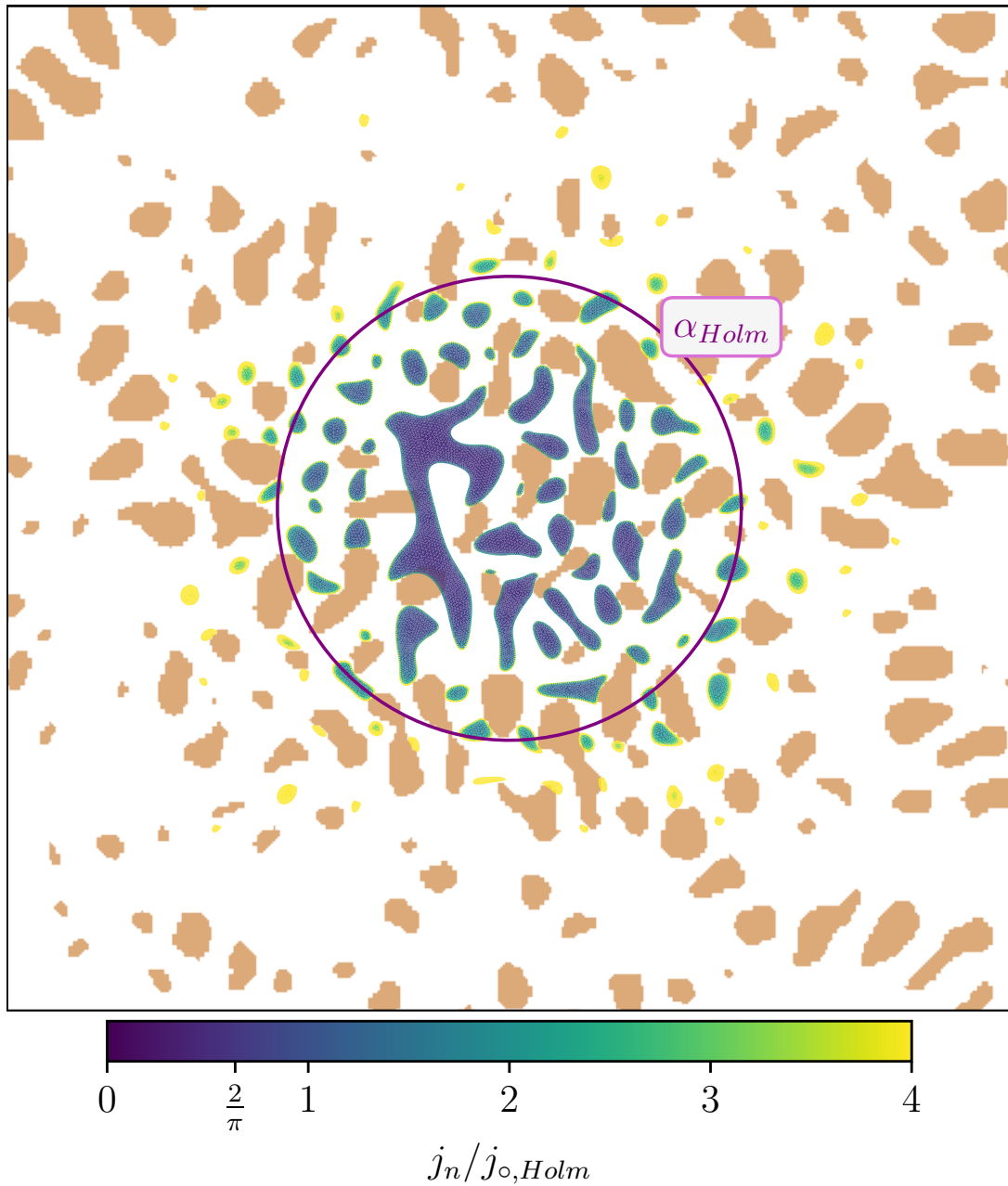


Figure 4.35: Representation of results for normal flux computed with BEM





## Conclusions

Since the earliest studies of contact between rough surfaces, the origin of constriction resistance emphasizes the reduction of the conductive section at the contact interface between solids. This phenomenon occurs in both electrical and thermal contacts, originating at the microscopic scale, where the real contact area is observed. This thesis has delved into the problem of constriction resistance by the resolution of the conduction problem in its static regime at the contact interface.

This problem in its simplest formulation is linear, defined at the contact interface, for a semi-infinite geometry. Thus the Boundary Element Method (BEM) is particularly well-suited, and this thesis is also the opportunity to adapt the BEM implementation for this study. To the best of our knowledge, this method has not been used for solving constriction resistance problems since Nakamura's studies [Nakamura, 1993] in the 1990s. To address prohibitively high memory and construction complexity, a Fast-BEM version has been developed. This implementation uses low-rank approximations (ACA+ & SVD), enabled by the use of  $\mathcal{H}$ -matrices. It has allowed us to handle larger problems for complex conduction surfaces requiring strong mesh refinement. This method can also be used for solving boundary elastic problems.

Returning to the initial problem of constriction resistance, and taking into account the observation of real contact surface, this method has been first applied to the problem of spots with complex geometry. Despite the apparent simplicity of the conduction problem, analytical solutions exist only for elliptical and annular contact spots. More complex spots have been studied here, highlighting the influence of certain geometric parameters. Flower-, star-, and gear-shaped contact spots have highlighted the role of the number of "petals". It has been noted that for a large number of petals, equivalent to a spot with a very "rough" contour, the flux value remains asymptotically lower than that of a circumscribed circular spot. More complex spots have been analyzed with a complete set of roughness parameters including fractal dimension and three first spectral moments. Their analysis was supported by the normalization of the transmitted flux and by analogy with multi-petal spot, a geometrically complete phenomenological model was suggested. This part is concluded by a study of truly fractal spots – the Koch snowflake.

Finally, we analyzed the most realistic situation when conductivity is determined by the complex area formed by the contact of rough surfaces. Starting from a simple multi-spot model, where every spot has a flower-shaped geometry, we adapted the Greenwood constriction model to capture such geometries and validated the results with full BEM simulations. Further a realistic morphology of contact interfaces was reproduced by

FFT-BEM solver (Tamaas) which was also used to solve conductivity problems based on the normal stiffness analogy. We introduced a continuous version of the Holm's radius which gives a simplified model for the constriction resistance of contact clusters. In practice, however, the conduction surface is often reduced due to oxidation. A model for generating oxide films was constructed based on a self-affine random field. We then solved the conductivity problem combining the true contact area with oxide-free conductive zones using both FFT-BEM and Fast-BEM. It could be demonstrated that the drop in conductivity is not proportional, and only weakly depends on the oxide surface fraction. The Holm's radius is merely affected by the considered range of oxide fractions.

Our Fast-BEM Python implementation is shared as open-source code [Beguin and Yastrebov, 2023].

## Perspectives

This work can now serve as a foundation for studying other forms of contact spots and real contact areas. Particularly, shapes with *non-injective contours* in terms of the angular coordinate can be studied, such as those occurring in real contact areas between rough surfaces.

Regarding the study of conduction within real contact areas, the analysis of our results could be improved in terms of accuracy and geometrical and physical interpretation. The *average size of oxide spots*, the *density of oxide patch* and the *Holm radius* could be further explored to carry out such an analysis. This analysis would allow us to move beyond the current framework which is constrained by parameterization of a self-affine random field used to construct oxide spots. A more physical model, potentially making a link between oxidation and roughness, would be more physically justifiable. The non-proportional relation between the oxide surface fraction and the drop of conductivity could be explained through the annulus contact spot. The average size of oxide patch overlaying the real contact area, might be responsible for the cubic conductivity drop  $\sim (1 - (\phi_o/A)^3)$  where  $A_c$  is the contact area.

Finally, our Fast-BEM model still suffers from a lack of speed, in spite of several enhancements in its implementation. Our work has already made it operational and accessible as Python open-source code. But this implementation could be considered as a prototype for implementation with a more powerful and optimized programming language such as C++, which could truly reveal the potential of the Fast-BEM and the  $\mathcal{H}$ -matrices. The implementation of additional tools, such as optimization of the matrix-vector product for iterative *solvers* could be also considered for the future. This code could eventually serve as a development base for modeling other physical phenomena, such as thermal diffusion or elasticity, and could be used in coupling with other methods like FFT-BEM and Finite Element Method. In addition to the performance, a methodology could be further adjusted. The particularity of the conductivity problem with singularity at contact boundary suggests that the choice of Legendre polynomial for interpolation functions at elements near the edge is not optimal and that this singularity could be properly captured with specific interpolation. Furthermore, a sub- or super-parametric elements could be considered with the objective to enhance the model accuracy.

---

 Transient solution for thermal diffusion problem between two bars
 

---

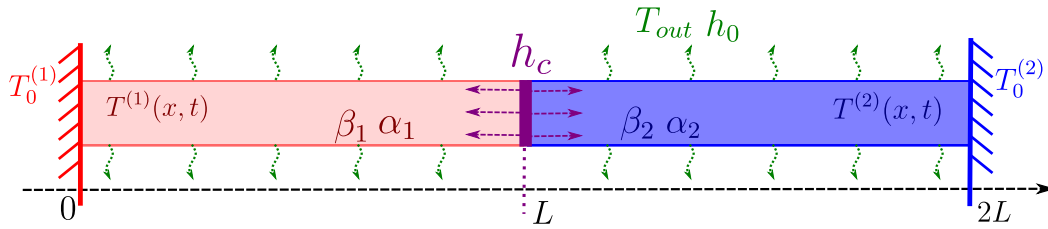


Figure A.1: Illustration of a thermal contact problem between two bars.

We consider a problem of two bars of length  $L$  and thermal diffusivity  $\beta_i$ ,  $i = 1, 2$  which are brought in contact<sup>1</sup> as shown in Fig. A.1. The thermal field is given by  $T^{(1)}(x, t)$  for  $x \in [0, L]$  (left bar), and  $T^{(2)}(x, t)$  for  $x \in [L, 2L]$  (right bar) and for  $t \in [0, t_0]$ . Bars are assumed cylindrical of radius  $R$ , we assume that  $R/L \ll 1$ , that is why the thermal field is assumed to depend on the  $x$  coordinate only disregarding the temperature variation along the radius. This problem illustrates heat exchange between two bars brought in contact and surrounded by a fluid at a temperature of  $T_{out}$  ensuring a convective heat exchange with parameters  $\alpha_i$ ,  $i = 1, 2$ ,  $\alpha_i = 2h_0/(R\rho_i C_{p_i})$ , where  $h_0$  is the convective factor,  $\rho_i$  and  $C_{p_i}$  are the density and heat capacity of the  $i$ -th bar. The temperature in two bars follows the diffusion equation supplemented with a convective heat exchange with the environment:

$$\beta_1 \frac{\partial^2 T^{(1)}}{\partial x^2} - \alpha_1 (T^{(1)} - T_{out}) = \frac{\partial T^{(1)}}{\partial t}, \quad \text{for } x \in [0, L] \quad (\text{A.1a})$$

$$\beta_2 \frac{\partial^2 T^{(2)}}{\partial x^2} - \alpha_2 (T^{(2)} - T_{out}) = \frac{\partial T^{(2)}}{\partial t}, \quad \text{for } x \in [L, 2L] \quad (\text{A.1b})$$

Assuming the following form for temperature  $T = T(x, t)$  and defining the axial flux as  $j_n^{(i)} = -k_i \partial T^{(i)} / \partial x$ , where  $k_i$  is the conductivity of bar  $i$ , the following boundary conditions are defined for each bar. For bar 1:

$$T^{(1)}(0, t) = T_0^{(1)} \quad (\text{A.2})$$

$$j_n^{(1)}(L^-, t) = h_c (T^{(1)}(L^-, t) - T^{(2)}(L^+, t)) \quad (\text{A.3})$$

---

<sup>1</sup>To the best of our knowledge the solution for this elementary problem is not available in the literature.

For bar 2:

$$T^{(2)}(2L, t) = T_0^{(2)} \quad (\text{A.4})$$

$$j_n^{(2)}(L^+, t) = -h_c \left( T^{(1)}(L^-, t) - T^{(2)}(L^+, t) \right), \quad (\text{A.5})$$

where  $h_c$  is the heat exchange parameter ( $\text{W} / (\text{m}^2 \cdot \text{K})$ ) in the contact interface controlling the heat for two surfaces at different temperatures brought in contact. This conductivity ensures the heat exchange between bars and renders their solutions coupled. The initial conditions are

$$T^{(1)} = T_0^{(1)}, \quad T^{(2)} = T_0^{(2)}. \quad (\text{A.6})$$

The combination of Dirichlet and coupled Neumann boundary conditions require to solve this problem using *Laplace transform*. Laplace transform denoted by  $\mathcal{L}$  is given by the following integral transformation:

$$\Theta^{(i)}(x, p) = \mathcal{L}\{T^{(i)}\}(p) = \int_0^{+\infty} e^{-pt} T^{(i)}(x, t) dt$$

Laplace transform allows to streamline the time derivative resulting in the following equations:

$$\beta_1 \frac{\partial^2 \Theta^{(1)}(x, p)}{\partial x^2} - (\alpha_1 + p) \Theta^{(1)}(x, p) = \alpha_1 \frac{T_{out}}{p} \quad (\text{A.7a})$$

$$\beta_2 \frac{\partial^2 \Theta^{(2)}(x, p)}{\partial x^2} - (\alpha_2 + p) \Theta^{(2)}(xp) = \alpha_2 \frac{T_{out}}{p} \quad (\text{A.7b})$$

These quasi ordinary differential equations could be solved as a sum of two hyperbolic functions for  $x$  combined with a particular solution:

$$\Theta_i = A_i(p) \sinh(q_i x) + B_i(p) \cosh(q_i x) + \Theta_{i,0}(p), \quad q_i = \sqrt{\frac{p + \alpha_i}{\beta_i}}, \quad \Theta_{i,0}(p) = T_{out} \left( \frac{1}{p} - \frac{1}{p + \alpha_i} \right) \quad (\text{A.8})$$

Where  $A_i$  and  $B_i$  are two function of Laplace variable  $p$ , and defined in agreement with the boundary conditions,  $q_i$  is a wavelength function of  $p$ , and  $\Theta_{i,0}$  is a function prescribed by the convective exchange with the ambient media.

The Laplace transform can be inverted using a semi-numerical method proposed by Stehfest [Stehfest, 1970], as developed below:

$$T^{(i)}(t) = \frac{\log(2)}{t} \sum_{j=1}^N V_j \Theta \left( \frac{j \log(2)}{t} \right) \quad (\text{A.9})$$

$$V_j = (-1)^{\frac{N}{2}+1} \sum_{k=\lfloor \frac{j+1}{2} \rfloor}^{\min(j, \frac{N}{2})} \frac{k^{\frac{N}{2}} (2k)!}{\left( \frac{N}{2} - k \right)! k! (k-1)! (j-k)! (2k-1)!} \quad (\text{A.10})$$

The precision of this method increases with the number of taken modes  $N$ , but in practice  $N = 10$  shows already quite accurate results for this problem.

Illustration of such a solution is presented in Fig A.2, represented in dashed lines, and compared with FEM results shown in dots. These results are displayed for three distinct time step, namely at 10 minutes, 1 hour, and 10 hours. The conductivity coefficients are set as  $h_0 = 10 \text{ W.m}^{-2}.\text{K}^{-1}$  and  $h_c = 100 \text{ W.m}^{-2}.\text{K}^{-1}$ . The radii of the cylindrical bar is set to  $R = 0.01 \text{ m}$ , with the one on the right-hand side made of copper, and the other on the left-hand side, assumed to be iron. Below we summarize physical parameters used for these materials.

Material coefficients for iron :

$$\begin{aligned} k_1 &= 50.2 \text{ W.m}^{-2}.\text{K}^{-1} \\ C_{p,1} &= 500 \text{ J.kg}^{-1}.\text{K}^{-1} \\ \rho_1 &= 7500 \text{ kg.m}^{-3} \end{aligned}$$

Material coefficients for copper :

$$\begin{aligned} k_2 &= 390 \text{ W.m}^{-2}.\text{K}^{-1} \\ C_{p,2} &= 385 \text{ J.kg}^{-1}.\text{K}^{-1} \\ \rho_2 &= 8920 \text{ kg.m}^{-3} \end{aligned}$$

The following temperatures were used:

$$T_0^{(1)} = 293.15\text{K}, \quad T_0^{(2)} = 313.15\text{K}, \quad T_{out} = 283.15\text{K}$$

As could be seen, the stationary solution, towards which the system converged after  $\approx 10$  hours, expectedly, preserves a temperature discontinuity at the contact interface and the interface fluxes on the left and right are compatible throughout the time. The comparison with the finite element solution demonstrates a very good agreement even for only  $N = 10$  modes in Stehfest inversion technique.

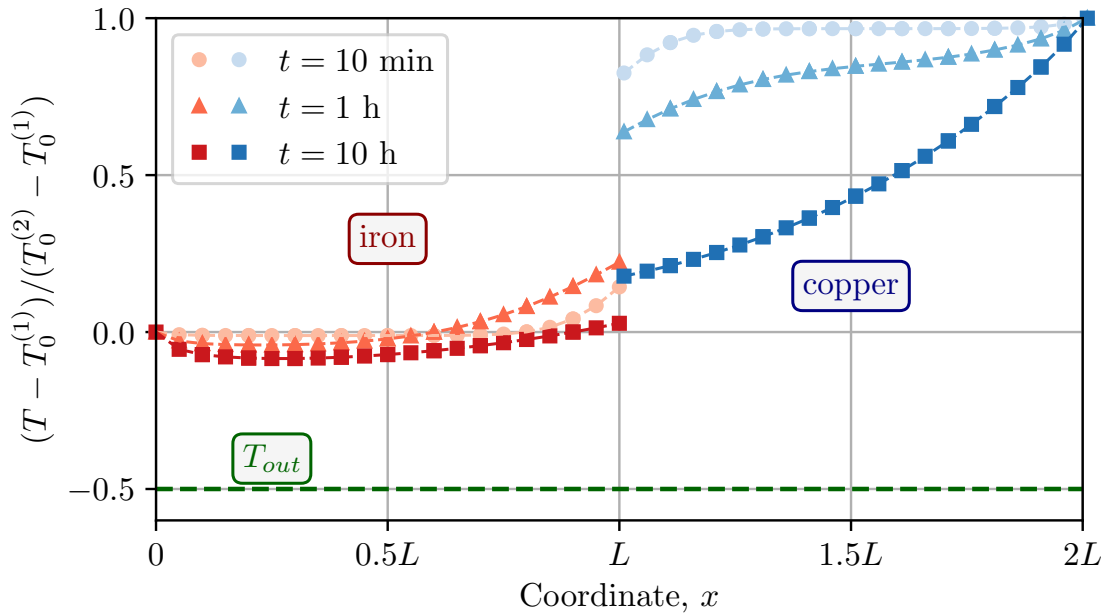


Figure A.2: Spatial distribution of a transient temperature evolution in two bars made of iron (left) and copper (right) which are brought in contact in a convective media at low temperature  $T_{out}$ . Markers show the finite element solution and dashed line represent our analytical solution.



---

Additional results for Fast-BEM

---

### B.1 Integration of H-function on the boundary

Let assume  $S$  a regular surface, oriented by its normal vector,  $\mathbf{n}$ , and with  $\mathbf{x}$  the observation point.

$$\int_S H(\mathbf{x}, \mathbf{y}) dS_y = \int_S \frac{-r_{,n}}{4\pi r^2} dS_y$$

It seems more convenient to compute this integral using spherical coordinates. The set of unit vector is defined as  $(\mathbf{e}_r, \mathbf{e}_\phi, \mathbf{e}_\theta)$ . The set of coordinate is defined by  $(r, \phi, \theta)$ , with  $r > 0$ ,  $\phi \in [0, \pi]$  and  $\theta \in [0, 2\pi]$ . The radius coordinate is defined  $\mathbf{r} = r(\phi, \theta)\mathbf{e}_r$ .

The domain of integration is split in half, describing the space of  $S$  embedded in the body surrounding the observation point. The angle  $\phi$  is rather defined lying within the interval  $[0, \pi/2]$ .

The classical parametrization enables to define  $r_{,n}$ , as,

$$r_{,n} = \mathbf{e}_r \cdot \mathbf{n}$$

The normal vector multiplied by the element of integration can be expressed in terms of the vectors  $\mathbf{r}_{,\phi}$ ,  $\mathbf{r}_{,\theta}$ ,

$$\mathbf{n} dS_y = (\mathbf{r}_{,\phi} \wedge \mathbf{r}_{,\theta}) d\phi d\theta$$

Those derivatives can be explicitly expressed as follows,

$$\mathbf{r}_{,\phi} = r_{,\phi} \mathbf{e}_r + r \mathbf{e}_\phi, \quad \mathbf{r}_{,\theta} = r_{,\theta} \mathbf{e}_r + r \sin(\phi) \mathbf{e}_\theta$$

Ultimately,

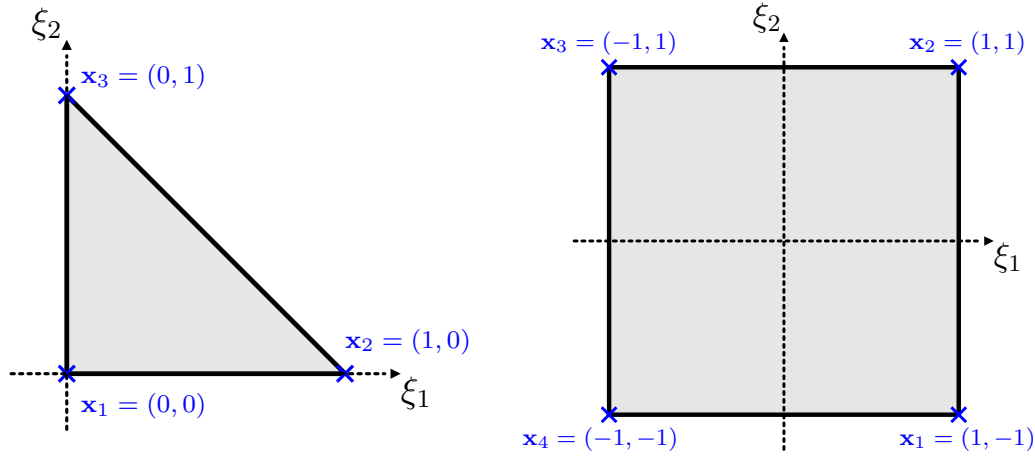
$$r_{,n} dS_y = r^2 \sin(\phi) d\phi d\theta$$

Substituting this term in the integral of  $H$ , it results in,

$$\int_S H(\mathbf{x}, \mathbf{y}) dS_y = \int_0^{2\pi} \int_0^{\pi/2} \frac{\sin(\phi)}{4\pi} d\phi d\theta$$

$$\boxed{\int_S H(\mathbf{x}, \mathbf{y}) dS_y = \frac{1}{2}} \text{ for } \mathbf{x} \in S \tag{B.1}$$





## B.2 Element of reference and shape function

**Triangular element** Shape functions  $(\xi_1, \xi_2) \in [0, 1]^2$ ,

$$N_1(\xi_1, \xi_2) = 1 - \xi_1 - \xi_2$$

$$N_2(\xi_1, \xi_2) = \xi_1$$

$$N_3(\xi_1, \xi_2) = \xi_2$$

Value at mesh node

$$N_i(\mathbf{x}_j) = \delta_{i,j}$$

**Square element** Shape functions  $(\xi_1, \xi_2) \in [-1, 1]^2$ ,

$$N_1(\xi_1, \xi_2) = \left(\frac{1 + \xi_1}{2}\right)\left(\frac{1 + \xi_2}{2}\right)$$

$$N_2(\xi_1, \xi_2) = \left(\frac{1 - \xi_1}{2}\right)\left(\frac{1 + \xi_2}{2}\right)$$

$$N_3(\xi_1, \xi_2) = \left(\frac{1 - \xi_1}{2}\right)\left(\frac{1 - \xi_2}{2}\right)$$

$$N_4(\xi_1, \xi_2) = \left(\frac{1 + \xi_1}{2}\right)\left(\frac{1 - \xi_2}{2}\right)$$

The value of the shaped function at the nodes is defined as,

$$N_i(\mathbf{x}_j) = \delta_{i,j}$$

With  $\delta$  is the Kronecker's symbol.

## B.3 Quasi-singular integration

### B.3.1 Cubic transformation

**Coefficient of the cubic polynomial** The cubic transformation aims to provide a change of variable following a third order polynomial,

$$\eta_i = a\xi_i^3 + b\xi_i^2 + c\xi_i + d, \quad i \in \{1, 2\}$$

Where the coefficients  $a, b, c, d$  are adjusted in function of the distance  $d$  from the observation points  $\bar{\xi}$ , to the element of reference  $\Delta_e$ . Its first derivative is defined using the following law,

$$J_\eta(\bar{\xi}) = \left. \frac{d\eta}{d\xi} \right|_{\bar{\xi}} = \begin{cases} 0.85 + 0.24\ln(d), & 0.05 \leq d \leq 1.3 \\ 0.893 + 0.0832\ln(d), & 1.3 \leq d \leq 3.618 \\ 1, & 3.618 \leq d \end{cases}$$

The slope rate is lowered by the law , to gather more the points of integration, around  $\bar{\xi}$ , when  $d$  decreases as well. It varies from 0.1 to 1. When the  $J = 1$ , there would not be any transformation applied, readily  $\eta = \xi$ , given by Eq. (2.61). This ensures to gather the integration point around  $\bar{\xi}$ . This condition is defined in terms of convexity change at the point  $\bar{\xi}$ , as,

$$\left. \frac{d^2\eta}{d\xi^2} \right|_{\bar{\xi}} = 0$$

Let consider  $\bar{\eta} = \bar{\xi}$ , making  $\eta(\bar{\xi}) = \bar{\xi}$ . Using the root formula of cubic polynom, we get the definition of  $\bar{\xi}$ .

$$\begin{aligned} \bar{\xi} &= \left[ -q + \sqrt{q^2 + p^3} \right]^{1/3} + \left[ -q - \sqrt{q^2 + p^3} \right]^{1/3} + \frac{\bar{\eta}}{1 + 2J_\eta} \\ q &= \frac{1}{2(1 + J_\eta)} \left[ \frac{1}{2(2 + J_\eta)} \left( \bar{\eta}(3 - 2J) - \frac{2\bar{\eta}^3}{1 + 2J_\eta} \right) - \bar{\eta} \right] \\ p &= \frac{1}{3(1 + J_\eta)^2} \left[ 4J_\eta(1 - J_\eta) + 3(1 - \bar{\eta}^2) \right] \end{aligned}$$

### Change of integration

$$\begin{aligned} \int_{\partial\mathcal{A}_e} G(\mathbf{x}, \mathbf{y}) dS_y &= \int_{\Delta_e} G(\mathbf{x}, \mathbf{y}(\xi)) J_\xi(\xi) dS_\xi \\ \Leftrightarrow &= \int_{\Delta_e} G(\mathbf{x}, \mathbf{y}(\xi(\eta))) J_\xi(\xi(\eta)) |\eta'_1(\xi_1)\eta'_2(\xi_2)| dS_\eta \end{aligned}$$

The integrating weights are modified using the chain formula of the change of variable. The modified weights, denoted by  $\tilde{\omega}$ , derive from the latter integral, as,

$$\tilde{\omega}_{i,j} = \omega_i \omega_j J_\xi(\xi_i, \xi_j) |\eta'_1(\xi_i)\eta'_2(\xi_j)|$$

Jacobian function,  $J_\eta$ , is set as the product of the separate function derivatives. The weights  $\tilde{\omega}_{i,j}$  refer to the following weighted sum, which used for the integral computation as

$$\int_{\mathcal{A}_e} G(\mathbf{x}, \mathbf{y}) dS_y \approx \sum_i \sum_j \tilde{\omega}_{i,j} G(\mathbf{x}, \mathbf{y}(\xi(\eta_i, \eta_j)))$$

### Cylindric transformation

**Parametrization of radial parameter** As presented in Fig. B.1, for each triangle  $\Delta_{e,n}$ , the angle varies in the interval  $[\theta_n^m, \theta_n^M]$ . The maximal radius is expressed in function of  $h_n$ ,  $\alpha_n$ , as follows,

$$\rho_{\max,n} = \frac{h_n}{\cos(\theta - \alpha_n)}, \quad \theta \in [\theta_n^m, \theta_n^M]$$

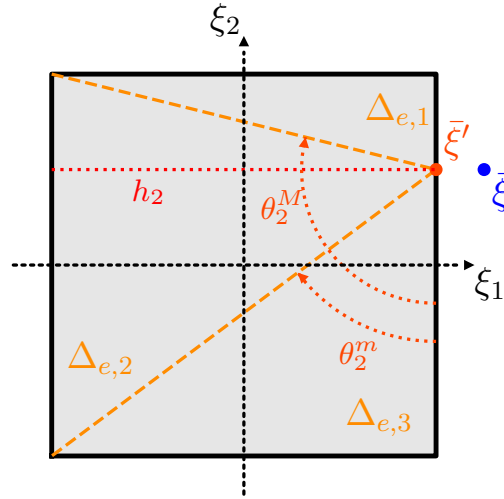


Figure B.1: Schematic of the division of the square element on integration using the triangular separation.

Using, the Gauss point with coordinate  $(x_i, x_j)$ , we can define new couple of coordinate using the cylindric parametrization  $(\theta_i, \rho_{i,j})$ , as expressed below,

$$\theta_i = \frac{(\theta_n^M - \theta_n^m)}{2}(x_i + 1) + \theta_n^m$$

$$\rho_{i,j} = \frac{\rho_{\max,n}(\theta_i)}{2}(x_j + 1)$$

The couple coordinate  $(\theta_i, \rho_{i,j})$  are adjusted to be defined in the intervals  $[\theta_n^m, \theta_n^M]$ , and  $[0, \rho_{\max,i}]$  respectively. The new cylindrical coordinates are centered around the centroid point  $(0, 0)$ . To get the final coordinate of the integration points, this needs to offset the coordinate by the position of  $\bar{\xi}'$ , which finally defines these coordinates, as,

$$\xi_1 = \rho \cos(\theta) + \bar{\xi}'_1$$

$$\xi_2 = \rho \sin(\theta) + \bar{\xi}'_2$$

**Change of integration** The quasi-singular integral can be computed as the sum of integral on the separate triangles, denoted by  $I_n$ .

$$I = \sum_n I_n$$

Each integral is expressed as followed, using the radial transformation and the agreed intervals for  $\theta$  and  $\rho$

$$I_n = \int_{\theta_n^m}^{\theta_n^M} \int_0^{\rho_{\max,n}(\theta)} G(\mathbf{x}, \mathbf{y}(\xi(\rho, \theta))) J_\xi(\xi) \rho d\rho d\theta$$

Similarly to the cubic transformation, the weights is adapted to take advantage of the Gaussian quadrature integration, based on the Gauss point coordinates  $(x_i, x_j)$ ,

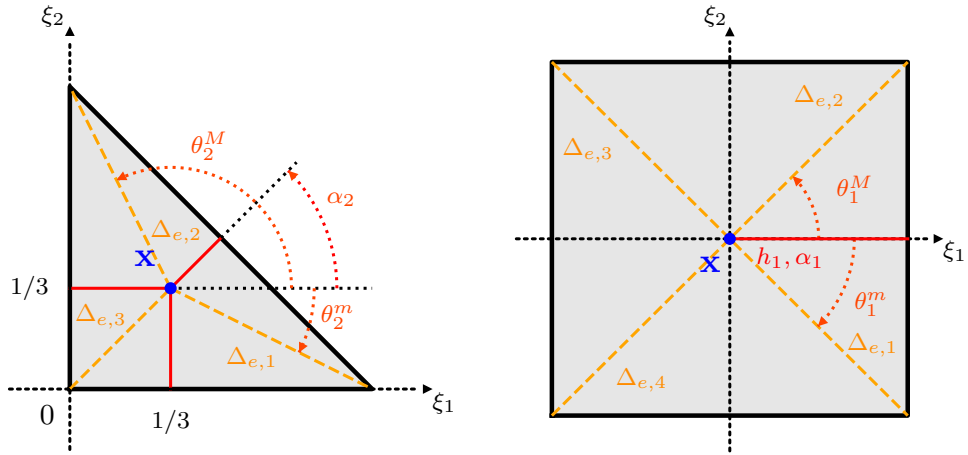
$$\tilde{\omega}_{i,j} = \omega_i \omega_j \frac{(\theta_n^M - \theta_n^m) \rho_{\max,n}(\theta_i)}{4} \rho_{i,j}$$

Finally, it leads to the following expression for  $I_n$ , on the triangular element part  $\Delta_{e,n}$ ,

$$I_n = \sum_j \sum_i \tilde{\omega}_{i,j} J_\xi(\xi(\rho_{i,j}, \theta_i)) G(\mathbf{x}, \mathbf{y}(\xi(\rho_{i,j}, \theta_j)))$$

## B.4 Singular integration

### B.4.1 Parametrization



For the square of reference

$$h_1 = 1, \quad h_2 = 1, \quad h_3 = 1, \quad h_4 = 1$$

$$\theta_1^m = -\frac{\pi}{4}, \quad \theta_2^m = \frac{\pi}{4}, \quad \theta_3^m = \frac{3\pi}{4}, \quad \theta_4^m = \frac{5\pi}{4}$$

$$\theta_1^M = \frac{\pi}{4}, \quad \theta_2^M = \frac{3\pi}{4}, \quad \theta_3^M = \frac{5\pi}{4}, \quad \theta_4^M = \frac{7\pi}{4}$$

$$\alpha_1 = 0, \quad \alpha_2 = \frac{\pi}{2}, \quad \alpha_3 = \pi, \quad \alpha_4 = \frac{3\pi}{2}$$

For the triangle of reference

$$h_1 = \frac{1}{3}, \quad h_2 = \frac{\sqrt{2}}{6}, \quad h_3 = \frac{1}{3}$$

$$\theta_1^m = -\frac{3\pi}{4}, \quad \theta_2^m = -\tan^{-1}(1/2), \quad \theta_3^m = \frac{\pi}{4} + \tan^{-1}(3)$$

$$\theta_1^M = -\tan^{-1}(1/2), \quad \theta_2^M = \frac{\pi}{4} + \tan^{-1}(3), \quad \theta_3^M = \frac{5\pi}{4}$$

$$\alpha_1 = -\frac{\pi}{2}, \quad \alpha_2 = \frac{\pi}{4}, \quad \alpha_3 = \pi$$

## B.4.2 Triangular singular integration

**Analytical expression** The exact expression of the integral of the Green function of the triangle of reference can be given. The expression is divided in three integrals corresponding to the triangles,  $\Delta_{e,1}$ ,  $\Delta_{e,2}$ , and  $\Delta_{e,3}$ .

$$I_0 = I_{\Delta_{e,1}} + I_{\Delta_{e,2}} + I_{\Delta_{e,3}} = 2I_{\Delta_{e,1}} + I_{\Delta_{e,2}}$$

The integrals are expressed using the cylindric transformation, and the expression of the contour in term of the  $1/\cos(\theta - \alpha_i)$ .

$$I_0 = 2 \int_{\theta_1^m}^{\theta_1^M} \frac{d\theta}{4\pi \cos(\theta - \alpha_1)} + 22 \int_{\theta_2^m}^{\alpha_2} \frac{d\theta}{4\pi \cos(\theta - \alpha_2)}$$

Using *Wolfram* software, one may find a numerical expression for these integrals,

$$I_{\Delta_{e,1}} = \frac{1}{12\pi} \log \left\{ \cot\left(\frac{\pi}{8}\right) \cot\left(\frac{1}{2} \tan^{-1}\left(\frac{1}{2}\right)\right) \right\} \approx 0.06167$$

$$I_{\Delta_{e,2}} = \frac{1}{6\sqrt{2}\pi} \sinh^{-1}(3) \approx 0.06822$$

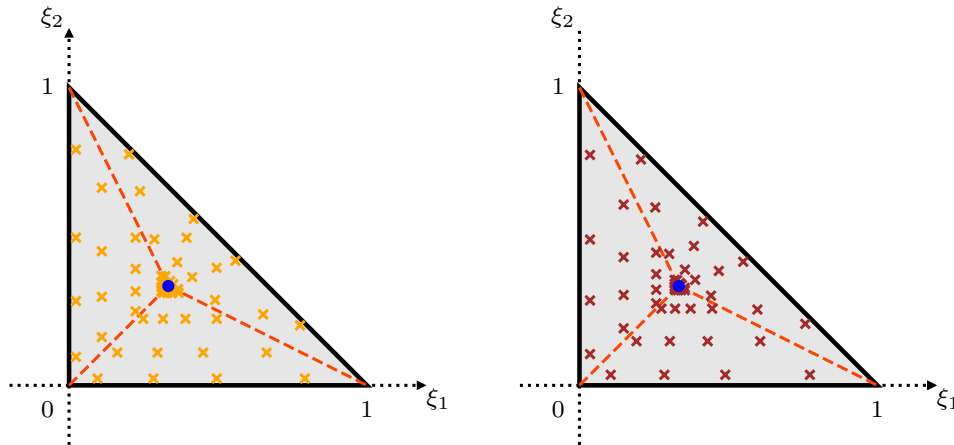


Figure B.2: Distribution of the integrating point for the cubic (left), cylindric (center), and PART (right) transformations in the case of the singular integral computation

**Cylindric and PART result** The figure B.2 shows distribution of point of integration, cylindric one on the left-hand side, and PART distribution on the right-hand side.

The numerical value given by those distribution might be compared with the value of  $I_0$ . Those results are presented in Fig. B.3. The error decreases as the number of integration point increases. The two distributions are giving the same results, similarly to the quadrangular reference element Fig. 2.20.

## B.5 Approximations

### B.5.1 ACA-full Algorithm

An algorithm for full ACA is presented in box 10.

### B.5.2 ACA+

An algorithm for ACA+ is presented in box 11.

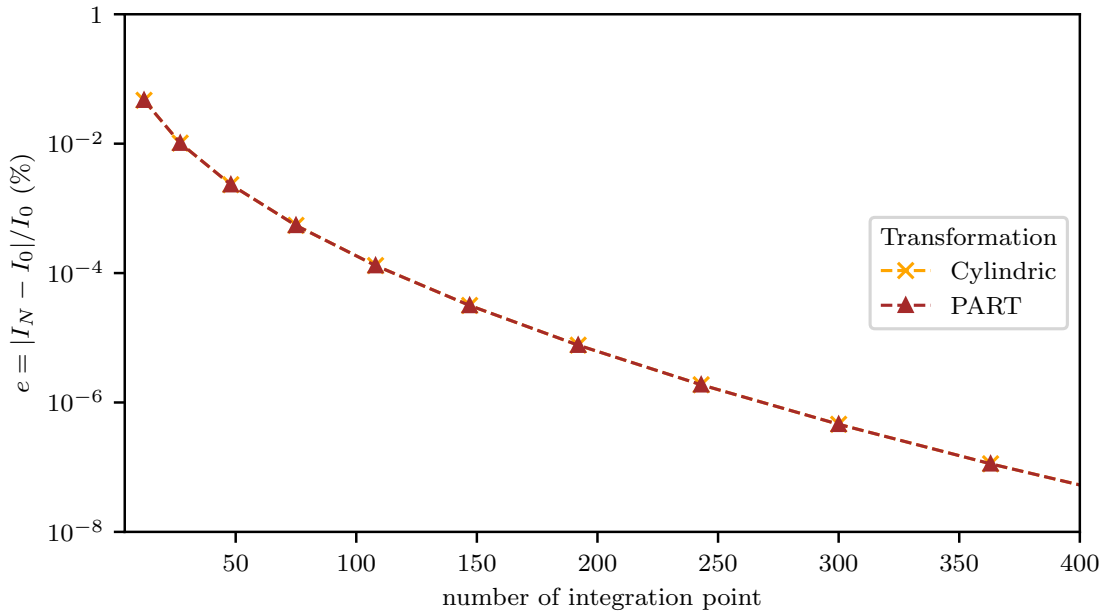


Figure B.3: Error on the numerical integration in function of the number of integration point

## B.6 Cluster tree of a non-compact shape

This section further study the cluster definition through various methods, on non-compact contours for mesh geometry model on a Marsupilami's contour. The mesh, created in a manner akin to the contact spot, is refined at the edges and coarser in the middle, featuring a non-uniform refinement. This mesh takes the form of and composed of 22,733 elements.

Three different clustering methods at level  $l = 5$  are depicted in the subsequent figures: *median separation* in Fig. B.4, *geometric separation* in Fig. B.5, and *K-means clustering* in Fig. B.5. These images highlight the variations in cluster geometry. The size of the clusters is very different from one to another across different clustering methods, even with geometric separation. However, an equal number of elements is always maintained across clusters using median separation.

Geometrical characteristics are summarized in Fig. B.7 and Fig. B.8, for different depths  $l_m$ . From Fig. B.7, it is observable that the ratio of elements in the clusters is preserved with median separation. Surprisingly, geometric separation, intended to produce clusters with equal box sizes, does not maintain this feature for this mesh geometry, and performs worse than the others. Fig. B.5 provides some insight, considering the size of  $C_{14}^{(5)}$  in comparison with others, for example. This will lead to an unbalanced  $\mathcal{H}$ -tree.

---

**Algorithm 10:** Implementation of ACA-full
 

---

**Data:** Global,  $\epsilon$

- 1 **Function** Aca-full ( $M$ ):
- 2    $\delta \leftarrow \max (M_k)$
- 3    $i_s, j_s \leftarrow \text{Argmax} (M_k)$
- 4    $A.\text{append} (M_k[:, i_s])$
- 5    $B.\text{append} (M_k[j_s, :]/\delta)$
- 6    $R_k = M - A.B$
- 7   **while**  $\|M - R_k\|_F > \epsilon \|M\|_F$  **do**
- 8      $\delta \leftarrow \max (R_k)$
- 9     **if**  $\delta == 0$  **then**
- 10      **return**  $A, B$
- 11      $i_s, j_s \leftarrow \text{Argmax} (R_k)$
- 12      $A.\text{append} (R_k[:, i_s])$
- 13      $B.\text{append} (R_k[j_s, :]/\delta)$
- 14      $R_k = R_k - A.B$
- 15   **return**  $A, B$

---

**Algorithm 11:** Implementation of ACA+

---

**Data:** Global,  $\epsilon$

**1 Function** Aca-plus ( $\sigma, \tau, \mathbf{f}\text{-bem}$ ):

2  $M_c, R \leftarrow \text{Init-M}(m, n), \text{Init-M}(m, n)$

3  $j_{ref} = 0$

4  $M_c[:, j_{ref}] = \mathbf{f}\text{-bem}(\sigma, \tau[j_{ref}])$

5  $i_{ref} = \text{Argmin}(M_c[:, j_{ref}])$

6  $M_c[i_{ref}, :] = \mathbf{f}\text{-bem}(\sigma[i_{ref}], \tau)$

7  $c_{ref}, l_{ref} \leftarrow M_c[:, j_{ref}], M_c[i_{ref}, :]$

8  $P_c, P_l \leftarrow [], []$

9  $A_k, B_k \leftarrow [], []$

10  $Continue \leftarrow True$

11 **while**  $Continue$  **do**

12  $\delta_l, i_l \leftarrow \text{Argmax}(l_{ref}, P_l)$

13  $\delta_c, j_c \leftarrow \text{Argmax}(c_{ref}, P_c)$

14 **if**  $\delta_c > \delta_l$  **then**

15  $M_c[i_l, :] = \mathbf{f}\text{-bem}(\sigma[i_l], \tau)$

16  $b_k = M_c[i_l, :] - R_k[i_s, :]$

17  $\delta, j_s = \text{Argmax}(|b_k|)$

18  $M_c[:, j_s] = \mathbf{f}\text{-bem}(\sigma, \tau[j_s])$

19  $a_k = (M_c[:, j_s] - R_k[:, j_s]) / \delta$

20 **else**

21  $M_c[:, j_c] = \mathbf{f}\text{-bem}(\sigma, \tau[j_c])$

22  $a_k = M_c[:, j_c] - R_k[:, j_c]$

23  $\delta, i_s = \text{Argmax}(|a_k|)$

24  $M_c[i_s, :] = \mathbf{f}\text{-bem}(\sigma[i_s], \tau)$

25  $b_k = (M_c[i_s, :] - R_k[i_s, :]) / \delta$

26  $P_l.append(i_l)$

27  $P_c.append(j_c)$

28  $r'_k = |a_k| \cdot |b_k|$

29  $r_k = r_k + \text{Residual}(A_k, a_k, B_k, b_k) + r'_k$

30 **if**  $r_k < \epsilon r'_k$  **then**

31  $Continue = True$

32  $A_k.append(a_k)$

33  $B_k.append(b_k)$

34 **if**  $i_s = i_{ref}$  **then**

35  $i_{ref} = \text{Next-Arg}(P_l)$

36  $M_c[:, j_{ref}] \leftarrow \mathbf{f}\text{-bem}(\sigma, \tau[j_{ref}])$

37  $l_{ref} \leftarrow M_c[:, j_{ref}]$

38 **if**  $j_s = j_{ref}$  **then**

39  $j_{ref} = \text{Next-Arg}(P_c)$

40  $M_c[i_{ref}, :] \leftarrow \mathbf{f}\text{-bem}(\sigma[i_{ref}], \tau)$

41  $c_{ref} \leftarrow M_c[i_{ref}, :]$

42 **return**  $A, B$

---



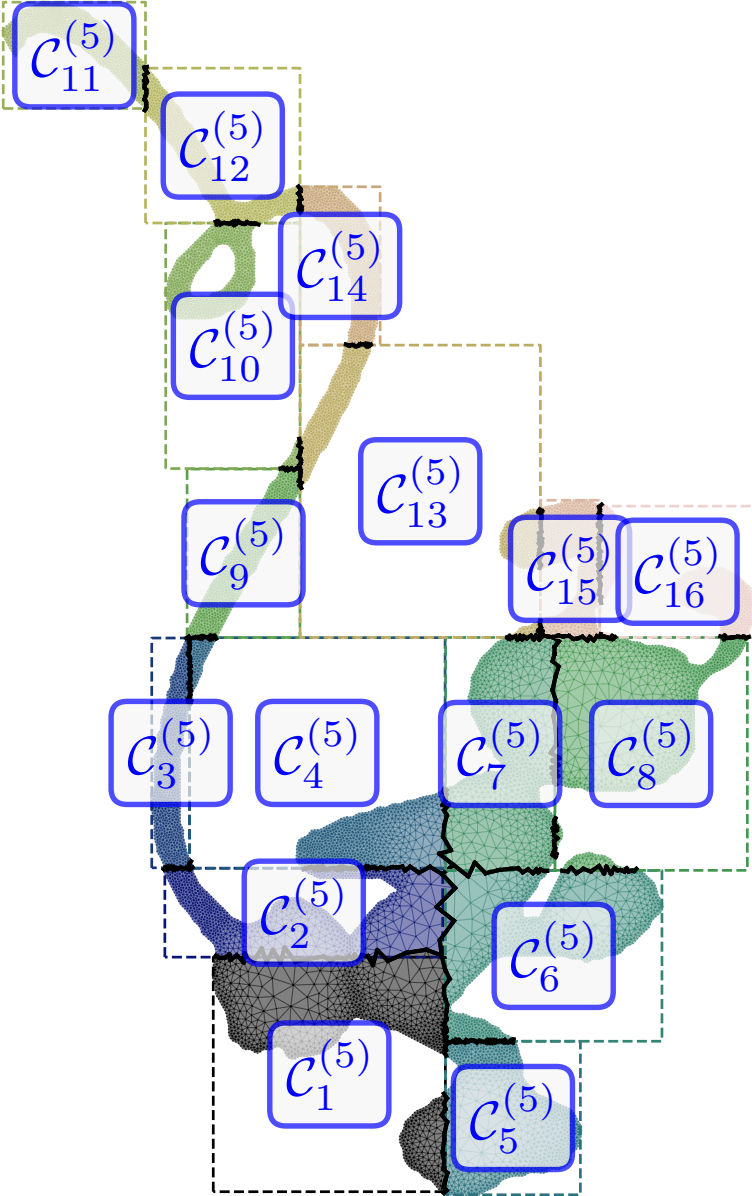


Figure B.4: Clustering using median separation for a mesh composed of  $N_e = 22733$  at the level  $l = 5$

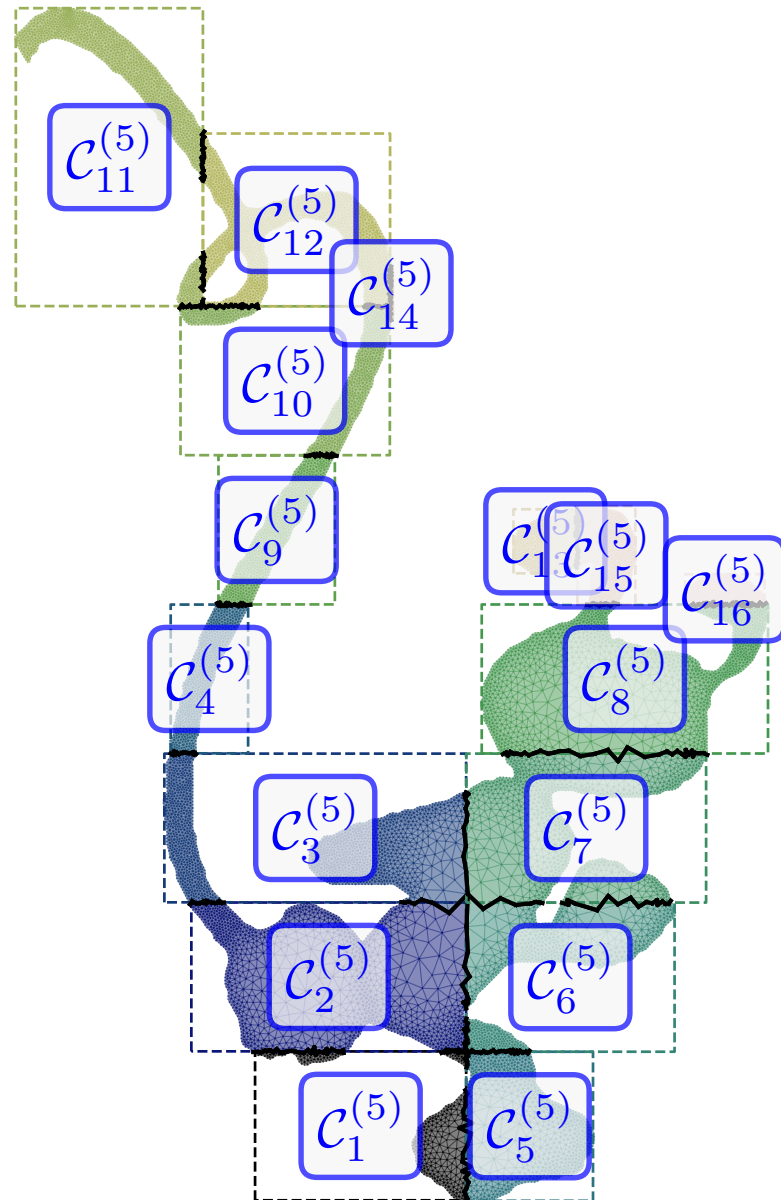


Figure B.5: Clustering using geometric separation for a mesh composed of  $N_e = 22733$ , at the level  $l = 5$

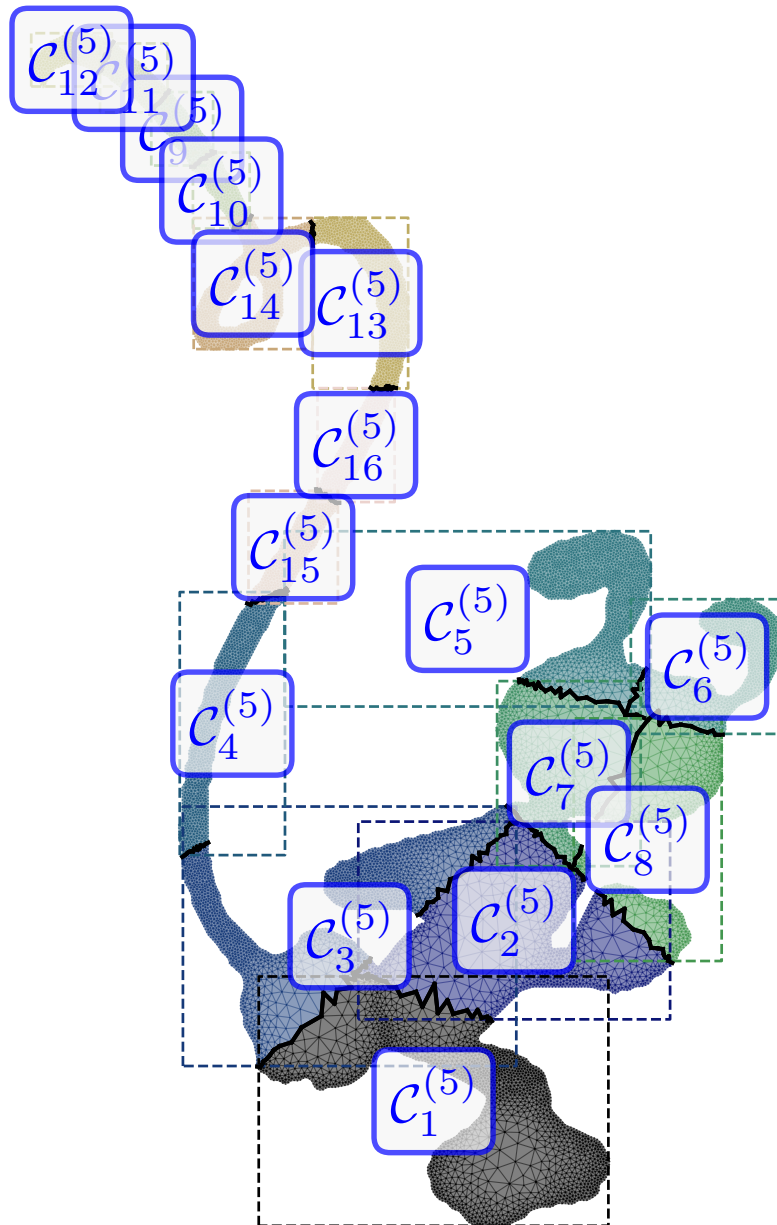


Figure B.6: Clustering using K-means method for a mesh composed of  $N_e = 22733$ , at the level  $l = 5$

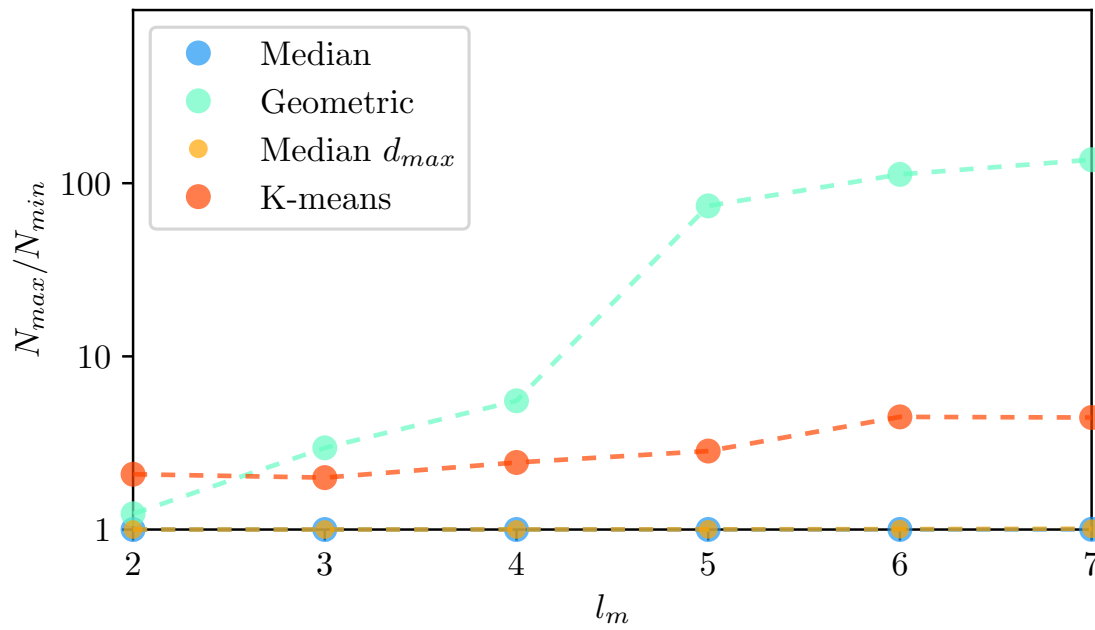


Figure B.7: Difference in number of elements between the clusters in function of the depth  $l_m$  for the marsupilami meshing

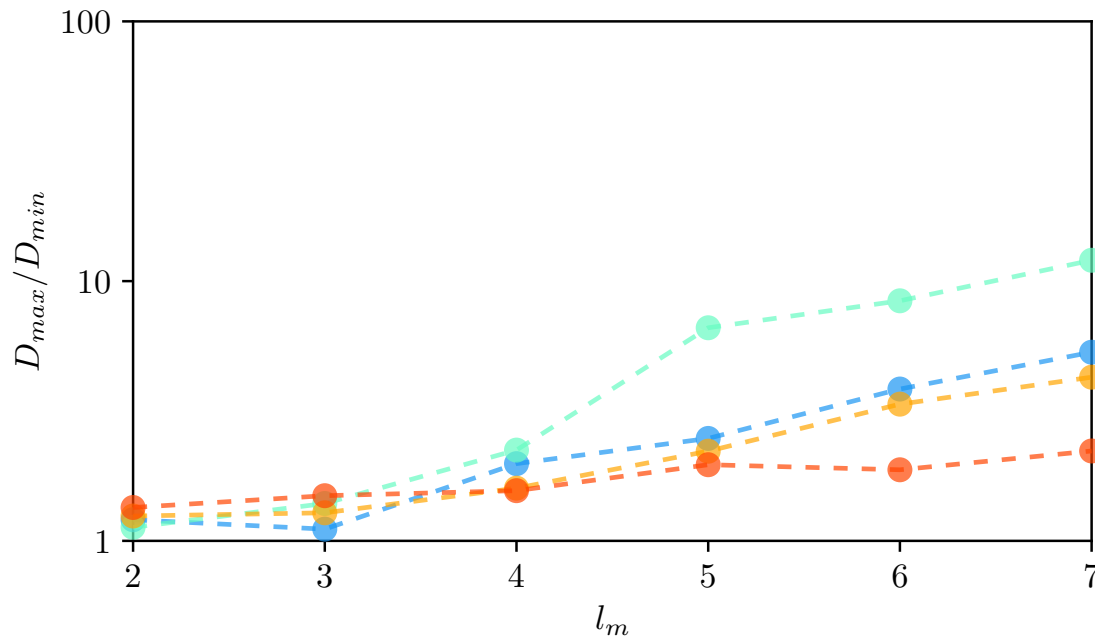


Figure B.8: Difference in geometric size between the clusters in function of the depth  $l_m$  for the marsupilami meshing



---

Conductivity of spots with complex shape

---

### C.1 Geometrical characteristics of self-affine spots

In Fig. C.1, the analytical form for the standard deviation of self-affine spots  $\sigma_s$  Eq. (3.21) is compared with the one evaluated over 1 000 generated spots for each combination of generative parameters:  $\xi = 0.05$ ,  $k_l \in \{2, 4, 8, 16, 32, 64, 126\}$ ,  $\zeta \in \{4, 8, 16, 32\}$  and  $H \in [0.2, 0.8]$ . These results are quite sensitive to  $k_l$ , but the maximal relative error is 0.05% for  $k_l = 32$  and  $\zeta = 8$ .

The second  $m_2$  and the forth  $m_4$  moments have been computed for the same set of generative parameters over the same 1 000 spots. These moments could be computed in three different ways. First, the discretized contour geometry could be used to evaluate these moments  $m_p^D$  using Eq. (3.22). The discretization consists of splitting the contour in  $N = \max\{10\,000, 100k_s\}$  straight segments with  $d\theta = 2\pi/N$  and evaluation gradient and laplacian as

$$\nabla r_i = \frac{2(r_{i+1} - r_i)}{(r_{i+1} + r_i)d\theta'}, \quad \Delta r_i = \frac{4(r_{i+1} - 2r_i + r_{i-1}))}{(r_{i+1} + 2r_i + r_{i-1})^2 d\theta'^2} \quad (\text{C.1})$$

where  $r_i = r(id\theta)$ ,  $i = 1, N$ . This method was used throughout the paper. Second, the moments could be approximated by discrete sums of all mode contributions as in Eq. (3.23):

$$m_p^S = \frac{(r_0\xi)^2}{2} \sum_{k_l}^{k_s} k_l^p \left(\frac{k}{k_l}\right)^{-(1+2H)}. \quad (\text{C.2})$$

This method is however valid only for relatively small values of  $\xi$  because it ignores the exponential transformation (3.18). Third, for sufficiently large values of  $k_l$ , these discrete sums could be turned into integrals with wavenumber  $k$  becoming continuum variables of integration:

$$m_p^C = \frac{1}{2} \int_{k_l}^{\zeta k_l} (r(k))^2 k^p dk, \quad (\text{C.3})$$

where  $r(k) = \xi r_0(k/k_l)^{-H-0.5}$ . Analytical formulas derive from the development for the moments  $m_0^C$ ,  $m_2^C$  and  $m_4^C$ , as follows:

$$m_0^C = -\frac{(r_0\xi)^2 k_l}{4H} (\zeta^{-2H} - 1), \quad m_2^C = -\frac{(r_0\xi)^2 k_l^3}{2(2-2H)} (\zeta^{2-2H} - 1), \quad m_4^C = -\frac{(r_0\xi)^2 k_l^5}{2(4-2H)} (\zeta^{4-2H} - 1). \quad (\text{C.4})$$

For high values of  $k_l$  the discrete spectrum is closer to a continuous one, and thus the spectral moments can be deduced from Eq. (3.23) as detailed by Nayak [Nayak, 1971].

These analytical values are compared with the numerically evaluated ones in Fig. C.2 and Fig. C.3. The maximum deviation is of only 0.7 % for the  $m_2$  for parameters  $k_l = 2, \zeta = 4$  and  $H = 0.2$ . However, for  $m_4$  an average discrepancy of 10 % is observed and could raise to as much as 27 % in certain instances. Nevertheless, in all results presented in the paper only actual values of the moments and of their combinations were used.

The Nayak's parameter is determined using the moments  $m_0, m_2$  and  $m_4, \alpha = m_0 m_4 / m_2^2$ . The three models mentioned above could be used to compute the Nayak parameter as  $\alpha^D, \alpha^S$  and  $\alpha^C$ , respectively. The average values computed over a set of 1000 spots are compared in Fig C.4. This analysis demonstrates that a continuum model could be successfully used in practical applications. In the limit of high magnification  $\zeta$ , the second moment and the Nayak parameter scale as  $m_2^C \sim \zeta^{2-2H}$  and  $\alpha^C \sim \zeta^{2H}$ .

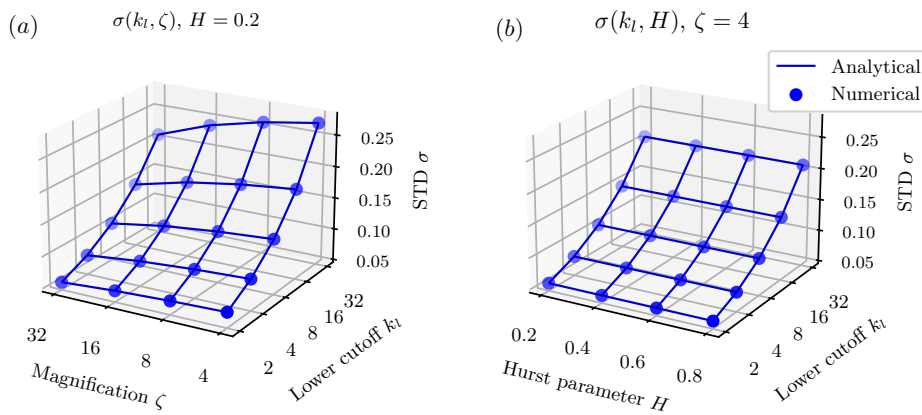


Figure C.1: Results of standard deviation by spectral and sample analysis, with  $k_l = \{2, 4, 8, 16, 32, 64, 128\}$  in both figures: (a)  $\zeta = \{4, 8, 16, 32\}$  and  $H = 0.2$ ; (b)  $H = \{0.2, 0.4, 0.6, 0.8\}$  and  $\zeta = 4$ .

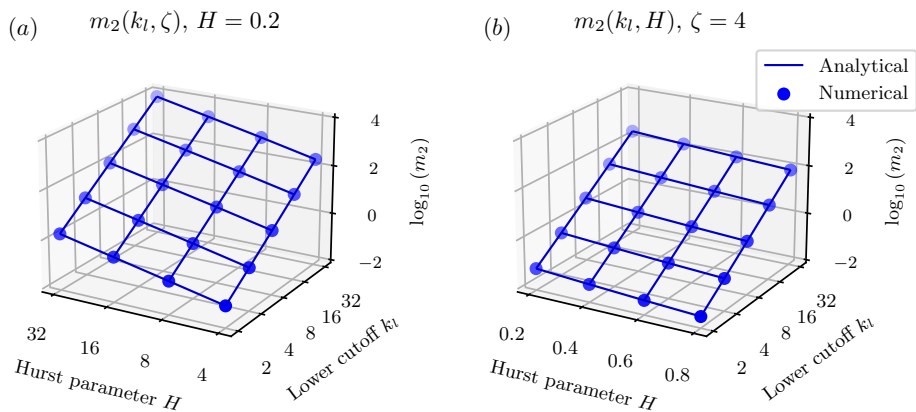


Figure C.2: Results of mean square gradient by spectral and sample analysis, with  $k_l = \{2, 4, 8, 16, 32, 64, 128\}$  in both figures: (a)  $\zeta = \{4, 8, 16, 32\}$  and  $H = 0.2$ ; (b)  $H = \{0.2, 0.4, 0.6, 0.8\}$  and  $\zeta = 4$ .

## C.2 Physical consistency of the phenomenological model

The phenomenological model of flux Eqs. (3.32),(3.33) exhibits an increasing behavior with respect of  $m_2$ , but decreases with  $\alpha$ . Nevertheless, from general physical considerations,

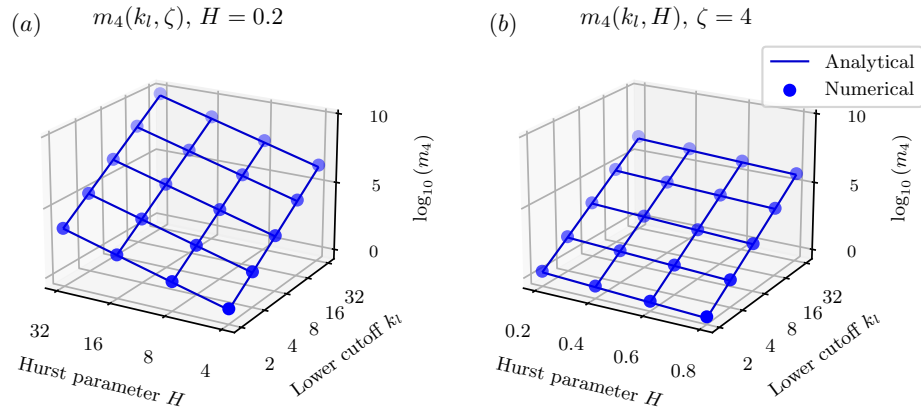


Figure C.3: Results of mean square Laplacian, with  $k_l = \{2, 4, 8, 16, 32, 64, 128\}$  in both figures: (a)  $\zeta = \{4, 8, 16, 32\}$  and  $H = 0.2$ ; (b)  $H = \{0.2, 0.4, 0.6, 0.8\}$  and  $\zeta = 4$ .

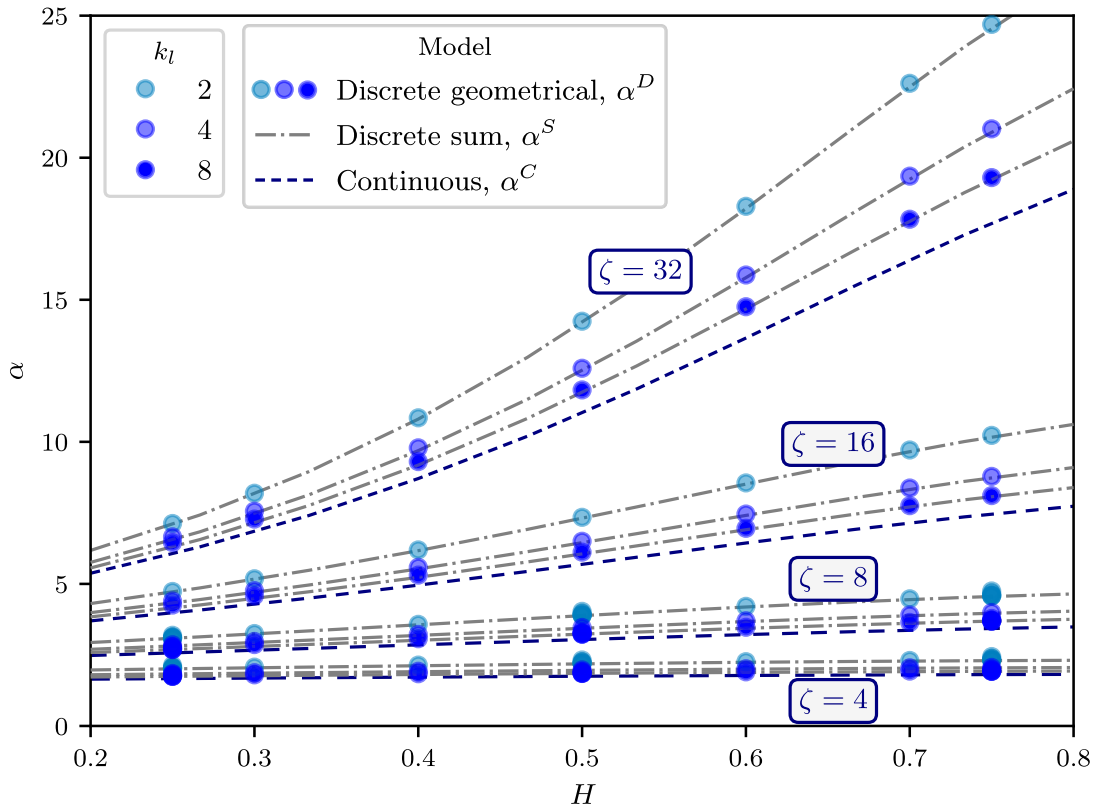


Figure C.4: Comparison of different models which could be used to evaluate spectral moments and the Nayak parameter: (1) discretized geometrical evaluation, (2) discrete sum for the generative function, (3) continuous version of this discrete sum.

we conjecture that the flux should be a monotonically non-decreasing function of the magnification  $\zeta$ . So, we require that the derivative of flux  $Q$  with respect to magnification  $\zeta$  remains non-negative:

$$\frac{\partial Q}{\partial \zeta} = \frac{\partial Q}{\partial m_2} \frac{\partial m_2}{\partial \zeta} + \frac{\partial Q}{\partial \alpha} \frac{\partial \alpha}{\partial \zeta} \geq 0 \tag{C.5}$$



The terms  $\partial Q/\partial m_2$  and  $\partial Q/\partial \alpha$  could be readily derived from Eq. (3.33).

$$\frac{\partial Q}{\partial m_2} = a \frac{b}{2\sqrt{m_2}(b\sqrt{m_2} + 1)^2} (1 + cH) \left( 1 + \frac{d}{e\alpha^f + 1} \right) \quad (\text{C.6a})$$

$$\frac{\partial Q}{\partial \alpha} = a \left\{ 1 - \frac{b}{b\sqrt{m_2} + 1} \right\} (1 + cH) \frac{-def\alpha^{f-1}}{(e\alpha^f + 1)^2} \quad (\text{C.6b})$$

The derivatives of  $m_2$  and  $\alpha$  with respect to  $\zeta$  could be found from Eq.(C.4), resulting in the following asymptotic forms:

$$\frac{\partial Q}{\partial m_2} \frac{\partial m_2}{\partial \zeta} \sim \frac{1}{\sqrt{m_2}(\sqrt{m_2} + 1)^2} \frac{\partial m_2}{\partial \zeta} \sim \zeta^{-2+H} \quad (\text{C.7a})$$

$$\frac{\partial Q}{\partial \alpha} \frac{\partial \alpha}{\partial \zeta} \sim \frac{\alpha^{f-1}}{(\alpha^f + 1)^2} \frac{\partial \alpha}{\partial \zeta} \sim \zeta^{-2fH-1} \quad (\text{C.7b})$$

These expressions enable us to define a constraint criteria to ensure the derivative of the flux law with respect to  $\zeta$  remains non-negative for all  $\zeta$ . The exponent of  $\zeta$  in Eq. (C.7a) must be lower than the one in Eq.(C.7b), resulting in the following inequality that the exponent  $f$  should satisfy:

$$f \geq \frac{1-H}{2H} \quad (\text{C.8})$$

The problem with this constraint is that it results in too high values of  $f$  for small  $H$  and, ultimately, it diverges for  $H \rightarrow 0$ . In the current study we set the minimal value of the Hurst exponent to  $H = 0.25$  thus resulting in  $f \geq 1.5$ . The results for derivatives using the continuous expressions for  $m_2$  and  $\alpha$  are presented Fig. C.5 for  $H = 0.25$ ,  $k_l = 8$ , and  $\xi = 0.05$ , and the fitting parameters shown in Table 3.6. The two derivative terms are distinguished: one positive, as given by Eq. (C.6a), and the other negative, as given by Eq. (C.6b). The full derivative remains positive, however, thus keeping the required assumptions true, even for value of  $\zeta$  significantly far from the initial set of parameter. The absolute values for these derivatives are also depicted in inset in log-log scale, showing similar power-laws of the two competing derivatives (in dots) for high values of  $\zeta$ .

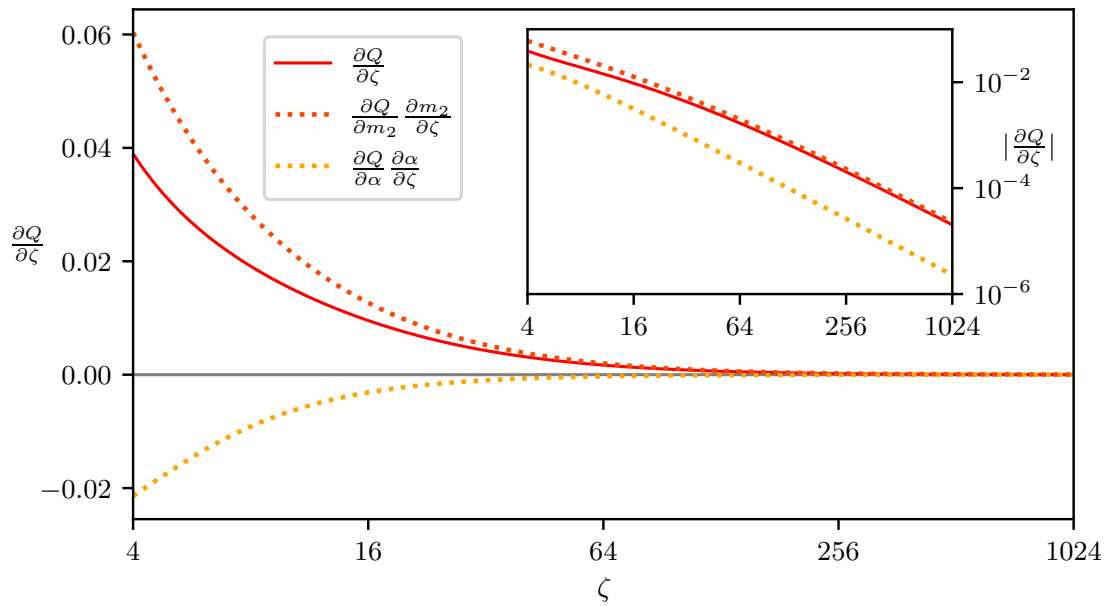


Figure C.5: Derivatives of the flux phenomenological model in function of the magnification  $\zeta$  for  $k_l = 8$ ,  $H = 0.25$ , and  $\xi = 0.05$  for parameters from Table 3.6.



## HBEM repository

Our implementation of Fast-BEM [Beguin and Yastrebov, 2023] follows the folder organization below. The folder `src` contains two folders `Gmsh`, `Hierarchy`. The first one includes all the functions related to reading mesh files `mesh.msh`, created by GMSH software, in format `.2` or `.4`. These mesh files are ASCII files and include all the coordinates and all element definition. The folder `Hierarchy` encloses the functions related to the integration in the folder `src`, the treatment of the  $\mathcal{H}$ -matrices, and finally the function `FastBem` called for the fast integration.

```
root/
├── src/
│   ├── Gmsh/
│   │   ├── GeomGmshRead()
│   │   ├── meshrotate()
│   │   └── meshsmirror()
│   └── Hierarchy/
│       ├── Cluster/
│       │   ├── split()
│       │   ├── splittilt()
│       │   ├── splitkmeans()
│       │   └── is()
│       └── src
│           ├── optim
│           │   └── G()
│           ├── interg6()
│           ├── integpartt()
│           ├── integqsing()
│           └── integsing()
├── Harithmetic
│   ├── ACAplus()
│   ├── HOptim()
│   ├── HAdmi()
│   ├── HAdd()
│   └── HMatVect()
├── FastInteg()
├── tests
└── examples
```



---

## Bibliography

---

- [Afferrante et al., 2012] Afferrante, L., Carbone, G., and Demelio, G. (2012). Interacting and coalescing hertzian asperities: A new multiasperity contact model. *Wear*, 278:28–33.
- [Aichi, 1994] Aichi, H. (1994). Analysis on the constriction resistance of the electric contact by the contact model using the electrolyte bath. In *Proc. 17th Intl. Conf. on Electrical Contacts*, pages 1–6.
- [Akarapu et al., 2011] Akarapu, S., Sharp, T., and Robbins, M. O. (2011). Stiffness of contacts between rough surfaces. *Physical Review Letters*, 106(20):204301.
- [Antler et al., 1975] Antler, M., Graddick, W., and Tompkins, H. (1975). Base metal contacts: An exploratory study of separable connection to tin-lead. *IEEE Transactions on Parts, Hybrids, and Packaging*, 11(1):35–44.
- [Araújo and Nowell, 1999] Araújo, J. and Nowell, D. (1999). Analysis of pad size effects in fretting fatigue using short crack arrest methodologies. *International Journal of Fatigue*, 21(9):947–956.
- [Archard, 1953] Archard, J. (1953). Contact and rubbing of flat surfaces. *Journal of applied physics*, 24(8):981–988.
- [Archard, 1957] Archard, J. (1957). Elastic deformation and the laws of friction. *Proceedings of the royal society of London. Series A. Mathematical and physical sciences*, 243(1233):190–205.
- [Arnaud et al., 2021] Arnaud, P., Baydoun, S., and Fouvry, S. (2021). Modeling adhesive and abrasive wear phenomena in fretting interfaces: A multiphysics approach coupling friction energy, third body and contact oxygenation concepts. *Tribology International*, 161:107077.
- [Bahrami et al., 2004] Bahrami, M., Yovanovich, M. M., and Culham, J. R. (2004). Thermal joint resistances of conforming rough surfaces with gas filled caps. *Journal of Thermophysics and Heat Transfer*, 18(3):318–325.
- [Barber, 2003] Barber, J. (2003). Bounds on the electrical resistance between contacting elastic rough bodies. *Proceedings of the royal society of London. Series A: mathematical, physical and engineering sciences*, 459(2029):53–66.
- [Barber, 2018] Barber, J. R. (2018). *Contact mechanics*, volume 250. Springer.
- [Bebendorf, 2000] Bebendorf, M. (2000). Approximation of boundary element matrices. *Numerische Mathematik*, 86:565–589.

- [Bebendorf, 2003] Bebendorf, M. (2003). Adaptive low-rank approximation of collocation matrices. *Computing*, 70:1–24.
- [Bebendorf, 2008] Bebendorf, M. (2008). *Hierarchical matrices*. Springer.
- [Bebendorf and Kunis, 2009] Bebendorf, M. and Kunis, S. (2009). Recompression techniques for adaptive cross approximation. *The Journal of Integral Equations and Applications*, pages 331–357.
- [Bebendorf and Venn, 2012] Bebendorf, M. and Venn, R. (2012). Constructing nested bases approximations from the entries of non-local operators. *Numerische Mathematik*, 121(4):609–635.
- [Beguin and Yastrebov, 2023] Beguin, P. and Yastrebov, V. (2023). Fast-BEM code for Poisson’s equation on a half-space. [github.com/vyastreb/HBEM](https://github.com/vyastreb/HBEM).
- [Berry et al., 1980] Berry, M. V., Lewis, Z., and Nye, J. F. (1980). On the weierstrass-mandelbrot fractal function. *Proceedings of the Royal Society of London. A. Mathematical and Physical Sciences*, 370(1743):459–484.
- [Beskos, 1987] Beskos, D. E. (1987). Boundary element methods in dynamic analysis. *Applied Mechanics Reviews*, 40(1):1–23.
- [Bettess, 1977] Bettess, P. (1977). Infinite elements. *International Journal for numerical methods in engineering*, 11(1):53–64.
- [Binney and Tremaine, 2011] Binney, J. and Tremaine, S. (2011). *Galactic dynamics*, volume 20. Princeton university press.
- [Blanchet, 1998] Blanchet, L. (1998). On the multipole expansion of the gravitational field. *Classical and Quantum Gravity*, 15(7):1971.
- [Blunt and Jiang, 2003] Blunt, L. and Jiang, X. (2003). *Advanced techniques for assessment surface topography: development of a basis for 3D surface texture standards” surfstand”*. Elsevier.
- [Bonnet, 1999] Bonnet, M. (1999). *Boundary integral equation methods for solids and fluids*. Springer.
- [Börm et al., 2003] Börm, S., Grasedyck, L., and Hackbusch, W. (2003). Introduction to hierarchical matrices with applications. *Engineering analysis with boundary elements*, 27(5):405–422.
- [Boussinesq, 1885] Boussinesq, J. (1885). *Application des potentiels à l’étude de l’équilibre et du mouvement des solides élastiques*. Gauthier-Villars.
- [Bouwkamp and Casimir, 1954] Bouwkamp, C. and Casimir, H. (1954). On multipole expansions in the theory of electromagnetic radiation. *Physica*, 20(1-6):539–554.
- [Bowden and Tabor, 1967] Bowden, F. P. and Tabor, D. (1967). *Friction and lubrication*.
- [Bower and Johnson, 1989] Bower, A. and Johnson, K. (1989). The influence of strain hardening on cumulative plastic deformation in rolling and sliding line contact. *Journal of the Mechanics and Physics of Solids*, 37(4):471–493.
- [Boyer, 2001a] Boyer, L. (2001a). Contact resistance calculations: generalizations of greenwood’s formula including interface films. *IEEE Transactions on Components and Packaging Technologies*, 24(1):50–58.

- [Boyer, 2001b] Boyer, L. (2001b). Contact resistance calculations: Generalizations of greenwood's formula including interface films. *IEEE Transactions on components and packaging technologies*, 24(1):50–58.
- [Bush et al., 1975] Bush, A., Gibson, R., and Thomas, T. (1975). The elastic contact of a rough surface. *Wear*, 35(1):87–111.
- [Cabrera and Mott, 1949] Cabrera, N. and Mott, N. F. (1949). Theory of the oxidation of metals. *Reports on progress in physics*, 12(1):163.
- [Carbone and Bottiglione, 2008] Carbone, G. and Bottiglione, F. (2008). Asperity contact theories: Do they predict linearity between contact area and load? *Journal of the Mechanics and Physics of Solids*, 56(8):2555–2572.
- [Carslaw et al., 1962] Carslaw, H. S., Jaeger, J. C., and Feshbach, H. (1962). Conduction of heat in solids. *Physics Today*, 15(11):74–76.
- [Carvalho et al., 2022] Carvalho, R. P., Carneiro, A. C., Pires, F. A., and Doca, T. (2022). An efficient multiscale strategy to predict the evolution of the real contact area between rough surfaces. *Tribology International*, 165:107255.
- [Ciavarella et al., 1998] Ciavarella, M., Hills, D., and Monno, G. (1998). The influence of rounded edges on indentation by a flat punch. *Proceedings of the Institution of Mechanical Engineers, Part C: Journal of Mechanical Engineering Science*, 212(4):319–327.
- [Collins, 1963] Collins, W. (1963). On the solution of some axisymmetric boundary value problems by means of integral equations: Viii. potential problems for a circular annulus. *Proceedings of the Edinburgh Mathematical Society*, 13(3):235–246.
- [Cooke, 1963] Cooke, J. (1963). Some further triple integral equation solutions. *Proceedings of the Edinburgh Mathematical Society*, 13(4):303–316.
- [Cooper et al., 1969] Cooper, M., Mikic, B., and Yovanovich, M. (1969). Thermal contact conductance. *International Journal of heat and mass transfer*, 12(3):279–300.
- [Devaney and Wolf, 1974] Devaney, A. and Wolf, E. (1974). Multipole expansions and plane wave representations of the electromagnetic field. *Journal of Mathematical Physics*, 15(2):234–244.
- [Dini et al., 2006] Dini, D., Nowell, D., and Dyson, I. N. (2006). The use of notch and short crack approaches to fretting fatigue threshold prediction: Theory and experimental validation. *Tribology international*, 39(10):1158–1165.
- [Dodds and Robson, 1973] Dodds, C. and Robson, J. (1973). The description of road surface roughness. *Journal of sound and vibration*, 31(2):175–183.
- [Doherty and Davis, 1963] Doherty, P. and Davis, R. (1963). Direct observation of the oxidation of aluminum single-crystal surfaces. *Journal of Applied Physics*, 34(3):619–628.
- [Dyson and Hirst, 1954] Dyson, J. and Hirst, W. (1954). The true contact area between solids. *Proceedings of the Physical Society. Section B*, 67(4):309.
- [Engheta et al., 1992] Engheta, N., Murphy, W. D., Rokhlin, V., and Vassiliou, M. S. (1992). The fast multipole method (fmm) for electromagnetic scattering problems. *IEEE Transactions on Antennas and Propagation*, 40(6):634–641.
- [Ermoline and Dreizin, 2011] Ermoline, A. and Dreizin, E. L. (2011). Equations for the cabrera–mott kinetics of oxidation for spherical nanoparticles. *Chemical Physics Letters*, 505(1-3):47–50.



- [Fabrikant, 1986] Fabrikant, V. (1986). Flat punch of arbitrary shape on an elastic half-space. *International journal of engineering science*, 24(11):1731–1740.
- [Fabrikant, 1993] Fabrikant, V. (1993). Dirichlet problem for an annular disk. *Zeitschrift für angewandte Mathematik und Physik ZAMP*, 44(2):333–347.
- [Fiutak, 1963] Fiutak, J. (1963). The multipole expansion in quantum theory. *Canadian Journal of Physics*, 41(1):12–20.
- [Frérot et al., 2020] Frérot, L., Anciaux, G., Rey, V., Pham-Ba, S., and Molinari, J.-F. (2020). Tamaas: a library for elastic-plastic contact of periodic rough surfaces. *Journal of Open Source Software*, 5(51):2121.
- [Frérot et al., 2019] Frérot, L., Bonnet, M., Molinari, J.-F., and Anciaux, G. (2019). A Fourier-accelerated volume integral method for elastoplastic contact. *Computer Methods in Applied Mechanics and Engineering*, 351:951–976.
- [Galín, 1961] Galín, L. A. (1961). *Contact problems in the theory of elasticity*. School of Physical Sciences and Applied Mathematics, North Carolina State College. translated from the Russian by H. Moss, editor I. N. Sneddon.
- [Gao et al., 2006] Gao, Y., Bower, A., Kim, K.-S., Lev, L., and Cheng, Y. (2006). The behavior of an elastic–perfectly plastic sinusoidal surface under contact loading. *Wear*, 261(2):145–154.
- [Gao and Bower, 2006] Gao, Y.-F. and Bower, A. (2006). Elastic–plastic contact of a rough surface with weierstrass profile. *Proceedings of the Royal Society A: Mathematical, Physical and Engineering Sciences*, 462(2065):319–348.
- [Geuzaine and Remacle, 2009] Geuzaine, C. and Remacle, J.-F. (2009). Gmsh: A 3-d finite element mesh generator with built-in pre- and post-processing facilities. *International journal for numerical methods in engineering*, 79(11):1309–1331.
- [Goodier and Timoshenko, 1970] Goodier, J. N. and Timoshenko, S. (1970). *Theory of elasticity*. McGraw-Hill.
- [Goreinov et al., 1997] Goreinov, S. A., Tyrtysnikov, E. E., and Zamarashkin, N. L. (1997). A theory of pseudoskeleton approximations. *Linear algebra and its applications*, 261(1-3):1–21.
- [Grasedyck, 2005] Grasedyck, L. (2005). Adaptive recompression of  $\langle$ -matrices for BEM. *Computing*, 74(3):205–223.
- [Grasedyck and Hackbusch, 2003] Grasedyck, L. and Hackbusch, W. (2003). Construction and arithmetics of  $\langle$ -matrices. *Computing*, 70:295–334.
- [Green and Zerna, 1992] Green, A. E. and Zerna, W. (1992). *Theoretical elasticity*. Courier Corporation.
- [Greengard and Rokhlin, 1987] Greengard, L. and Rokhlin, V. (1987). A fast algorithm for particle simulations. *Journal of computational physics*, 73(2):325–348.
- [Greengard and Rokhlin, 1997] Greengard, L. and Rokhlin, V. (1997). A new version of the fast multipole method for the laplace equation in three dimensions. *Acta numerica*, 6:229–269.
- [Greenwood, 2006] Greenwood, J. (2006). A simplified elliptic model of rough surface contact. *Wear*, 261(2):191–200.

- [Greenwood, 2007] Greenwood, J. (2007). A note on nayak's third paper. *Wear*, 262(1-2):225–227.
- [Greenwood et al., 1984] Greenwood, J., Johnson, K., and Matsubara, E. (1984). A surface roughness parameter in hertz contact. *wear*, 100(1-3):47–57.
- [Greenwood, 1966] Greenwood, J. A. (1966). Constriction resistance and the real area of contact. *British Journal of Applied Physics*, 17(12):1621.
- [Greenwood and Tripp, 1967] Greenwood, J. A. and Tripp, J. H. (1967). The elastic contact of rough spheres. *Journal of Applied Mechanics*, 34(1):153–159.
- [Greenwood and Williamson, 1966] Greenwood, J. A. and Williamson, J. P. (1966). Contact of nominally flat surfaces. *Proceedings of the royal society of London. Series A. Mathematical and physical sciences*, 295(1442):300–319.
- [Grzesik et al., 2007] Grzesik, W., Rech, J., and Wanat, T. (2007). Surface finish on hardened bearing steel parts produced by superhard and abrasive tools. *International Journal of Machine Tools and Manufacture*, 47(2):255–262.
- [Gujjula and Ambikasaran, 2022] Gujjula, V. and Ambikasaran, S. (2022). A new nested cross approximation. *arXiv preprint arXiv:2203.14832*.
- [Hackbusch and Nowak, 1989] Hackbusch, W. and Nowak, Z. P. (1989). On the fast matrix multiplication in the boundary element method by panel clustering. *Numerische Mathematik*, 54(4):463–491.
- [Hart and Maurin, 1970] Hart, R. and Maurin, J. (1970). The nucleation and growth of oxide islands on aluminum. *Surface Science*, 20(2):285–303.
- [Hayami and Matsumoto, 1994] Hayami, K. and Matsumoto, H. (1994). A numerical quadrature for nearly singular boundary element integrals. *Engineering Analysis with Boundary Elements*, 13(2):143–154.
- [Hertz, 1881] Hertz, H. (1881). Über die berührung fester elastischer körper. *J reine und angewandte Mathematik*, 92:156.
- [Hills et al., 2012] Hills, D., Thaitirarot, A., Barber, J., and Dini, D. (2012). Correlation of fretting fatigue experimental results using an asymptotic approach. *International Journal of Fatigue*, 43:62–75.
- [Holm, 1967] Holm, R. (1967). *Electric Contacts*. Springer Berlin Heidelberg.
- [Hu and Tonder, 1992] Hu, Y. and Tonder, K. (1992). Simulation of 3-D random rough surface by 2-D digital filter and Fourier analysis. *International journal of machine tools and manufacture*, 32(1-2):83–90.
- [Hughes et al., 2005] Hughes, T., Cottrell, J., and Bazilevs, Y. (2005). Isogeometric analysis: Cad, finite elements, nurbs, exact geometry and mesh refinement. *Computer Methods in Applied Mechanics and Engineering*, 194(39):4135–4195.
- [Huin et al., 2005] Huin, D., Flauder, P., and Leblond, J.-B. (2005). Numerical simulation of internal oxidation of steels during annealing treatments. *Oxidation of Metals*, 64:131–167.
- [Hyun et al., 2004] Hyun, S., Pei, L., Molinari, J.-F., and Robbins, M. O. (2004). Finite-element analysis of contact between elastic self-affine surfaces. *Physical review E*, 70(2):026117.

- [Jeurgens et al., 2002] Jeurgens, L., Sloof, W., Tichelaar, F., and Mittemeijer, E. (2002). Growth kinetics and mechanisms of aluminum-oxide films formed by thermal oxidation of aluminum. *Journal of applied physics*, 92(3):1649–1656.
- [Jiang and Sehitoglu, 1999] Jiang, Y. and Sehitoglu, H. (1999). A model for rolling contact failure. *Wear*, 224(1):38–49.
- [Joe et al., 2022] Joe, J., Barber, J., and Raeymaekers, B. (2022). A general load–displacement relationship between random rough surfaces in elastic, non-adhesive contact, with application in metal additive manufacturing. *Tribology Letters*, 70(3):77.
- [Johnson, 1987] Johnson, K. L. (1987). *Contact mechanics*. Cambridge university press.
- [Kandler and Schröder, 2014] Kandler, U. and Schröder, C. (2014). Spectral error bounds for hermitian inexact krylov methods. *Preprint*, 11.
- [Kikuchi and Oden, 1988] Kikuchi, N. and Oden, J. T. (1988). *Contact problems in elasticity: a study of variational inequalities and finite element methods*. SIAM.
- [Kim et al., 2007] Kim, J.-Y., Kang, S.-K., Lee, J.-J., Jang, J.-i., Lee, Y.-H., and Kwon, D. (2007). Influence of surface-roughness on indentation size effect. *Acta materialia*, 55(10):3555–3562.
- [Kluppel and Heinrich, 2000] Kluppel, M. and Heinrich, G. (2000). Rubber friction on self-affine road tracks. *Rubber chemistry and technology*, 73(4):578–606.
- [Kogut and Komvopoulos, 2004] Kogut, L. and Komvopoulos, K. (2004). Analysis of the spherical indentation cycle for elastic–perfectly plastic solids. *Journal of materials research*, 19(12):3641–3653.
- [Konyukhov and Izi, 2015] Konyukhov, A. and Izi, R. (2015). *Introduction to computational contact mechanics: a geometrical approach*. John Wiley & Sons.
- [Kumar et al., 2000] Kumar, R., Kumar, S., Prakash, B., and Sethuramiah, A. (2000). Assessment of engine liner wear from bearing area curves. *Wear*, 239(2):282–286.
- [Lampimäki et al., 2007] Lampimäki, M., Lahtonen, K., Hirsimäki, M., and Valden, M. (2007). Nanoscale oxidation of cu (100): Oxide morphology and surface reactivity. *The Journal of chemical physics*, 126(3).
- [Lang, 1962] Lang, P. M. (1962). Calculating heat transfer across small gas-filled gaps. *Nucleonics (US) Ceased Publication*, 20(1).
- [Las Casas et al., 2008] Las Casas, E., Bastos, F., Godoy, G., and Buono, V. (2008). Enamel wear and surface roughness characterization using 3d profilometry. *Tribology International*, 41(12):1232–1236.
- [Lawless, 1974] Lawless, K. R. (1974). The oxidation of metals. *Reports on Progress in Physics*, 37(2):231.
- [Leach, 2014] Leach, R. (2014). *Fundamental principles of engineering nanometrology*. Elsevier.
- [Leach et al., 2015] Leach, R. K., Giusca, C., Haitjema, H., Evans, C., and Jiang, X. (2015). Calibration and verification of areal surface texture measuring instruments. *CIRP Annals*, 64(2):797–813.
- [Lee and Cho, 2012] Lee, D.-H. and Cho, N.-G. (2012). Assessment of surface profile data acquired by a stylus profilometer. *Measurement science and technology*, 23(10):105601.

- [Lichinchi et al., 1998] Lichinchi, M., Lenardi, C., Haupt, J., and Vitali, R. (1998). Simulation of berkovich nanoindentation experiments on thin films using finite element method. *Thin solid films*, 312(1-2):240–248.
- [Liu et al., 2000] Liu, S., Wang, Q., and Liu, G. (2000). A versatile method of discrete convolution and FFT (DC-FFT) for contact analyses. *Wear*, 243(1-2):101–111.
- [Liu, 2009] Liu, Y. (2009). *Fast multipole boundary element method: theory and applications in engineering*. Cambridge university press.
- [Longuet-Higgins, 1957] Longuet-Higgins, M. S. (1957). The statistical analysis of a random, moving surface. *Philosophical Transactions of the Royal Society of London. Series A, Mathematical and Physical Sciences*, 249(966):321–387.
- [Love, 1976] Love, E. R. (1976). Inequalities for the capacity of an electrified conducting annular disc. *Proceedings of the Royal Society of Edinburgh Section A: Mathematics*, 74:257–270.
- [MacQueen, 1967] MacQueen, J. (1967). Some methods for classification and analysis of multivariate observations. In *Proceedings of the Fifth Berkeley Symposium on Mathematical Statistics and Probability, 1967*, pages 281–297. Oakland, CA, USA.
- [Madhusudana, 1996] Madhusudana, C. V. (1996). *Thermal contact conductance*, volume 79. Springer.
- [Majumdar and Tien, 1990] Majumdar, A. and Tien, C. L. (1990). Fractal characterization and simulation of rough surfaces. *Wear*, 136(2):313–327.
- [Mandelbrot, 1967] Mandelbrot, B. (1967). How long is the coast of britain? statistical self-similarity and fractional dimension. *Science*, 156(3775):636–638.
- [Mandelbrot, 1982] Mandelbrot, B. B. (1982). *The fractal geometry of nature*, volume 1. WH freeman New York.
- [Mandelbrot, 1985] Mandelbrot, B. B. (1985). Self-affine fractals and fractal dimension. *Physica scripta*, 32(4):257.
- [Manners and Greenwood, 2006] Manners, W. and Greenwood, J. (2006). Some observations on persson’s diffusion theory of elastic contact. *Wear*, 261(5-6):600–610.
- [Meakin, 1998] Meakin, P. (1998). *Fractals, scaling and growth far from equilibrium*, volume 5. Cambridge university press.
- [Mendeleyev, 1997] Mendeleyev, V. Y. (1997). Dependence of measuring errors of rms roughness on stylus tip size for mechanical profilers. *Applied optics*, 36(34):9005–9009.
- [Meyer, 1908] Meyer, E. (1908). Untersuchungen über härteprüfung und härte. *Zeitschrift des Vereines Deutscher Ingenieure*, 52(17):645–654.
- [Meymand et al., 2016] Meymand, S. Z., Keylin, A., and Ahmadian, M. (2016). A survey of wheel–rail contact models for rail vehicles. *Vehicle System Dynamics*, 54(3):386–428.
- [Monti et al., 2021] Monti, J. M., Pastewka, L., and Robbins, M. O. (2021). Green’s function method for dynamic contact calculations. *Physical Review E*, 103(5):053305.
- [Monti et al., 2022] Monti, J. M., Pastewka, L., and Robbins, M. O. (2022). Fractal geometry of contacting patches in rough elastic contacts. *Journal of the Mechanics and Physics of Solids*, 160:104797.

- [Nakamura, 1993] Nakamura, M. (1993). Constriction resistance of conducting spots by the boundary element method. *IEEE transactions on components, hybrids, and manufacturing technology*, 16(3):339–343.
- [Nakamura, 1995] Nakamura, M. (1995). Computer simulation for the constriction resistance depending on the form of conducting spots. *IEEE Transactions on Components, Packaging, and Manufacturing Technology: Part A*, 18(2):382–384.
- [Nakamura and Minowa, 1986] Nakamura, M. and Minowa, I. (1986). Computer simulation for the conductance of a contact interface. *IEEE transactions on components, Hybrids, and Manufacturing technology*, 9(2):150–155.
- [Nakamura and Minowa, 1989] Nakamura, M. and Minowa, I. (1989). Film resistance and constriction effect of current in a contact interface. *IEEE transactions on components, hybrids, and manufacturing technology*, 12(1):109–113.
- [Nayak, 1971] Nayak, P. R. (1971). Random process model of rough surfaces. *Journal of tribology*.
- [Nayak, 1973] Nayak, P. R. (1973). Random process model of rough surfaces in plastic contact. *Wear*, 26(3):305–333.
- [Osias and Tripp, 1966] Osias, J. and Tripp, J. (1966). Mechanical disruption of surface films on metals. *Wear*, 9(5):388–397.
- [Papangelo et al., 2017] Papangelo, A., Hoffmann, N., and Ciavarella, M. (2017). Load-separation curves for the contact of self-affine rough surfaces. *Scientific reports*, 7(1):6900.
- [Park et al., 2006] Park, J.-j., Kwon, K., and Cho, N. (2006). Development of a coordinate measuring machine (cmm) touch probe using a multi-axis force sensor. *Measurement Science and Technology*, 17(9):2380.
- [Pastewka et al., 2013] Pastewka, L., Prodanov, N., Lorenz, B., Müser, M. H., Robbins, M. O., and Persson, B. N. (2013). Finite-size scaling in the interfacial stiffness of rough elastic contacts. *Physical Review E*, 87(6):062809.
- [Pastewka and Robbins, 2014] Pastewka, L. and Robbins, M. O. (2014). Contact between rough surfaces and a criterion for macroscopic adhesion. *Proceedings of the National Academy of Sciences*, 111(9):3298–3303.
- [Pastewka and Robbins, 2016] Pastewka, L. and Robbins, M. O. (2016). Contact area of rough spheres: Large scale simulations and simple scaling laws. *Applied Physics Letters*, 108(22).
- [Pei et al., 2005] Pei, L., Hyun, S., Molinari, J., and Robbins, M. O. (2005). Finite element modeling of elasto-plastic contact between rough surfaces. *Journal of the Mechanics and Physics of Solids*, 53(11):2385–2409.
- [Persson, 2001a] Persson, B. (2001a). Elastoplastic contact between randomly rough surfaces. *Physical Review Letters*, 87(11):116101.
- [Persson, 2001b] Persson, B. N. (2001b). Theory of rubber friction and contact mechanics. *The Journal of Chemical Physics*, 115(8):3840–3861.
- [Persson et al., 2004] Persson, B. N., Albohr, O., Tartaglino, U., Volokitin, A., and Tosatti, E. (2004). On the nature of surface roughness with application to contact mechanics, sealing, rubber friction and adhesion. *Journal of physics: Condensed matter*, 17(1):R1.
- [Pillai et al., 2021] Pillai, R., Chyrkin, A., and Quadackers, W. (2021). Modeling in high temperature corrosion: a review and outlook. *Oxidation of Metals*, 96(5-6):385–436.

- [Pinnel and Bradford, 1980] Pinnel, M. and Bradford, K. (1980). Influence of some geometric factors on contact resistance probe measurements. *IEEE Transactions on Components, Hybrids, and Manufacturing Technology*, 3(1):159–165.
- [Podio-Guidugli et al., 2014] Podio-Guidugli, P., Favata, A., et al. (2014). Elasticity for geotechnicians. In *A modern exposition of Kelvin, Boussinesq, Flammand, Cerrutti, Melan and Mindlin problems*. Springer.
- [Polonsky and Keer, 1999] Polonsky, I. and Keer, L. (1999). A numerical method for solving rough contact problems based on the multi-level multi-summation and conjugate gradient techniques. *Wear*, 231(2):206–219.
- [Popp and Wriggers, 2018] Popp, A. and Wriggers, P. (2018). *Contact modeling for solids and particles*, volume 585. Springer.
- [Rey et al., 2017] Rey, V., Anciaux, G., and Molinari, J.-F. (2017). Normal adhesive contact on rough surfaces: efficient algorithm for FFT-based BEM resolution. *Computational Mechanics*, 60:69–81.
- [Rezayat et al., 1986] Rezayat, M., Shippy, D., and Rizzo, F. (1986). On time-harmonic elastic-wave analysis by the boundary element method for moderate to high frequencies. *Computer methods in applied mechanics and engineering*, 55(3):349–367.
- [Rice, 2017] Rice, J. R. (2017). Heating, weakening and shear localization in earthquake rupture. *Philosophical Transactions of the Royal Society A: Mathematical, Physical and Engineering Sciences*, 375(2103):20160015.
- [Richardson, 1911] Richardson, L. F. (1911). The approximate arithmetical solution by finite differences with an application to stresses in a masonry dam. *Philosophical Transactions of the Royal Society of America*, 210:307–357.
- [Rokhlin, 1985] Rokhlin, V. (1985). Rapid solution of integral equations of classical potential theory. *Journal of computational physics*, 60(2):187–207.
- [Saad and Schultz, 1986] Saad, Y. and Schultz, M. H. (1986). Gmres: A generalized minimal residual algorithm for solving nonsymmetric linear systems. *SIAM Journal on scientific and statistical computing*, 7(3):856–869.
- [Sackfield et al., 2003] Sackfield, A., Mugadu, A., Barber, J., and Hills, D. (2003). The application of asymptotic solutions to characterising the process zone in almost complete frictionless contacts. *Journal of the Mechanics and Physics of Solids*, 51(7):1333–1346.
- [Semyonov et al., 1984] Semyonov, Y. G., Borisov, S., and Suetin, P. (1984). Investigation of heat transfer in rarefied gases over a wide range of knudsen numbers. *International journal of heat and mass transfer*, 27(10):1789–1799.
- [Slade, 2017] Slade, P. G. (2017). *Electrical contacts: principles and applications*. CRC press.
- [Smythe, 1951] Smythe, W. (1951). The capacitance of a circular annulus. *Journal of Applied Physics*, 22(12):1499–1501.
- [Song and Yovanovich, 1987] Song, S. and Yovanovich, M. (1987). Correlation of thermal accommodation coefficient for engineering surfaces. *ASME HTD*, 69:107–116.
- [Stehfest, 1970] Stehfest, H. (1970). Algorithm 368: Numerical inversion of laplace transforms [d5]. *Communications of the ACM*, 13(1):47–49.
- [Sun et al., 2007] Sun, A. C., Moffat, H. K., Enos, D. G., and George, C. S. (2007). Pore corrosion model for gold-plated copper contacts. *IEEE Transactions on Components and Packaging Technologies*, 30(4):796–804.

- [Telles, 1987] Telles, J. (1987). A self-adaptive co-ordinate transformation for efficient numerical evaluation of general boundary element integrals. *International journal for numerical methods in engineering*, 24(5):959–973.
- [Thomas and Roberts, 1961] Thomas, K. and Roberts, M. (1961). Direct observation in the electron microscope of oxide layers on aluminum. *Journal of Applied Physics*, 32(1):70–75.
- [Thomas and Probert, 1970] Thomas, T. and Probert, S. (1970). Establishment of contact parameters from surface profiles. *Journal of Physics D: Applied Physics*, 3(3):277.
- [Thorne, 1953] Thorne, R. C. (1953). Multipole expansions in the theory of surface waves. *Mathematical Proceedings of the Cambridge Philosophical Society*, 49(4):707–716.
- [Timsit, 1980] Timsit, R. (1980). Some fundamental properties of aluminum-aluminum electrical contacts. *IEEE Transactions on Components, Hybrids, and Manufacturing Technology*, 3(1):71–79.
- [Timsit, 1983] Timsit, R. (1983). On the evaluation of contact temperature from potential-drop measurements. *IEEE Transactions on Components, Hybrids, and Manufacturing Technology*, 6(1):115–121.
- [Urakawa et al., 2013] Urakawa, S., Tomai, S., Ueoka, Y., Yamazaki, H., Kasami, M., Yano, K., Wang, D., Furuta, M., Horita, M., Ishikawa, Y., et al. (2013). Thermal analysis of amorphous oxide thin-film transistor degraded by combination of joule heating and hot carrier effect. *Applied Physics Letters*, 102(5).
- [Van Loan and Golub, 1996] Van Loan, C. F. and Golub, G. (1996). Matrix computations (johns hopkins studies in mathematical sciences). *Matrix Computations*, 5.
- [Westergaard, 1939] Westergaard, H. M. (1939). Bearing pressures and cracks: Bearing pressures through a slightly waved surface or through a nearly flat part of a cylinder, and related problems of cracks. *Journal of Applied Mechanics*.
- [Wexler, 1966] Wexler, G. (1966). The size effect and the non-local boltzmann transport equation in orifice and disk geometry. *Proceedings of the Physical Society*, 89(4):927.
- [Williamson and Greenwood, 1989] Williamson, J. and Greenwood, J. (1989). The constriction resistance between electroplated surfaces. In *Proc. Int. Conf. on Electrical Contacts and Electromechanical Components*, pages 563–568.
- [Wriggers, 2006] Wriggers, P. (2006). *Computational contact mechanics*, volume 2. Springer.
- [Yang et al., 1998] Yang, J., Kolasa, B., Gibson, J., and Yeadon, M. (1998). Self-limiting oxidation of copper. *Applied Physics Letters*, 73(19):2841–2843.
- [Yastrebov, 2013] Yastrebov, V. A. (2013). *Numerical methods in contact mechanics*. John Wiley & Sons.
- [Yastrebov, 2019] Yastrebov, V. A. (2019). The elastic contact of rough spheres investigated using a deterministic multi-asperity model. *Journal of Multiscale Modelling*, 10(01):1841002.
- [Yastrebov et al., 2015a] Yastrebov, V. A., Anciaux, G., and cois Molinari, J.-F. (2015a). From infinitesimal to full contact between rough surfaces: evolution of the contact area. *International Journal of Solids and Structures*, 52:83–102.
- [Yastrebov et al., 2012] Yastrebov, V. A., Anciaux, G., and Molinari, J.-F. (2012). Contact between representative rough surfaces. *Physical Review E*, 86(3):035601.

- [Yastrebov et al., 2015b] Yastrebov, V. A., Anciaux, G., and Molinari, J.-F. (2015b). From infinitesimal to full contact between rough surfaces: evolution of the contact area. *International Journal of Solids and Structures*, 52:83–102.
- [Yastrebov et al., 2017a] Yastrebov, V. A., Anciaux, G., and Molinari, J.-F. (2017a). On the accurate computation of the true contact-area in mechanical contact of random rough surfaces. *Tribology International*, 114:161–171.
- [Yastrebov et al., 2017b] Yastrebov, V. A., Anciaux, G., and Molinari, J.-F. (2017b). The role of the roughness spectral breadth in elastic contact of rough surfaces. *Journal of the Mechanics and Physics of Solids*, 107:469–493.
- [Yastrebov et al., 2014] Yastrebov, V. A., Anciaux, G., and Molinari, J.-F. c. (2014). The contact of elastic regular wavy surfaces revisited. *Tribology Letters*, pages 1–13.
- [Yastrebov et al., 2015c] Yastrebov, V. A., Cailletaud, G., Proudhon, H., Mballa, F. S. M., Noël, S., Testé, P., and Houzé, F. (2015c). Three-level multi-scale modeling of electrical contacts sensitivity study and experimental validation. In *2015 IEEE 61st Holm conference on electrical contacts (Holm)*, pages 414–422. IEEE.
- [Yastrebov et al., 2011] Yastrebov, V. A., Durand, J., Proudhon, H., and Cailletaud, G. (2011). Rough surface contact analysis by means of the finite element method and of a new reduced model. *Comptes Rendus Mécanique*, 339(7-8):473–490.
- [Ye and Komvopoulos, 2003] Ye, N. and Komvopoulos, K. (2003). Indentation analysis of elastic-plastic homogeneous and layered media: Criteria for determining the real material hardness. *J. Trib.*, 125(4):685–691.
- [Zhang et al., 2011] Zhang, P., Lau, Y., and Gilgenbach, R. (2011). Thin film contact resistance with dissimilar materials. *Journal of Applied Physics*, 109(12).
- [Zhang et al., 2012] Zhang, P., Lau, Y., and Timsit, R. S. (2012). On the spreading resistance of thin-film contacts. *IEEE Transactions on electron devices*, 59(7):1936–1940.





# RÉSUMÉ

---

Le problème de la résistance à la conduction aux interfaces de contact représente un défi important en ingénierie. À ces interfaces, la section réduite pour la conduction – définie comme la disparité entre les zones de contact réelles et nominales – entraîne une augmentation de la résistance. Ce phénomène affecte à la fois la conductivité thermique et électrique, marqué par un écart de température ou de potentiel à l'interface. Par conséquent, c'est un phénomène multi-échelle, découlant de la rugosité des surfaces en contact et ayant son origine à l'échelle microscopique. L'objectif de cette étude est d'approfondir notre compréhension des origines de ce phénomène.

Pour aborder le problème de conduction à l'interface de contact, une méthode des éléments de frontière rapide (BEM) a été mise en œuvre. Cette méthode, bénéficiant d'une formulation précise en demi-espace, démontre sa précision et sa cohérence géométrique. Simultanément, le Fast-BEM contourne la complexité excessive  $O(N^2)$  associée au stockage et à la construction d'une matrice dense, qui a été un goulot d'étranglement pour le BEM classique. Cette amélioration des performances est obtenue grâce à l'utilisation de matrices hiérarchiques (H-matrices), qui bénéficient d'une approximation de bas rang, telle que l'approximation croisée adaptative partielle (ACA+). Cette mise en œuvre réduit considérablement le stockage en mémoire, encore amélioré par l'utilisation de la décomposition en valeurs singulières (SVD), et est finalement exploitée pour résoudre le problème avec un solveur itératif GMRES. Par conséquent, ce nouvel outil a démontré sa capacité à aborder des problèmes de conductivité impliquant des géométries complexes.

L'étude de la conductivité commence par une tache conductrice unique sur un demi-espace. Initialement, la forme la plus simple d'une tache non simplement connectée, un anneau, est examinée. Elle est suivie par une investigation de formes "multi-pétales", telles que des fleurs, étoiles et engrenages, révélant comment le nombre de pétales impacte la conductivité. L'étude de taches isolées se conclut par un examen élaboré de géométries auto-affines. Pour les taches multi-pétales et auto-affines, des modèles phénoménologiques sont développés, basés sur des caractéristiques géométriques pertinentes, incluant l'exposant de Hurst et les trois premiers moments spectraux du contour auto-affine. Ces modèles permettent de prédire la conductivité pour un nombre infini de "pétales" et dans la limite auto-affine fractale. Le rôle de la dimension fractale est également souligné, accompagné d'une brève exploration des flocons de Koch. L'étude s'étend à un scénario multi-taches plus réaliste, employant le modèle de résistance à la constriction de Greenwood étendu pour inclure des taches multi-pétales, validé par des simulations BEM. Enfin, l'étude examine la conductivité des zones de contact réelles avec des morphologies complexes produites par le contact élastique entre surfaces rugueuses. Cette étude finale utilise la méthode FFT-BEM pour résoudre le problème de contact et de conductivité rugueux, en s'appuyant sur une analogie de poinçon plat entre la rigidité normale et la résistance thermique ou électrique. De plus, le problème des surfaces rugueuses oxydées est exploré, fusionnant FFT-BEM et Fast-BEM avec des îlots d'oxyde isolants construits à partir d'un champ aléatoire auto-affine. Un modèle phénoménologique préliminaire est également suggéré.

Cette thèse représente une synthèse de la mise en œuvre de H-matrices pour le Fast-BEM, combinée à une caractérisation géométrique détaillée et une analyse physique complète de la résistance à la constriction. Cette analyse s'étend des interfaces conductrices à une seule tache aux zones de contact oxydées de topologie complexe produites par le contact de surfaces rugueuses. Une attention particulière a été accordée à maintenir la précision des résultats numériques. De plus, la mise en œuvre du Fast-BEM développée est disponible en open-source pour une utilisation plus large.

## MOTS CLÉS

---

Conductivité, taches auto-affine, contact rugueux, oxidation, H-matrice, Fast-BEM

## ABSTRACT

---

The problem of conduction resistance at contact interfaces represents an important engineering challenge. At these interfaces, the reduced section for conduction – defined as the disparity between the actual and nominal contact areas – results in increased resistance. This phenomenon affects both thermal and electrical conductivity, marked by a temperature or potential gap at the interface. Hence, it is a multi-scale phenomenon, stemming from the roughness of contacting surfaces and originating at the microscopic level. The objective of this study is to deepen our understanding of this phenomenon's origins.

To address the conduction problem at the contact interface, a Fast-Boundary Element Method (BEM) has been implemented. This method, benefiting from an accurate half-space formulation, demonstrates its precision and geometric consistency. Simultaneously, the Fast-BEM circumvents the excessive  $O(N^2)$  complexity associated with storing and constructing a dense matrix, which has been a bottleneck for the classical BEM. This performance enhancement is achieved through the use of hierarchical matrices (H-matrices), which benefit from a low-rank approximation, such as Adaptive Cross Approximation+ (ACA+). This implementation significantly reduces memory storage, further enhanced by employing Singular Value Decomposition (SVD), and is ultimately exploited in solving the problem with a GMRES iterative solver. Consequently, this new tool has demonstrated its capability to tackle realistic conductivity problems involving complex geometries.

The conductivity study starts with a single conductive spot on a half-space. Initially, the simplest form of a non-simply connected spot, an annulus, is examined. This is followed by an investigation of "multi-petal" shapes, such as flowers, stars, and gears, revealing how the number of petals impacts conductivity. The study of single spots concludes with an elaborate examination of self-affine geometries. For both multi-petal and self-affine spots, phenomenological models are developed, grounded in relevant geometrical characteristics, including the Hurst exponent and the first three spectral moments of the self-affine contour. These models enable predicting conductivity for an infinite number of "petals" and in the fractal self-affine limit. The role of fractal dimension is also underscored, accompanied by a brief exploration of Koch snowflakes.

The study extends to a more realistic multi-spot scenario, employing the Greenwood constriction resistance model extended to include multi-petal spots, validated through BEM simulations. Ultimately, the study examines the conductivity of true contact areas with complex morphologies produced by elastic contact between rough surfaces. This final study utilizes the FFT-BEM method to resolve rough contact and conductivity problem, drawing on a flat-punch analogy between normal stiffness and thermal or electrical resistance. Additionally, the issue of rough oxidized surfaces is explored, merging FFT-BEM and Fast-BEM with insulating oxide islands constructed from a self-affine random field. A preliminary phenomenological model is also suggested.

This thesis represents a synthesis of H-matrices implementation for Fast-BEM, combined with detailed geometrical characterization and a comprehensive physical analysis of constriction resistance. This analysis spans from single-spot conductive interfaces to oxidized contact areas of complex topology produced by the contact of rough surfaces. Particular attention has been devoted to maintaining the precision of the numerical results. Furthermore, the developed Fast-BEM implementation is available as an open-source for broader use.

## KEYWORDS

---

Conductivity, self-affine spots, rough contact, H-matrix, Fast-BEM